

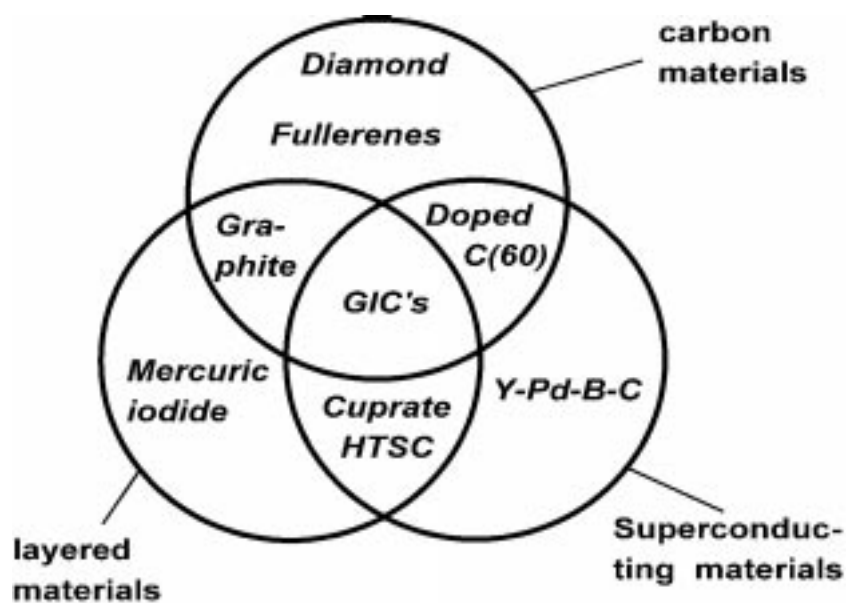
**SCANNING TUNNELING MICROSCOPY OF
LAYERED HIGH TEMPERATURE SUPER-
CONDUCTORS AND CARBON ALLOTROPES**

INAUGURALDISSERTATION

**zur
Erlangung der Würde eines Doktors der Philosophie
vorgelegt der
Philosophisch-Naturwissenschaftlichen Fakultät
der Universität Basel**

**von
Hans Peter Lang
aus Basel**

Basel, 1994



Genehmigt von der Philosophisch-Naturwissenschaftlichen Fakultät
auf Antrag der Herren:

Prof. Dr. H.-J. Güntherodt

Prof. Dr. H. Rudin

Basel, den 30. Mai 1994

Prof. Dr. Hugh Rowell, Dekan

Contents

1	Introduction	10
1.1	Methods	10
1.1.1	Microscopical standard techniques	10
1.1.2	Local probe methods	14
1.2	Materials	20
1.2.1	Layered High-Temperature Superconductors	20
1.2.2	Allotropes of Carbon	25
2	HTSC single crystals	30
2.1	YBCO single crystals	30
2.1.1	Experimental	30
2.1.2	STM investigations on thin YBCO crystal platelets	32
2.1.3	Investigations on thick YBCO crystals	36
2.1.4	Friction force microscopy on thick YBCO crystals	42
2.1.5	Conclusion	46
2.2	BSCCO 2212 single crystals	48
2.2.1	Crystal growth	48
2.2.2	Characterization	48
2.2.3	Structure and TEM	50
2.2.4	Micron scale (SEM and STM)	53
2.2.5	Nanometer scale	53
2.2.6	Atomic scale images	54
2.2.7	Substitution of Ca with La	55
2.2.8	Conclusion	56
3	YBCO thin films	59
3.1	Introduction	59
3.1.1	Pulsed laser deposition	61
3.1.2	Preparation of YBCO thin films	62
3.1.3	Half shadow technique	63
3.1.4	Some remarks on thin film growth	64
3.1.5	Crystal surfaces	65
3.2	YBCO thin films on LaAlO ₃	67
3.2.1	Experimental conditions	67

3.2.2	Superconducting and structural properties	68
3.2.3	STM results on a thickness-gradient film	68
3.2.4	Special types of growth hills	72
3.2.5	Surface modification	75
3.2.6	Conclusion	78
3.3	YBCO thin films on SrTiO ₃ (100)	79
3.3.1	Experimental conditions	79
3.3.2	Analysis of an optimized YBCO film	80
3.3.3	Film orientation	82
3.3.4	Film morphology	84
3.3.5	Superconducting properties	85
3.3.6	Thickness-gradient films	87
3.3.7	Conclusion	89
3.4	YBCO thin films on MgO(001)	90
3.4.1	Experimental conditions	90
3.4.2	Film orientation	90
3.4.3	Film morphology	91
3.4.4	Transmission electron microscopy	92
3.4.5	Thickness-gradient films	96
3.4.6	Conclusion	98
3.5	YBCO thin films by MOCVD	99
3.5.1	Film preparation	99
3.5.2	STM/SFM investigations	100
3.6	YBCO thin films by thermal coevaporation (MBE)	102
3.6.1	Film preparation	102
3.6.2	Reflection high energy electron diffraction	102
3.6.3	Scanning tunneling microscopy	105
3.6.4	Comparing RHEED intensity with STM topography	109
3.6.5	Conclusion	110
3.7	MXPS investigations of YBCO thin films	111
3.7.1	Atomic resolution on YBCO	111
3.7.2	Interpretation based on STM data	111
3.7.3	X-ray photoelectron spectroscopy	114
3.7.4	Previous studies of YBCO by XPS	114
3.7.5	Angle-resolved photoemission	114
3.7.6	Two YBCO thin films for MXPS investigations	117
3.7.7	Determination of the YBCO toplayer	121
3.8	YBCO thin films by LPE	125
3.8.1	Film preparation	125
3.8.2	SFM investigations	126
3.9	ErBaCuO 124 thin films	127
3.9.1	ErBa ₂ Cu ₄ O ₈ ceramics and thin films	127
3.9.2	Structural investigations	127

3.9.3	Conclusion	129
3.10	Summary	130
4	Traditional carbon allotropes and GIC's	136
4.1	Graphite	136
4.2	Graphite intercalation compounds	139
4.2.1	Introduction	139
4.2.2	Experimental conditions	140
4.2.3	STM on binary alkali metal GIC's	143
4.2.4	STM on ternary alkali metal GIC's	149
4.2.5	Discussion	153
4.2.6	Summary	156
4.3	Diamond	157
4.3.1	Introduction	157
4.3.2	Experimental conditions	157
4.3.3	STM on homoepitaxial diamond films on diamond(110)	158
4.3.4	Herringbone-type atomic structure	159
4.3.5	Diamond(100)2x1 reconstruction	159
4.4	Conclusion	165
5	Fullerenes	171
5.1	Introduction	171
5.2	Fullerene films on HOPG and Pt substrates	177
5.2.1	Film casting	177
5.2.2	Fullerene films on HOPG	177
5.2.3	Fullerene films on polycrystalline platinum	178
5.3	Fullerene films on monocrystalline Au substrates	182
5.3.1	Experimental	182
5.3.2	Results	186
5.3.3	STM images of Au(111) substrates	189
5.3.4	Step structure of fullerene films	189
5.3.5	Fullerene films of pure C(60) and mixtures C(60)/C(70)	191
5.3.6	Variation of sublimation parameters	193
5.3.7	Variation of sublimation distance	196
5.3.8	Variation of substrate temperature	199
5.3.9	Dynamic processes	200
5.3.10	Variation of coverage	202
5.3.11	Lattice defects	204
5.3.12	C(70) films	207
5.3.13	Intramolecular contrast	208
5.3.14	Conclusion	209
5.4	Collapsed fullerite	210
5.4.1	Introduction	210

5.4.2	Experimental procedure	211
5.4.3	Results	212
5.4.4	Pair correlation function	216
5.4.5	Angular distribution function	218
5.4.6	Bonding-type distribution	220
5.4.7	Conclusion	221
5.5	Doped/intercalated fullerenes	223
5.5.1	Introduction	223
5.5.2	Materials	226
5.5.3	STM results on granular Rb ₃ C ₆₀	226
5.5.4	STM results on KTI- and RbTI-doped C(60)	228
5.5.5	Conclusion	231
5.5.6	Outlook	231
A	List of Publications	238
B	Oral presentations	244
C	Poster presentations	246
D	Acknowledgements	248
	Index	250
	Curriculum Vitae	254

Preface

When starting to work towards a PhD there is the quest for new scientific issues. Having encountered them specific methods are used to obtain further information. In most cases complementary experiments will be necessary to interpret the results correctly.

The work related to this PhD thesis basically consists of two main parts. Each part is dedicated to a different class of materials: high critical temperature superconductors and different carbon allotropes.¹ The basic method which has been used to characterize these materials is scanning probe microscopy, especially scanning tunneling microscopy (STM). STM is a local imaging technique which is able to provide topographical images of a sample's surface on a micrometre scale as well as on an atomic scale. This is possible taking advantage of the exponential dependence of the tunneling current on the separation distance (in the Å range) between the metallic STM tip and the (conductive) sample when a bias voltage is applied. By means of piezoresistive ceramics – which change in length when a voltage is applied – and a feedback loop electronics that keeps constant the tunneling current (and therewith the tip-sample distance), it is possible to obtain a topography profile of the sample's surface by scanning the tip over the sample and recording the vertical movement of the tip.

The two groups of materials investigated here have not only in common some structural aspects, but also have to some extent similar properties. The high critical temperature superconductors (HTSC) are layered multiple-metal-oxide materials which allow resistance-free current transport at temperatures well above the boiling point of liquid helium (4.2 K). The HTSC investigated here — Y-Ba-Cu-O ($T_c = 92$ K) and Bi-Sr-Ca-Cu-O ($T_c = 80$ K) — even show superconductivity at temperatures above the boiling point of liquid nitrogen (77 K).

Some forms of carbon, such as hexagonal graphite, are also layered materials similar to the HTSC. On doping graphite with alkali metals, graphite intercalation compounds (GIC's) are obtained which are also superconductors, but at very low temperatures (0.55 K for a K-GIC). Cubic diamond becomes conducting if it is doped with boron, and can be studied by STM, too. However, diamond is rather a three-dimensional than a two-dimensional structure. Recently discovered carbon clusters with 60 carbon atoms arranged in a truncated icosahedron structure (C_{60} fullerene) represent an example of an actual three-dimensional molecule which nevertheless forms layers as a solid. Surprisingly upon doping C_{60} with some alkali metals in the ratio 1:3 (C_{60} : alkali metal), new HTSCs are obtained (Rb_3C_{60} with a T_c of 28 K). By application of pressure in the GPa range to these C_{60} fullerenes a new amorphous form of carbon is obtained which is investigated by STM, too.

Even if the invent of scanning probe methods has provided for the first time an easy way to image a surface of a sample in real space with lateral and vertical resolution on

¹Allotropes are the individual forms of an element that occur when more than one type of bonding between atoms of the element is possible. The individual allotropes of an element usually have different physical and chemical properties.

an atomic scale, the results obtained by these methods have always to be compared to information obtained by traditional methods (e.g. diffraction methods or conventional electron microscopy), since artifacts due to the imaging process might influence the information obtained by scanning probe methods.

Overall Summary and Scope

In this thesis the surface morphology of high critical-temperature superconductors (single crystals and thin films) and carbon allotropes (diamond, undoped and doped graphite and fullerenes) prepared under different conditions and by various methods is investigated by local probes (scanning tunneling and force microscopy) and complementary techniques (electron microscopy, X-ray diffraction and photoelectron spectroscopy).

The introductory chapter gives a brief overview on the lateral and vertical resolution capabilities of different microscopical techniques like optical, electron, scanning tunneling and scanning force microscopies illustrated by the example of a high temperature superconductor (HTSC) single crystal. The materials investigated in this thesis are introduced: HTSC and allotropes of carbon.

The growth morphology of HTSC single crystals is investigated in Chapter 2. Very thin (10-30 μm thick) $\text{Y}_2\text{Ba}_4\text{Cu}_{6+N}\text{O}_{14+N}$ ($N=0,1,2$) single crystals show by scanning tunneling microscopy (STM) clean, stepped terraces. It is reported on the first observation of two different square atomic surface lattices (lattice constants 0.38 nm and 0.27 nm) by STM. Thicker $\text{Y}_2\text{Ba}_4\text{Cu}_{6+N}\text{O}_{14+N}$ crystal platelets (30-50 μm) are partially covered by a BaCuO_2 flux layer originating from the crystal growth process. This flux layer is studied by scanning force microscopy (SFM) and friction force microscopy (FFM). The highly curved boundary line of the flux layer imaged by SFM is found to be fractal over more than a decade of length scales. The complexity of the flux layer is related to the different wetting properties of BaCuO_2 and YBCO. FFM is used to show the different tribological properties of BaCuO_2 and YBCO.

The growth of a further HTSC compound ($\text{Bi}_2\text{Sr}_2\text{CaCu}_2\text{O}_8$, BSCCO 2212) as a single crystal is reported in the second part of Chapter 2. The atomic structure and a 27 \AA modulation is studied by STM and transmission electron microscopy (TEM). Performing STM in air leads to modification of the BSCCO 2212 crystal surface. This process is used to intentionally 'write' lines of a width of less than 40 nm on the surface. Stable imaging of the atomic structure is demonstrated to be possible by operating the STM in an argon-filled glove-box. A crystal growth experiment of $\text{Bi}_2\text{Sr}_2\text{LaCu}_2\text{O}_8$ single crystals aimed at the study of the crystals by STM shows that the presence of the 27 \AA modulation can be suppressed.

Chapter 3 treats the growth of thin films of $\text{YBa}_2\text{Cu}_3\text{O}_{7-\delta}$ HTSC by different methods like pulsed laser deposition, metalorganic chemical vapour deposition, liquid phase epitaxy and thermal co-evaporation on various substrate crystals (SrTiO_3 , MgO and LaAlO_3) and preparation conditions. The application of a half-shadow technique (partially shading of the substrate during deposition) allows to study by STM and SFM different growth stages of $\text{YBa}_2\text{Cu}_3\text{O}_{7-\delta}$ thin films prepared under identical conditions

on a single substrate. The images are discussed using film growth models. Structural information on YBCO film growth obtained by X-ray diffraction ($\Theta - 2\Theta$, mosaic spread and azimuth scans) and TEM are related to STM data.

For the first time the correspondence of reflection high energy electron diffraction (RHEED) oscillations to the completion of individual YBCO monolayers is demonstrated by STM images.

The STM observation of two different square atomic surface lattices (0.38 nm and 0.27 nm) on YBCO thin films is given an interpretation by complementary X-ray photoelectron spectroscopy data (monochromatized radiation) implying that the topmost layers of YBCO are the Ba-O and CuO_2 plane layers.

Pulsed laser deposition has been used to prepare $\text{ErBa}_2\text{Cu}_4\text{O}_8$ (ErBCO 124) thin films. STM and TEM investigations are shown to demonstrate for the first time that the stable growth unit of ErBCO 124 comprises two $\text{ErBa}_2\text{Cu}_4\text{O}_8$ units and not only one.

Chapter 4 discusses the classical allotropes of carbon — diamond and graphite. On doping graphite with alkali metals graphite intercalation compounds are obtained. These are subject of a detailed STM study in an inert argon environment. Various superstructures due to intercalated alkali metal atoms are observed.

The last part of Chapter 4 deals with the first observation of atomic structures on boron-doped homoepitaxial diamond films on diamond crystals by STM. Images of the reconstructed (110) and (100) surfaces of diamond are discussed using structure models of diamond.

The last chapter, Chapter 5, is devoted to the recently discovered third allotrope of carbon: fullerenes (C_{60} and C_{70}). Since bulk fullerenes are semiconductors with a large band gap it is not possible to investigate this material by STM. Preparation of thin films by film casting or sublimation onto metal substrates (preferentially Au(111) substrates) yields conductive samples. STM images illustrate the growth of this hexagonal close-packed f.c.c. material. Point defects (vacancies and interstitials) and boundaries are analyzed in fullerene films. Variation of sublimation parameters (substrate temperature and sublimation distance) has a tremendous influence on the $\text{C}_{70}/\text{C}_{60}$ ratio in fullerene films prepared from mixtures of C_{60} and C_{70} .

By application of pressure in the GPa range using a STM operated at high tunneling currents in the low tunneling resistance regime it is possible for the first time to transform part of a C_{60} film into amorphous carbon and image this structure by STM. A pair correlation function calculated for this amorphous 'collapsed fullerite' structure yields a nearest-neighbour distances of 2.7 Å. The angular distribution function (3-atom distribution function) is characteristic of an amorphous structure.

Doping of fullerenes with alkali metals results in superconducting compounds. A study by STM, however, shows only the fullerene molecules, but no intercalant atoms since a complete charge transfer from the alkali metal atom to the fullerene molecule takes place.

Concluding remarks emphasize again the impact of STM/SFM to basic research on novel materials like cuprate and fullerene HTSC, but also re-question the usability of these materials in technical application.

Chapter 1

Introduction

1.1 Methods

1.1.1 Microscopical standard techniques

A way of understanding matter, its properties and morphology is examining it by just looking at it. Various methods have been developed in the course of time to investigate matter. In this introductory part the strengths, the capabilities and the disadvantages of several microscopical methods are discussed and compared in order to show how a specific piece of matter can be examined. In the present case it is a single crystal of a high-temperature superconductor. These crystals¹ with a chemical composition of $\text{YBa}_2\text{Cu}_4\text{O}_8$ have a rectangular, platelike shape.

The optical micrograph (fig. 1.1) shows macrosteps and flat terraces. At higher magnification smaller details become visible like some distinct step pattern (marked with 'A' and 'B' in fig. 1.2). The contrast in the image is mainly due to the different nature and reflective properties of some parts of the surface. In classical optical microscopy² the resolution is limited by the wavelength of the light used for imaging. This limit is about $0.3 \mu\text{m}$ for visible light.³ A typical magnification achieved in optical microscopy is $\times 1000$. The vertical resolution in optical microscopy is comparatively low.⁴ However, by using special interference techniques like differential interference contrast (Nomarski) or phase contrast [1.3, 1.4] a vertical resolution of well below a fraction of the light wavelength (in some cases below 1 nm) can be achieved.

The invention of electron microscopes⁵ has enabled higher image magnifications up

¹The crystals have been grown by J. Karpinski and E. Kaldis, Federal Institute of Technology, Zürich (Switzerland).

²The recent development of scanning near-field optical microscopy (SNOM) by using piezoceramic positioning elements and actuators shall not be discussed here. This technique does no longer suffer from the limitations due to diffraction of a light wave in a lens-based focusing system, since no lenses are used. The method yields a resolution of better than 50 nm [1.1, 1.2].

³The resolution limit in conventional (lens-system based) far-field optical microscopy is given by the Rayleigh criterion: $\Delta x > 0.61\lambda/n \cdot \sin \theta$. Δx denotes the resolution limit, λ the wavelength of the employed radiation and $n \cdot \sin \theta$ the numerical aperture.

⁴The vertical resolution of optical microscopy is also in the order of one light wavelength.

⁵In the following electron microscopes in transmission geometry (TEM) shall not be considered here since that type of microscope yields diffraction images rather of the bulk of a sample than of its surface.

to $\times 100'000$ in lateral and vertical directions.⁶

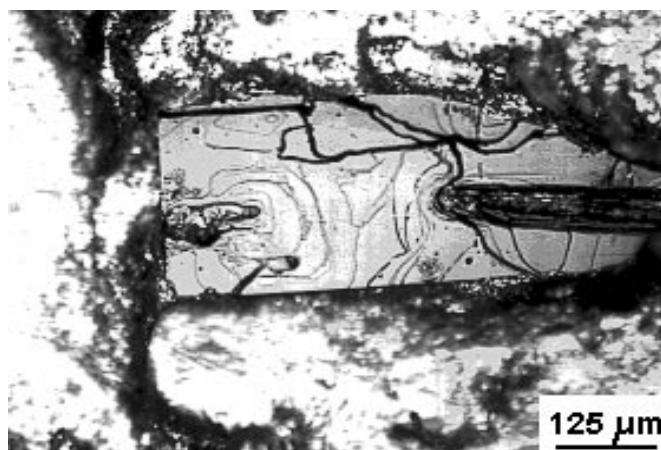


Figure 1.1: Optical micrograph of a $\text{YBa}_2\text{Cu}_4\text{O}_8$ high critical transition temperature (high- T_c) single crystal. The crystal dimensions are $600 \mu\text{m} \times 250 \mu\text{m} \times 40 \mu\text{m}$, approximately.

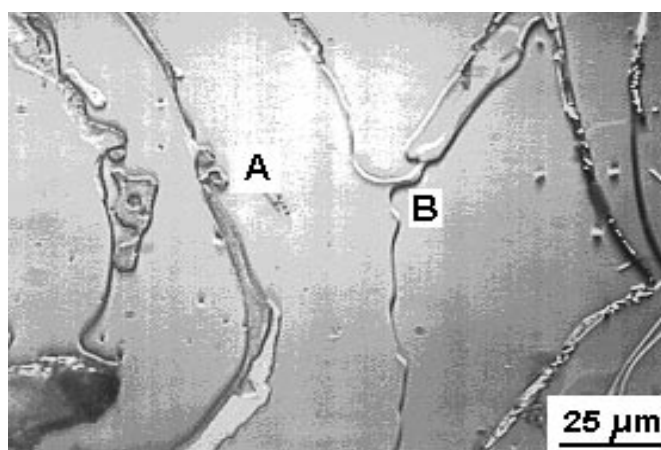


Figure 1.2: Optical micrograph at higher magnification of the same $\text{YBa}_2\text{Cu}_4\text{O}_8$ crystal as in fig. 1.1. Distinct step patterns are marked by 'A' and 'B'. The contrast in the image is explained by the different reflective properties in some areas on the sample. Step contrast is enhanced by illuminating the sample from the left side.

Special modified types of electron microscopes in reflection geometry with grazing incidence of the electron beam (reflection electron microscope, REM; scanning reflection electron microscope, SREM [1.5]) give indeed an image of the surface of a sample but are based on diffraction, too. The resolution may be as good as 1 nm in directions perpendicular to the incident electron beam, but much less parallel to the electron beam. This results in severely foreshortened images in direction of the incident beam.

⁶Modern electron microscopes offer lateral and vertical resolutions of about 10 nm.

Upon irradiating the sample by a focused beam of electrons secondary electrons are emitted. These are used to reconstruct an image of the sample's surface. The possibility to scan the electron beam rapidly over the sample's surface with a frequency of about 50 images per second allows a quick investigation of different spots of the sample's surface under different tilt and rotation angles. The imaging process in such a scanning electron microscope (SEM) consists of splitting up a planar projection of a three-dimensional object in a time component (depending on the coordinates of the scanning electron beam) and an amplitude component (electron detector yield). Reuniting the two components gives an image of the sample's surface. In contrast to optical microscopes electron microscopes require conductive samples and a vacuum for operation since the mean free path of electrons is limited by their energy and the surrounding pressure.

Various information can be extracted from a SEM image: according to the energy of the detected electrons a secondary-electron-image or a backscattered-electron-image (e.g. by elastic scattering of primary electrons of the electron beam) is obtained. In the latter case element-specific information is obtained. The contrast is due to the different Z-numbers. Since the secondary electrons have a low kinetic energy (typically 15 eV) the information depth is also very low (≈ 1 nm for metals, ≈ 10 nm for carbon). This yields a high surface sensitivity of the SEM technique.

Accelerated electrons convert approximately 1 % of their kinetic energy loss in X-ray radiation. These X-ray photons have an energy which is equal to the kinetic energy loss of the secondary electron. Measuring the energy distribution of the X-ray photons yields a bremsstrahlung background with element-specific peaks (energy disperse analysis of X-rays, EDAX). The element-specific intensity is proportional to the amount of elements present in the sample.

The contrast mechanism in SEM images is based on the dependence of the counting rate on the angle between electron beam and sample (*plane tilt contrast*). This is amplified by the *shading contrast* resulting from the fact that secondary electrons are able to reach the detector with a small probability even if they are shaded by other parts of the sample (curved electron trajectories according to the electric field distribution generated by the acceleration voltage). The contrast at edges is enhanced since secondary electrons preferably emerge from sample edges due to the higher electric field at edges (*edge contrast*). The presence of materials of different conductivity gives rise to an image contrast, too (*conductivity contrast*).

Figure 1.3 shows a SEM image of the same high- T_c crystal as previously imaged by optical microscopy (figs. 1.1 and 1.2). The previously mentioned features 'A' and 'B' are shown in figs. 1.4 and 1.5. Tilting the sample gives a better contrast in the SEM image. Further structure is revealed on the surface of the $\text{YBa}_2\text{Cu}_4\text{O}_8$ single crystal (marked by 's' in figs. 1.4 and 1.5). This structure — which is apparently a very thin layer of material on the surface of the crystal — is revealed by SEM only since this material has a conductivity different from that of the crystal material (conductivity contrast).

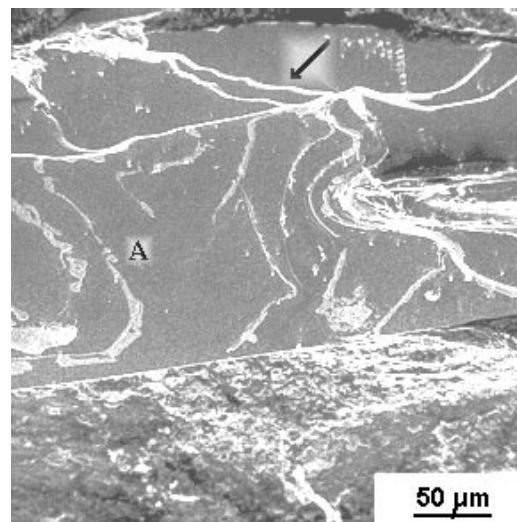


Figure 1.3: Scanning electron micrograph of the same $\text{YBa}_2\text{Cu}_4\text{O}_8$ crystal as shown in fig. 1.1 and 1.2. The contrast in the image is caused by conductivity differences and edge contrast close to crystal steps (see arrow). The surface feature labelled by 'A' in fig. 1.2. is also observed in the scanning electron micrograph.

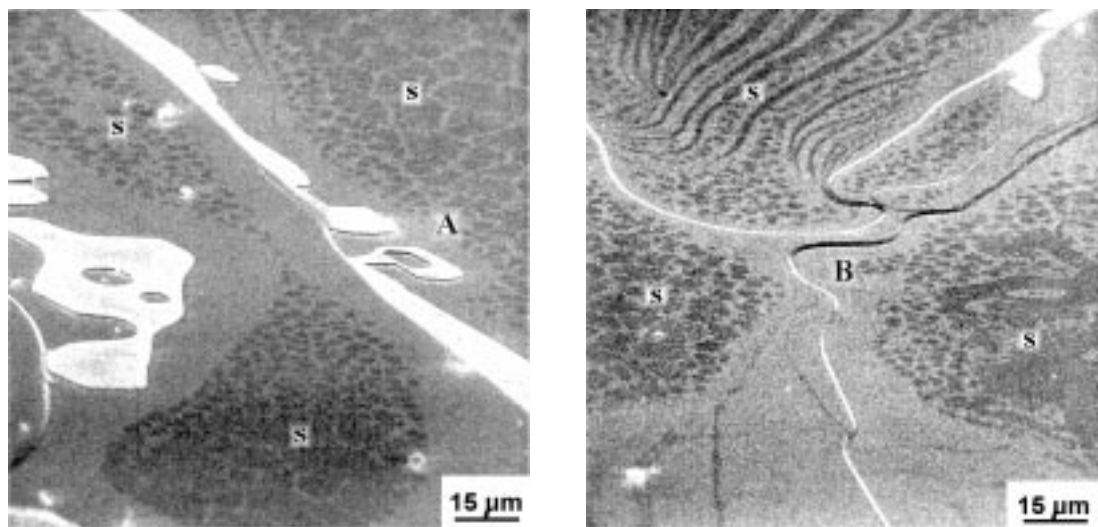


Figure 1.4: *LEFT:* Close view by scanning electron microscopy of the distinct feature labelled with 'A' in the previous images. Note that the crystal was tilted in the electron microscope to increase the step contrast (tilt angle: 50°). Additional structures are revealed by SEM (marked by 's' in the image). These structures are interpreted as a material on the surface of the crystal with a conductivity different to the one of the crystal.

Figure 1.5: *RIGHT:* Close view by SEM of the feature labelled with 'B' in the previous images. Again additional structures are observed by SEM (marked by 's' in the image).

1.1.2 Local probe methods

In contrast to the microscopical methods described in the previous section, which are all based on magnification and focussing by lenses (conventional, magnetic or electrostatic), this section introduces a new class of microscopical instruments that are operated without lenses and therefore do not suffer from limitations due to diffraction. These methods use a local probe⁷ that is scanned at a very close distance over the sample's surface. The first of these methods – scanning tunneling microscopy (STM) – was introduced by *Binnig and Rohrer* in 1982 [1.6]. Based on the fundamental work on quantum-mechanical tunneling of electrons through a thin insulating barrier between superconductors, normal metals or a combination of them by *J. Bardeen* [1.7] and *J.G. Simmons* [1.8, 1.9], *Binnig and Rohrer* have substituted the conventional thin insulating layer⁸ between conducting electrodes by a vacuum gap. One electrode is shaped as a sharp tip while the other is represented by the (conducting) sample. Since the tunneling current depends exponentially on the distance z between tip and sample the scanning tunneling microscopy method is extremely sensitive to height changes along the axis of the tip. Figure 1.6 schematically shows a tunneling junction of a STM tip and a sample. The theory of STM has been developed by *Tersoff and Hamann* [1.10]. For a successful operation of the tunneling device *Binnig and Rohrer* developed a positioning system which is able to vary the relative distance between the two electrodes with an accuracy of fractions of an Ångstrom. This positioning system was realized by means of piezoresistive ceramics: a sharp tip at the common vertex of three piezoresistive ceramic bars glued together with respective angles of 90 degrees (see fig. 1.8). Application of suitable voltages to the piezoresistive bars causes them to bend in all three directions. Today, piezoceramic tubes with four isolated electrodes are used. Application of voltages with opposite polarity to opposite-lying electrodes allows a movement in x - or y -direction. Length change in z -direction is made possible by applying simultaneously an unipolar voltage to all four electrodes.

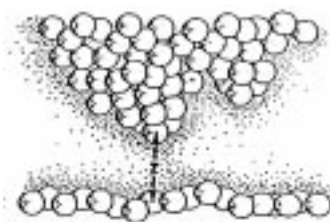


Figure 1.6: Schematic view of the tunneling junction in a scanning tunneling microscope. Since the tunneling current depends exponentially on the distance z between tip and sample a high sensitivity with respect to vertical height changes results.

Fig. 1.7 shows the basic idea behind scanning probe methods: Two (not necessarily conductive) electrodes – of which one is shaped as a sharp probe and the other is repre-

⁷Usually a sharp tip (metallic or non-metallic), a thin capillary or a glass fiber.

⁸Only a few Ångstrom in thickness.

sented by the sample to be investigated – are brought together at a very close distance of only a few Ångstroms. The distance is adjusted by a piezoelectric approach mechanism. By means of a local control interaction⁹ the distance between tip and sample is kept constant by using a feedback loop electronics. By scanning the tip over the surface using the piezoelectric positioning system, and recording the correction movement of the feedback loop the surface topography can be reconstructed directly from the feedback signal. By calibration the movement of the piezo positioning system in x -, y - and z -direction, vertical and lateral topography information can be quantified.

In case of scanning tunneling microscopy (STM) the control interaction is the tun-

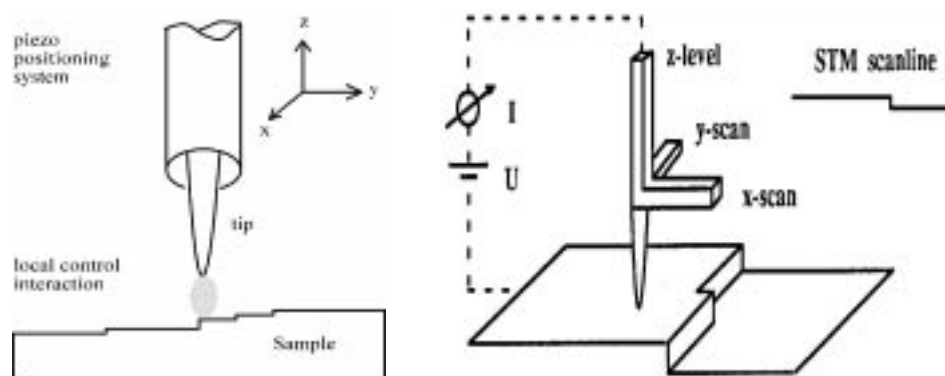


Figure 1.7: LEFT: Schematics of scanning probe methods: a sharp tip is moved by a piezoelectric positioning system over a sample surface. The distance is controlled via a local interaction. In case of the scanning tunneling microscope the tip and the sample must be conductive. By applying a voltage between tip and sample a weak tunneling current (in the nA range) is flowing if the tip is sufficiently close to the sample.

Figure 1.8: RIGHT: Positioning system made of three orthogonal piezoelectric bars. The local probe sensor (in most cases a tip) is fixed at the common point of the three piezo bars. Application of suitable voltages allows movement of the tip in x -, y - and z -direction. A regulating circuit keeps the local interaction constant during scanning the sample. The feedback loop signal is then a measure for the topography.

neling current¹⁰ flowing between (metallic) tip and (conductive) sample. Since STM requires conductive samples *Binnig et al.* [1.11] have developed 1987 a further type of microscope which can be used to investigate both insulators and conductors. It is based on repulsive forces as a local control interaction. This type of microscope is called *Atomic Force Microscope* (AFM) or *Scanning Force Microscope* (SFM). The principle is shown in fig. 1.9. A microfabricated cantilever with an integrated tip is used as a local probe. The sample is approached to the cantilever tip and is being scanned.¹¹ The deflection of

⁹In case of STM this is the tunneling current.

¹⁰Typically in the order of 0.1 - 5 nA.

¹¹The inverse procedure is used, too: The sample is fixed and the cantilever is scanned.

the cantilever can be read by several methods.¹² Most often the *beam deflection* method is used. A beam of a laser diode is focused on the metallized end of the cantilever and is then reflected to a position sensitive detector consisting of four photo diodes¹³ (labelled by 'A' to 'D' in fig. 1.9). Each segment gives a voltage on being illuminated by the laser beam. Evaluating the voltage difference between segment 'A' and 'B' (voltage **A-B**) yields the vertical deflection of the cantilever and thus the topographic information. The voltage difference between segment 'C' and 'D' (voltage **C-D**) measures the torsion of the cantilever. When both the forward and the backward scan of the cantilever are considered the **C-D** signal gives information on the local friction properties of the system cantilever tip and sample.¹⁴

By using other interactions as a local control interaction different other types of scanning probe microscopes have been invented, e.g. Magnetic Force Microscopy (MFM) by using the magnetic interaction between a magnetic sample and a magnetic cantilever tip.

Regarding the resolution capabilities of STM/SFM they yield both lateral and vertical resolutions in the atomic range. However, by using appropriate piezo tube scanners, even scan ranges of 100 μm (laterally) or 5 μm (vertically) are possible. This resolution range surpasses the capabilities of the other microscopical methods like optical microscopy, SEM and TEM. Fig. 1.10 summarizes the vertical and lateral resolution ranges of several microscopical methods including STM/SFM.

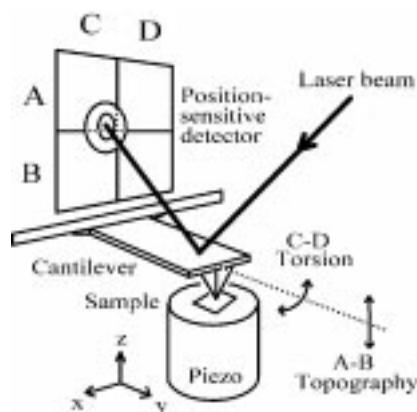


Figure 1.9: Setup used for Friction Force Microscopy (FFM). A laser beam is focused onto the back of a metallized cantilever having a sharp tip. The beam is reflected to a position sensitive photodiode. By measuring the voltages **A-B** the deflection of the cantilever is observed. **C-D** gives the torsion of the cantilever. The forces between tip and sample (both not necessarily conductive) are used to keep constant the distance between tip and sample by means of a piezo positioning system.

¹²Among the most commonly used methods are: beam deflection, laser beam interferometer, capacitive reading. Even a STM may be used to detect the bending of the cantilever.

¹³Called 'four-quadrant detector'.

¹⁴This technique modified from pure SFM is called Friction Force Microscopy (FFM).

However, it should be noted that the geometry of the tip might have an influence on the measured topography of the sample. A blunt tip, for example, will broaden the image of step edges. The pyramid-shaped tip of a SFM probe makes it impossible to image correctly the wall of a pit with an aperture angle of the pit being smaller than that of the tip. A STM tip having several 'minitips' will yield multiple images of a step. Only very sharp STM tips will allow atomic resolution.

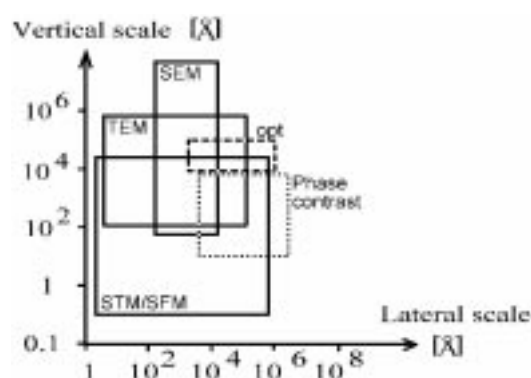


Figure 1.10: Overview of the lateral and vertical resolution capabilities of various imaging methods: optical microscopy (opt), phase contrast microscopy, scanning electron microscopy (SEM), transmission electron microscopy (TEM) and scanning tunneling / scanning force microscopy (STM/SFM). The unsurpassed resolution capability of STM/SFM in vertical direction allows to image features on an atomic scale (after *Binnig and Rohrer 1982* [1.6]).

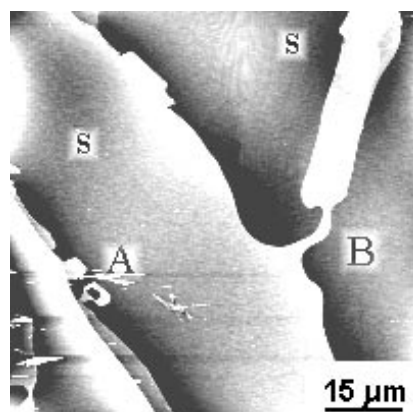


Figure 1.11: Scanning force microscopy (SFM) image of the same part of the $\text{YBa}_2\text{Cu}_4\text{O}_8$ crystal as imaged by optical microscopy and scanning electron microscopy. The two surface step features previously described are labelled by 'A' and 'B'. Label 's' denotes additional surface structure.

In the following the same $\text{YBa}_2\text{Cu}_4\text{O}_8$ crystal as investigated in detail in the previous section is examined by scanning force microscopy (SFM). The surface features 'A' and 'B' can easily be found using the SFM technique. Fig. 1.11 shows a low resolution SFM image of the crystal. A closer view of the features 'A' and 'B' is given in fig. 1.12. The line section through feature 'A' indicates that its height is about 200 nm. The traditional microscopy methods would not have been able to give that accurate height information without breaking the sample.

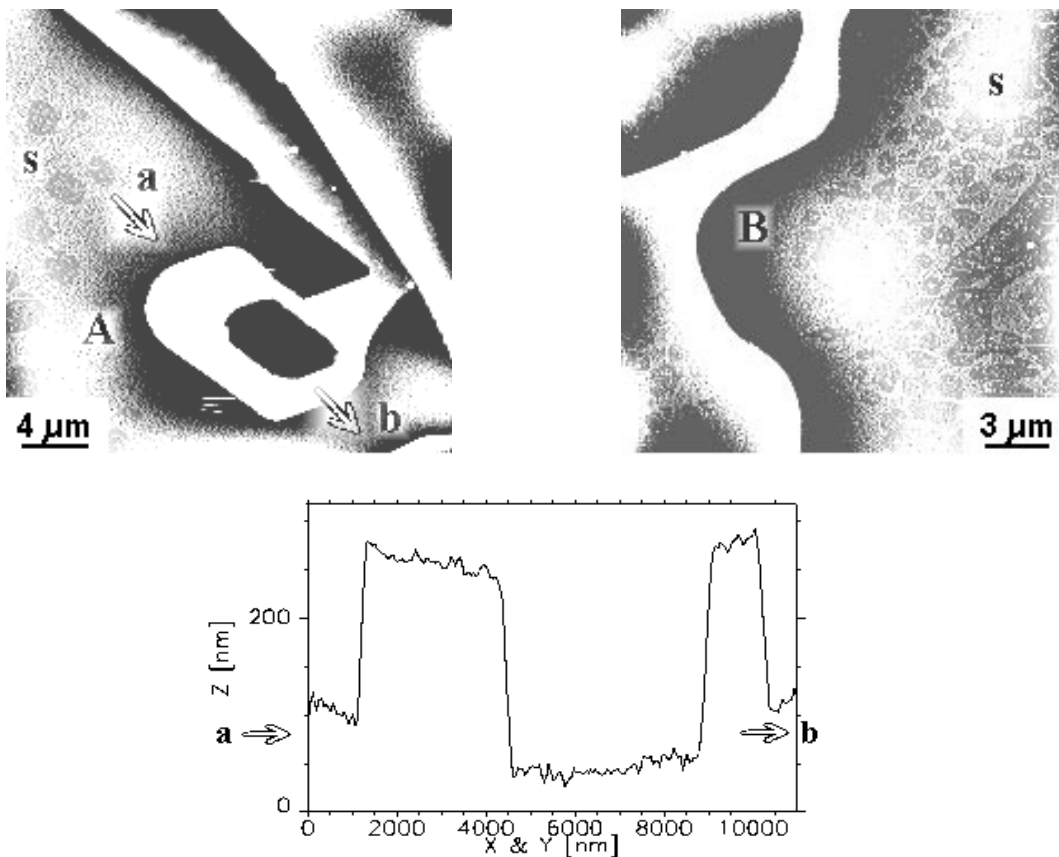


Figure 1.12: SFM images of the surface structures 'A' and 'B'. The fine structure already imaged in the SEM is present on the terraces (marked by 's'). In contrast to optical microscopy and scanning electron microscopy, scanning probe methods are able to give quantitative values of step heights. A line section through feature 'A' (between arrows 'a' and 'b') yields the information that feature 'A' is about 200 nm high.

The spotty surface structure as revealed by SEM is being imaged by SFM as well. In contrast to the SEM pictures (figs. 1.4 and 1.5), it has now become clear that the spotty structure (labelled by 's') actually is a topographic surface layer on top of the $\text{YBa}_2\text{Cu}_4\text{O}_8$ crystal surface. Its height can even be deduced from the image (see fig. 1.13). It amounts to only a few nanometres.

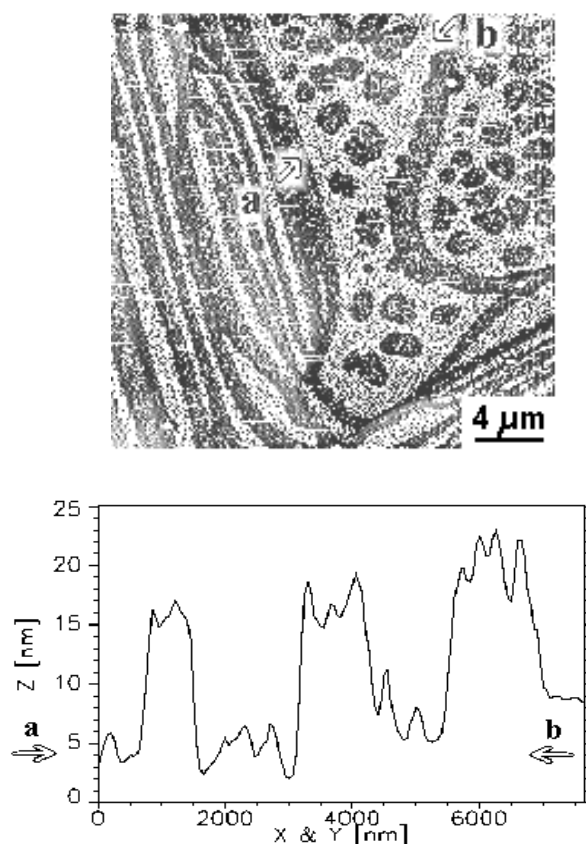


Figure 1.13: Detailed view by scanning force microscopy of the topography of a terrace on a $\text{YBa}_2\text{Cu}_4\text{O}_8$ crystal. The spotty structure (labelled 's' in the previous images) is shown here in detail. This additional layer on the crystal's surface is only a few nanometre thick as can be deduced from the SFM line section. According to the growth process used to grow these crystals it is most probable that this layer consists of BaCuO_2 and CuO , which are the materials used as a flux for crystal growth (see Chapter 2). This interpretation is supported by the different conductivities of $\text{YBa}_2\text{Cu}_4\text{O}_8$ and the flux material as observed by SEM. Without this difference in conductivity SEM would not have been able to image a layer only a few nanometres in height.

1.2 Materials

The materials which will be discussed in the following include various compounds of current interest, especially synthetic¹⁵ materials. The investigations are basically divided into two major classes of materials, namely layered high- T_c superconductors and allotropes of carbon (including fullerenes¹⁶). These two classes of materials have some properties in common, e.g. the graphite allotrope of carbon being also a layered material. On doping with alkali metal atoms graphite becomes even a superconductor at 0.55 K (potassium-doped graphite). On the other hand some layered high- T_c superconductors can be intercalated with iodine.¹⁷ Among the other allotropes of carbon a further superconductive species is found if it is doped: the fullerenes. At high pressure the fullerenes – although a very stable species – can undergo a transformation [1.16] to the other allotropes of carbon like graphite, diamond and amorphous carbon. These forms of carbon are discussed in Chapters 4 and 5.

1.2.1 Layered High-Temperature Superconductors

The surprising discovery of superconductivity in a $\text{La}_{1.85}\text{Ba}_{0.15}\text{CuO}_4$ compound at a comparatively high temperature of about 30 K by *Bednorz and Müller* at the IBM Research Laboratory in Rüschlikon in 1986 [1.17] has caused a widespread research activity in the field of these oxides termed *high-temperature superconductors* (HTSC). Substitution of some of the elements in these compounds has led to materials with even higher critical transition temperatures T_c such as $\text{YBa}_2\text{Cu}_3\text{O}_{7-\delta}$ (*C.W. Chu et al.* in 1987 [1.18]) with a $T_c = 92$ K which is well above the boiling point of liquid nitrogen (77 K). In 1988, *H. Maeda et al.* have discovered a compound with the stoichiometry $\text{Bi}_2\text{Sr}_2\text{Ca}_2\text{Cu}_3\text{O}_{10}$ with a T_c of 105 K [1.19]. In the same year *Z.Z. Sheng and A.M. Hermann* [1.20] presented the discovery of a $\text{Tl}_2\text{Ba}_2\text{Ca}_2\text{Cu}_3\text{O}_{10}$ ceramic with a T_c of 125 K. In mid-1993 *A. Schilling et al.* have announced the discovery of a 133.5 K superconductor $\text{HgBa}_2\text{Ca}_2\text{Cu}_3\text{O}_9$ [1.21]. Its T_c can be increased under pressure up to 164 K [1.22]. In late 1993 information on new superconducting compounds with an even higher T_c of up to 250 K has become available [1.23, 1.24]. A group from Paris (*M. Laguës et al.*) have prepared a thin film sample of Bi-Sr-Ca-Cu-O built up of the so called 'infinite layer compound' $(\text{Sr}_{0.7}\text{Ca}_{0.3})_{0.9}\text{Cu}_2$ ($T_c = 110$ K [1.10]) with a Bi-O sheet every eighth CuO_2 layer [1.23]. The authors present in their paper resistivity evidence for a T_c of 250 K. *J.-L. Tholence et al.* [1.9] claim to

¹⁵A material will be called 'synthetic' if it does not already exist in nature and is synthesized by an artificial process.

¹⁶Fullerenes: the name goes back to Buckminster Fuller whose dome-like architecture resembles to the cage-like structure of the fullerenes. The most abundant fullerene species is a cage with 60 carbon atoms having a symmetry of a soccer ball.

¹⁷ $\text{IBi}_4\text{Sr}_4\text{Ca}_2\text{Cu}_4\text{O}_x$ is the stage 2 intercalation compound of the $\text{Bi}_2\text{Sr}_2\text{CaCu}_2\text{O}_8$ superconductor. The iodine layers are inserted between every other BiO double sheets resulting in an enlarged c -axis parameter of the unit cell (6.85 nm instead of 3.06 nm for the undoped compound). A stage 1 iodine intercalation compound with a c -axis parameter of 1.89 nm is also known [1.12-1.15]. The critical transition temperature T_c is lowered by 2-10 K compared to the undoped compounds.

have observed a resistivity drop in a ceramic $\text{HgBa}_2\text{Ca}_2\text{Cu}_3\text{O}_9$ sample at about 250 K [1.24]. This resistivity drop was later found to coincide with a phase transition of elemental mercury which is often present in that type of ceramic $\text{HgBa}_2\text{Ca}_2\text{Cu}_3\text{O}_9$ samples. It remains to be clarified whether the (unreproduced) result by *M. Laguës et al.* [1.23] has to be abandoned as well. Figure 1.14 summarizes the increase of T_c with time.

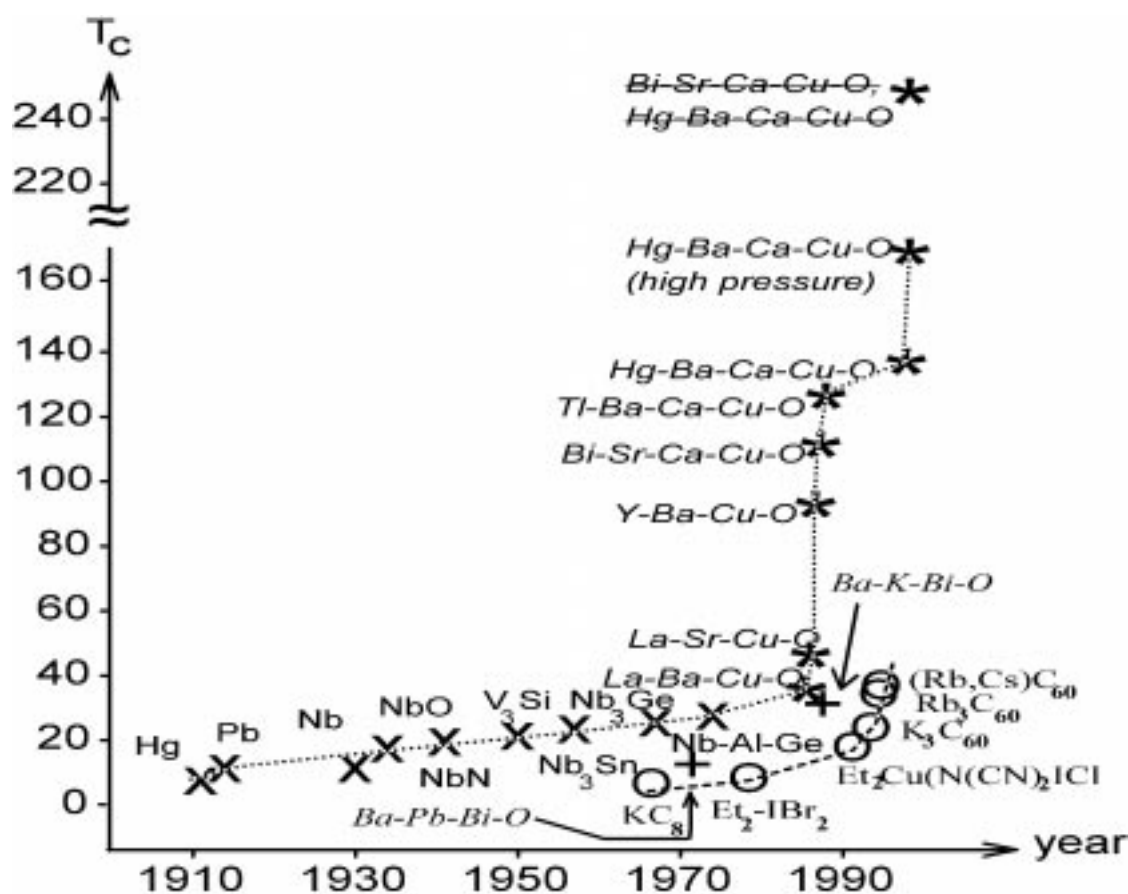


Figure 1.14: Increase of T_c with time. The symbols 'x' represent conventional superconductors, the symbols '*' are cuprate high temperature superconductors. A '+' stands for copperless high temperature superconductors. The dotted line is a guide for the eye. The existence of the compounds with a T_c of about 250 K is not yet confirmed (crossed through). Organic superconductors (including fullerene-based ones) are marked by the symbol 'o'. The dashed line indicates the trend to higher transition temperatures in this class of compounds.

The first synthesis route to HTSC was sintering metal oxide powders in a furnace. The ceramic material obtained by this process consists of small (micrometre-sized) grains that are only loosely connected. These *weak links* between the individual grains prevent

the ceramic HTSC from having a high critical current density j_c that would be important for technical applications of the material. Due to the extreme properties of the HTSC (very short coherence length below 1–2 nm and complexity of the structure) it is desirable to prepare atomically flat surfaces. Sample quality has been improved by different preparation methods in addition to the original powder processing of granular HTSC materials. Examples of such preparation methods are melt-texturing of polycrystalline materials, growth of single crystals and deposition of thin films onto suitable substrates by physical vapour deposition (PVD) and chemical vapour deposition (CVD) from various precursor compounds. In a review article *Schieber* [1.26] has analyzed the problems in HTSC film growth by PVD and CVD methods and has compared the film properties. Thin film growth by PVD methods includes thermal co-evaporation [1.27], composite-target magnetron sputtering [1.28], off-axis sputtering [1.29], pulsed laser deposition [1.30] and others. For a comprehensive study of magnetron-sputtered films the reader is referred to an article by *Eom et al.* [1.31]. Many questions concerning the outstanding properties of HTSC thin films, compared to bulk material, are still unanswered. Explanations for the high values of critical current densities j_c in thin film samples require a large number of pinning centres for magnetic flux vortices. Structural defects such as twin planes [1.32], stacking faults [1.33, 1.34], oxygen vacancies [1.35], screw dislocations [1.36, 1.37] and others have been suggested as potential pinning centres. Experimental evidence of structural defects in $\text{YBa}_2\text{Cu}_3\text{O}_{7-\delta}$ (YBCO) is summarized in an article by *Kulik* [1.38].

In the following the structure of some HTSC compounds will be discussed. Figure 1.15 shows the members of the $\text{Y}_2\text{Ba}_4\text{Cu}_{6+N}\text{O}_{14+N}$ ($N=0,1,2$) superconductors (in short YBCO [2 4 (6+N)], or to be compatible with other notations: YBCO 123 (instead of 246), and YBCO 124 (instead of 248)) and the $\text{Bi}_2\text{Sr}_2\text{CaCu}_2\text{O}_{8+x}$ compound, which is the $n=2$ member of the $(\text{SrBiO})_2(\text{CuO}_2\text{Ca})_{n-1}\text{CuO}_4$ ($n=1,2,3$) series. These compounds can be more generally written as $\text{BM}_r\text{B}(\text{CuO}_2\text{Ca})_{n-1}\text{CuO}_2$ (abbreviated as [r 2 (n-1) n] compound). B stands for Sr or Ba, M is Bi, Tl or Hg.

The $\text{BM}_r\text{B}(\text{CuO}_2\text{Ca})_{n-1}\text{CuO}_2$ compounds may be derived from the infinite layer compound $((\text{Sr}_{0.7}\text{Ca}_{0.3})_{0.9}\text{Cu}_2)$ by introducing MO planes. Chapter 2 summarizes my investigations of YBCO 123, 247, 124 and Bi[2212] single crystals.

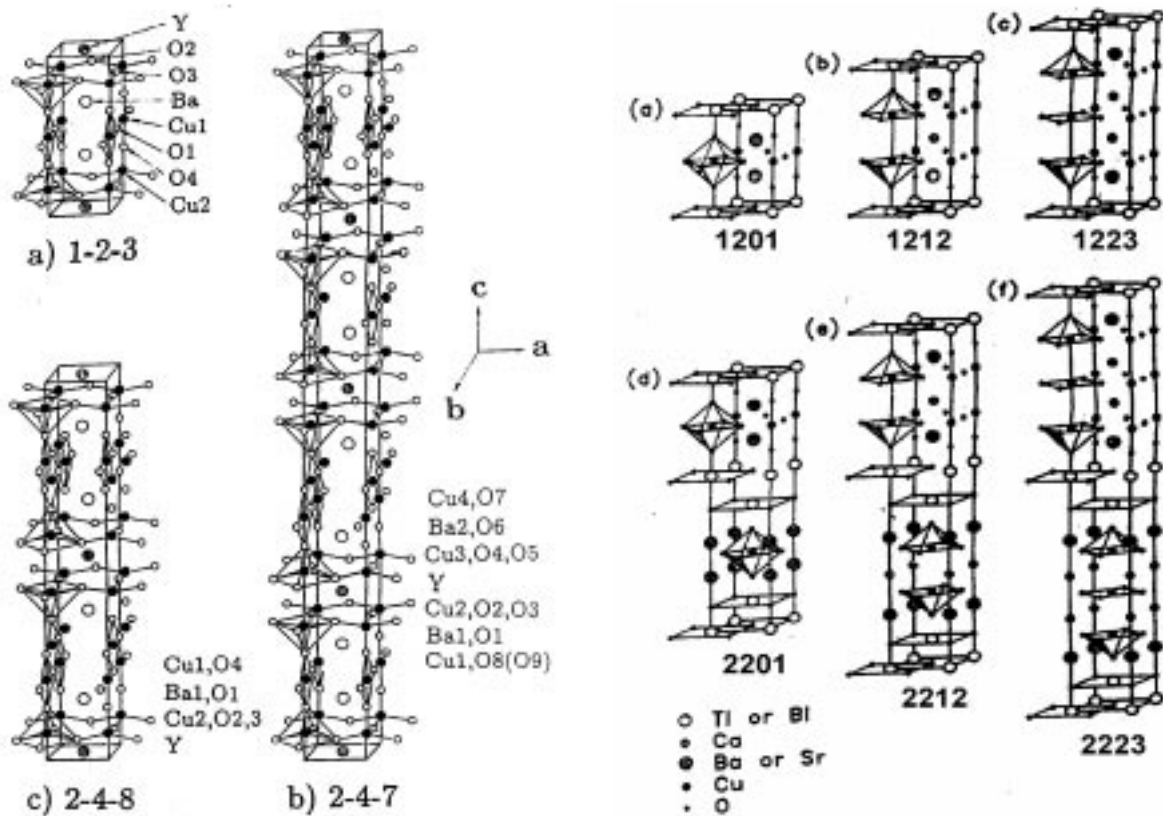


Figure 1.15: *LEFT:* Structures of the $Y_2Ba_4Cu_{6+N}O_{14+N}$ ($N=0,1,2$) high- T_c superconductors. The 123 compound has single copper oxide chains (Cu(1)-O(1)) serving as a charge reservoir and copper oxide planes (Cu(2)-O(2)/O(3)). Its T_c is about 92 K. The 248 (124) compound has double copper oxide chains (Cu(1)-O(4)) and is superconducting below 80 K. YBCO 247 has both single and double copper oxide chains (T_c can be varied as a function of oxygen content in the range of 20-95 K).

Figure 1.16: *RIGHT:* Structures of the Bi-Sr-Ca-Cu-O (only (d)-(f)) and Tl-Ba-Ca-Cu-O ((a)-(f)) superconductors. In the Bi-Sr-Ca-Cu-O series T_c increases from 20 K (Bi[2201], one CuO_2 plane) over 80 K (Bi[2212], two CuO_2 planes) to 105 K (Bi[2223], three CuO_2 planes).

All these cuprate HTSC have one structural feature in common: they are two-dimensional layered compounds.¹⁸ Of special importance are the CuO_2 layers. High-temperature superconductivity is now believed to be confined in the CuO_2 planes, but quite strongly depending on the so called charge reservoir blocks (i.e the $(\text{SrBiO})_2$ blocks in Bi[2212] and the Cu-O single or double chain elements in the YBCO compounds). The layered nature of the cuprate HTSC is impressively demonstrated in fig. 1.17 showing a STM image of a YBCO thin film prepared by pulsed laser deposition in a three-dimensional representation. Investigations of different types of YBCO 123 films will be discussed in Chapter 3.

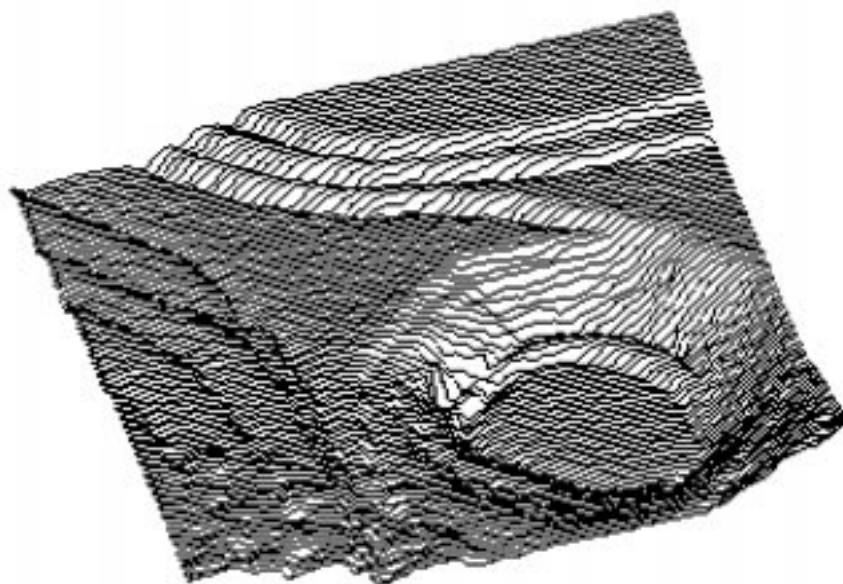


Figure 1.17: Three-dimensional representation of a STM image of a YBCO thin film beautifully demonstrating the layered nature of the cuprate high-temperature superconductors (image size $300 \text{ nm} \times 300 \text{ nm}$, step heights 1.2 nm).

¹⁸In contrast to the conventional intermetallic compounds, K-Bi-Ba-O or the doped fullerenes which are real three-dimensional superconductors.

1.2.2 Allotropes of Carbon

Carbon plays an important role in biology, chemistry and physics since it forms a huge number of compounds with manifold properties. The different forms of elemental carbon are called *allotropes*. The classical¹⁹ allotropes of carbon include graphite and diamond. Graphite is a layered structure with a sp^2 hybridization type of bonding, whereas diamond has a sp^3 bonding type. These 'traditional' allotropes of carbon are subject of Chapter 4. In addition to these there exist disordered forms of carbon: disordered graphite (or turbostratic graphite) and amorphous carbon (see fig. 1.19).

Recently a third ordered form of carbon has been discovered by *Kroto et al.* [1.39]: a closed-cage molecule consisting of 60 carbon atoms which was given the name *Fullerene*. Until 1990 these molecules could only be produced as a molecular beam²⁰ which could be studied by mass spectrometry. The presently known three allotropes of carbon are displayed in fig. 1.18.

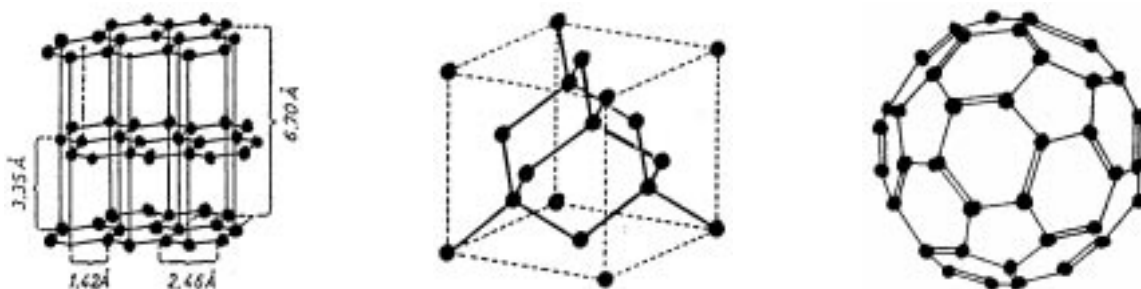


Figure 1.18: Structures of the three allotropes of carbon. *LEFT:* Graphite, *MIDDLE:* Diamond, *RIGHT:* Fullerene C_{60} .

Fullerenes have been first produced in macroscopic amounts by *Krättschmer et al.* [1.40] in 1990. The possibility to do solid-state-physics-experiments with this new allotrope of carbon has stimulated widespread research activity all over the world [1.41, 1.42]. C_{60} as a solid is found to form under ambient conditions a face-centred cubic lattice with a nearest-neighbour distance of 1 nm [1.43, 1.44] (see fig. 1.20). Growth of fullerene single crystals [1.45] and highly-ordered thin-film samples by sublimation permits more detailed investigations of the structural properties of fullerenes. Diffraction methods such as neutron scattering [1.46], electron diffraction [1.40] and X-ray diffraction [1.43, 1.44] provide structure refinement of the bulk structure.

¹⁹'Classical' means in this sense the time before 1985 which was the year of the discovery of the fullerenes.

²⁰*Kroto et al.* have used a laser beam focussed onto a rotating graphite disk to prepare a molecular beam of fullerenes.

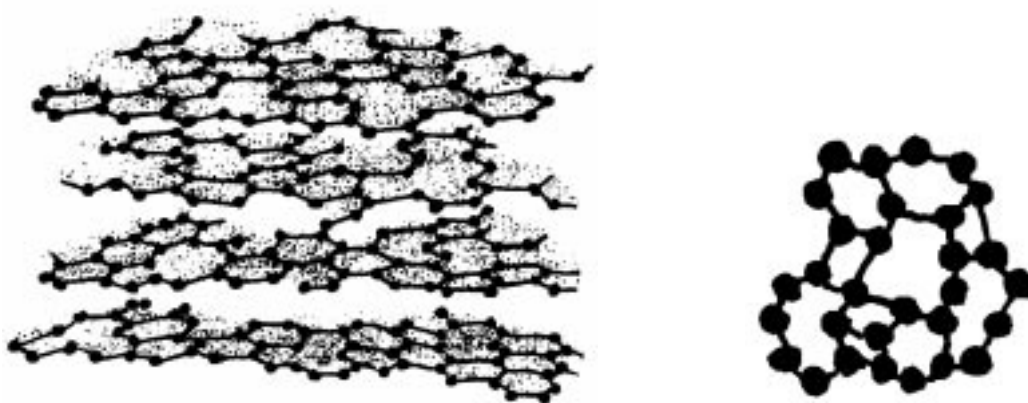


Figure 1.19: Disordered forms of carbon. *LEFT:* Turbostratic graphite. The coordination is still similar to that of graphite even though some extra bonds between carbon atoms are formed or others are missing. The structure is a quasi-layered one. *RIGHT:* Amorphous carbon. The coordination can vary in a wide range from sp^2 (graphite-like) to sp^3 (diamond-like). Its structure is more three-dimensional.

Local imaging methods such as TEM [1.47, 1.48] and scanning probe microscopy [1.49, 1.50] allow a more detailed understanding of the local structure and morphology of bulk and surface, respectively. STM has been successfully applied to image surfaces of thin fullerene films obtained by sublimation of fullerene powders onto Au(111) substrates [1.49, 1.50]. The results will be presented in Chapter 5.

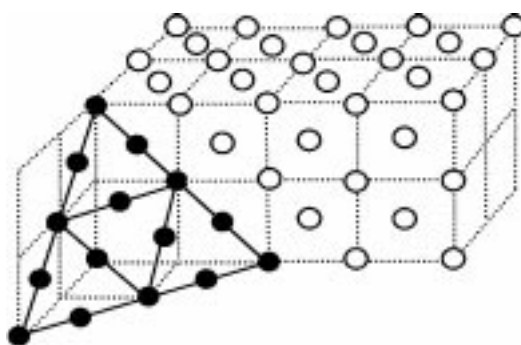


Figure 1.20: C_{60} as a solid. Schematic of the fcc(111) and fcc{100} faces. The (111) face is shown by black balls (representing individual C_{60} molecules). The {100} faces are shown by white balls. The fcc lattice constant of C_{60} is 1.42 nm leading to a closest-neighbour distance of 1 nm (fcc(111) distance). The diameter of the C_{60} molecules is about 0.7 nm.

References

- [1.1] D.W. Pohl, W. Denk and M. Lanz, *Appl. Phys. Lett.* 44 (1984) 651.
- [1.2] U. Dürig, D.W. Pohl and F. Rohner, *J. Appl. Phys.* 59 (1986) 3318.
- [1.3] H. Wolter, *Microscopia Acta* 77 (1975) 2.
- [1.4] F. Zernike, *Z. Tech. Physik* 16 (1935) 454.
- [1.5] J. Liu and J.M. Cowley, *Ultramicroscopy* 48 (1993) 381.
- [1.6] G. Binnig and H. Rohrer, *Helv. Phys. Acta* 55 (1982) 726.
- [1.7] J. Bardeen, *Phys. Rev. Lett.* 6 (1961) 57.
- [1.8] J.G. Simmons, *J. Appl. Phys.* 34 (1963) 1793.
- [1.9] J.G. Simmons, *J. Appl. Phys.* 34 (1963) 2581.
- [1.10] J. Tersoff, D.R. Hamann, *Phys. Rev. Lett.* 50 (1983) 1998, *Phys. Rev. B* 31 (1985) 805.
- [1.11] G. Binnig, C.F. Quate and Ch. Gerber, *Phys. Rev. Lett.* 56 (1986) 930.
- [1.12] X.-D. Xiang, S. Mc Kernan, W.A. Vareka, A. Zettl, J.L. Corkill, T.W. Barbee III and M.L. Cohen, *Nature* 348 (1990) 145.
- [1.13] X.-D. Xiang, A. Zettl, W.A. Vareka, J.L. Corkill and M.L. Cohen, *Phys. Rev. B* 43 (1991) 11496.
- [1.14] N. Kijima, R. Gronsky, X.-D. Xiang, W.A. Vareka, J.L. Corkill and M.L. Cohen, *Physica C* 181 (1991) 18.
- [1.15] X.-D. Xiang, A. Zettl, W.A. Vareka, J.L. Corkill and M.L. Cohen, *Physica C* 184 (1991) 127.
- [1.16] F. Moshary, N.H. Chen, I.F. Silvera, C.A. Brown, H.C. Dorn, M.S. de Vries and D.S. Bethune, *Phys. Rev. Lett.* 69 (1992) 466.
- [1.17] J.G. Bednorz and K.A. Müller, *Z. Phys. B* 64 (1986) 189.
- [1.18] M.K. Wu, J.R. Ashburn, C.J. Torng, P.H. Hor, R.L. Meng, L. Gao, Z.J. Huang, Y.U. Wang and C.W. Chu, *Phys. Rev. Lett.* 58 (1987) 908.

- [1.19] H. Maeda, Y. Tanaka, M. Fukutomi and T. Asano, *Jpn. J. Appl. Phys. Lett.* 27 (1988) L209.
- [1.20] Z.Z. Sheng and A.M. Hermann, *Nature* 332 (1988) 55.
- [1.21] A. Schilling, M. Cantoni, J.D. Guo and H.R. Ott, *Nature* 363 (1993) 55.
- [1.22] L. Gao, Y.Y. Xue, F. Chen, Q. Xiong, R.J. Meng, D. Ramirez, C.W. Chu, J.H. Eggert and H.K. Mao, *Phys. Rev. Lett.* (submitted).
- [1.23] M. Laguës, X.M. Xie, H. Tebbji, X.Z. Xu, V. Mairret, C. Hatterer, C.F. Beuran and C. Deville-Cavellin, *Science* 262 (1993) 1850.
- [1.24] J.-L. Tholence, B. Souletle, O. Laborde, J.-J. Capponi, C. Chaillout and M. Marezio, *Phys. Lett. A* 184 (1994) 215.
- [1.25] M. Azuma, Z. Hiroi, M. Takano, Y. Bando and Y. Takeda, *Nature* 356 (1992) 775.
- [1.26] M. Schieber, *J. Cryst. Growth* 109 (1991) 401.
- [1.27] T. Terashima, K. Iijima, K. Yamamoto, Y. Bando and H. Mazaki, *Jpn. J. Appl. Phys.* 27 (1988) L91.
- [1.28] H.C. Li, G. Linker, F. Ratzel, R. Smithey and J. Geerk, *Appl. Phys. Lett.* 52 (1988) 1098.
- [1.29] R.L. Sandstrom, W.J. Gallagher, T.R. Dinger and R.H. Koch, *Appl. Phys. Lett.* 53 (1988) 444.
- [1.30] D. Dijkamp, T. Venkatesan, X.D. Wu, S.A. Shaheen, N. Jisrawi, Y.H. Min-Lee, W.L. McLean and M. Croft, *Appl. Phys Lett.* 51 (1987) 619.
- [1.31] C.B. Eom, J.Z. Sun, B.M. Lairson, S.K. Streiffer, A.F Marshall, K. Yamamoto, S.M. Anlage, J.C. Bravman and T.H. Geballe, *Physica C* 171 (1990) 354.
- [1.32] P.H. Kes and J. van den Berg, in: 'Studies of High Temperature Superconductors', Vol. 5, ed. A. Narlikar (NOVA Science Publishers, NewYork. 1990), p.83.
- [1.33] E.J Kramer, *Philos. Mag.* 33 (1976) 331.
- [1.34] C.S. Pande, *Appl. Phys. Lett.* 28 (1976) 462.
- [1.35] C.J. van der Beek and P.H. Kes, *Phys. Rev. B* 43 (1991) 13032.
- [1.36] C. Gerber, D. Anselmetti, J.G. Bednorz, J. Mannhart and D. G. Schlom, *Nature* 350 (1991) 279.
- [1.37] M. Hawley, I.D. Raistrick, J.G. Beery and R.J. Houlton, *Science* 251 (1991) 1587.
- [1.38] J. Kulik, *J. Appl. Phys.* 70 (1991) 4398.
- [1.39] H.W. Kroto, J.R. Heath, S.C. O'Brian, R.F. Curl, R.E. Smalley, *Nature* 318 (1985) 162.

- [1.40] W. Krätschmer, L.D. Lamb, K. Fostiropoulos, R. Huffman, *Nature* 347 (1990) 354.
- [1.41] H.W Kroto, A.W. Allaf, S.P. Balm, *Chem. Rev.* 91 (1991) 1213.
- [1.42] *Acc. Chem. Res.* 25, March issue (1992).
- [1.43] J.E. Fischer, P.A. Heiney, A.R. McGhie, W.J. Romanov, A.M Denenstein, J.P. McCauley Jr., A.B. Smith III, *Science* 251 (1991) 1288.
- [1.44] P.A. Heiney, J.E. Fischer, A.R. McGhie, W.J. Romanow, A.M. Denenstein, J.P. McCauley Jr., A.B. Smith, D.F. Cox, *Phys. Rev. Lett.* 66 (1991) 2911.
- [1.45] R.M. Fleming, B. Hessen, A.R. Kortan, T. Siegrist, P. Marsh, D.W. Murphy, R.C. Haddon, R. Tycko, G. Dabbagh, A.M. Muzsca, M.L. Kaplan, S.M. Zahurak, *Mater. Res. Soc. Symp. Proc.* 206 (1991) 691.
- [1.46] W.I.F. David, R.M. Ibberson, J.C. Matthewman, K. Prassides, T.J.S. Dennis, J.P. Hare, I.W. Kroto, R. Taylor, D.R.M. Walton, *Nature* 353 (1991) 147.
- [1.47] Y. Saito, N. Suzuki, H. Shinohara, T. Hayashi, M. Tomita, *Ultramicroscopy* 41 (1992) 1.
- [1.48] W. Krakow, N.M. Rivera, R.A. Roy, R.S. Ruoff, J.J. Cuomo, *J. Mater. Res.* 7 (1992) 784.
- [1.49] R.J. Wilson, G. Meijer, D.S. Bethune, R.D. Johnson, D.D. Chambliss, M.S. deVries, H.E. Hunziker, H.R. Wendt, *Nature* 348 (1990) 621.
- [1.50] J.L. Wragg, J.E. Chamberlain, H.W. White, W. Krätschmer, D.R. Huffman, *Nature* 348 (1990) 623.

Chapter 2

HTSC single crystals

Performing experiments on single crystals is the most desirable condition. Single crystals should predominantly contain only a small number of defects. This should simplify experiments. Similarly single crystals are 'ideal' samples for the scanning probe techniques since the surface is (in most cases) sufficiently flat. However, growing HTSC single crystals is not very easy due to the complexity of these materials.

2.1 YBCO single crystals

Obtaining *clean* single-phase crystals of the YBCO superconductors is still a problem since for the growth of these crystals a flux-method has to be used. Most crystal growth experiments use an eutectic of YBCO and BaCuO_2 / CuO flux because YBCO is not melting congruently. This raises the problem that the surface of these crystals might be contaminated by some flux. As demonstrated in the introductory chapter (Chapter 1) this contamination is often present on the crystal's surface. In the following the different types of YBCO crystals will be discussed.

2.1.1 Experimental

YBCO 123, 124 and 247 are the three presently known members of the YBCO HTSC family.¹ YBCO 124 and YBCO 247 high- T_c superconductors differ from YBCO 123 by the presence of CuO double chains. This prevents these materials from being twinned² since the CuO double chains are more rigid than the CuO single chains present in YBCO 123. An investigation of single crystals in polarized light in an optical microscope demonstrates this clearly. Fig. 2.1 shows thin single crystalline platelets (thickness $< 20 \mu\text{m}$) of YBCO 123,³ 124 and 247.⁴ The corresponding structures of YBCO 123 and YBCO 124 are shown in fig. 2.2. The single or double CuO chains are marked by open and bold

¹YBCO 125 and 126 have been observed as stacking faults in YBCO 124 and 247 samples, but could not yet be synthesized as bulk materials.

²Twinning means in this case interchange of crystallographic a - and b -axes.

³The YBCO 123 single crystals were grown by Th. Wolf, ITP Kernforschungszentrum Karlsruhe, Germany, see ref. [2.1].

⁴The YBCO 124 and 247 single crystals were grown by J. Karpinski and E. Kaldis, Federal Institute of Technology, Zürich (Switzerland), see ref. [2.2, 2.4].

arrows, respectively.

The lattice parameters in the CuO_2 planes are similar for all YBCO compounds ($a = 0.387$ nm, $b = 0.382$ nm). The c -parameters of the structures, however, are different. The heights of the YBCO 123, 124 and 247 orthorhombic unit cells in c -axis direction are 1.17 nm, 2.73 nm and 5.03 nm, respectively. For a discussion of the structural and thermodynamic properties of the double-chain compounds the reader is referred to a previous study by *Kaldis and Karpinski* [2.2].

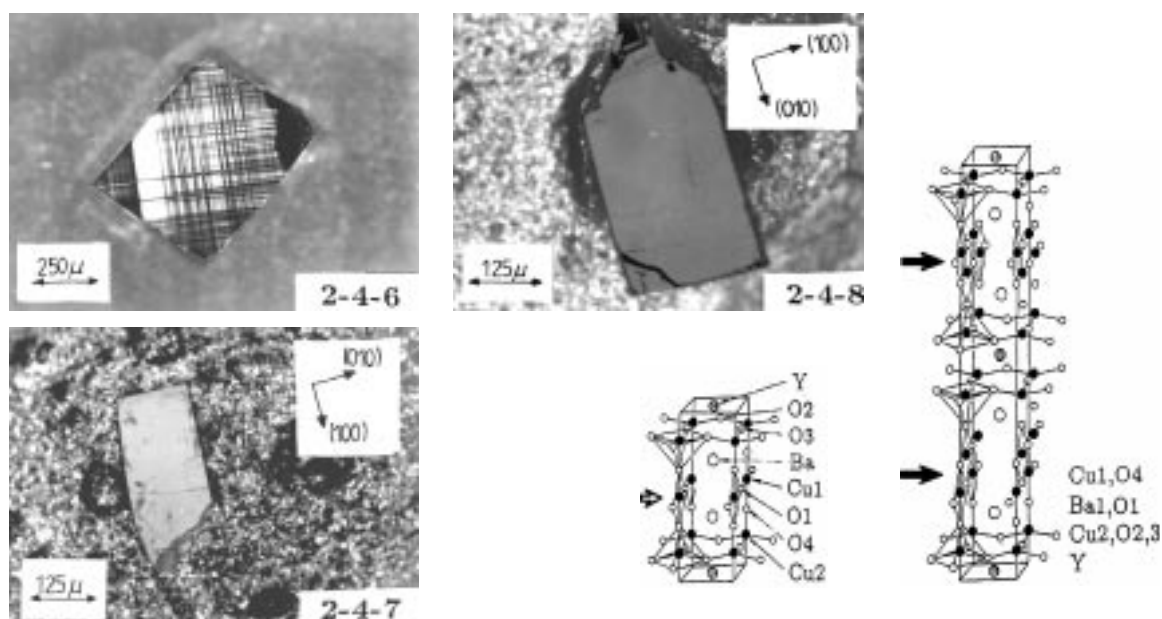


Figure 2.1: *LEFT:* Optical micrographs of YBCO 123, 124 and 247 single crystal platelets (thickness $< 20 \mu\text{m}$) in polarized light. The anisotropy of these structures in the ab -plane leads to an enhanced charge carrier density parallel to the (single or double) chain directions. This results in a higher reflectivity of the crystal in polarized light when it is aligned parallel to the chain-direction (b -direction). Since YBCO 123 is twinned (interchange of a and b) a pattern of crossed stripes is observed whereas the YBCO 124 and 247 surfaces show no structure. On rotating YBCO 124 and 247 crystals in polarized light they appear golden (analyzer parallel to b) or black (parallel to a).

Figure 2.2: *RIGHT:* Structure of YBCO 123 and YBCO 124. The single Cu–O chains in YBCO 123 are marked by an open arrow. The double Cu–O chains in YBCO 124 are indicated by a bold arrow.

According to the phase diagram [2.2]–[2.4] (see fig. 2.3) YBCO 124 and 247 single crystals can only be grown under high oxygen pressure. The c -axis oriented single crystals investigated here have been grown in a flux consisting of BaCuO_2 , CuO and YBCO 123 with a total atomic ratio of $\text{Y}:\text{Ba}:\text{Cu} = 1:3:7.5$. The 124 (respectively 247) single crystals were prepared under an oxygen pressure of 840 bar (400 bar) at a maximum temperature

of 1100°C, which was held for 24 h. Then the crystals were cooled to 1050°C at a typical rate of 1–3°C/h and to room temperature at a rate of 1–2°C/min. Precise temperature control is essential since e.g. at 1000 bar only a small temperature window exists between the BaCuO₂ – CuO eutectic (1100°C) and peritectic temperature (1120°C). Only temperatures within this range can be used for crystal growth [2.3].

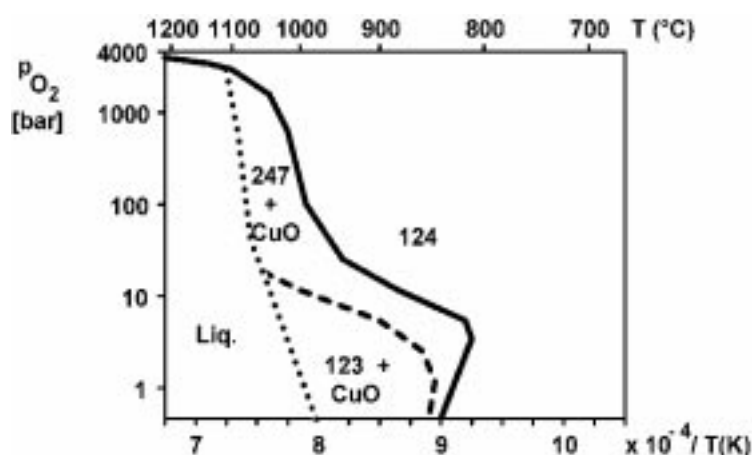


Figure 2.3: Pressure–temperature phase diagram for the composition YBCO 123 + CuO (schematically after ref. [2.5]). Besides the liquid phase region (denoted 'Liq.')

there are stability regions of YBCO 123, YBCO 247 and YBCO 124. Whereas YBCO 123 is preferentially formed at ambient pressure, at high pressures (> 1 kbar) only YBCO 124 is found. At intermediate pressures (0.01 – 1 kbar) YBCO 247 has a narrow stability range.

2.1.2 STM investigations on thin YBCO crystal platelets

2.1.2.1 Large scale

First, the morphology of thin single crystalline platelets of the YBCO superconductors will be discussed. The thickness of the platelets is below 20 μm (typical crystals are shown in fig. 2.1). In contrast to these crystals there are somewhat thicker crystals (thickness 30–50 μm) which are subject of section 2.1.3.⁵

STM images of the single crystals on a micron scale exhibit flat layers with single or multiple unit cell steps. The step height is in agreement with the corresponding X-ray diffraction data, i.e. 1.2 nm (YBCO 123), 2.7 nm (YBCO 124) and 5.0 nm (YBCO 247). The surface of the stoichiometric compounds YBCO 247 and YBCO 124 is smoother than that of the 123 compound demonstrating the higher thermodynamic stability of the former phases. As an example fig. 2.4 shows an illuminated view of crystal terraces with

⁵Such a crystal is shown in fig. 1.1.

unit cell steps (5 nm) on a YBCO 247 single crystal.

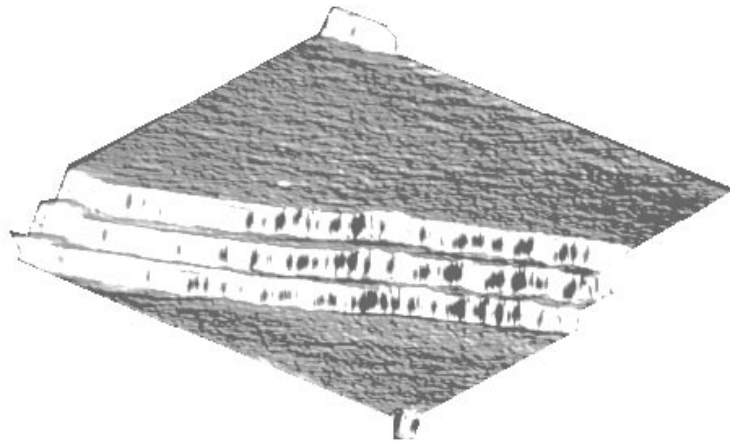


Figure 2.4: Illuminated view of the surface of a YBCO 247 single crystal with unit cell steps (5.0 nm in height, c -direction). The image size is 500 nm \times 500 nm. Tunneling current $I_t = 1$ nA, sample bias voltage $U_s = -200$ mV.

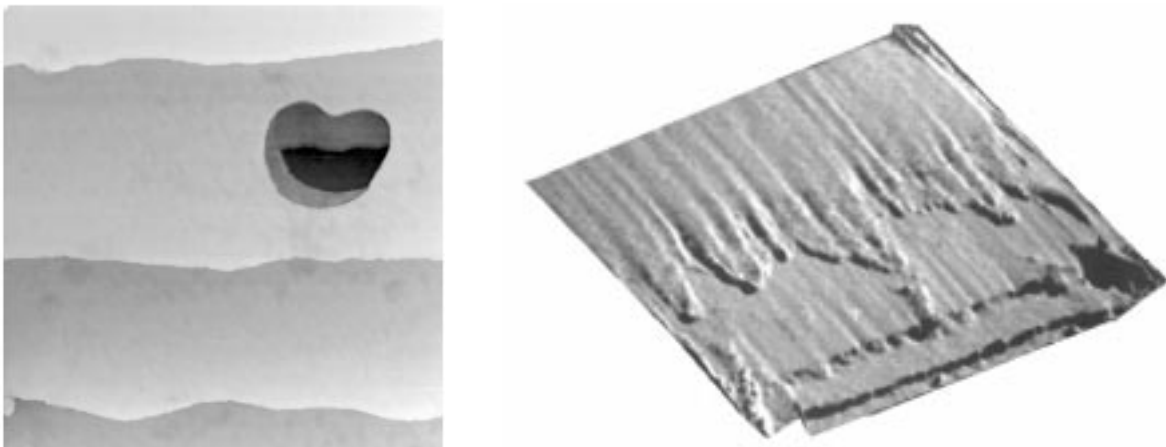


Figure 2.5: *LEFT:* Modified surface of a YBCO 247 single crystal. The indentation in the upper right half of the image is 2 unit cell deep (at the centre is the depth 3 unit cells). The steps on the terraces are of one unit cell height in crystallographic c -direction. Image size: 620 nm \times 620 nm. Tunneling current $I_t = 0.3$ nA, sample bias voltage $U_s = 800$ mV.

Figure 2.6: *RIGHT:* Surface modification caused by increasing and decreasing the bias voltage which resulted in steps having only a fraction of the height of a full unit cell: the individual layers are separated by approximately 1.4, 1.8 and 0.8 nm. Image size: 400 nm \times 400 nm. $I_t = 0.17$ nA, $U_s = -195$ mV.

The surface of the YBCO 247 compound can be modified using STM by decrease and increase of the tunneling bias voltage in such a way that holes of multiple unit cell depth can be created (see fig. 2.5). Similar surface modification experiments on YBCO 123 single crystals are already known in the literature [2.6]. In some cases step heights corresponding to a fraction of the full unit cell are observed (see fig. 2.6). Careful step height calibration on unit cell steps before the modification experiment validates this observation. A possible explanation might be the off-thermodynamic-equilibrium state of 247, which favours the bond-breaking between the stable 123 and 124 sub-units.

2.1.2.2 Atomic scale

On an atomic scale approximately square atomic arrangements with two different lattice constants (0.38 nm and 0.27 nm) are observed in all three systems (see fig. 2.7).

Clear atomic resolution is achieved with the 124 compound, which is thermodynamically the most stable [2.2, 2.4] among the three members of the series $Y_2Ba_4Cu_{6+N}O_{14+N}$, ($N=0,1,2$). Due to the lack of twinning in 247 and 124, $\langle 100 \rangle$ and $\langle 010 \rangle$ directions can be distinguished. In 123, only atomic rows can be resolved. This observation is in agreement with earlier reports [2.7].

Possible distances of 0.38 nm in the $YBa_2Cu_3O_7$ crystal structure include Y-Y, Ba-Ba, Cu(1)-Cu(1), O(1)-O(1) in the planes, Cu(2)-Cu(2) and O(4)-O(4) in the chains (see fig. 2.2). For the $N=1$ and $N=2$ compounds, similar arguments hold [2.8].

Additionally, on all compounds a second square atomic arrangement is observed with

Sample	lattice constant	I_{tunnel}	U_{bias}
123 thin film	0.38 nm	0.29 nA	179 mV
123 single crystal	0.38 nm	0.61 nA	408 mV
247 single crystal	0.38 nm	1.22 nA	450 mV
124 single crystal	0.38 nm	0.61 nA	1382 mV
123 thin film	0.27 nm	0.29 nA	179 mV
123 single crystal	0.27 nm	0.90 nA	408 mV
247 single crystal	0.27 nm	0.29 nA	543 mV
124 single crystal	0.27 nm	0.61 nA	408 mV

Table 2.1: Tunneling parameters for the atomically resolved images of YBCO 123 thin films, YBCO 123, 124 and 247 single crystals.

a lattice constant of 0.27 nm which can be unambiguously attributed to the O(2)-O(3) spacing in the Cu-O planes (see fig. 2.2). Both atomic lattices can be imaged consecutively by variation of bias voltage (the voltage and current parameters for the images shown in fig. 2.7 are compiled in table 2.1). No surface damage was observed after atomic resolution imaging. Therefore it is suggested that the 0.38 nm lattice may correspond to

the Cu(2), Y, O(1) or Ba arrangement. However, a possible surface reconstruction of the $Y_2Ba_4Cu_{6+N}O_{14+N}$ unit cells or resonant tunneling processes can not be excluded as an explanation for the observed atomic arrangements.

On thin film samples of YBCO 123 similar atomic lattices with spacings of 0.38 nm and 0.27 nm are observed. Since the surface of thin film samples is cleaner than that of a single crystal angle-resolved X-ray photoemission spectroscopy experiments (using monochromatic radiation) have been performed to determine the surface layer of YBCO 123.⁶ These experiments show that the topmost layers of YBCO 123 are the Ba-O and the CuO_2 layers. These results will be discussed in detail in chapter 3, section 3.7.

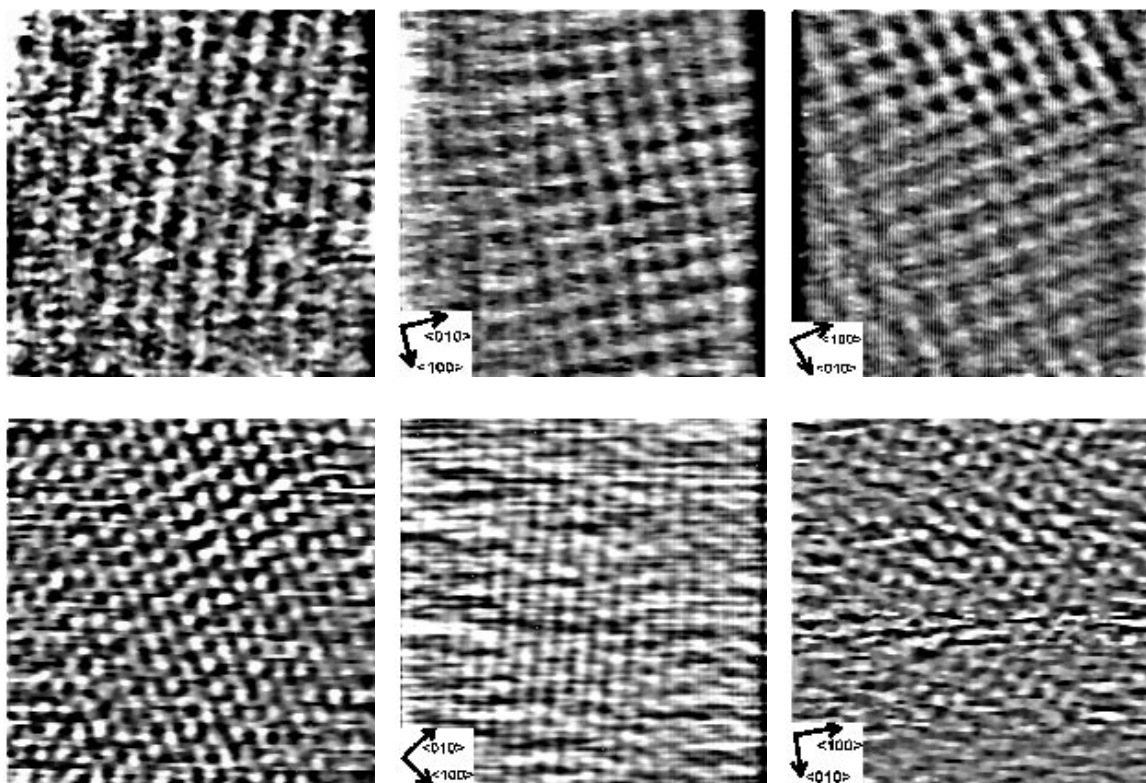


Figure 2.7: Atomically resolved images of the surface of YBCO 123 (left), YBCO 247 (middle) and YBCO 124 (right) single crystals (image size 5 nm \times 5 nm). The crystallographic directions are indicated for the untwinned compounds. *UPPER ROW:* Approximately square atomic arrangement with a lattice constant of 0.38 nm. This lattice may be interpreted as spacings Y–Y, Ba–Ba, Cu–Cu (in the planes or chains) or O–O (in the chains or in the Ba–O layer). *LOWER ROW:* Atomic lattice with a periodicity of 0.27 nm. Provided only a single atomic species is imaged this spacing is attributed to the O(2)–O(3) distance in the CuO_2 planes.

⁶Experiments in collaboration with H.-G. Boyen and P. Oelhafen, Institute of Physics, Univ. Basel.

2.1.3 Investigations on thick YBCO crystals

2.1.3.1 STM results

As demonstrated in the introductory Chapter 1 thicker YBCO crystals⁷ are often contaminated by flux originating from the growth process in a eutectic $\text{YBa}_2\text{Cu}_3\text{O}_7 / \text{BaCuO}_2 / \text{CuO}$ melt. STM imaging on this type of thicker YBCO crystals leads to instable imaging since $\text{BaCuO}_2 / \text{CuO}$ flux is not conductive. However, this flux contamination of the crystals can be removed partly by scanning the sample for a while. The images (see fig. 2.8) obtained by this process give a first idea of how the contaminated surfaces look like.⁸

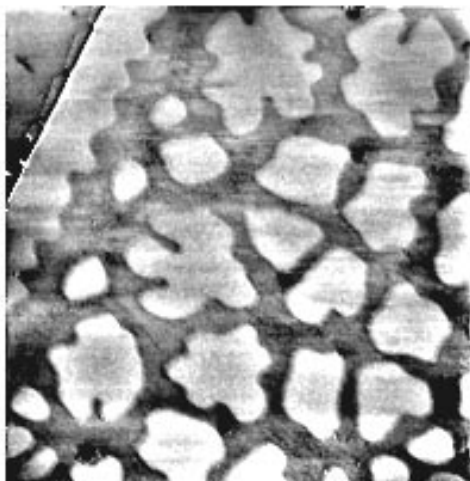


Figure 2.8: Surface of a flux-contaminated YBCO 124 single crystal after having scanned the sample for some minutes with the STM tip. Some flux has been removed. The surface shows characteristic curved islands that are not present on the surface of the thin single crystal platelets. Image size: $8 \mu\text{m} \times 8 \mu\text{m}$. Island height: about 2 nm.

2.1.3.2 SFM on 'thicker' YBCO crystals

In contrast to the thin YBCO 124 and 247 crystals which show clean flat terraces with steps of a unit cell in height (see fig. 2.9 and the discussion in section 2.1.2.) thicker⁹ crystals seem to be contaminated with residual flux from the growth process. This material of low conductivity causes problems during investigations by STM. For this reason the scanning force microscope has been applied.

⁷The thickness of the platelet is between 30 and 50 μm .

⁸'Correct' imaging of the flux-contaminated surfaces is possible with Scanning Force Microscopy. This is subject of the following section.

⁹30 and 50 μm .

2.1.3.3 Experimental conditions

The STM and SFM investigations have been performed at ambient temperature and pressure without previously cleaving or treating the crystals. The STM images have been acquired in constant-current mode with a tunneling current of less than 0.5 nA and a tip bias voltage above +0.8 V. Different, mechanically sharpened Pt₉₀Ir₁₀ tips have been used for STM to exclude tip-induced artifacts. For beam-deflection-type SFM, commercially available micro-fabricated cantilevers with integrated Si₃N₄ tips (force constant 0.12 N/m) have been employed. All images shown have been recorded in constant-force mode.

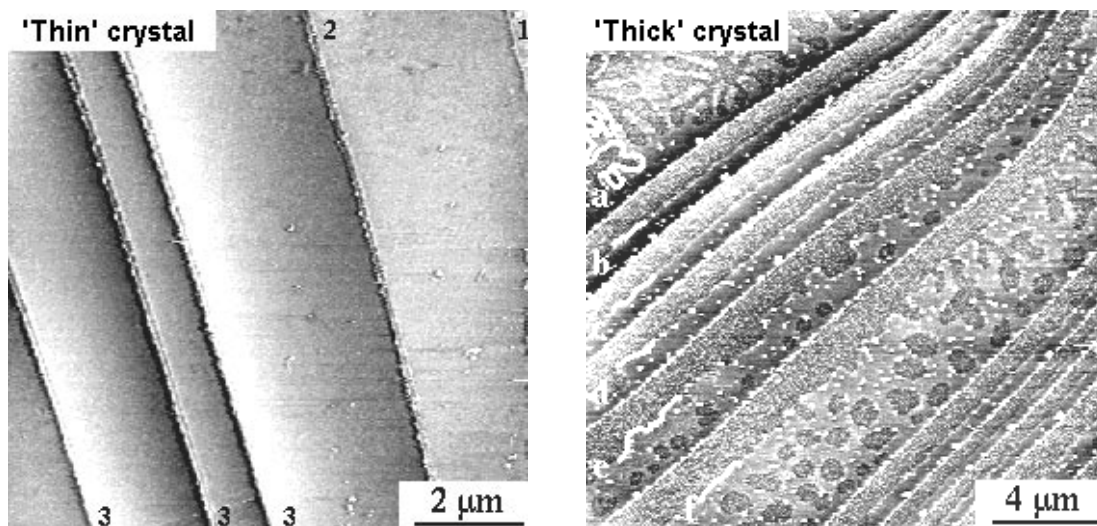


Figure 2.9: *LEFT:* STM image of a thin ($< 10\mu\text{m}$) YBCO 124 single crystal platelet. The numbers in black denote the numbers of unit cell steps in c -axis direction. No structures are observed on the terraces.

Figure 2.10: *RIGHT:* SFM image of a thicker ($30\text{--}40\mu\text{m}$) YBCO 247 crystal platelet. The height of the steps is about 5 nm. The terraces, however, are covered by barium cuprate/copper oxide flux (originating from the crystal growth process) with a highly curved (fractal) periphery line (perimeter). The small letters mark structures (partly highlighted by a white line) on a wide terrace ('a') and boundary lines of flux on narrower terraces ('b'-'f'). Small particles (white spots in the image) decorate the flux structures.

2.1.3.4 Large scale SFM data

A typical SFM image acquired from a thicker YBCO 247 single crystalline platelet is shown in fig. 2.10. The steps are 5 nm (one c -axis spacing) in height, but in contrast to thin crystals the terraces are covered by some material. This material is likely to cause the difficulties with STM imaging. The boundary of this surface contamination layer is highly curved, at least on large terraces. Some of the boundary lines (partly highlighted

by a white line) are labeled with small letters: 'a' is a highly curved boundary on a large terrace, 'b' – 'd' are comparatively smooth boundaries, 'e' and 'f' show a higher degree of complexity.

2.1.3.5 Some remarks on the crystal growth process

Kaldis and Karpinski have observed [2.2] that the single crystals of YBCO 124 and 247 are growing out of the barium cuprate / copper oxide flux at the constant temperature of 1100°C, but are wetted by flux when the growing time exceeds approximately 24 h. Shorter growing times yield smaller crystals. Thicker crystals are obtained when a slower cooling rate is applied. Such crystals, however, are not free from defects and residual flux. Similarly, residual flux is observed on the crystals if the cooling rate is too fast. The crystals selected for this SFM study are prepared under conditions expected to yield flux-covered surfaces. Indeed, scanning electron microscopy investigations with energy dispersive analysis of X-rays (EDAX) have revealed that the thicker crystals are actually contaminated by flux. An analysis of the apparent height of the contamination layer observed by SFM agrees well with the height of the BaCuO₂ unit cell (cubic, $a = 1.8285$ nm). Hence, the observed surface layer is identified as residual flux.

2.1.3.6 Discussion of the curved boundary of the flux

Figure 2.12a shows the surface of a YBCO 124 single crystal as imaged by SFM. Some areas of the surface with a highly curved boundary line are not covered by flux. Four such regions are labelled in fig. 2.12a with '1' to '4'.

The complexity of a boundary line can be characterized by determination of its

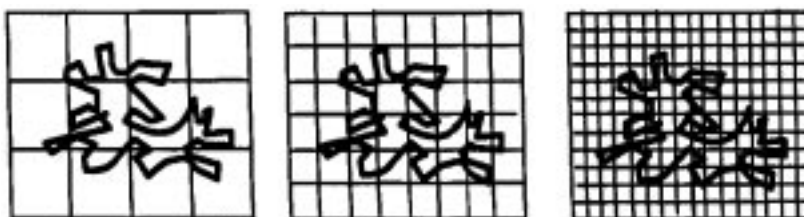


Figure 2.11: Determination of the Hausdorff dimension of a curved line by using the box counting method. Grids with gradually decreasing meshwidth r ('yardstick') are put over the curve and the number of boxes $N(r)$ which contain a segment of the curve are counted. The Hausdorff dimension is equal to $\log(N(r))/\log(1/r)$ in the limit $r \rightarrow 0$.

Hausdorff dimension which equals 1 if the curve is smooth, or has a value between 1 and 2 if the curve is fractal (with a fractal dimension d_f). For an introduction to fractals see a recent book by *Schroeder* [2.9]. A self-similar curve is characterized by a power law which connects the apparent length L of the curve to the length of the scale unit r ('yardstick').

The power law exponent ϵ is zero for a smooth curve and non-integer negative for a fractal curve. A practical method usually applied to determine the Hausdorff dimension is the box counting method (this procedure is shown in fig. 2.11): a grid with a gradually decreasing meshwidth ('yardstick') is put over the curve and the number of boxes $N(r)$ which contain a segment of the curve is determined approximating L on different length scales. d_f equals $\log(N(r))/\log(1/r)$ in the limit $r \rightarrow 0$. When L is plotted vs. r in a double-logarithmic plot, a straight line is obtained. The slope of this straight line equals ϵ and d_f is determined by $1-\epsilon$.

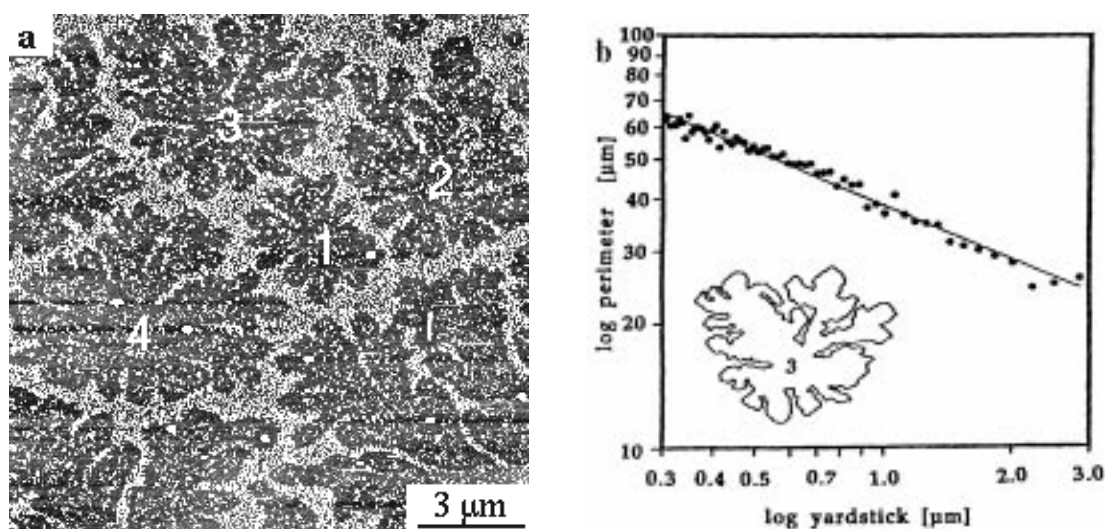


Figure 2.12: (a) Fractal flux patterns on the surface of a YBCO 124 single crystal imaged by SFM. The perimeter of four different fractal structures is marked by numbers '1' to '4'. (b) Fractal analysis of the perimeter of the structure labeled '3'. The double logarithmic plot of yardstick to measure the perimeter ('meshwidth of the grid') vs. perimeter reveals a linear relation. The straight line is a least-square-fit to the datapoints ('Pearson r ' correlation coefficient = 0.988). From its slope (-0.42), a fractal dimension of 1.42 can be deduced.

For the analysis meshwidths from $3 \mu\text{m}$ to $0.1 \mu\text{m}$ were used (this is larger than the pixel resolution of the SFM image; otherwise this analysis would not make sense). Figure 2.12b shows how the fractal dimension of the boundary line labeled by '3' in fig. 2.12a is determined: the apparent perimeter of the boundary line vs. the length scale ('yardstick') is displayed in a double logarithmic plot. The data is fitted by a straight line (least-square-fit) with a slope of $\epsilon = -0.42$. This leads to a fractal dimension of 1.42 which is typical of a fractal boundary line. For the boundary lines of the other uncovered areas '1', '2' and '4', similar values of the d_f are derived documenting the uniform nature of the flux layer (see Table 2.2).

Fig. 2.10	a	b	c	d	e	f
d_f	1.32	0.97	0.97	0.98	1.01	1.26
Fig. 2.12			1	2	3	4
d_f			1.36	1.36	1.42	1.46
Fig. 2.13			5	6	A	B
d_f			1.67	1.45	1.71	1.59

Table 2.2: Fractal dimensions d_f of BaCuO₂ flux structures. The letters and numbers refer to the corresponding labels in the respective figures.

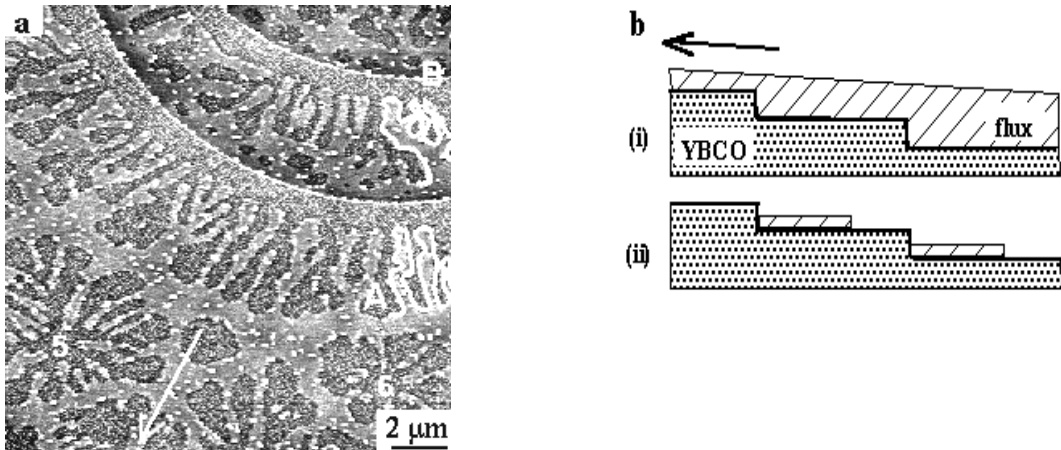


Figure 2.13: (a) SFM image of the surface of a YBCO 247 single crystal showing a flux contamination layer with fractal boundaries. The fractal dimension is larger close to steps than on flat terraces. Note the 'fingering' of flux close to steps (boundary lines 'A' and 'B', partly highlighted by a white line). The flux contamination is always in contact with the step from a lower terrace. The arrow indicates the migration direction of the shrinking flux. (b) Model for the migration of flux on the crystal surface during the growth process: (i) YBCO crystal covered by flux. After some time the flux shrinks and migrates to the direction indicated by the arrow. (ii) Residual flux is stopped at crystal steps and solidifies.

2.1.3.7 Flux morphology close to crystal steps

The SFM image in fig. 2.13a shows the behaviour of solidified flux in the vicinity of steps on the surface of a YBCO 247 single crystal. A determination of d_f yields significantly

higher values than those observed on large terraces. The flux features labeled with '5' and '6' as well as the boundary lines 'A' and 'B' close to the steps exhibit a fractal dimension between 1.45 and 1.71 (see Table 2.2). Note the fingering of the flux in boundaries 'A' and 'B'.

The boundary line can also exhibit a lower fractal dimension or a non-fractal behaviour if the steps are too close and the terrace width is too small (see fig. 2.10: boundary line 'f' only shows $d_f = 1.26$ and 'b' - 'e' are not fractal at all.

2.1.3.8 Interpretation and a model for flux migration

In the following possible reasons for the fractal behaviour of the flux will be discussed and a model for flux migration on YBCO single crystals will be suggested.

Morphologies of two-dimensional fractal structures similar to the SFM images of barium cuprate/copper oxide flux are described in literature [2.10, 2.11] in terms of dense branching morphology and unstable viscous fingering models. Typical examples are e.g. aggregate growth by electrochemical deposition, solidification from supersaturated solution, precipitation from undercooled melts and structures generated in Hele-Shaw cells [2.12]. This might be an indication that similar mechanisms are operative. Actually, crystal growth from supersaturated flux, especially in the regime of high pressure, is a non-equilibrium process. The surface tension at the interface flux/crystal might be responsible for the occurrence of fractal boundary lines of flux.

From the fact that flux is always touches a step from the lower terrace (cf. fig. 2.13a and the schematic in fig. 2.13b) a model for flux migration on the crystal can be suggested. At temperatures above the liquidification point of the $\text{BaCuO}_2/\text{CuO}$ eutectic flux, YBCO is expected to grow from the flux until all yttrium is used-up. The crystal is fully covered by flux (fig. 2.13b(i)). It is known from the experiments [2.8] that the flux shrinks during cooling and migrates in direction of larger crystal thickness (indicated by an arrow in fig. 2.13a and 2.13b(i)). Obviously, some residual flux remains on the crystal terraces and is stopped at crystal steps (fig. 2.13b(ii)). Due to surface tension the solidified flux forms structures with highly curved boundary lines caused by the surface wetting properties of YBCO and flux.

2.1.3.9 Surface wetting

Some limited information on surface wetting properties of the barium cuprate / copper oxide flux may be inferred from the fractal dimension of the solidified flux.¹⁰ Assumed 'A' to be the barium cuprate / copper oxide flux and 'B' to be the YBCO single crystal it depends on the cohesion energies ϵ_{AA} and ϵ_{AB} how the flux 'A' wets the surface 'B'. In the present experiment there is only access to the morphology of the solidified flux. If ϵ_{AA} is larger than ϵ_{AB} , then the flux tends to form large compact islands with a smooth

¹⁰The ideas to this paragraph originate from a discussion with D. Tománek, Michigan State University, U.S.A.

(non-fractal) boundary since it is energetically more favourable to reduce the number of atoms that constitute the boundary of the island. In this case the boundary line is as short as possible. In case of ϵ_{AA} much smaller than ϵ_{AB} bulk 'A' atoms are energetically less favoured than boundary line atoms. This results in very small islands having boundary lines as long as possible. The case of a fractal boundary line is between these two extremal cases. It might be closer to the second one.

2.1.4 Friction force microscopy on thick YBCO crystals

2.1.4.1 Distinguishing different materials

To support the claim that the previously described contamination structure is actually different from the crystal material friction force microscopy has been performed.¹¹ As discussed in the introductory part friction force microscopy is capable to distinguish between different friction properties of materials. To demonstrate this fig. 2.14 shows the topography ('A-B' signal) and the friction channel ('C-D' signal) of a SFM/FFM image acquired from the surface of a YBCO 124 single crystal.¹² A platelet (labeled 'A' in fig. 2.14) is clearly seen in the topography image. With the topography information alone the question can not be answered whether this platelet is of the same material as the underlying crystal surface or of a different material. The friction force microscopy data (middle and right image in fig. 2.14, forward and backward scan) clarifies this issue: since there is no difference in friction between the crystal's surface and the platelet's surface both consist of a material with the same friction properties, most likely of the same material.¹³ This is quantified in the 'friction loop' displayed in fig. 2.17.¹⁴

A seemingly very similar situation is encountered in fig. 2.18. This topography image shows similar platelets (labeled 'B') on the crystal's surface¹⁵ as in fig. 2.14. But the platelets are of a different material compared to the underlying crystal surface as can be inferred from the friction force microscopy data (figs. 2.19, 2.20). In these FFM images clear friction contrast is observed. This is additionally demonstrated in the friction loop (fig. 2.21) where two different levels of friction can be distinguished clearly ('1' and '2'). The friction forces acting on scanning the crystal compare as a ratio of 2:11 yielding a five times smaller friction force¹⁶ when the platelets are scanned.

¹¹Collaboration with R. Lüthi, Institute of Physics, Univ. Basel, Switzerland.

¹²The topography 'forward' and 'backward' scans yield the same image of course.

¹³The step edges cause some contrast in the FFM image.

¹⁴A friction loop consists of two scanlines. One is taken from the FFM forward scan and one from the FFM backward scan. The corresponding topography scanline is shown in white.

¹⁵The crystal's surface exhibits again that type of flux contaminations as described previously. See label 'F' in fig. 2.20.

¹⁶A friction loop has a horizontal symmetry axis 's' (it might be slightly sheared due to the tip's geometry or to distortions due to piezo creep). The ratio of friction forces is determined by evaluating the ratio of the distances ('s'-1' : 's'-2') of the two different levels of friction from the symmetry axis 's'.

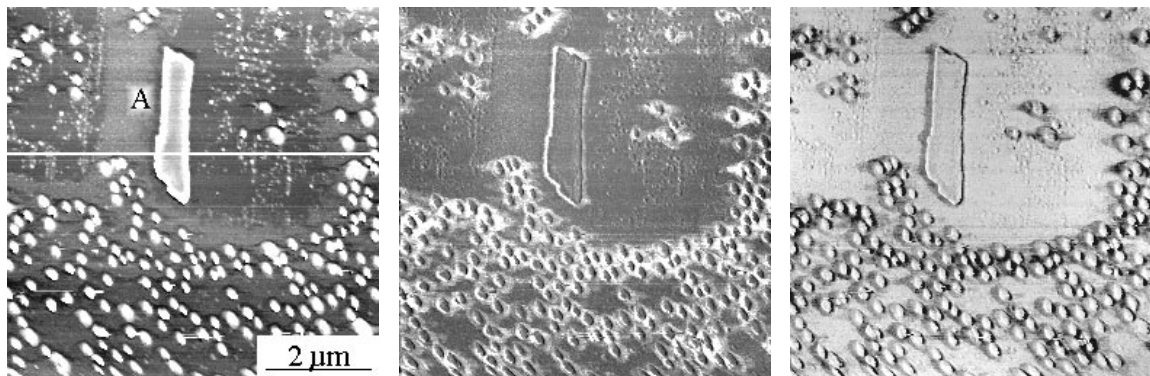


Figure 2.14: *LEFT:* SFM topography image of the surface of a YBCO 124 single crystal. 'A' denotes a platelet on the crystal's surface. From the topography alone it can not be determined whether the platelet and the crystal's surface consist of the same material or not. The white line indicates the scanline that has been used to generate the friction loop shown below.

Figure 2.15: *MIDDLE:* friction force microscopy image (forward scan). Both the platelet and the crystal's surface show the same contrast in friction properties. Most likely they consist of the same material.

Figure 2.16: *RIGHT:* friction force microscopy image (backward scan). No friction contrast is seen beside step edge contrast.



Figure 2.17: Friction loop of the topography scanline marked in white above. No contrast is seen in the friction signal irrespective of step edge contrast (sharp peaks). 'A' denotes the position of the platelet.

Since the spring constant (normal forces: $c_n = 0.1$ N/m, transversal forces: $c_t = 2.42$ N/m) and geometry of the cantilever (length $l = 200$ μm , width $b = 21$ μm , thickness $d = 0.6$ μm , tip radius $r = 12.5$ μm) is known the lateral force can be calculated: $F_L = (3/2)A_l S c_t (r/l)$. A_l is the amplitude of the lateral signal (in [V]), S is the sensitivity factor of the high-voltage piezo-driver-amplifiers ($S = 50.5$ nmV^{-1}). An absolute value

for the lateral force on the platelets is 1.1 nN. The lateral force on the crystal surface is higher, namely 5.8 nN (values only accurate within an calibration error of 20 %).

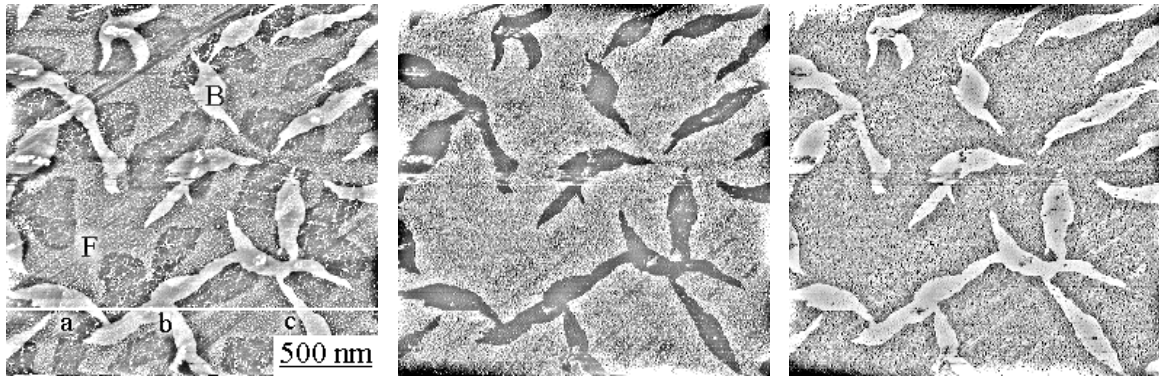


Figure 2.18: *LEFT:* SFM topography image of the surface of a YBCO 124 single crystal with flux contaminations 'F' and platelets 'B'. The white line indicates the scanline that has been used to generate the friction loop shown below. Three positions are labeled by 'a', 'b' and 'c'.

Figure 2.19: *MIDDLE:* friction force microscopy image (forward scan). The platelets and the crystal's surface show the different contrast in friction properties implying that they consist of different materials.

Figure 2.20: *RIGHT:* friction force microscopy image (backward scan). Again two different levels of contrast are observed.

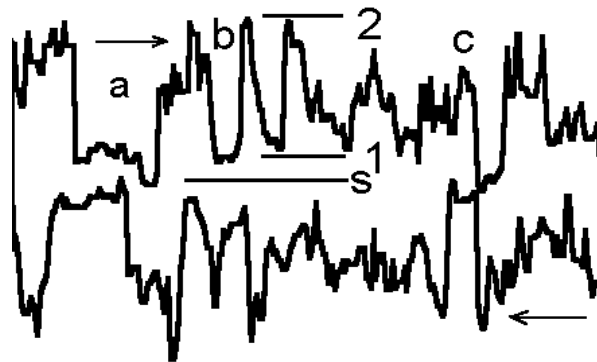


Figure 2.21: Friction loop of the topography scanline marked in white above. Two different levels of friction are observed. 's' stands for the symmetry axis of the friction loop. '1' and '2' indicate the two different levels of friction. They compare with the ratio 2:11 implying more than 5 times smaller friction on the platelet structures. 'a', 'b' and 'c' denote the positions indicated in the topography scanline.

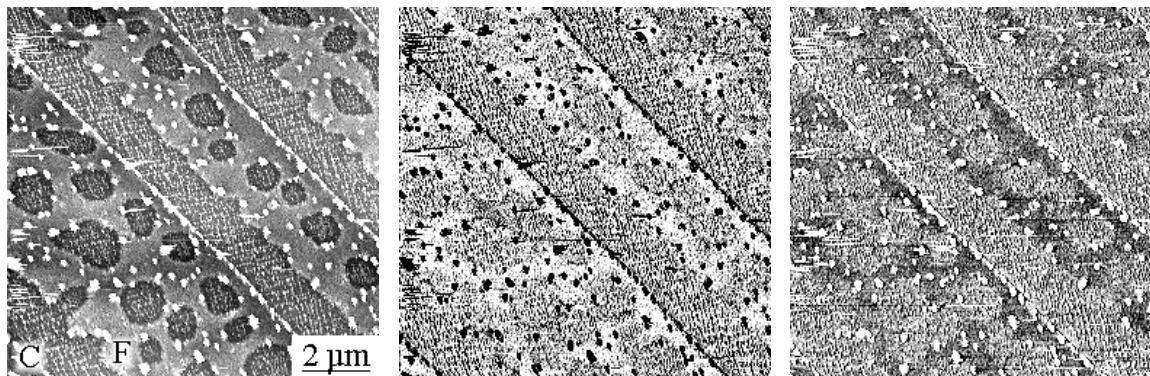


Figure 2.22: *LEFT:* SFM topography image of the surface of a YBCO 247 single crystal with flux contaminations 'F' and slab-like particles 'C' on the crystal surface which are aligned to directions perpendicular to each other. Small particles decorate the flux contamination layer 'F' and not the area 'C' which might be an indication of a different reactivity.

Figure 2.23: *MIDDLE:* friction force microscopy image (forward scan). The flux layer (BaCuO_2), the aligned slab-like particles (possibly CuO) and the decoration particles on the flux layer show all different contrast.

Figure 2.24: *RIGHT:* friction force microscopy image (backward scan). The contrast is reverse in the backward scan compared to the forward scan implying the presence of different materials.

2.1.4.2 FFM results on flux-contaminated crystals

To interpret the SFM images of the thick YBCO crystals FFM data of the BaCuO_2 / CuO flux contamination is shown. Figs. 2.22 – 2.24 show SFM/FFM images of the surface of a YBCO 247 single crystal with typical flux contamination. Three types of structure are distinguished: the crystal surface with some slab-like particles aligned in two directions perpendicular to each other¹⁷ ('C'), the BaCuO_2 flux layer¹⁸ ('F') and some small particles¹⁹ decorating the flux layer. As seen from the FFM data (figs. 2.23 and 2.24) all three types of structure yield different contrast in the friction channel implying the presence of three materials with different friction properties.²⁰ Since the friction data is comparatively noisy a quantitative analysis of the friction forces is not useful.

¹⁷From the crystallographic point of view and if the crystal growth conditions (growth in a BaCuO_2 / CuO flux) are taken into account it may be suggested that these slab-like particles could be CuO particles.

¹⁸The height corresponds to a single layer of BaCuO_2 (1.8 nm). The structure of BaCuO_2 is cubic with $a = 1.8285$ nm.

¹⁹Their sizes are below 100 nm. However, it cannot be excluded that some tip-geometry induced artifacts affect the apparent diameter of much smaller particles.

²⁰The small decoration particles give the highest friction force.

SFM/FFM images depicting BaCuO_2 flux structure with a fractal boundary line as discussed in section 2.1.3 are shown in figs. 2.25 – 2.27.



Figure 2.25: *LEFT:* BaCuO_2 flux structure with a fractal boundary line (SFM topview image). Note that the step in the middle of the image is decorated with small particles.

Figure 2.26: *MIDDLE:* FFM forward scan. The BaCuO_2 -covered areas differ in friction signal from the uncovered areas.

Figure 2.27: *RIGHT:* FFM backward scan. The contrast is reverse compared to the forward scan.

2.1.4.3 Relevance in terms of crystal growth

The friction force microscopy information can be used to obtain information on crystal growth. Fig. 2.28 shows the topography image of a YBCO 247 single crystal. Obviously the flow of crystal steps ('S', upper right half of fig. 2.28) has been obstructed at a position on the crystal's surface which would be classically called a *pinning centre for growth steps* ('P'). With the topographical information only it is not possible to explain why the steps are pinned. The lateral force information (figs. 2.29 and 2.30) reveals the answer: the growth steps have been obstructed by some stick-shaped particle that causes different lateral forces in the friction force signal. It is covered by the same kind of small particles ('cp', contaminant particles) as those decorating the BaCuO_2 flux ('F').

2.1.5 Conclusion

STM and AFM images of the surface of YBCO 124 and 247 single crystals have been presented. Thin crystal platelets have been found to exhibit clean terraces with steps of one or multiple unit cell spacings in c -direction, whereas thicker platelets are contaminated by residual barium cuprate/copper oxide flux with a fractal boundary line. The fractal dimension of this outline is about 1.4 for flux-covered regions on large terraces.

However, it is significantly larger close to crystal steps. A possible origin for the fractal boundary line may be found in the different surface wetting properties of YBCO and barium cuprate / CuO flux leading to a competition between formation of small flux islands with a total periphery line as long as possible on one hand and coalescence of islands to a compact flux layer on the other hand. A model has been presented for flux migration during the growth process based on the observation of flux shrinking during the cooling process. SFM images show residual flux stopped at crystal steps. The migration direction of the shrinking flux as inferred from the crystal growth experiment is the same as the one derived from the SFM images.

The application of friction force microscopy (FFM) to thick YBCO crystals with flux contamination has been found to be a useful supplement to interpret the results in a more general way. FFM has shown that the suggested interpretation²¹ of the surface layer with a fractal boundary line as a non-YBCO contamination layer (possibly barium cuprate/copper oxide) is correct. In some cases information on the crystal growth process is obtained by relating the morphology to friction contrast.

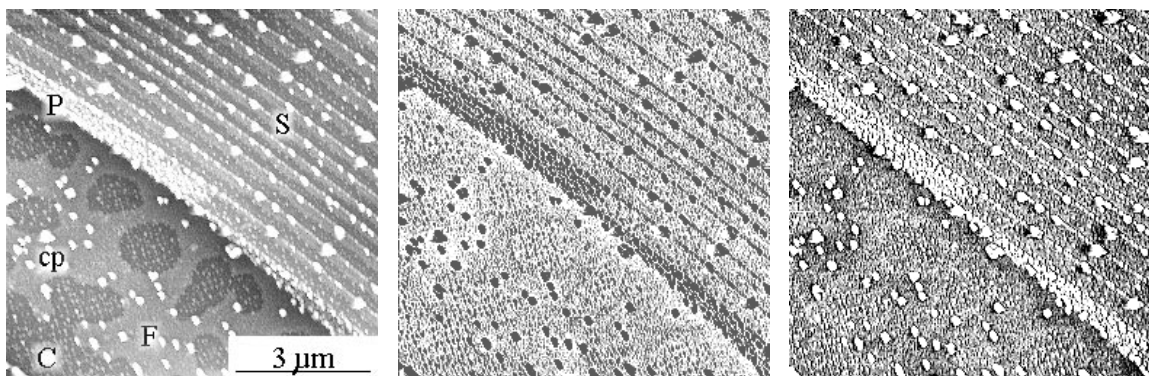


Figure 2.28: *LEFT:* Topography of a YBCO 247 single crystal. The step flow ('S') during the growth process has been obstructed by a pinning centre for steps ('P'). 'F' denotes BaCuO₂ flux on the crystal surface. Contaminant particles ('cp') decorate the flux.

Figure 2.29: *MIDDLE:* FFM forward scan. The pinning centre for steps reveals different friction properties than those of the crystal surface implying the presence of a secondary phase in the crystal responsible for the obstruction of step flow.

Figure 2.30: *RIGHT:* FFM backward scan. The contrast reversal confirms the interpretation of different contrast in the lateral force image in terms of friction.

²¹Based on the observation of different conductivities in SEM, and on thickness measurement of the contaminant layer.

2.2 BSCCO 2212 single crystals

Evidence of superconductivity above 77 K in a Bi-Sr-Ca-Cu-O compound was first reported by *Maeda et al.* in 1988 [2.13]. A superconducting phase ($T_c = 80$ K) with an approximate stoichiometry of $\text{Bi}_2\text{Sr}_2\text{CaCu}_2\text{O}_8$ (in short BSCCO 2212) was rapidly identified [2.14, 2.15].

2.2.1 Crystal growth

In contrast to the YBCO compounds that melt incongruently BSCCO compounds melt congruently, i.e. it is not necessary to use a flux solution for crystal growth.

Single crystals of BSCCO 2212 were grown by use of a self-flux technique. Appropriate amounts of analytical-grade powders of Bi_2O_3 , CaCO_3 , SrCO_3 and CuO were placed in an alumina crucible and melted in an electrically heated chamber furnace at about 970°C for 24 h and then cooled to 820°C at a typical rate of 2 K/h. Thereafter, the solidified melt was furnace-cooled to room temperature. Shiny BSCCO(001) crystal platelets (typical size: 2 mm \times 1 mm) were mechanically removed from the solidified matrix. Images of a cleaved crystal obtained by optical microscopy are shown in fig. 2.31.

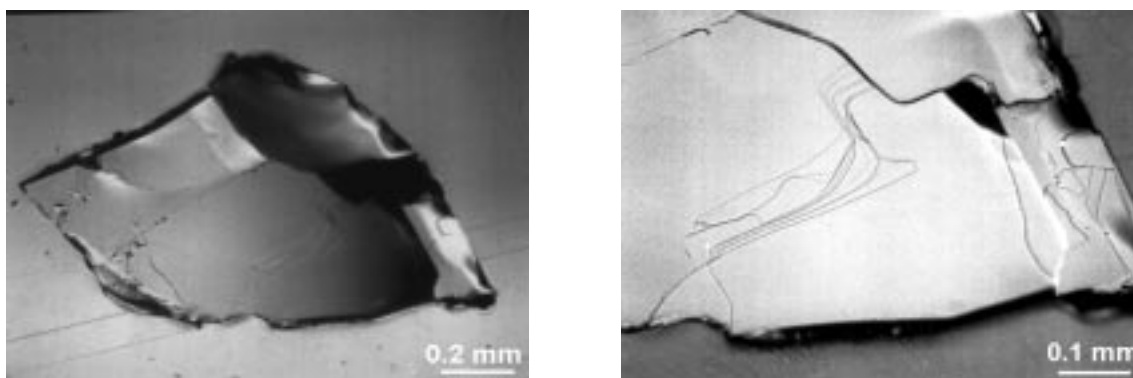


Figure 2.31: Optical micrographs of a cleaved BSCCO 2212 single crystal showing flat terraces and cleavage steps.

2.2.2 Characterization

The orientation of the platelets was confirmed by X-ray diffraction (see fig. 2.32). The stoichiometry was determined using energy dispersive scattering of X-rays analysis (EDAX, EDS) in a scanning electron microscope (SEM) by comparing it to the spectrum of a BSCCO 2212 powder sample (fig. 2.33). The 'Al' and 'Ag' lines are caused by the sample holder (aluminum) and the silver paint used to mount the samples. A quantitative analysis of the spectra yields a approximate stoichiometry of $\text{Bi}:\text{Sr}:\text{Ca}:\text{Cu} = 2:2:1:2$.

However, the accuracy of the determination is limited to about $\pm 20\%$ since no elemental standards were used.

The electrical and magnetic properties of the BSCCO 2212 single crystals were determined using the standard 4-probe resistivity measurement technique and a vibrating sample magnetometer. Both methods reveal a transition to superconductivity at $T_c = 80$ K ($R = 0$) (see figs. 2.34 and 2.35).

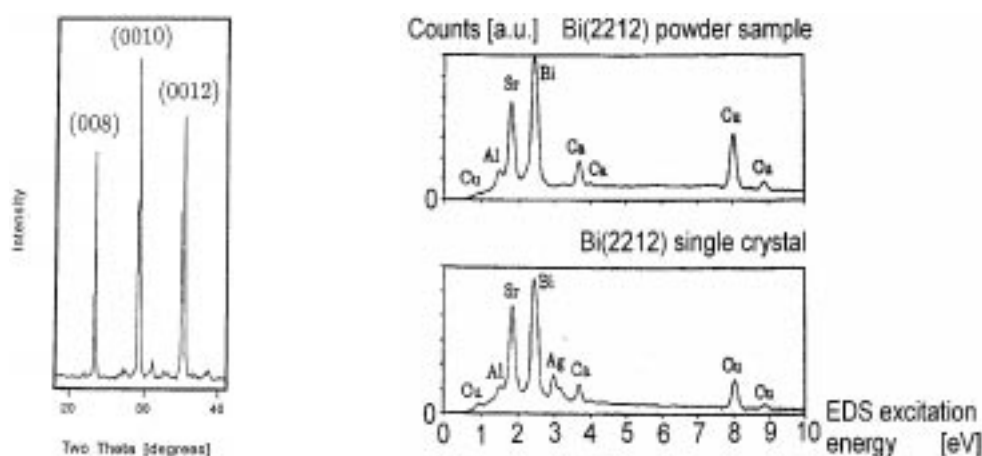


Figure 2.32: *LEFT:* X-ray diffraction (XRD) $\text{Cu K}\alpha$ spectrum of a BSCCO 2212 single crystal platelet. The occurrence of (002ℓ) reflections implies the (001) orientation of the platelet.

Figure 2.33: *RIGHT:* Energy dispersive scattering of X-rays analysis (EDAX, EDS) performed in a scanning electron microscope. *Top:* BSCCO 2212 powder reference spectrum. *Bottom:* EDS spectrum of the BSCCO 2212 single crystal.

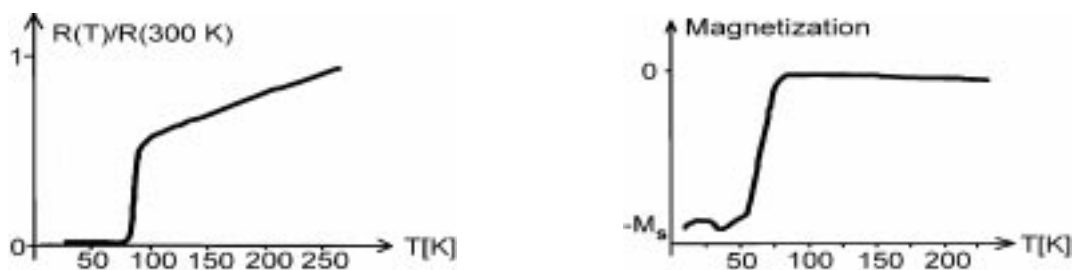


Figure 2.34: *LEFT:* Four-probe resistivity measurement of a BSCCO 2212 single crystal. A sharp transition to superconductivity is observed at $T_c = 80$ K.

Figure 2.35: *RIGHT:* Meissner effect of the BSCCO 2212 single crystal sample demonstrated by a diamagnetic signal below $T_c = 80$ K. The diamagnetic signal saturates at a value $-M_s$.

2.2.3 Structure and TEM

BSCCO 2212 has an orthorhombic crystal structure ($a = 5.41 \text{ \AA}$, $b = 5.42 \text{ \AA}$, $c = 30.9 \text{ \AA}$, see tetragonal sub-cell with lattice constants $a_t = 3.8 \text{ \AA}$ and $c_t = 30.9 \text{ \AA}$ in fig. 2.40 for comparison). It shows a one-dimensional (1d) superstructure modulation with a period of 27 \AA in transmission electron microscopy [2.15, 2.16]. The origin of this modulation was found to be due an additional row of oxygen atoms which is inserted between two rows of Bi atoms every ten rows of Bi atoms [2.17] or modulated displacement of the Bi atoms along b . Fig. 2.36 shows a transmission electron microscopy (TEM) image (cross-section geometry) of a BSCCO 2212 single crystal (reproduced after *Y. Matsui et al.* [2.16]). A plane-view TEM image is shown in fig 2.37.²² The superstructure modulation with a periodicity of 2.7 nm appears as parallel stripes spaced by 1.35 nm . The distance between the stripes is only half the value which would be naively expected since the BSCCO 2212 is shifted at its half height by a lattice vector $(a/2, b/2, 0)$. This is reflected by the space group $A2aa$ (no.37) which causes extinction rules for the $(h00)$, $(0k0)$ and $(hk0)$ reflections if h and k are odd. Thus only the even reflections will contribute to the image and the distances between superstructure lines will be reduced to half the value ($= 13.5 \text{ \AA}$). This is intuitively obvious when electron transmission along $[001]$ is considered.

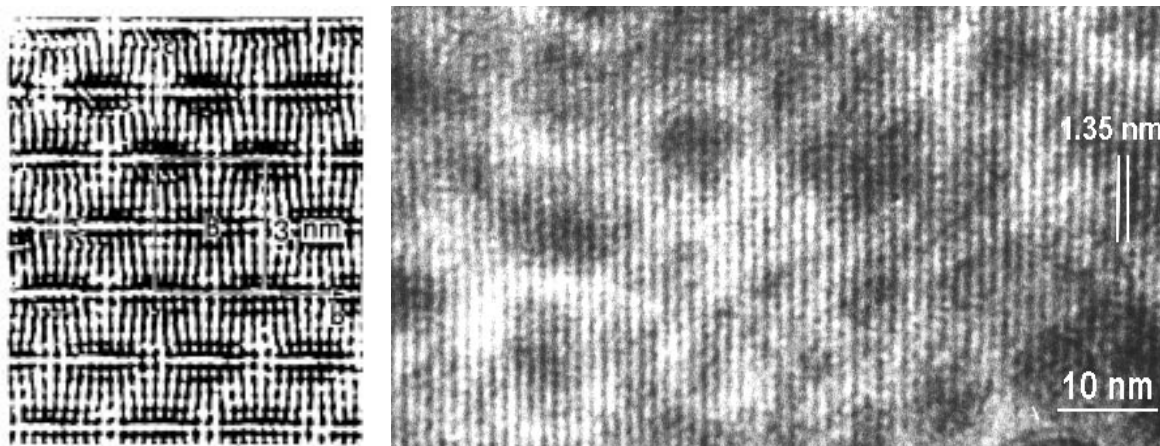


Figure 2.36: *LEFT:* Transmission electron micrograph of a BSCCO 2212 single crystal. The 27 \AA modulation is visible as ellipsoidal areas of darker contrast in the image. The view direction is perpendicular to the $[001]$ direction (cross-section image). This TEM image is taken from *Y. Matsui et al.* [2.16].

Figure 2.37: *RIGHT:* Transmission electron micrograph of a BSCCO 2212 single crystal in planar geometry (the crystal is of the same batch as those investigated in this chapter). The superstructure appears as stripes at a distance of 27 \AA .

²²This transmission electron micrograph has been acquired from a BSCCO single crystal grown at Basel. A Philips CM 200T TEM was used. Image by Dr. D. Hesse and Dr. S. Senz, Max-Planck-Institute for Microstructure Physics, Weinberg 2, D-06120 Halle (Saale).

The diffraction image (fig. 2.38) shows a rectangular spot pattern due to an atomic lattice plane distance of 2.7 \AA . This is half the spacing of the orthorhombic unit cell of BSCCO 2212. Due to the above mentioned extinction rules only $(h00)$, $(0k0)$ and $(hk0)$ reflections with h and k both even are allowed. This leads to a closest lattice-plane distance of 2.7 \AA . The (200) reflection is marked by an arrow in fig. 2.38. Additional reflections due to the superstructure are only found along the $[100]$ direction. These reflections (labelled 's') are attributed to the superstructure with a distance of 13.5 \AA (about $5 \times 2.7 \text{ \AA}$). The corresponding lattice image is shown in fig. 2.39. The lattice plane spacing is 2.7 \AA corresponding to the half length of the a and b axis parameters of BSCCO 2212 (see fig. 2.41).

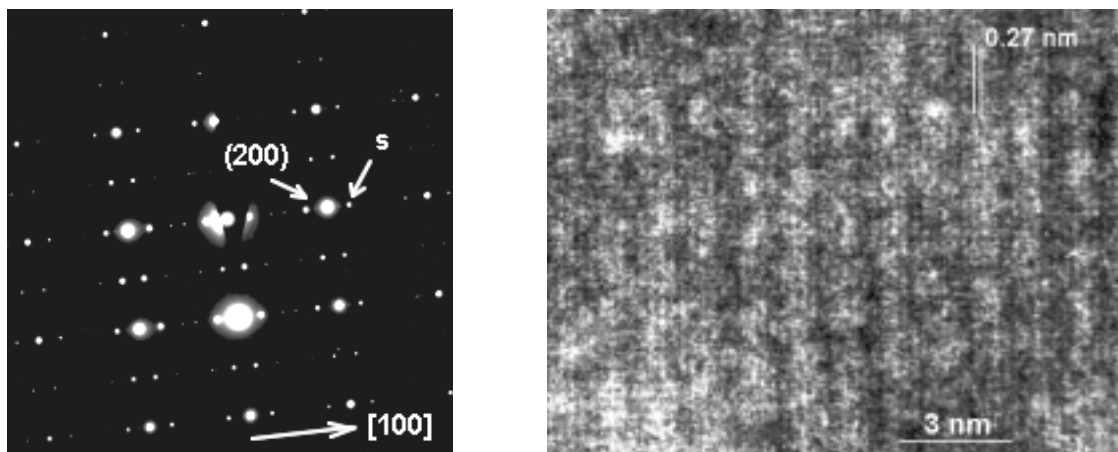


Figure 2.38: *LEFT:* Electron diffraction image of a BSCCO 2212 single crystal in planar TEM geometry (incident electron beam along $[001]$). The (200) reflection of the atomic lattice is indicated. Label 's' denotes a superstructure modulation reflection. The superstructure is solely found along $[100]$.

Figure 2.39: *RIGHT:* High resolution transmission electron micrograph of a BSCCO 2212 single crystal in planar geometry using the $\{200\}$ and $\{220\}$ reflections for interference. Atomic columns are clearly resolved at a distance of 2.7 \AA . The superstructure modulation appears with a periodicity of about 5 times the atomic distance (about 13.5 \AA). The 'missing' factor of 2 to the expected values is explained by the extinction rules of the space group of BSCCO 2212 ($A2aa$, no. 37).

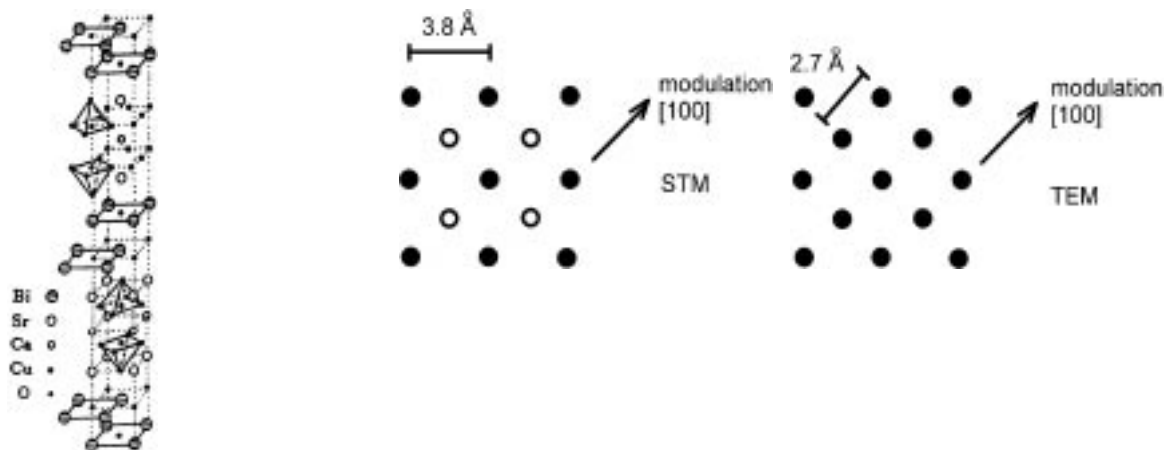


Figure 2.40: Structure model of BSCCO 2212. The crystal class is orthorhombic with $a = 5.41 \text{ \AA}$, $b = 5.42 \text{ \AA}$, $c = 30.9 \text{ \AA}$. A tetragonal sub-cell is shown ($a_t = 3.8 \text{ \AA}$ and $c_t = 30.9 \text{ \AA}$).

Figure 2.41: Schematic view of the atomic lattice expected for a surface sensitive method like STM (middle) and for a bulk method like TEM (right). The STM senses the Bi (or O) atoms at a distance of 3.8 \AA (a lower BiO plane is shown by open circles), and the superstructure runs at an angle of 45° with respect to the atomic lattice. The TEM however, shows atomic columns spaced by 2.7 \AA and the superstructure runs parallel to the atom rows.

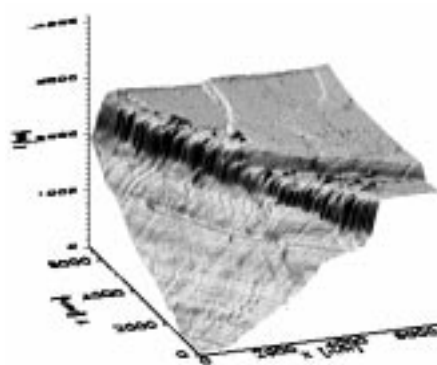
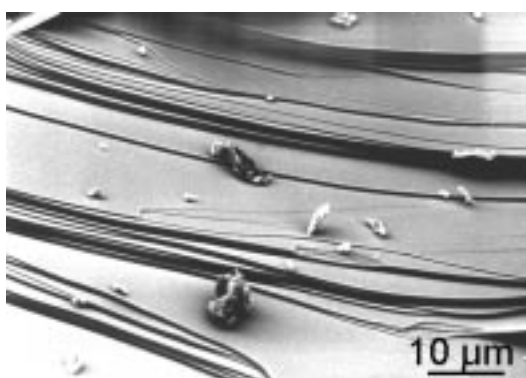


Figure 2.42: *LEFT:* Scanning electron micrograph of a BSCCO 2212 single crystal showing macrosteps and flat terraces.

Figure 2.43: *RIGHT:* Three dimensional rendition of a STM image of a BSCCO 2212 single crystal. Apart from the big macrostep in the foreground STM is also capable to image unit-cell steps (on the terrace).

2.2.4 Micron scale (SEM and STM)

To obtain information on the morphology of the BSCCO 2212 single crystals grown as described above scanning electron microscopy and scanning tunneling microscopy have been performed. Fig. 2.42 shows a SEM micrograph of a BSCCO 2212 single crystal with macroscopic growth steps. A similar step is imaged by STM as well (see fig. 2.43). In contrast to SEM, STM is capable to image unit cell steps and to give quantitative information on step heights.

2.2.5 Nanometer scale

Imaging the surface of BSCCO 2212 single crystals on atomic scale under ambient conditions²³ is reported to be very difficult. This is due to the high surface reactivity of BSCCO 2212 with the ambient. BSCCO 2212 is not as sensitive to humidity as YBCO²⁴ but the BiO layers²⁵ are hygroscopic.

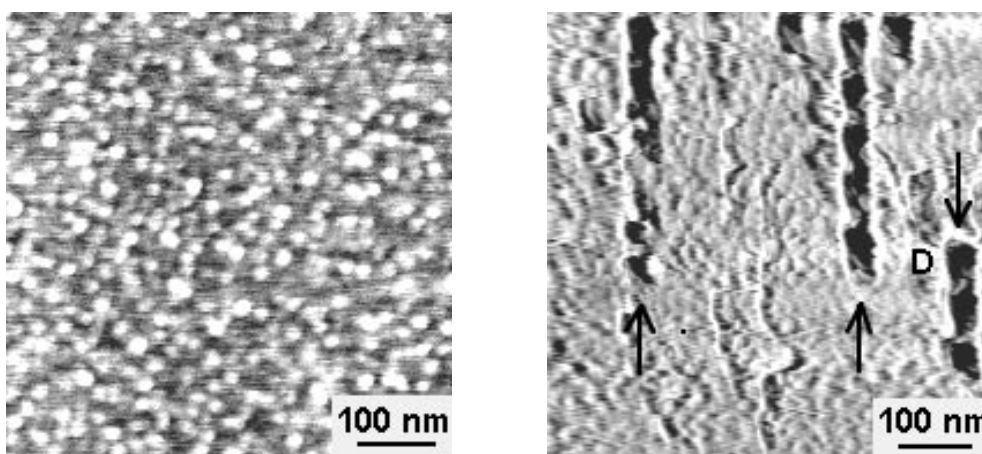


Figure 2.44: *LEFT:* Scanning force micrograph of a BSCCO 2212 single crystal imaged in air. Small flat ball-like structures (about 20 nm in diameter) cover the surface.

Figure 2.45: *RIGHT:* Writing of 'dots' (labelled 'D') and 'lines' (marked by arrows) with a STM tip. Consecutive scanning of a small area with an higher tunneling current (larger than 2 nA) removes the particles and leaves a trough instead. The 'written structure' is 'read' afterwards by scanning a larger area with a tunneling current well below 1 nA.

Scanning force microscopy reveals that the surface of BSCCO 2212 single crystals is

²³In air, at room temperature.

²⁴YBCO is forming barium hydroxides and carbonates on being exposed to humidity.

²⁵The BiO layers constitute the surface layer (and cleavage plane) in [001] direction of the BSCCO 2212 compound.

actually contaminated if investigated in air. Figure 2.44 shows small particles covering the crystal's surface.²⁶ The particles can be removed by continuously scanning an area for a few minutes. This process can be used for patterning the crystal's surface.²⁷ Figure 2.45 shows an example of three lines 'written' by scanning a small area with the STM tip and imaging later a larger area.

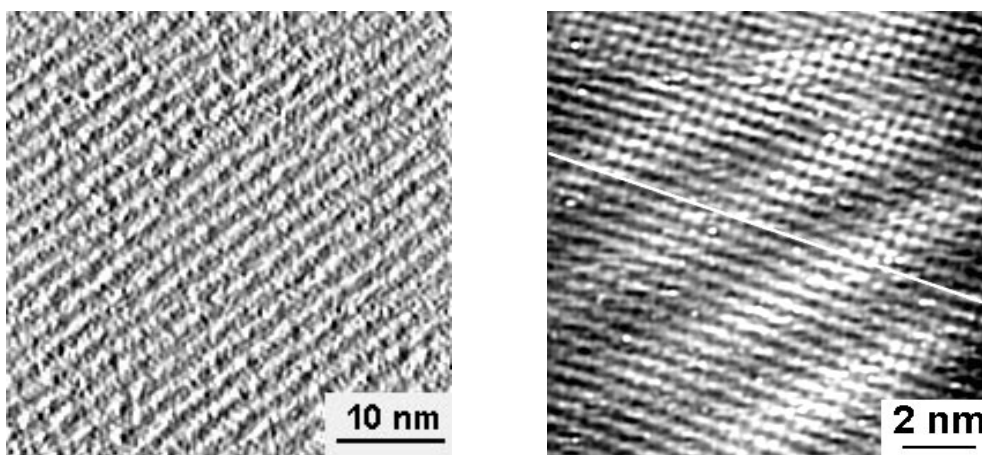


Figure 2.46: *LEFT:* STM topview revealing the 1d modulation with a period of 27 Å (parallel stripes in the image).

Figure 2.47: *RIGHT:* Atomically resolved modulation structure of BSCCO 2212. The square atomic lattice has a lattice constant of 3.8 Å which is interpreted as either the Bi or the O lattice in the Bi-O surface layer. The white line indicates the section shown below.

2.2.6 Atomic scale images

To obtain atomically resolved STM images a different procedure is necessary [2.22]. STM imaging of the superstructure with atomic resolution on cleaved BSCCO 2212(001) single crystals has been obtained in ultrahigh vacuum or noble gas environment [2.18, 2.19].

In the present work a stainless steel glove box containing high purity argon is used to perform STM on BSCCO 2212 single crystals. A gas purification system lowers the O₂, N₂ and H₂O impurity levels beyond the detection limit of 1 ppm. Prior to STM imaging, the crystals were cleaved in the glove box along the [001] direction to prepare an uncontaminated surface. Figure 2.46 shows a STM image of the one-dimensional superstructure modulation with a periodicity of 27 Å. This superstructure is shown with

²⁶SFM image courtesy by L. Howald, Institute of Physics, University of Basel.

²⁷However, it should be noted that this patterning is not long-lasting. Since the contamination from the ambient is continuously covering the crystal's surface the 'written' structures disappear after a short time.

atomic resolution in fig. 2.47.²⁸ The approximately square atomic lattice with a spacing of 3.8 Å is attributed to the Bi or O atoms in the Bi-O planes which represent the cleavage planes of BSCCO 2212. A section (fig. 2.48) is indicated by a white line showing the atomic corrugations and distances (3.8 Å). Since the section is chosen along the atomic rows the superstructure modulation is running at an angle of 45 degrees. This leads to an apparent modulation period of $\sqrt{2} \cdot 27$ Å.

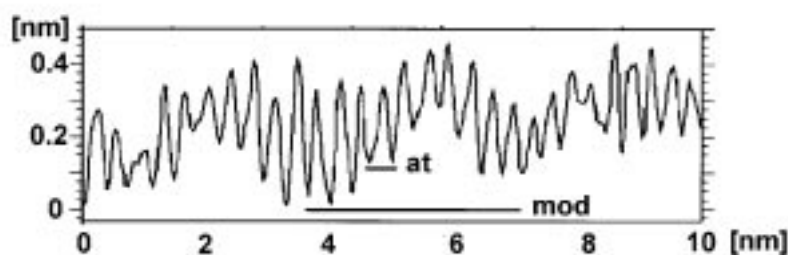


Figure 2.48: Line section along the atomic rows of BSCCO 2212. The atomic spacing ('at') is 3.8Å. Since the modulation runs at an angle of 45 degrees with respect to the atomic rows the superstructure modulation period ('mod') appears as $\sqrt{2} \cdot 27$ Å.

2.2.7 Substitution of Ca with La

Substitution of certain elements in BSCCO 2212 leads to suppression of this modulation without affecting superconductivity [2.20, 2.21]. Substitution of Ca with La leads to a compound that is isostructural to BSCCO 2212 but exhibits no superstructure modulation. Its composition is $\text{Bi}_2\text{Sr}_2\text{LaCu}_2\text{O}_8$,²⁹ in short BSLCO 2212. Motivated by this fact BSCCO 2212 and BSLCO 2212 single crystals are compared by performing STM.

BSLCO single crystals³⁰ were obtained by melting the appropriate mixture of the powders (using La_2O_3 instead of CaCO_3) at 1000°C and cooling at a rate of 8 K/h to 800°C followed by furnace cooling.

Figures 2.49 and 2.50 show atomically resolved images of the surfaces of BSCCO 2212 and BSLCO 2212. Whereas the superstructure modulation is clearly observed in BSCCO 2212 no modulation is found in BSLCO 2212.

²⁸Tunneling conditions: $I_t = 0.6$ nA, $U_t = 140$ mV.

²⁹This compound is not superconductive to the present knowledge (no superconductivity was found down to 4.2 K). In this context emphasis is put on the fact that BSLCO 2212 is *isostructural* to BSCCO 2212.

³⁰The BSLCO crystals are very tiny. The edges of the thin platelets are only 0.1 mm in length.

2.2.8 Conclusion

BSCCO 2212 has several advantages compared to YBCO 123. First, the compound melts congruently which facilitates the growth of single crystals. Second, BSCCO 2212 has a well-defined cleavage plane in $[001]$ direction since the weakest bonds between atom planes are between the Bi-O layers. For that reason the surface of BSCCO 2212 is well known.³¹ However, a strong surface reactivity of the BSCCO compounds with the ambient leads to surface contamination. For that reason surface investigations³² require an inert environment (noble gas or vacuum) and the possibility to cleave the crystal prior to measurement.

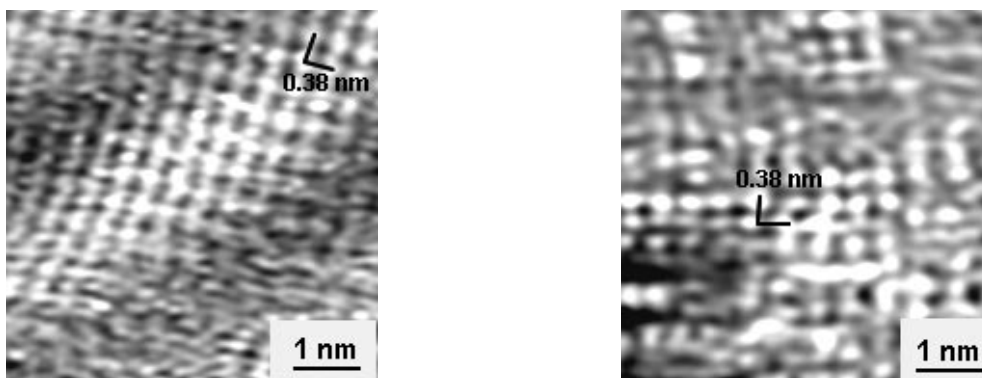


Figure 2.49: *LEFT:* STM topview showing the one-dimensional superstructure modulation of BSCCO 2212 with a period of 27 Å. A mesh of the atomic lattice is marked.

Figure 2.50: *RIGHT:* STM image (same scale as the image on the left side) of a compound isostructural to BSCCO 2212 with the composition $\text{Bi}_2\text{Sr}_2\text{LaCu}_2\text{O}_8$ (BSLCO 2212). No modulation is observed.

³¹The surface layer of YBCO 123 is still not yet completely determined. See the XPS experiments in section 3.7.

³²like STM, XPS etc.

References

- [2.1] Th. Wolf, W. Goldacker, B. Obst, G. Roth, R. Flückiger, *Jour. Cryst. Growth* 96 (1989) 1010.
- [2.2] E. Kaldis and J. Karpinski, *Eur. J. Solid State Chem.* 27 (1990) 143.
- [2.3] J. Karpinski, H. Schwer, K. Conder, E. Jilek, E. Kaldis, C. Rossel, H.P. Lang and T. Baumann, *Applied Superconductivity* 1 (1993) 333.
- [2.4] J. Karpinski, E. Kaldis, K. Conder, S. Rusieki and E. Jilek, *Mat. Res. Soc. Symp. Proc.* 251 (1992) 291.
- [2.5] J. Karpinski, S. Rusieki, E. Kaldis, E. Jilek, *Jour. Less-Common Met.* 164 & 165 (1990) 3.
- [2.6] H. Heinzelmann, D. Anselmetti, R. Wiesendanger, H.-J. Güntherodt, E. Kaldis, A. Wisard, *Appl. Phys. Lett.* 53 (1988) 2447.
- [2.7] L.E.C. van Leemput, P.J.M. van Bentum, L.W.M. Schreurs, and H. van Kempen, *Physica C* 152 (1988) 99.
- [2.8] H.P. Lang, J.P. Ramseyer, D. Brodbeck, T. Frey, J. Karpinski, E. Kaldis and T.H. Wolf, *Ultramicroscopy* 42-44 (1992) 715.
- [2.9] M.R. Schroeder, in 'Fractals, Chaos, Power Laws', W.H. Freeman and Company (New York 1991).
- [2.10] E. Ben-Jacob and P. Garik, *Physica D* 38 (1989) 16.
- [2.11] T. Vicsek, in 'Fractal Growth Phenomena (second edition)', World Scientific (Singapore, New Jersey, London, Hongkong 1992).
- [2.12] D. Bensimon, L.P. Kadanoff, S. Liang, B.I. Shraiman and C. Tang, *Rev. Mod. Phys.* 58 (1986) 977.
- [2.13] H. Maeda, Y. Tanaka, M. Fukutomi and T. Asano, *Jpn. J. Appl. Phys.* 27 (1988) L209.
- [2.14] E. Takayama-Muromachi, Y. Uchida, A. Ono, F. Izumi, M. Onoda, Y. Matsui, K. Kosuda, S. Takekawa and K. Kato, *Jpn. J. Appl. Phys.* 27 (1988) L365.
- [2.15] R.M. Hazen, C.T. Prewitt, R.J. Angel, N.L. Ross, L.W. Finger, C.G. Hadidiacos, D.R. Veblen, P.J. Heaney, P.H. Hor, R.L. Meng, Y.Y. Sun, Y.Q. Wang, Y.Y. Xue, Z.J. Huang, L. Gao, J. Bechtold and C.W. Chu, *Phys. Rev. Lett.* 60 (1988) 1174.

- [2.16] Y. Matsui, H. Maeda, Y. Tanaka and S. Horiuchi, *Jpn. J. Appl. Phys.* 27 (1988) L361, *idem Jpn. J. Appl. Phys.* 27 (1988) L372.
- [2.17] Y. LePage, W.R. McKinnon, J.-M. Tarascon and P. Barboux, *Phys. Rev. B* 40 (1989) 6810.
- [2.18] M.D. Kirk, J. Nogami, A.A. Baski, D.B. Mitzi, A. Kapitulnik, T.H. Geballe and C.F. Quate, *Science* 242 (1988) 954.
- [2.19] C.K. Shih, R.M. Feenstra, J.R. Kirtley and G.V. Chandrashekhar, *Phys. Rev. B* 40 (1989) 2682.
- [2.20] J.M. Tarascon, W.R. McKinnon, Y. LePage, K. Reimann, R. Ramesh, R. Jones, G. Pleizier and G.W. Hull, *Physica C* 172 (1990) 13.
- [2.21] S. Takebayashi, A. Maeda and K. Uchinokura, *Annu. Rep. Eng. Res. Inst. Fac. Eng. Univ. Tokyo*, 49 (1990) 105.
- [2.22] H.P. Lang and H.-J. Güntherodt, *Helv. Phys. Acta* 66 (1993) 65.

Chapter 3

YBCO thin films

Unlike single crystals the growth of thin films requires no flux. For that reason a clean surface of the films is to be expected. This chapter is divided into several sections describing the growth of YBCO thin films by pulsed laser deposition on different substrates and by different methods like metalorganic chemical vapour deposition, thermal co-evaporation (molecular beam epitaxy) and liquid phase epitaxy. Each section introduces a new method or initiative in addition to scanning tunneling microscopy in order to provide further information on YBCO growth. This includes for instance:

- the application of a half-shadow technique to grow films with a thickness-gradient for a study of the growth stages occurring at different film thickness,
- relating X-ray diffraction data to the film morphology,
- a study of the film morphology by transmission electron microscopy,
- the use of reflection high energy electron diffraction (RHEED) to characterize film growth and the relationship to STM images,
- and assigning atomic surface lattices of YBCO observed by STM to the chemical information on the YBCO toplayer obtained by monochromatized X-ray photoelectron spectroscopy.

3.1 Introduction

Deposition of thin films onto suitable substrates by physical vapour deposition (PVD) and chemical vapour deposition (CVD) from various precursor compounds has nowadays become a reliable method to prepare high-quality samples of the high-temperature superconductors. In a review article *Schieber* [3.1] has analyzed the problems in HTSC film growth by PVD and CVD methods, and has compared the film properties. Thin film growth by PVD methods includes thermal co-evaporation [3.2], composite-target magnetron sputtering [3.3], off-axis sputtering [3.4], pulsed laser deposition [3.5] and others. For a comprehensive study of magnetron-sputtered films the reader is referred to an article by *Eom et al.* [3.6]. Many questions concerning the outstanding properties of

HTSC thin films, compared to bulk material, are still unanswered. Explanations for the high values of critical current densities, j_c , in thin film samples require a large number of pinning centres for flux vortices. Structural defects such as twin planes [3.7], stacking faults [3.8, 3.9], oxygen vacancies [3.10] and others have been suggested as potential pinning centres. Experimental evidence of structural defects in $\text{YBa}_2\text{Cu}_3\text{O}_{7-\delta}$ (YBCO) is summarized in an article by *Kulik* [3.11].

Recently, it has been proposed that screw dislocations observed by STM in thin films of YBCO could act as pinning centres [3.12, 3.13]. The high number density of screw dislocations (about $10^9/\text{cm}^2$) should partially explain the critical current densities j_c (at 77 K) greater than $10^6 \text{ A}/\text{cm}^2$ measured for magnetron-sputtered YBCO thin films.

Similar STM images have been obtained also from thin films prepared by pulsed laser deposition. Fig. 3.1 shows the surfaces of YBCO 123 films on $\text{MgO}(100)$ and $\text{SrTiO}_3(100)$. Each growth hill clearly shows a screw dislocation with a Burgers vector component perpendicular to the film's surface. In SEM images, however, no such structure is observed.

Since electrical transport properties and film structure are closely related, close control over film growth is essential for an improvement of electrical transport properties. Using thermal co-evaporation, early stages of YBCO film growth on $\text{SrTiO}_3(100)$ have been monitored *in situ* by reflection high-energy electron diffraction (RHEED) as reported by *Terashima et al.* [3.14]. Scanning electron microscopy (SEM) images of such films reveal very little contrast [3.15]. Transmission electron microscopy (TEM) gives valuable information on film growth as well; TEM studies on the initial growth of YBCO on $\text{MgO}(100)$ have been performed by several groups [3.16, 3.17].

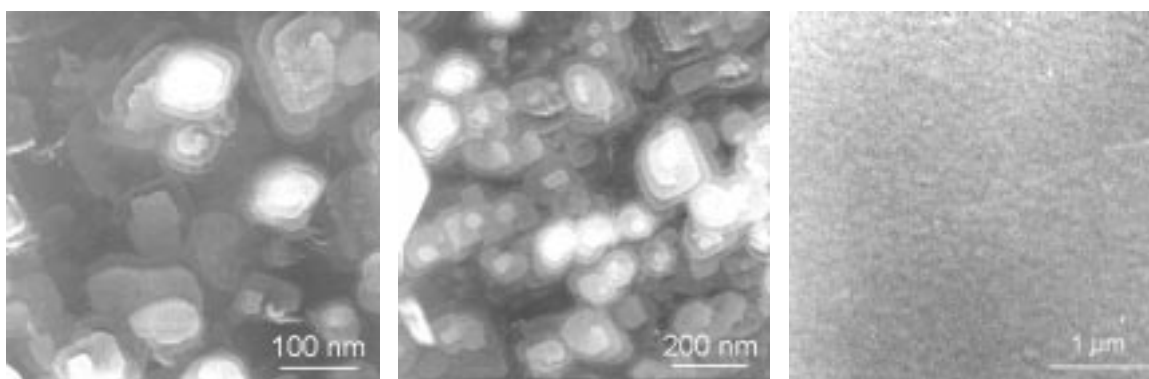


Figure 3.1: *LEFT:* STM image of a YBCO thin film grown by pulsed laser deposition (PLD) on a $\text{MgO}(100)$ substrate. *MIDDLE:* STM image of a YBCO thin film grown by PLD on a $\text{SrTiO}_3(100)$ substrate. *RIGHT:* SEM image of a YBCO thin film prepared by PLD on $\text{MgO}(100)$. Only a glimpse of the growth hill structure can be observed due to the limited vertical resolution of SEM.

STM has already been successfully applied to high-temperature superconductors. Step structure imaging and atomic resolution have been achieved on freshly cleaved single crystals of $\text{Bi}_2\text{Sr}_2\text{CaCu}_2\text{O}_8$ [3.19] and $\text{Tl}_2\text{Ba}_2\text{CaCu}_2\text{O}_8$ [3.20] in ultrahigh vacuum or inert gas environment. Thin films of $\text{YBa}_2\text{Cu}_3\text{O}_{7-\delta}$, as mentioned before, exhibit an abundance of lattice defects, especially screw dislocations, revealed by STM [3.12, 3.13]. Similar results have been reported by several groups [3.21] – [3.31] using different methods for thin film preparation. Now the STM results obtained from the surface of YBCO thin films prepared by pulsed laser deposition will be presented.

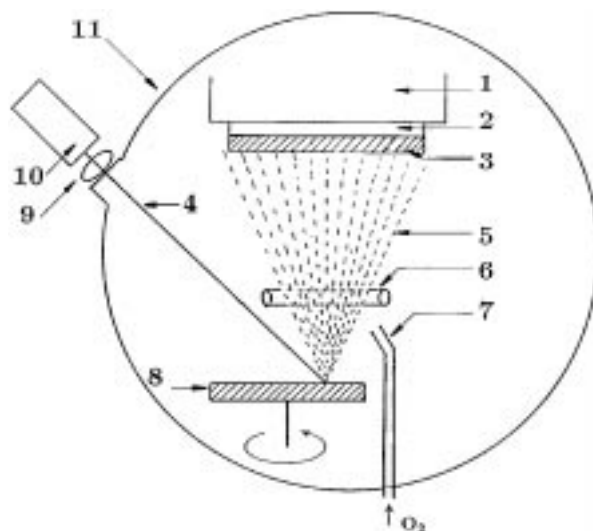


Figure 3.2: Schematic view of a vacuum chamber for pulsed laser deposition. (1) substrate heater, (2) substrate, (3) thin film, (4) laser beam, (5) laser plume, (6) electrostatic lens, (7) hose for the introduction of oxygen to the chamber, (8) target pellet (rotatable), (9) focussing lens system, (10) excimer laser, (11) vacuum chamber.

3.1.1 Pulsed laser deposition

The successful application of the method of pulsed laser deposition (PLD) to the growth of high T_c superconductor thin films goes back to a study by *D. Dijkkamp, T. Venkatesan and co-workers* [3.5] in 1987. By focusing an Excimer¹ laser beam² onto a polycrystalline target of the superconductor, material is removed (ablated) without heating the target.³

¹Excimer = excited dimer. Frequently gas mixtures like KrF, ArF and XeCl are used. A high voltage discharge ionizes, e.g., a mixture of Kr and F_2 gases. Kr^+ and F^- form a metastable excited dimer that decays on a nanosecond time scale by an optical/UV transition to its initial components. Since an excimer does not have a stable ground state, population inversion is obtained automatically leading to laser radiation.

²Excimer lasers are used because of its short wavelength in the UV.

³This is essential for not changing the stoichiometry of the material to be ablated. When using lasers of larger wavelength, e.g. CO lasers or Nd-YAG lasers (wavelengths around $1\ \mu\text{m}$), the energy of the laser

The advantage of this technique is the possibility of conserving the stoichiometry of the target material and transferring it to the film being grown.

Figure 3.2 shows schematically the basic principle of PLD as realized in the PLD chamber in Basel.⁴ A high vacuum chamber (11) contains the polycrystalline target (8) made of the material that should be grown as a thin film (3) on a substrate (2). The target may be rotated to avoid preferential ablation. The substrate can be heated by an electrical heater (1). The beam (4) of the excimer laser (10) is focussed by a lens system⁵ (9) through a window of the vacuum chamber onto the rotating target.⁶ Some target material is being ablated in a plume (5) and is condensed on the substrate to form a thin film. For the growth of HTSC the introduction of oxygen by a hose (7) [3.32, 3.33] and the use of an electrostatic lens (5) is advantageous.

3.1.2 Preparation of YBCO thin films

Thin films of YBCO were deposited by PLD on single crystal substrates⁷ in a high-vacuum chamber. Prior to film deposition, the substrate was optically polished⁸ and ultrasonically cleaned in acetone and then attached with silver paste to the heating block which enables heating up to 900°C. The temperature was measured using a chromel-alumel thermocouple embedded in the block.⁹ After evacuating the deposition chamber to 10^{-4} Pa, oxygen was inserted through a needle valve to equilibrate at a partial pressure of 27 Pa. YBCO was evaporated with a KrF excimer laser¹⁰ focussed to an energy density of about 2.5 J/cm^2 onto a stoichiometric target being rotated to ensure continuous ablation. The target was prepared by a solid state reaction of Y_2O_3 , BaCO_3 and CuO in appropriate amounts at 950°C for 12 h in an oxygen atmosphere. This process was repeated at least five times with intermediate grinding and pressing steps at a hydrostatic pressure of about 10^9 Pa. Careful target preparation aimed at perfect stoichiometry (Y:Ba:Cu = 1:2:3) and high density turned out to be essential for the growth of high quality films. Following the YBCO films were deposited at temperatures between 575 and 805°C. Films of a typical

beam is dissipated to heating of the target. Excimer lasers, however, cause photolysis of the material without heating it to such an extent that its stoichiometry is changed.

⁴This chamber has been built by T. Frey and R. Sum.

⁵Lenses for UV transmission (KrF, 248 nm wavelength) are made of high quality quartz glass.

⁶For geometrical reasons an angle of 45 degrees between incident laser beam and target normal is frequently used.

⁷Single crystalline platelets of LaAlO_3 , SrTiO_3 , MgO and Mg_2TiO_4 -coated MgO have been used. The thickness is 0.5 – 1.0 mm and the size ranged from 2 to 100 mm^2 .

⁸This means if investigated in an optical microscope no scratches are found. This does of course not imply smoothness on an atomic scale. A study of the substrate topography is found in [3.34].

⁹For comparison an optical pyrometer was used. The temperatures measured by the pyrometer are about 20°C lower than those measured by the thermocouple. To correct for that a thermocouple was put into a small hole drilled into a MgO crystal platelet yielding the temperature close to the surface of the substrate crystal. This temperature agrees very well with the one determined by the pyrometer. All temperatures given below are to be understood as pyrometer temperatures.

¹⁰Lambda Physik LPX 301i, $\lambda = 248 \text{ nm}$, 1.2 J/shot.

nominal thickness of 200 nm¹¹ were grown at laser repetition rates between 5 and 10 Hz. To induce the tetragonal-to-orthorhombic phase transition,¹² oxygen atmosphere of 10⁵ Pa was equilibrated and the heating block was subsequently cooled to 500°C at a cooling rate of 5 deg/min and then cooled down to room temperature as fast as possible¹³

3.1.3 Half shadow technique

For a study of thin film growth it is desirable to prepare films with different film thicknesses under similar deposition conditions using identical target and substrate materials. Therefore a half-shadow technique¹⁴ was used which permits the preparation of thin films with thickness gradients. Thus different film thicknesses are created on a single substrate crystal applying identical deposition parameters. These films are referred to as *thickness-gradient films*. Figure 3.3 shows a schematic drawing of the laser evaporation chamber modified for the half-shadow technique. A shutter between the rotatable target and the substrate crystal partially shades the substrate, so that material is deposited on the substrate at different rates, depending on the lateral position on the crystal.

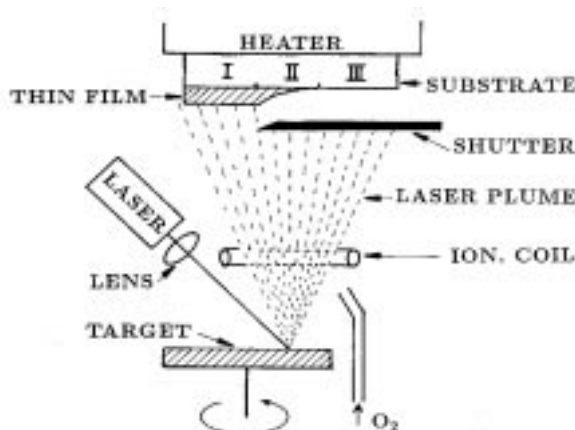


Figure 3.3: Modified setup for the growth of thickness-gradient films. The insertion of a shutter partially shades the substrate and causes three different regions: (I) continuous film of defined thickness, (II) half-shadow region with steadily decreasing film thickness, and (III) uncoated substrate surface.

Thus basically three different regions on the substrate crystal are distinguished (indicated in fig. 3.3). In the first region (I) a continuous film of defined thickness is formed. In the half-shadow region (II) the film thickness steadily decreases. Finally, in the third

¹¹In case of YBCO on LaAlO₃ the thickness amounted up to 1.2 μm (deposition time 20 minutes).

¹²This is important to obtain the superconducting orthorhombic phase of YBCO.

¹³The heater was simply switched off.

¹⁴This suggestion is due to Dr. H. Haefke.

region (III) the substrate surface remains uncoated. By this simple procedure, different growth stages of YBCO thin films can be prepared under identical conditions in a single run taking advantage of the gradual decrease of film thickness. The lateral extent of the half-shadow region can be influenced by varying the distance between shutter and substrate. However, it should be mentioned that the thickness gradient depends on a gradient in the deposition rate which varies in the half-shadow region from zero up to the rate determined for the continuous film. This fact is of minor importance for these studies due to the use of pulsed laser deposition in the experiment.¹⁵ A photograph of a thickness gradient film is shown in fig. 3.4.



Figure 3.4: Photograph of a thickness-gradient film as prepared by the half-shadow technique described above (YBCO film on LaAlO_3). (I) – (III) see above.

3.1.4 Some remarks on thin film growth

The classical theory of film growth in thermodynamic equilibrium suggests three basic growth mechanisms. For film growth a substrate 's' is required. An overlayer 'o' (film) is grown. The surface of the overlayer is exposed to the vacuum 'v' (fig. 3.5). The interfaces substrate–overlayer, substrate–vacuum and overlayer–vacuum and the free energies are crucial for the way the film growth proceeds.

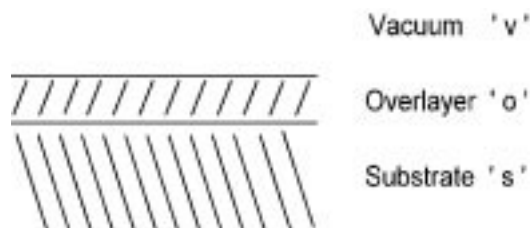


Figure 3.5: Schematic view of a thin film sample.

¹⁵Pulsed laser deposition is, as the name implies, a growth method with discontinuous material flow. For that reason the growth is not a continuous process.

The three mechanisms are distinguished by the relations between the free energies σ_{ov} , σ_{sv} and σ_{so} .¹⁶ The energy gained by overlayer growth is determined by:

$$\Delta\sigma = \sigma_{ov} - \sigma_{sv} - \sigma_{so}$$

In case of the so-called *Frank-van-der-Merwe* or *layer-by-layer* growth mode $\Delta\sigma$ is equal to 0. For the *Vollmer-Weber* or *island growth* $\Delta\sigma$ is smaller than 0, and for the *Stranski-Krastanov* or *layer-island* growth mode $\Delta\sigma$ is larger than 0. Figure 3.6 illustrates these three possibilities of film growth.



Figure 3.6: The three basic modes discussed in thin film growth.

3.1.5 Crystal surfaces

This section briefly summarizes the basic defects which may occur on a real crystal surface. Please refer to fig. 3.7. On perfect flat terraces (T) some additional atoms, called ad-atoms (A) may be present. Other atoms, called vacancies (V) are missing. Monatomic (monomolecular) steps (M) separate the terraces from each other. These ledges may have steps as well called kinks (K). Missing or additional atoms in the ledge are called vacancies in the ledge (VL) or adatoms in the ledge (AL). If an additional lattice plane perpendicular to the terrace intersects with the terrace it is termed an edge dislocation (E). If the additional lattice plane is inserted parallel to the terrace it is called an emerging screw dislocation (S). The vaporization energy of surface atoms bound in a terrace (5 neighbours) is much larger than that of atoms bound to a step (3 neighbours) in a simple box model. The smallest vaporization energy is that of an adatom since it is only bound to one other atom. On reversing this concept addition of material during growth will preferentially occur at step edges.

The focus in the next section will be on screw dislocations. For that reason this defect is discussed in more detail. Figure 3.8 shows a screw dislocation in a box model. An additional lattice plane causes a screw dislocation defect (with a Burgers vector¹⁷

¹⁶For example, σ_{ov} denotes the free energy of the interface overlayer ('o') and vacuum ('v'). The other free energies are to be understood in a similar way.

¹⁷A Burgers vector is the translation vector in direct space to close a loop of lattice vectors $\vec{a} + \vec{b} - \vec{a} - \vec{b}$ around a dislocation ($\vec{a} \neq \vec{b}$). In case of a screw dislocation the Burgers vector is parallel to the dislocation line, in case of an edge dislocation it is perpendicular to the dislocation line and lies within the gliding plane.

perpendicular to the surface). The growth proceeds in spiral turns since material will be preferentially added at step edges. Figure 3.9 depicts the evolution of a screw dislocation on growth.

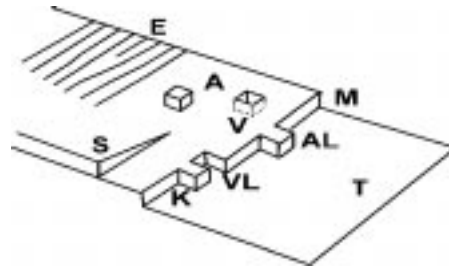


Figure 3.7: Defects that may occur on a real crystal: (T) perfect flat terrace, (S) an emerging screw dislocation, (E) the intersection of an edge dislocation with the terrace, (M) a monatomic/monomolecular step in the surface (also called a ledge), (K) a kink (a step in the ledge), (AL) an adatom in the ledge, (VL) a vacancy in the ledge, (A) an adatom in the terrace, (V) a vacancy in the terrace.

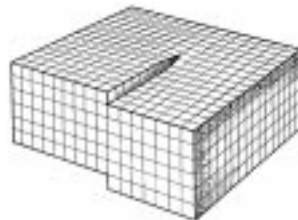


Figure 3.8: Simple box model explaining the emergence of a screw dislocation as an insertion of an additional lattice plane parallel to the surface.

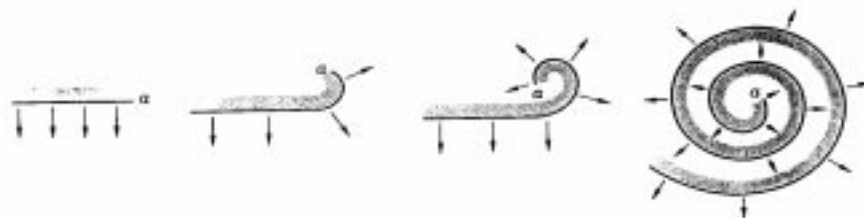


Figure 3.9: Evolution of a screw dislocation as seen from the top. New material is being added at step edges leading to a revolution in spiral turns of steps (illustration taken from: H. Kittel, *Einführung in die Festkörperphysik*, 7.Auflage, R. Oldenburg Verlag, München (1988), p. 653).

3.2 YBCO thin films on LaAlO₃

LaAlO₃ is used as a substrate for HTSC thin films because of its good dielectric properties¹⁸ which make it suitable for RF-applications.¹⁹ Since the surface resistance is an important quantity in RF-electronics a smooth film surface is desired. Scanning probe methods with their unsurpassed vertical resolution capability are the methods of choice to characterize the film surface quality. In the following the properties and the morphology of thin YBCO 123 films on LaAlO₃ are discussed [3.35, 3.42, 3.43].

3.2.1 Experimental conditions

Thin films of YBCO were grown²⁰ by PLD on LaAlO₃(100) crystals at substrate temperatures between 790 and 805°C and 27 Pa O₂. A deposition time of 20 minutes at a laser repetition rate of 8 Hz yields a nominal film thickness of 1.2 μm. The cooling rate was 5 deg/min. to 500°C in 10⁵ Pa of oxygen, followed by annealing for 30 minutes and cooling to room temperature.

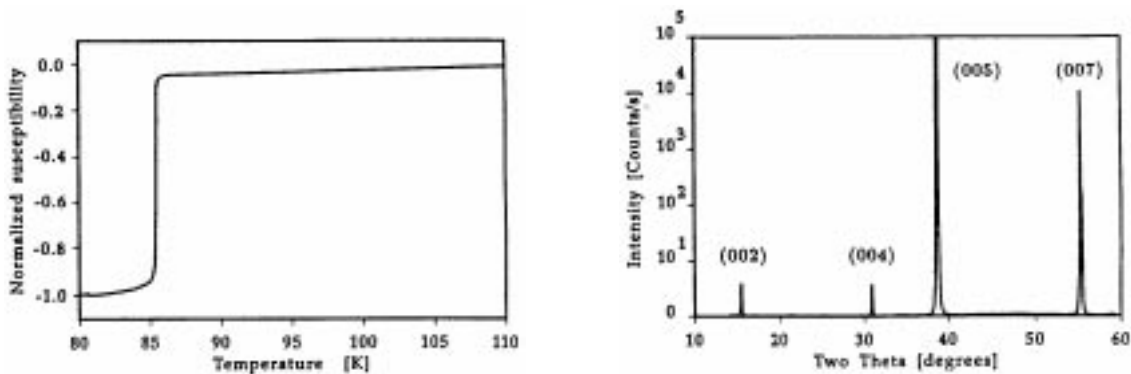


Figure 3.10: *LEFT:* Temperature-dependent magnetic susceptibility of a PLD YBCO thin film on LaAlO₃ (normalized to the value at 80 K). The critical transition temperature is 86 K (at a transition width of 0.5 K).

Figure 3.11: *RIGHT:* Cu K_α X-ray diffraction pattern of a YBCO film on LaAlO₃(100). The diffraction peak originating from the substrate is not shown.

¹⁸High dielectric constant $\epsilon = 25$ and low loss tangent $\tan \delta = 3 \cdot 10^{-4}$.

¹⁹HTSC thin films on a substrate patterned in stripline resonators, antennas or filters have a much better gain and signal-to-noise ratio than equivalent devices made from copper since no losses occur due to superconductivity. In other words HTSC RF-devices can be built much smaller than copper-based devices (with the same figures of merit) which makes them appropriate for the use in space.

²⁰The YBCO thin films on LaAlO₃ were grown by G. Leemann, Univ. of Basel.

3.2.2 Superconducting and structural properties

The critical transition temperature T_c of a typical film was measured by an inductive method. Figure 3.10 shows the transition to superconductivity at 86 K (onset) with a transition width of 0.5 K (determined from the first derivative of the transition curve). Critical current densities measured by a four-probe electrical transport method range from 1×10^6 to 4×10^6 A/cm² at 77 K. X-ray diffraction in conventional Bragg-Brentano geometry ($\Theta - 2\Theta$) exhibits a (001) orientation of the films (see fig. 3.11) [3.35].

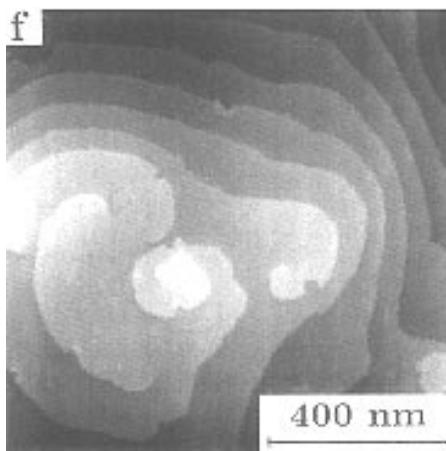
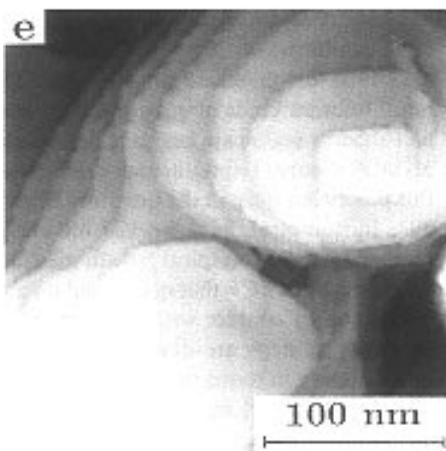
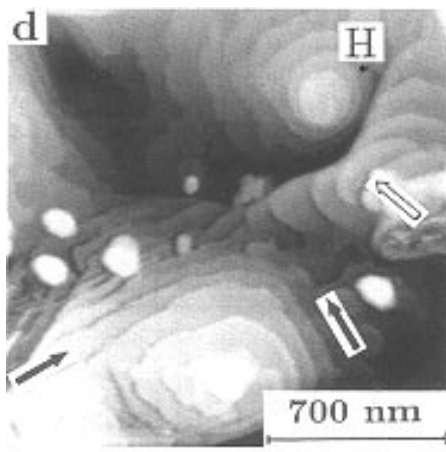
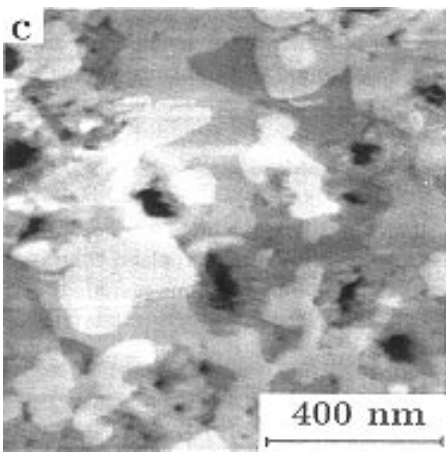
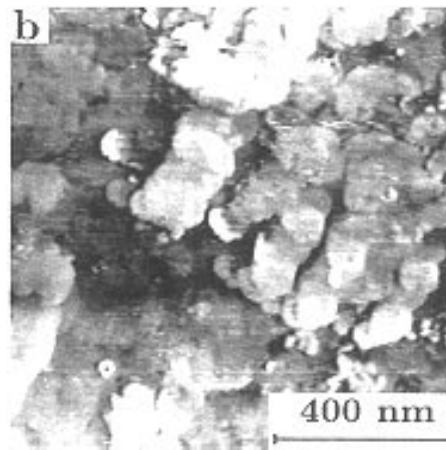
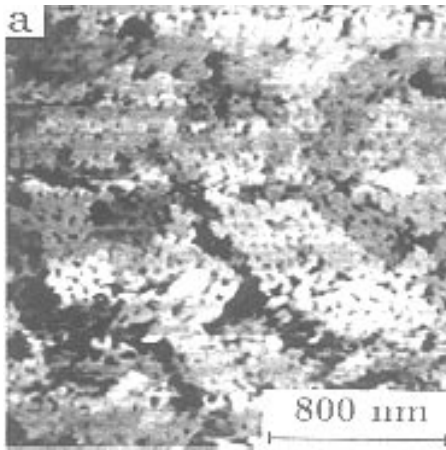
3.2.3 STM results on a thickness-gradient film

The surface structure of the YBCO thin films was investigated by STM using a commercially available instrument (Nanoscope II, Digital Instruments) operated in air. To minimize deterioration effects due to surface reactions of the YBCO films with humidity, STM measurements were carried out immediately after the film deposition. Tip-induced artifacts were widely excluded by use of different mechanically prepared Pt₉₀Ir₁₀ tips for the same kind of samples. For all large scale images, a tunneling current of less than 300 pA and tip bias voltage above +1V was applied. The constant current mode was used for large scale STM imaging in order to obtain topographical information.

In a first step the dependence of the morphology on the film thickness is discussed using a thickness-gradient film prepared by the half-shadow technique. Figure 3.12 shows scanning tunneling micrographs at different growth stages in a *c*-axis oriented YBCO film with a thickness gradient. The film is grown on LaAlO₃(100) at a substrate temperature of 800°C at a laser repetition rate of 8 Hz for 20 minutes yielding a maximum film thickness of 1.2 μm. Since STM requires conducting samples the uncoated substrate area (substrate, region III in fig. 3.3) could not be imaged.

STM images of the early growth stage are dominated by spreading of rather two-dimensional (2D) than three-dimensional (3D) islands of YBCO (fig. 3.12a). It can be concluded from this STM image that at this stage the YBCO film consists of numerous small islands coalesced over a substantial part of the substrate surface. Discontinuous island/channel structures provide electrical paths for the tunneling current.

With increasing film thickness, larger 2D islands formed by coalescence and growth are observed (fig. 3.12b). The measured height (1.2 nm) of individual islands is one unit cell in the crystallographic *c*-direction of YBCO. These individual islands coalesce at larger film thicknesses and form terrace structures with steps of unit cell height (1.17 nm, fig. 3.12c). The YBCO film still contains holes, visible as dark areas in fig. 3.12c. At this thickness (presumably on the order of ten unit cells), the film growth is characterized by 2D nucleation and layer growth (Frank-van der Merwe mode).



(continued on following page)

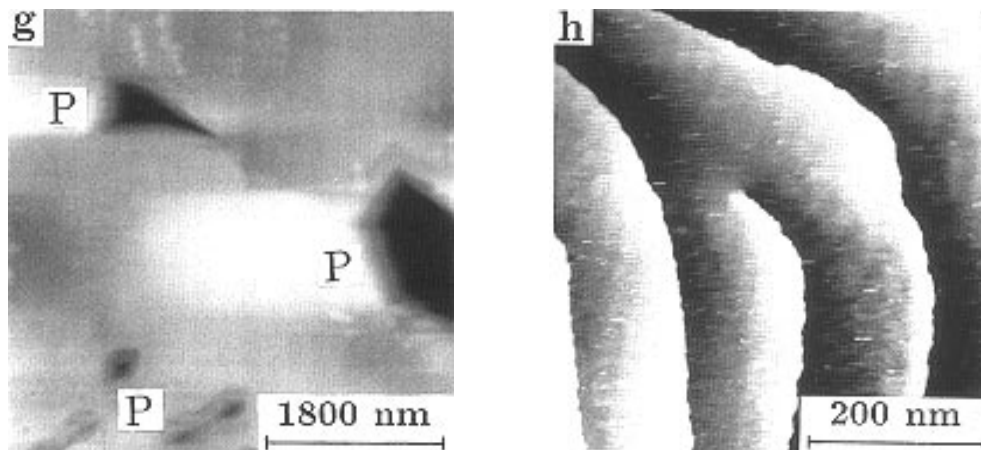


Figure 3.12: Growth stages of a YBCO film on $\text{LaAlO}_3(100)$ laser-deposited at a substrate temperature of 800°C : (a) spreading of 2D islands, (b) growth of the islands, (c) formation of a terrace structure, (d) hill formation, (e) growth hills with circular steps, (f) merging of growth hills to a continuous film (g) continuous film with growth pits (P) and (h) individual growth steps in the flat surface areas between growth pits. Nominal thickness of the continuous film: $1.2 \mu\text{m}$.

With further increase in film thickness a film surface completely covered by well-developed growth hills consisting of concentric and spiral step patterns is observed (fig. 3.12d). A typical growth hill formed by spiral steps is marked with a **H** in fig. 3.12d. The growth steps are in some cases aligned to the crystallographic *a*- and *b*-directions of YBCO (marked by bold arrows). In other cases the step course is more rounded (marked by an open arrow). Figure 3.12e shows a growth hill consisting of concentric steps. A film surface dominated by growth hills is characteristic of a film thickness ranging from 100 to 600 nm. Similar growth structures have been reported by many other groups performing STM [3.12, 3.13], [3.21] – [3.31]. The occurrence of growth hills with concentric as well as spiral steps implies that — in addition to repeated 2D nucleation — Frank’s spiral mechanism of growth [3.36] is also operative. The spiral growth steps start or end at emergence points of dislocations with a Burgers vector component (one *c*-axis lattice parameter) perpendicular to the film surface. These dislocations, termed screw dislocations, can be interpreted either as misfit dislocations which occurred above a certain film thickness [3.37], or as screw dislocations which have grown through from the substrate. Special kinds of growth hills are discussed below.

At larger thickness the gaps between individual growth hills are filled in to a continuous film. Spiral growth steps originating from screw dislocations of opposite sign may meet and thus be annihilated (fig. 3.12f). The film thickness at this stage is about 800 nm. The continuous film of a constant thickness of $1.2 \mu\text{m}$ is characterized by a terrace structure with steps of one unit cell height in the crystallographic *c*-axis direction of

YBCO and by growth pits with diameters in the micrometre range.²¹ (fig. 3.12g). At this stage film growth is dominated by regular propagation of the terrace steps. Typical height variations in the film surface are only a few nanometres per μm^2 . The steps are piled up at the border of the growth pits (marked by **P**) or are levelled by propagating adjacent steps. Figure 3.12h shows the surface structure in flat areas between growth pits. The surface is characterized by step trains. The emergence of a screw dislocation, where a growth step starts, is seen in the centre of fig. 3.12h.

The scanning electron micrograph (fig. 3.13) shows numerous growth pits of different shapes and sizes. However, the unit cell step structure does not provide enough contrast in SEM. Note that the film surface is free of any outgrowths or droplets. This is due to a careful choice of the energy density on the target (ca. 2.5 J/cm^2) giving a stoichiometric material transfer from the target to the film.

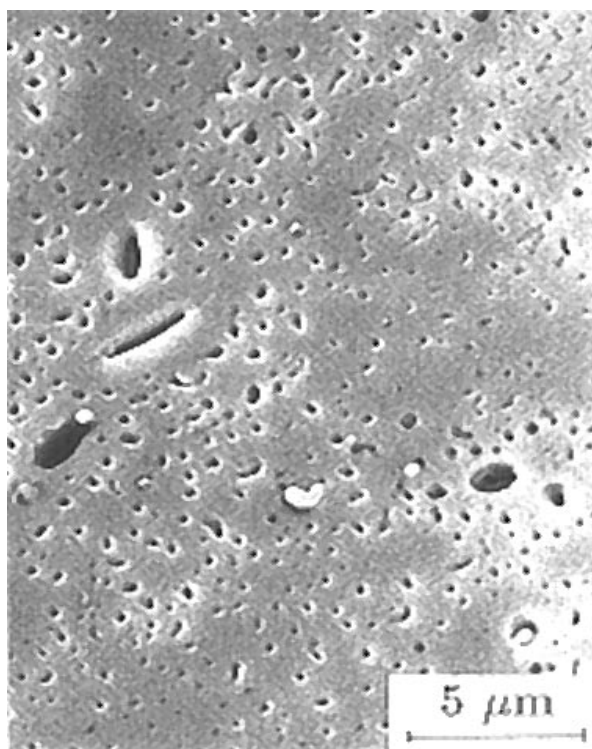


Figure 3.13: Scanning electron micrograph revealing the surface morphology of the continuous YBCO film (nominal thickness $1.2 \mu\text{m}$) as imaged previously by STM. Most striking features are growth pits of various shape and size.

²¹These growth pits are caused by inclusions in the film. Copper oxide needles, e.g., may spontaneously grow on the substrate and impede the growth of the YBCO film at that position on the substrate. Further evidence obtained by SFM that needles are actually situated in that type of growth pits will be discussed in section 3.5 on YBCO thin films grown by metallorganic chemical vapour deposition.

3.2.4 Special types of growth hills

The part of the half-shadow region of the YBCO films exhibiting distinct growth hills corresponds to a nominal film thickness ranging from 100 nm to 600 nm. Different kinds of growth hills observed in the half-shadow region are analyzed below in the context of BCF theory. Experimental evidence supporting this theory has been in the literature since 1950 [3.38] – [3.41]. *Burton et al.* have worked out the theoretical fundamentals of the spiral growth mechanism [3.36]. The concept of BCF theory (*Burton-Cabrera-Frank*, [3.39]) is based on a crystal surface being in contact with its vapour. Adsorption processes at steps are described with classical diffusion theory in terms of supersaturation of vapour. *Burton et al.* [3.36] introduced a certain *critical* 2D nucleus with radius ρ_c that is in unstable equilibrium with the vapour. If a nucleus is larger than the critical nucleus, it will grow. In the following paragraphs different kinds of spiral growth hills are discussed with respect to ρ_c .

3.2.4.1 Single screw dislocations

It is assumed that crystals are growing under a supersaturated environment. A step due to the emergence of a screw dislocation on the crystal surface will wind itself in a spiral when new material is added. The direction of this dislocation will remain perpendicular to the crystal surface for reasons of minimization of elastic energy. When the supersaturation increases the spiral will send out successive turns separated by unit cell steps until the curvature of the steps at the centre of the dislocation reaches the critical value $1/\rho_c$, at which point the whole spiral will rotate steadily with stationary shape. Using *Frank's* concept of a critical nucleus, the shape of such a growth spiral can be parametrized as an Archimedian spiral in polar coordinates (r, Θ) in the plane:

$$r = 2 \cdot \rho_c \cdot \Theta. \quad (3.1)$$

The distance ℓ between successive turns of a growth spiral at large radius can be calculated as

$$\ell = 4 \cdot \pi \cdot \rho_c. \quad (3.2)$$

An example of the step course in this kind of single screw dislocation is shown in fig. 3.14a. Both signs of screw dislocations, left- and right-handed, are observed with similar frequency. The radius ρ_c of the critical nucleus can be calculated from equation (3.2). For the spiral in fig. 3.14a $\rho_c = 2.4$ nm is calculated assuming $\ell = 30$ nm. Similar values of ρ_c can be inferred from other growth spirals. The small value determined for the radius ρ_c of the critical nucleus of the particular growth spiral shown in fig. 3.14a corresponds to a 2D nucleus consisting of about only 120 unit cells. This estimate might explain why spiral growth occurs in such abundance (screw dislocation number density of about $10^9/\text{cm}^2$) in YBCO films, since only a few hundred unit cells assembled in a 2D nucleus are necessary to initiate spiral growth.

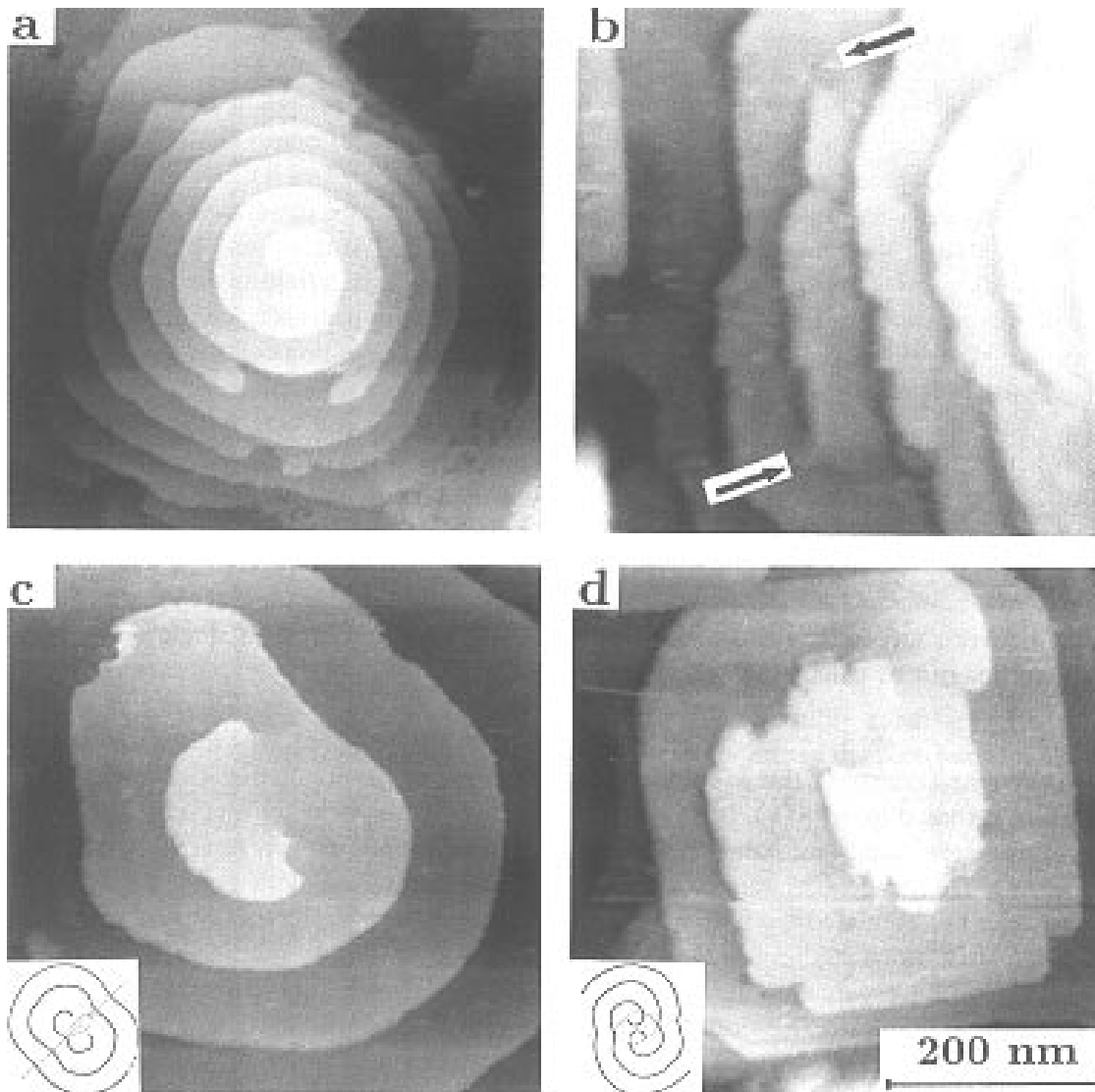


Figure 3.14: Different kinds of growth hills with screw dislocations: (a) single right-handed screw dislocation with about 8 turns of growth steps, (b) annihilated pair of dislocations (marked by arrows) of opposite sign, (c) pair of screw dislocations of opposite sign further apart from each other than $2\rho_c$ sending out loops of steps, (d) pair of screw dislocations of like sign further apart than $2 \cdot \pi \cdot \rho_c$ with a step activity indistinguishable from that of a single spiral. The scale bar is valid for all figures.

3.2.4.2 Pairs of screw dislocations of opposite sign

Frank introduced a term called *activity* to characterize the growth speed of spiral steps. The activity equals the number of turns per second of a spiral step. Pairs of screw dislocations of opposite sign differ in some cases from pairs of like sign by their activity. For a pair of opposite sign different cases have to be distinguished.

First, if the two dislocations of opposite sign are closer than a critical distance of $2\rho_c$, then no growth appears. A similar situation is also observed at an advanced stage of growth (growth hills are levelled) in the thickness-gradient films. Figure 3.14b shows such a pair of screw dislocations of opposite sign (marked by arrows). Their growth steps have encountered and the growth spirals have annihilated each other. At this point, no spiral growth occurs and the growth step linking the two dislocations will preserve its appearance. The second case is a pair of screw dislocations of opposite sign further apart than $2\rho_c$. The two growth spirals intersect along a straight line and send out successive loops of steps (see fig. 3.16). This is illustrated by the pair of dislocations of opposite sign shown in fig. 3.14c. Such pairs of screws have the same activity as a single screw dislocation. Sometimes whole bundles of screw dislocations of opposite sign are observed (see fig. 3.15) [3.42, 3.43].

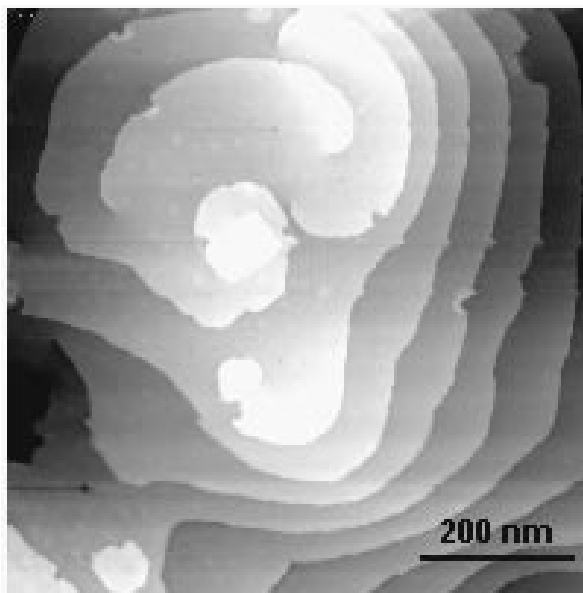


Figure 3.15: A bundle of screw dislocations of opposite sign on the surface of a YBCO thin film.

3.2.4.3 Pairs of screw dislocations of like sign

Again, different cases are distinguished. First, if the two spirals of like sign are further apart than $2 \cdot \pi \cdot \rho_c$, then the two spirals intersect along an S-shaped curve (see fig. 3.16). The two spirals feed each other with steps, but the activity is indistinguishable from that of a single dislocation. This case of a pair of spirals of like sign is shown in fig. 3.14d.

If the two spirals of like sign are closer than $2 \cdot \pi \cdot \rho_c$, then no intersection of the spirals occurs except near their origin. Spiral growth similar to that observed from a single spiral is observable, but twice the activity. During the investigations such a pair of spirals has not been found in the STM images of laser-deposited YBCO-films, but it is frequently observed in films grown by liquid phase epitaxy (section 3.8).

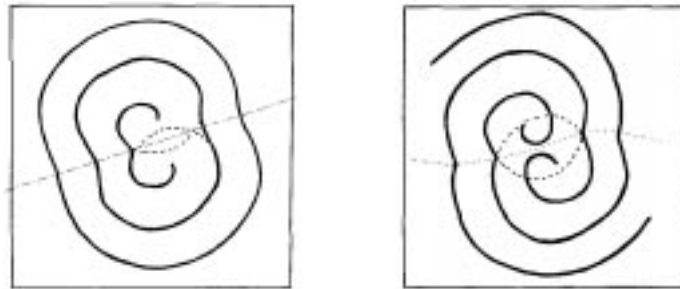


Figure 3.16: *LEFT:* Schematic view of a pair of screw dislocations of opposite sign annihilating each other. *RIGHT:* Pair of screw dislocations of like sign separated further than $2\pi\rho_c$.

3.2.5 Surface modification

An interesting aspect would be to image a screw dislocation with atomic resolution by STM to determine the Burgers vector in real space or to clear the question if screw dislocations in YBCO have a hollow core.²² Unfortunately STM does not seem to be the appropriate technique to solve this problem, even if atomic resolution can be achieved on flat terraces.²³ The main problem that occurs is that the film surface close to the screw dislocation is being modified on investigating the screw dislocation on a small scale. The high electric field²⁴ and insufficient response time of the feedback loop causes modification of the film's surface, e.g. unit cell layers are torn off. It should be added that atoms at step edges are far more easier removed than surface atoms in terraces. The two following sequences of images (figs. 3.17 and 3.18) demonstrate the effect.

²²This is of special importance to answer the question whether the screw dislocations act as dominant pinning centres in thin films. If they had a hollow core its pinning strength would be comparable to that of a columnar defect (track of a high energetic heavy particle) created by irradiation with heavy ions.

²³For atomic resolution of YBCO see 2.1.2.2 Atomic scale, and 3.7.1 Atomic resolution.

²⁴At a voltage of 0.1 V and at a distance of typically 1 nm the electric field is in the order of 10^8 V/m.

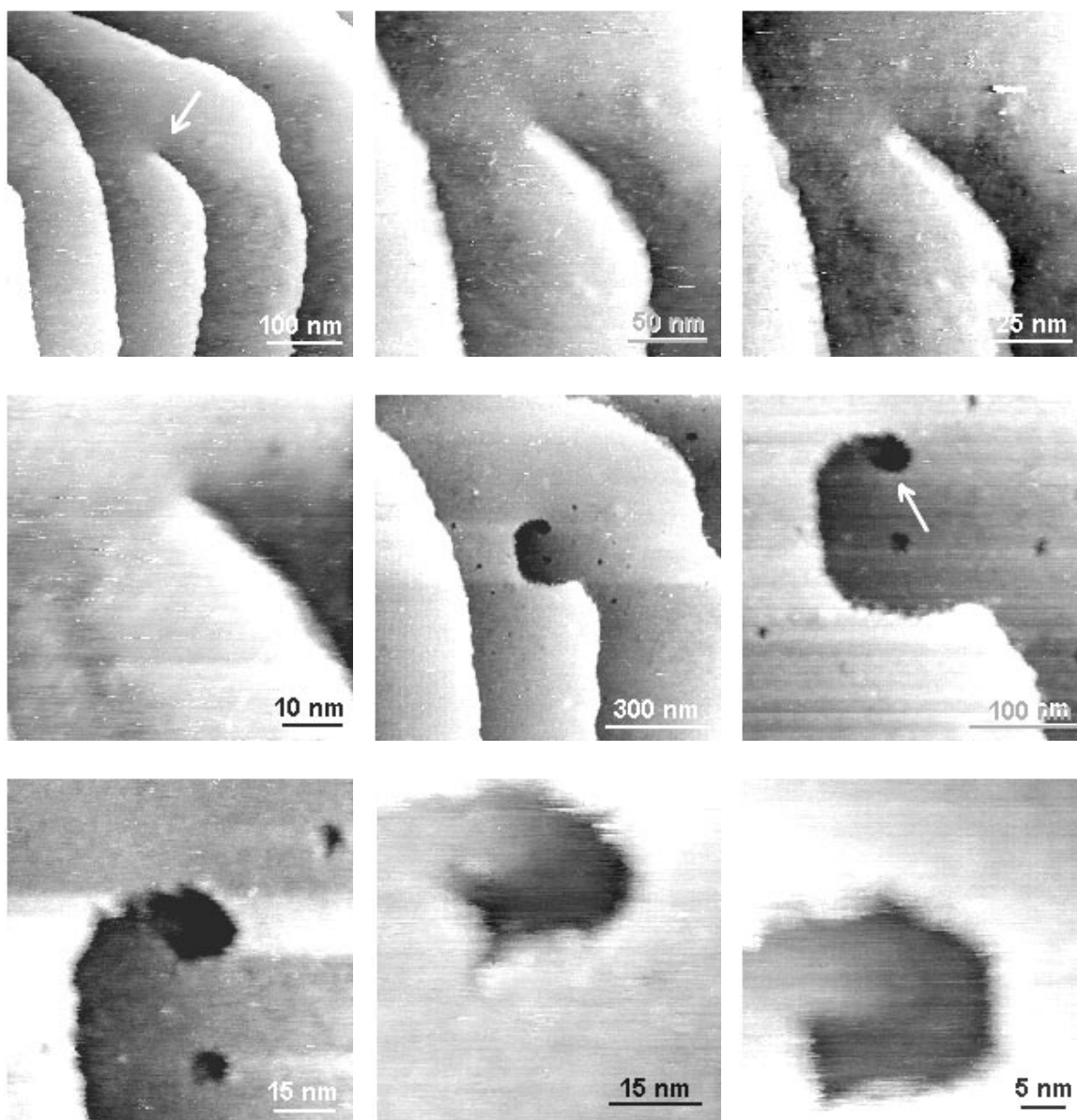


Figure 3.17: Sequence of STM images of the surface of a YBCO thin film on LaAlO_3 showing an isolated screw dislocation (arrow). Upon imaging the screw dislocation in more detail some material is torn off. All steps visible in the image are steps of one unit cell in height. It was not possible to image the screw dislocation with atomic resolution. The arrow indicates the position of a possible hollow core of the screw dislocation.

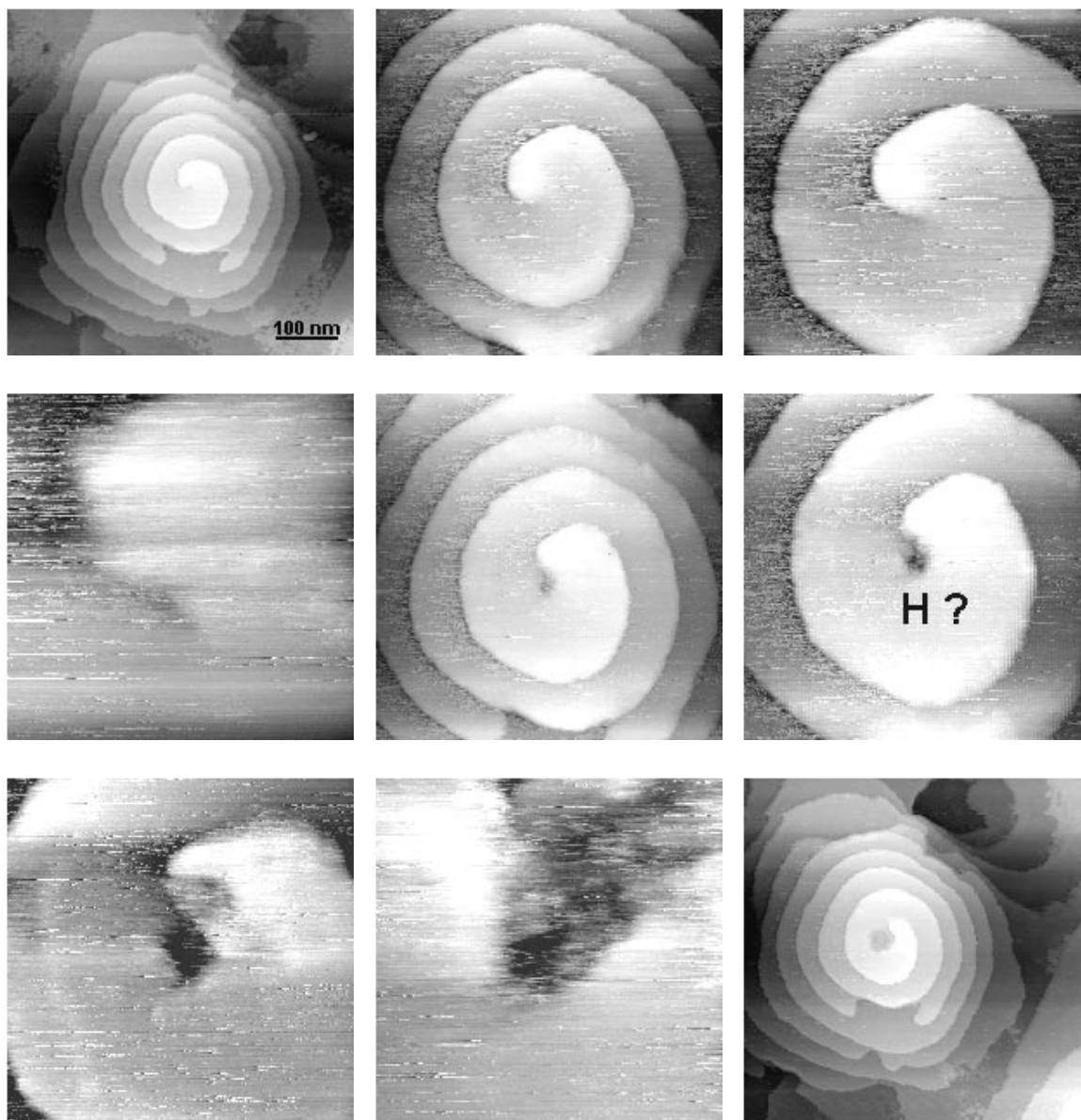


Figure 3.18: Series of STM images showing a screw dislocation situated in the centre of a spiral growth hill. On investigating the screw dislocation at a smaller scale some modification of the surface took place leading to the removal of YBCO material. The possible observation of a hollow core of the screw dislocation is marked (H ?).

3.2.6 Conclusion

The surface structure of laser-deposited YBCO thin films on $\text{LaAlO}_3(100)$ has been studied by STM. Using a special half-shadow technique, different film thicknesses and their associated growth stages could be prepared simultaneously. The observed growth stages include nucleation and spreading of two-dimensional YBCO islands, their coalescence and growth, formation of well-developed growth hills in the half-shadow region and, finally, a continuous film. Layer growth of the films is found with respect to the height of the YBCO unit cell in the crystallographic c -direction. In addition to growth processes dominated by repeated 2D nucleation, *Frank's* spiral growth mechanism is also operative. The growth hills characteristic of film growth at a film thickness ranging from 100 to 600 nm have been analyzed using classical BCF theory. Analysis of the step separation of a particular growth spiral gives a critical nucleus for spiral growth of only a few nanometres radius, which could be a possible explanation for the abundance of growth spirals observed in YBCO thin films prepared under the conditions described above. An estimate has shown that only a few hundred YBCO unit cells are necessary to initiate rapid spiral growth. The investigation of the screw dislocations with atomic resolution was not successful since unit cell layers of YBCO close to the screw dislocation were removed.

3.3 YBCO thin films on SrTiO₃(100)

SrTiO₃ is a substrate with a (100) face that is very well adapted²⁵ to the lattice of YBCO. For this reason the structural and electrical properties of YBCO thin films on this type of substrate are better than on other substrates. The electrical properties — especially the critical current density — surpass those of single crystals, polycrystalline bulk material or melt-textured samples by powers of ten. The structural properties — as characterized by X-ray diffraction — of epitaxial HTSC thin films do not differ very much from those of HTSC single crystals. Here the morphology of the films illustrated by STM images shall be related to the structural properties (X-ray data) with substrate temperature and film thickness as parameters [3.44].

3.3.1 Experimental conditions

Thin films of YBCO are prepared in a range of substrate temperatures of 550 to 800°C by standard PLD. For good reproducibility a 1 inch SrTiO₃(100) wafer is cleaved to obtain many substrates of identical quality.²⁶ The film thickness is 220 nm at nominal growth rate of 0.6 nm/s. All films have been subjected to slow cooling to 600°C at a rate of 4 K/min and oxygen treatment at a pressure of 4×10^4 Pa at 500°C for 30 min and cooling to room temperature.

Standard Cu K_α XRD in Bragg-Brentano geometry is used to determine the structural bulk properties of the films. The samples are mounted on the XRD stage and oriented using the YBCO(005) reflection. The azimuth angle is varied to obtain maximum intensity (Φ -scan, in-plane orientation of the grains).²⁷ Thereafter, the sample stage rock (Θ) is varied while leaving the detector at the 2Θ position of the YBCO(005) reflection (mosaic spread, out-of-plane orientation of the grains).²⁸ The analysis is completed by a

²⁵SrTiO₃ is pseudocubic with $a = 0.3905$ nm, $b = 0.3908$ nm and $c = 0.3890$ nm.

²⁶This is of major importance for a reliable characterization of film growth by STM. Due to the high vertical resolution capability of STM any miscut of the substrate off the specified direction (here the [100] direction) will influence the film morphology.

²⁷X-ray diffraction is — as the name suggests — a diffraction method yielding information on the reciprocal space. For an orthorhombic lattice we expect on irradiation along [001] a rectangular diffraction pattern. On rotating the sample the rectangular diffraction pattern is also rotated. Thus only twice in a full 360°-turn the detector will see a non-vanishing intensity (provided the diffractometer is set to the Θ - 2Θ values of a higher order reflection, e.g. YBCO(005)). This results in two peaks in the Φ -scan. Due to sample tilt perpendicular to the Θ -circle of the goniometer the intensity of the two peaks may be different. The width of the Φ -scan peaks gives information on growth quality of the film (in our case parallel to [001]), i.e. whether the crystallographic axes (in the film plane) are randomly distributed (constant intensity in Φ -scan) or well aligned (sharp peak in Φ -scan). The relative position of the peaks (compared to substrate peaks belonging to directions parallel to those in question, e.g. SrTiO₃[001]/YBCO[001]) reveals the epitaxy relations along [001].

²⁸Some grains in the sample may be tilted. By tilting the sample (Θ -scan) the distribution of tilted grains can be determined (mosaic spread). The width of the mosaic spread peak is a measure for the out-of-plane orientation of the film.

$\Theta - 2\Theta$ scan.²⁹ Figure 3.19 illustrates the different procedures of measurement.

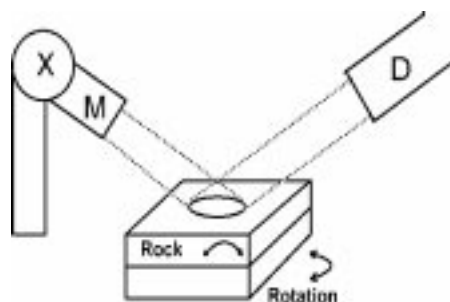


Figure 3.19: Schematic of X-ray diffraction technique: The radiation of an X-ray tube (X) is monochromatized (M). By a slit system (not shown) it is directed to the sample. The scattered X-ray photons are collected by a detector (D). The incidence angle Θ of the radiation and the detector angle 2Θ can be changed ($\Theta - 2\Theta$ scan). The sample can be rotated (Φ -scan) or tilted (Mosaic spread, rock/rocking curve).

The surface morphology of YBCO thin films is imaged by STM and SFM. The roughness of the surface imaged is indicated by the maximum height difference and the standard deviation of the data points measured. SFM has been used to image the SrTiO_3 substrate and early growth stages of the YBCO film using cantilevers with integrated Si_3N_4 tips and a spring constant of 0.12 N/m.

The critical transition temperature T_c of the YBCO films has been determined by a standard four-probe DC technique and compared to the values obtained by an inductive method. Critical current densities j_c are determined at 77 K by use of a microbridge ($100\mu\text{m} \times 1\text{mm}$) patterned by laser ablation.

3.3.2 Analysis of an optimized YBCO film

The structural and superconducting properties of YBCO thin films grown on $\text{SrTiO}_3(100)$ substrates at different substrate temperatures T_s , ranging from 550 to 800°C are discussed. As an example, the structural properties of a thin film sample prepared at $T_s = 740^\circ\text{C}$ ³⁰ as obtained by XRD are compared to STM results. XRD ($\Theta - 2\Theta$) reveals that the film is (001) oriented. The determination of the mosaic spread (fig. 3.20) shows that the rock of the grains is less than 0.26° (full width at half maximum (FWHM) of the YBCO (005) reflection).

The in-plane misorientation relative to the substrate (fig. 3.21) of the YBCO grains is

²⁹The peak width in the $\Theta - 2\Theta$ scan is a measure for the degree of crystallinity of a film sample. For a perfect single crystal δ -peaks are expected. However, the use of apertures and slits to shape the X-ray beam gives a finite lower limit of the peak width. Broadening of peaks occurs when investigating very small (nanometre-size) grains.

³⁰These conditions have turned out to be optimized for the growth of YBCO on $\text{SrTiO}_3(100)$ in our pulsed laser deposition setup.

within 6° (FWHM of Φ -scan of YBCO(005) reflection). Figure 3.22 shows a STM image and a line section of the surface (indicated as a white line in the STM topograph).

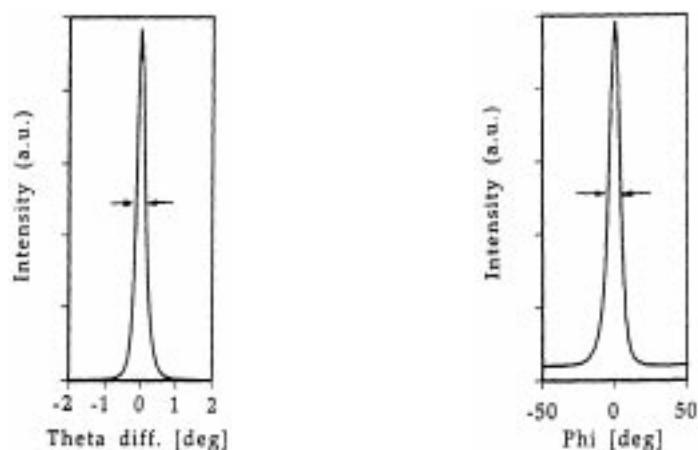


Figure 3.20: *LEFT:* YBCO thin film prepared at 740° . Mosaic spread of YBCO(005) reflection (FWHM = 0.26°). The narrowness of the peak demonstrates the YBCO film is well aligned.

Figure 3.21: *RIGHT:* Φ -scan of YBCO(005) (FWHM = 6°). The small FWHM value reflects the good epitaxy and in-plane alignment of the film.

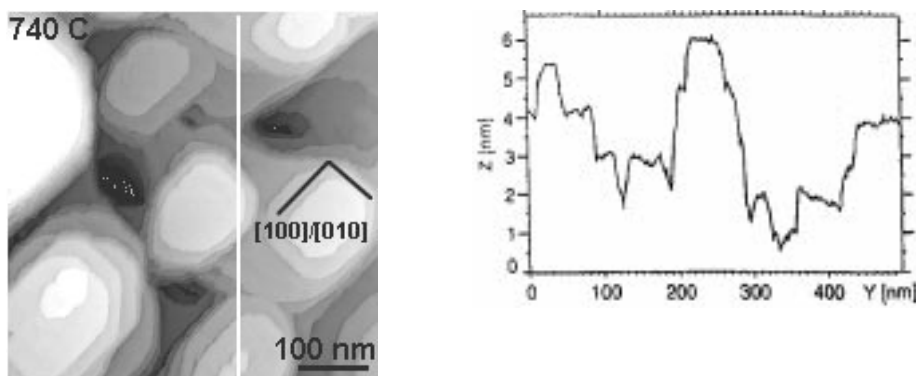


Figure 3.22: *LEFT:* Surface of a sample prepared at 740°C . STM topview showing growth hills with steps aligned to $[100]$ and $[010]$ of YBCO (indicated). The step height is one c -axis length.

Figure 3.23: *RIGHT:* A line section along the white line indicated in the STM image. The steps are identified as unit cell steps in $[001]$ direction.

The surface morphology is dominated by growth hills with steps aligned in two main directions (indicated), corresponding to the crystallographic $[100]$ and $[010]$ directions of

YBCO as determined by XRD (Φ -scan). Only occasionally, screw dislocations are observed (see fig. 3.24). The height of the growth steps (1.2 nm) corresponds to the height of a unit cell in the YBCO[001] direction (1.17 nm) as can be seen from the line section (fig. 3.23). The rock of YBCO grains is too small (0.26°) to be seen in the STM image.

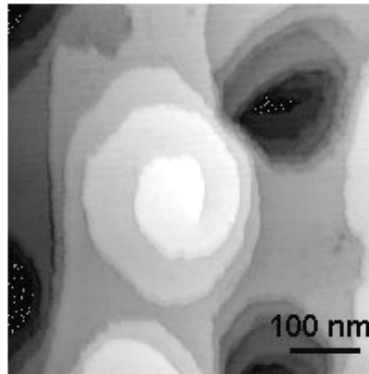


Figure 3.24: A rare case of the observation of a screw dislocation in a film in this series of YBCO films deposited on substrates obtained by cleaving a SrTiO_3 wafer. The substrate miscut angle is the same for all substrates in this series.

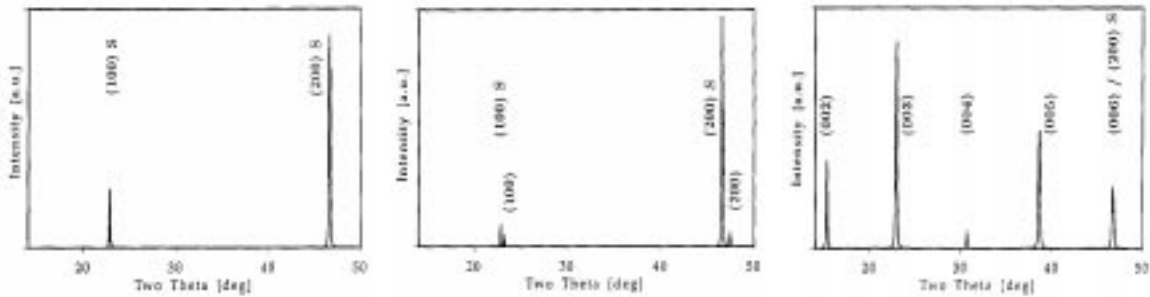


Figure 3.25: *LEFT:* Typical XRD spectrum of a YBCO film on $\text{SrTiO}_3(100)$ prepared at a substrate temperature below 600°C . Only the $\text{SrTiO}_3(h00)$ reflections can be observed. Owing to the absence of YBCO peaks the film is termed 'amorphous'. *MIDDLE:* Typical XRD spectrum of a YBCO film on $\text{SrTiO}_3(100)$ prepared between 610 and 650°C . In addition to the $\text{SrTiO}_3(h00)$ reflections the YBCO($h00$) reflections are observed. *RIGHT:* Typical XRD spectrum of a YBCO film on $\text{SrTiO}_3(100)$ grown between 660 and 800°C . The YBCO(00ℓ) reflections dominate.

3.3.3 Film orientation

Table 3.1 summarizes the XRD data and the surface roughness values determined by STM for the samples prepared at different substrate temperature T_s . XRD reveals that the

samples prepared above 660°C are (001) oriented (fig. 3.25), and the samples prepared below 660°C are (100) oriented or show no YBCO reflections at all. Figure 3.26 displays these dependences of the XRD data on the substrate temperature.

T_s	$2\Theta^a$ [deg]	Mosaic ^a [deg]	Φ -scan ^a [deg]	Roughness ^b [nm]
550°	– ^c	– ^c	– ^c	7±1
575°	– ^c	– ^c	– ^c	6±2
610°	0.12 ^d	0.24 ^d	6.5 ^d	14±2
640°	0.14 ^d	0.68 ^d	5.6 ^d	19±3
660°	0.48	0.90	17	16±2
680°	0.27	0.45	15.8	20±3
700°	0.23	0.42	13	21±3
720°	0.21	0.29	7.2	24±4
740°	0.19	0.26	6	28±4
750°	0.19	0.24	6	20±4
770°	0.18	0.26	6	15±3
800°	0.20	0.53	7	10±1

^a XRD: FWHM of YBCO(005) reflection.

^b STM: maximum height difference and standard deviation of data points measured.

^c no YBCO reflections observed.

^d YBCO(100) reflection.

Table 3.1: Structural properties of YBCO films on SrTiO₃(100) prepared at different substrate temperatures T_s .

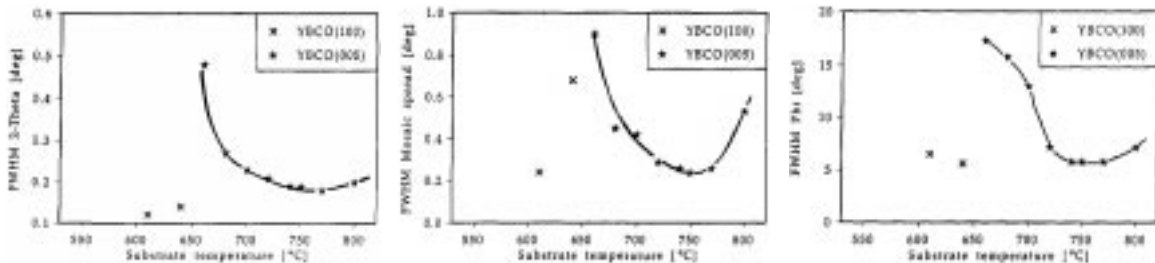
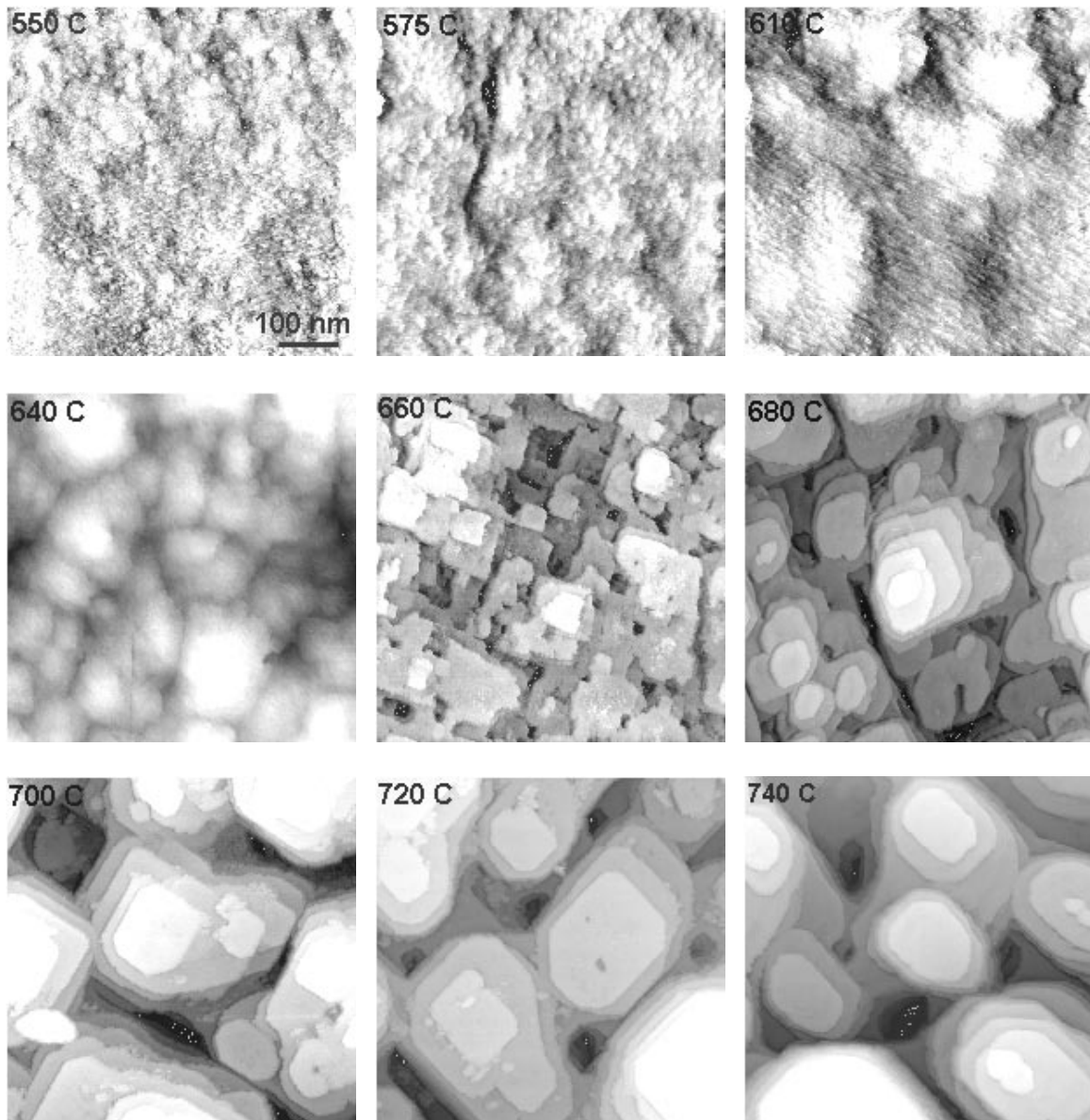


Figure 3.26: LEFT: Dependence of the FWHM of the YBCO(005) reflection on the substrate temperature applied for film growth. MIDDLE: Dependence of the mosaic spread of the YBCO(005) on the substrate temperature. RIGHT: Dependence of the Φ -scan (FWHM) of the YBCO(005) reflection on T_s .

3.3.4 Film morphology

The surface morphology of samples prepared at different T_s is compared. Figure 3.27 shows STM images of YBCO films on SrTiO₃(100) prepared at 550, 575, 610, 640, 660, 680, 700, 720, 740, 750, 770 and 800°C, respectively. Films prepared at 550 and 575°C exhibit a grainy, disordered surface, those prepared at $T_s=610$ and 640°C show a -axis growth steps with a height of 0.4 nm. The films prepared at $T_s \geq 660^\circ\text{C}$ exhibit growth hills with unit cell steps in the YBCO[001] direction.



(continued on following page)

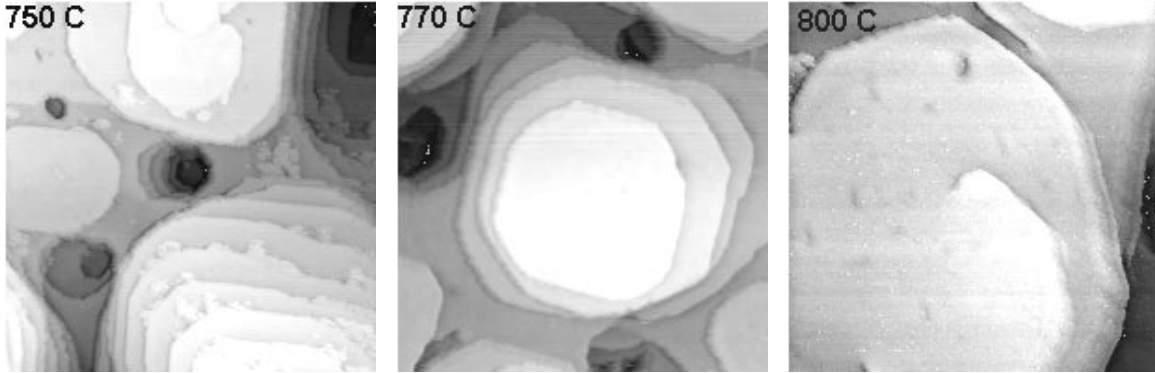


Figure 3.27: STM topviews of YBCO films on SrTiO₃(100) prepared at different substrate temperatures (indicated in the top left corner of each image). The scale bar applies to all figures.

With increasing T_s the growth hill diameter increases, too. This is caused by the higher T_s applied and the prolonged cooling process to 600°C leading to increased thermal diffusion. These relations are graphically shown in figs. 3.28 and 3.29.

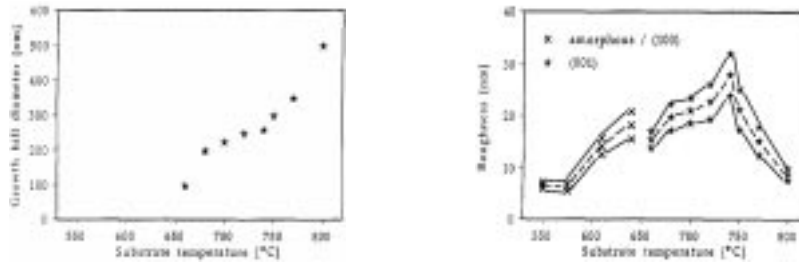


Figure 3.28: LEFT: Growth hill diameter as a function of the substrate temperature applied for film growth (the values are deduced from the STM images).

Figure 3.29: RIGHT: Maximum height difference (symbols connected by a dashed line) on a area of 500 nm × 500 nm and roughness values (symbols linked by lines) as computed as standard deviation of all image pixels.

3.3.5 Superconducting properties

The transition temperatures T_c to superconductivity, the transition widths ΔT_c and the ratios of the resistivity at 300 K to the resistivity at 100 K (R_{300K}/R_{100K}) of the samples prepared at different T_s are compiled in Table 3.2 and displayed in fig. 3.30.

Best resistively determined T_c 's are obtained at a T_s of 740 to 750°C. The critical current density of a sample prepared at 740°C amounts to 3×10^6 A/cm² at 77 K. Such films are also optimized with respect to their structural properties (Table 3.1). STM

images of these films reveal a surface morphology dominated by well-developed growth hills. Films having a smoother surface morphology (e.g. samples prepared at 660°C) exhibit inferior structural and electrical properties compared to the 740°C sample.

T_s	T_c^a	ΔT_c^a	T_c^b	R_{300K}/R_{100K}
550°	– ^c	– ^c	– ^d	0.3
575°	– ^c	– ^c	– ^e	1.8
610°	– ^c	– ^c	– ^e	1.3
640°	60 K	15 K	87 K	1.3
660°	71 K	7 K	89 K	1.5
680°	84 K	3 K	89 K	2.1
700°	86 K	3 K	87.5 K	2.0
720°	87.5 K	2.5 K	92 K	2.4
740°	88 K	4 K	91 K	1.9
750°	87.6 K	2.5 K	92 K	2.4
770°	89 K	2.5 K	92 K	3.1
800°	87.5 K	2.5 K	90 K	3.3

^a determined by an inductive method (onset).

^b determined by a resistive DC method (onset).

^c no transition observed.

^d semiconducting.

^e metallic.

Table 3.2: Electrical properties of YBCO films on SrTiO₃(100) prepared at different T_s .

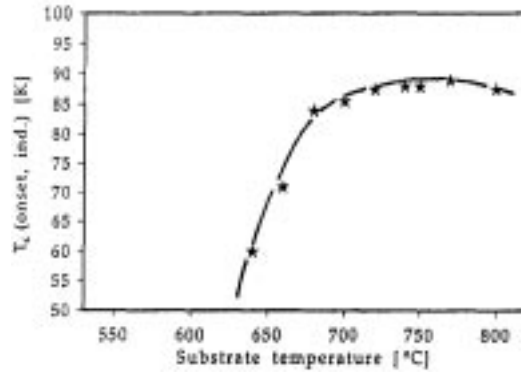
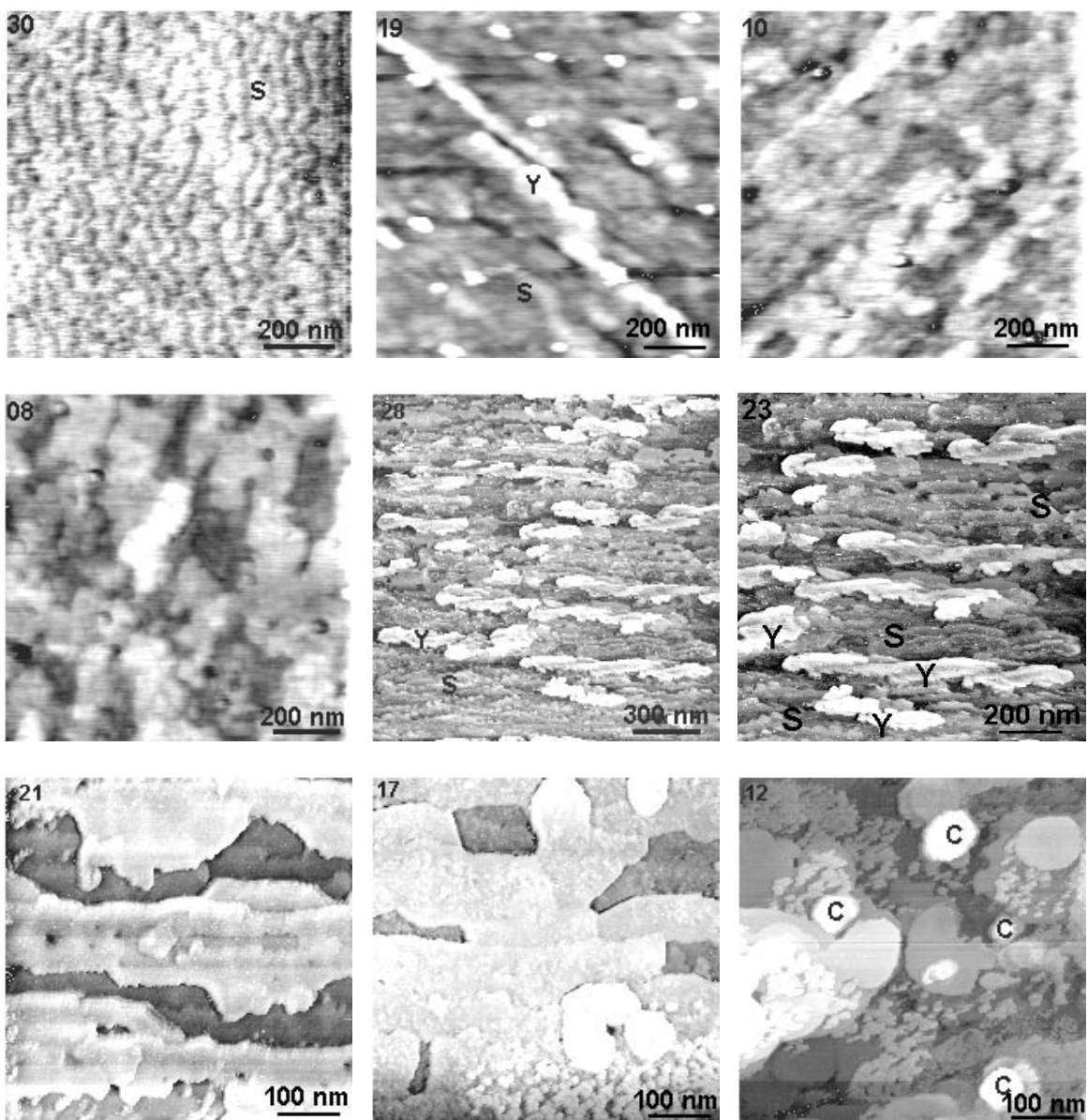


Figure 3.30: Dependence of inductively determined values of T_c (onset) on the substrate temperature applied for film growth.

3.3.6 Thickness-gradient films

In order to study the relationship between film thickness — i.e. different growth stage — and film morphology, thickness-gradient films have been investigated. Figure 3.31 shows four SFM and eight STM images of the surface morphology of a thickness-gradient film prepared at 740°C.³¹ SFM and STM investigations have been performed along the thickness-gradient film, i.e. from the film of well-defined thickness (220 nm) over the part of decreasing thickness to the uncovered substrate.



(continued on following page)

³¹This substrate temperature is considered to be optimized.

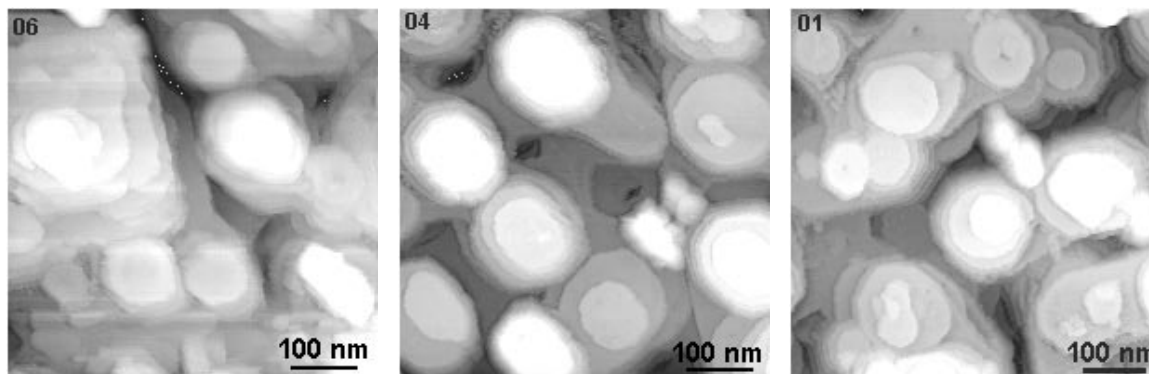


Figure 3.31: SFM and STM topviews of a YBCO thickness-gradient film on $\text{SrTiO}_3(100)$ prepared at 740°C . The numbers indicate the position on the film surface ('01' = thick film, '30' = substrate).

The position on the substrate is referred to by indicating numbers between **01** and **30**.³² The bare substrate is imaged by SFM. The image in the top left corner of fig. 3.27 (labelled '30') shows a surface covered by steps of a height of about 0.4 nm that agrees well with the step height expected for SrTiO_3 . Moving along the thickness gradient ('19') SFM reveals islands (**Y**) nucleated at substrate steps (**S**). The island step height is about 1.2 nm which is the step height expected for YBCO. Thus we interpret this image as the observation of YBCO nucleation on the SrTiO_3 surface. At a later stage ('10' and '08') the formation of terraces and growth of new island atop of these layers is observed. The discussion of the morphology of the thickness-gradient film is continued by showing STM images since they give a clearer view of the surface. The nucleation of YBCO islands (**Y**) on SrTiO_3 surface step is also observed by STM³³ ('28'). '23' is showing the YBCO islands (**Y**) nucleated at the SrTiO_3 steps (**S**) in greater detail. Coalesced YBCO layers ('21') and growth of further YBCO layers on complete YBCO terraces ('17') is found at a presumable thickness of a few monolayers. At a thickness of about 50 nm, sites ('C') for the preferred formation of growth hills are imaged ('12'). Their number per unit area is very similar to the number of growth hills observed in the thick³⁴ region of the YBCO film ('04' and '01'). Up to now it is not yet clear what is responsible for this increase of YBCO growth at these preferred nucleation centres 'C'.

Going back to the SFM image of the bare SrTiO_3 substrate ('30' in fig. 3.31) the substrate miscut off (100) is clearly demonstrated by the observed SrTiO_3 step pattern. Fig. 3.32 illustrates the situation schematically: a height difference z is observed over a lateral distance x . In fig. 3.31, '30', about 16 unit cell steps of SrTiO_3 are observed

³²These are the file numbers of the STM images: **01** is the thick part of the film, **30** is the uncoated substrate or thin part of the film.

³³However, a very, very slow scanning speed is required (1 image in 30 minutes) to ensure that the feedback-loop is working properly since the conductivity of this very thin part of the film (thickness below 1 monolayer) is very low.

³⁴220 nm.

corresponding to a z of 6.2 nm³⁵ and a x of 1000 nm. The tilt angle of the substrate is derived from $\tan \alpha = z/x$ and amounts to 0.35° which seem to be a quite low value.³⁶ Especially for STM investigations of ultrathin films and a study of initial growth stages the use of substrates with a very low miscut angle is obligatory as will be demonstrated in section 3.6.3.3. A recent work by *Schlom et al.* [3.45] implying the absence of screw dislocations only in YBCO films deposited on substrates having a misorientation off the (100) face of at least 3.5° is not confirmed by the data shown here.

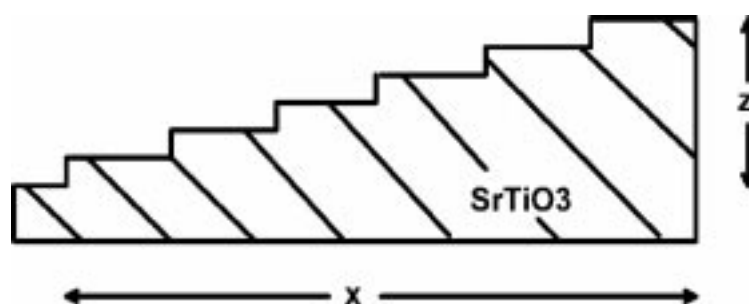


Figure 3.32: Schematic view of a SrTiO₃ substrate with a miscut angle resulting in a distinct unit-cell-step pattern. The tilt angle of the substrate is derived from $\tan \alpha = z/x$.

3.3.7 Conclusion

Depending on the substrate temperature different orientations of the films are revealed by X-ray diffraction: (001) orientation between 660 and 800°C, (100) orientation between 610 and 660°C, and no YBCO reflections for films prepared at lower T_s . In-plane orientation (Φ -scan) and out-of-plane orientation data (mosaic spread) of the grains are compared to scanning tunneling microscopy (STM) images. The images show rectangular-shaped growth hills. Their growth steps are aligned along the [100] and [010] directions of YBCO and are one c -axis spacing in height (1.2 nm). Occasionally screw dislocations are observed. Highest critical transition temperatures are reached at about $T_s = 750^\circ\text{C}$. Such films with optimized structural and electrical properties exhibit a surface morphology dominated by growth hills, whereas films optimized for a smooth surface morphology have inferior structural and electrical properties. The relationship between film thickness and surface morphology has been studied using YBCO films with a thickness gradient prepared by a half-shadow technique. Thus different film thicknesses can be obtained simultaneously under identical conditions. STM images give evidence of different growth stages such as nucleation and coalescence of two-dimensional islands, their growth and, finally, the formation of growth hills.

³⁵The c spacing in SrTiO₃ is 0.389 nm.

³⁶Many manufacturers of single crystal substrates specify a maximum miscut angle of 1° off the (100) face.

3.4 YBCO thin films on MgO(001)

MgO is a cheap substrate material, but its (001) face is not very well adapted³⁷ to the (001) face of YBCO. Similar to the chapter on YBCO growth on SrTiO₃(100) the film morphology (STM/SFM data) will be discussed as a function of substrate temperature and film thickness (by use of thickness-gradient films). The images are interpreted with the help of XRD results [3.46].

3.4.1 Experimental conditions

Smooth YBCO films on polished MgO(001) substrates can be grown between 600 and 725°C. Four different deposition temperatures have been chosen, such as 600°C (sample Y-600), 675°C (sample Y-675), 700°C (sample Y-700) and 725°C (sample Y-725). Films grown at temperatures above 725°C show reactions between YBCO and the MgO substrate leading to degradation of film properties and roughening of surface morphology. Therefore, such films will not be considered here. Typical film thickness attained amounts to 150 nm.

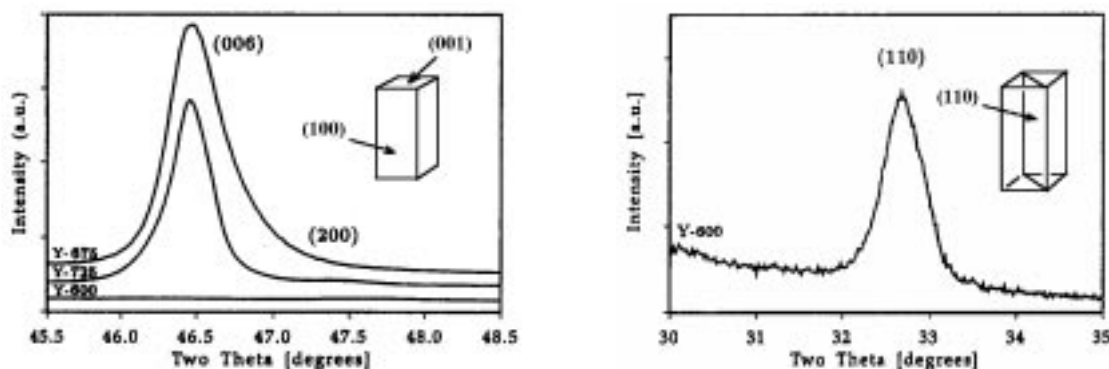


Figure 3.33: *LEFT:* Cu K_α Θ-2Θ X-ray diffraction patterns. (006) peak of sample Y-675, (006) and small (200) peak of sample Y-725, background of sample Y-600. The inset shows the relevant crystallographic faces of YBCO.

Figure 3.34: *RIGHT:* (110) peak of sample Y-600. This sample does not show further peaks.

3.4.2 Film orientation

Bulk structure of the films has been investigated by X-ray diffraction (XRD) in conventional Bragg-Brentano Θ-2Θ geometry using Cu K_α radiation. As displayed in fig. 3.33

³⁷Space group Fm $\bar{3}$ m (face-centred cubic), $a = 0.421$ nm.

sample Y-675 shows (001) orientation, whereas sample Y-725 exhibits both (001) and (100) orientations. For sample Y-700, a smaller percentage of (100) orientation has been observed (not shown). Figure 3.34 reveals that sample Y-600 is (110) oriented.

3.4.3 Film morphology

The surfaces of the YBCO thin-film samples described above have been investigated by SEM, STM and SFM. Figure 3.35 shows SEM images of the film surface of the samples Y-600, Y-675 and Y-725. Sample Y-600 exhibits a surface with a fine, grainy structure (fig. 3.35 left). Y-675 shows a very smooth surface (fig. 3.35 middle) and Y-725 shows slabs and grainy structure (fig. 3.35 right). A more detailed view of the surface is obtained by applying scanning probe methods.

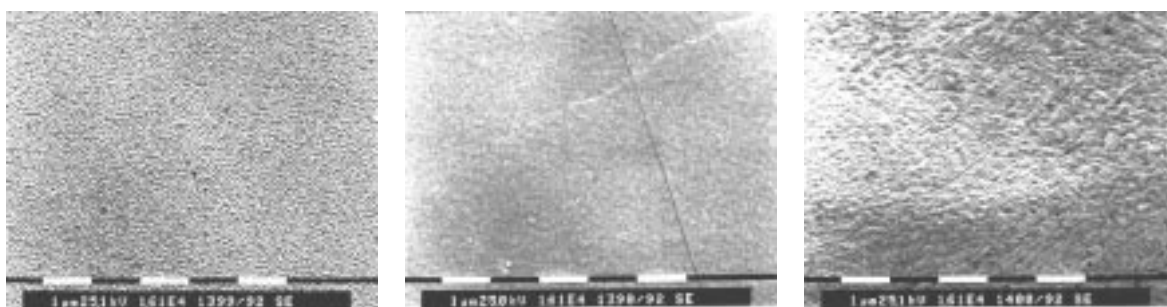


Figure 3.35: SEM images of the samples Y-600 (left), Y-675 (middle) and Y-725 (right).

Figures 3.36a–d show the topography of these samples prepared at different substrate temperatures. Figure 3.36a depicts the platelets which form the morphology of sample Y-600 having (110) orientation. Maximum height differences visible in fig. 3.36 are 20 nm. Figures 3.36b (sample Y-675) and 3.36c (sample Y-700) show the typical surface of (001) oriented films. Spiral step courses originating from screw dislocations with a Burgers vector component perpendicular to the film surface dominate the images. Estimated number densities of screw dislocations are in the range of 10^{10} cm^{-2} . The SFM image (fig. 3.36d) visualizes the surface of a film exhibiting (001) and (100) orientations (Y-725). The (100) and (010) grains correspond to the slabs aligned along two directions perpendicular to each other. The rounded grains in fig. 3.36d are to be identified with the (001) growth hills.

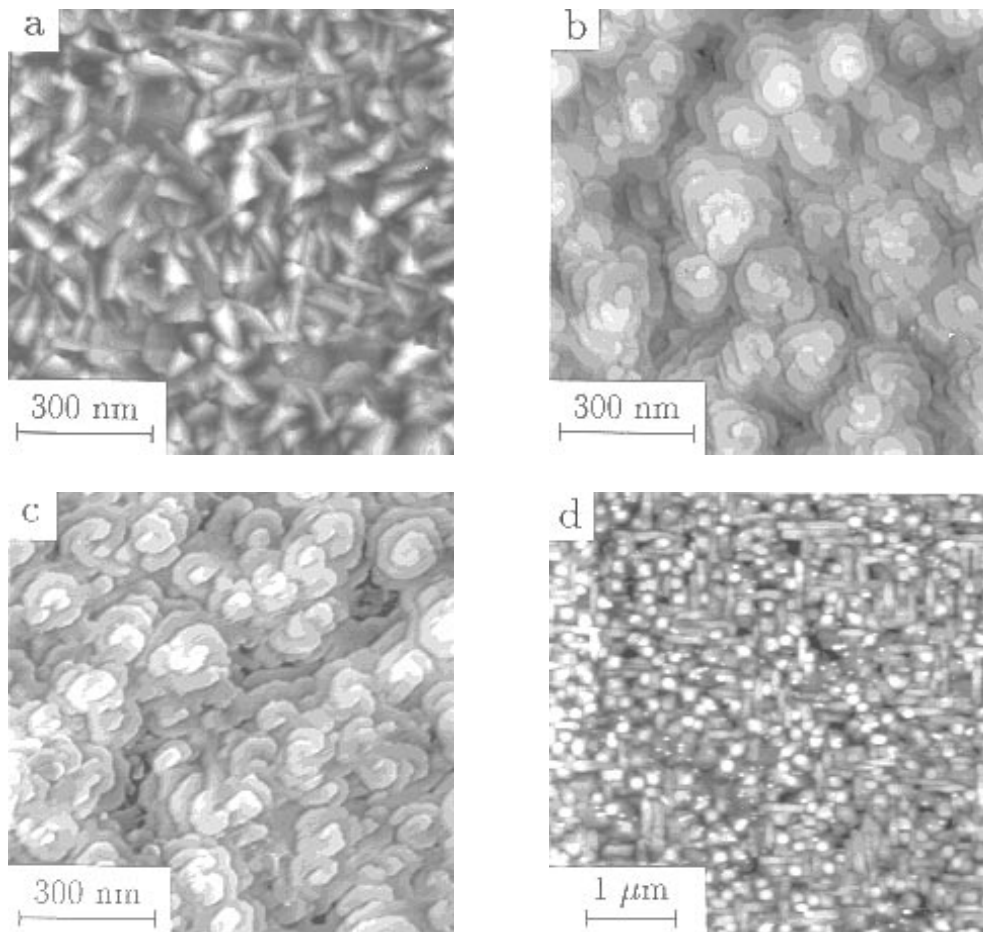


Figure 3.36: YBCO films prepared at different deposition temperatures. (a) STM image of sample Y-600 with (110) orientation; (b) STM image of (001)-oriented sample Y-675; (c) STM image of (001)-oriented sample Y-700; (d) SFM image of sample Y-725 showing (001) and (100) growth.

3.4.4 Transmission electron microscopy

In collaboration with Dr. D. Hesse³⁸ transmission electron microscopy of thin YBCO 123 films on MgO substrates has been performed. The film has been thinned by dimpling and ion-etching for the in-plane investigation in a transmission electron microscope.³⁹

³⁸Max-Planck-Institute for Microstructure Physics, Weinberg 2, D-06120 Halle (Saale)

³⁹The TEM used is a Philips CM 20T with 200 kV acceleration voltage. The point resolution is 0.27nm.

By accident the small hole etched into the film is close to an area where both the (001) oriented YBCO film and an area of YBCO(100) particles are present. For that reason both orientations are accessible. Figure 3.37 shows a TEM image of the border of the small hole⁴⁰ (upper right corner of the image).



Figure 3.37: TEM image of a YBCO thin film on MgO(100). Most of the film is YBCO(001) '1', but a small area (labelled '2') close to the etched hole (upper right corner of the image) exhibits (100)-oriented platelets. An individual platelet is marked by 'P'.

Transmission electron microscopy also yields electron diffraction images. Figures 3.38 and 3.39 show electron diffraction images of the areas '1' and '2'. The diffraction image of region '1' (fig. 3.38) shows the square unit mesh of MgO ('M', labelled reflex $\bar{2}00_M$) and the orthorhombic mesh of YBCO ('Y', labelled reflex 100_Y).⁴¹ Region '2' however, shows a different diffraction image (fig. 3.39): the spots are understood when assuming a YBCO(100) area. The arrow shows the *c*-direction of the (100)-oriented platelet 'A'

⁴⁰Only the very thin region close to the small hole in the sample allows the transmission of electrons through the sample.

⁴¹The orthorhombic splitting YBCO{400} in YBCO(400) and (040) is shown by arrows labelled with an asterisk. This proves that actually the orthorhombic (and therewith superconducting) phase of YBCO is imaged.

in figs. 3.40 and 3.41. The other spots on the rings are due to other (100)-oriented platelets being rotated randomly around the film normal. The four small arrows indicate the position where the contrast diaphragm was set to obtain the dark field image shown in fig. 3.41.

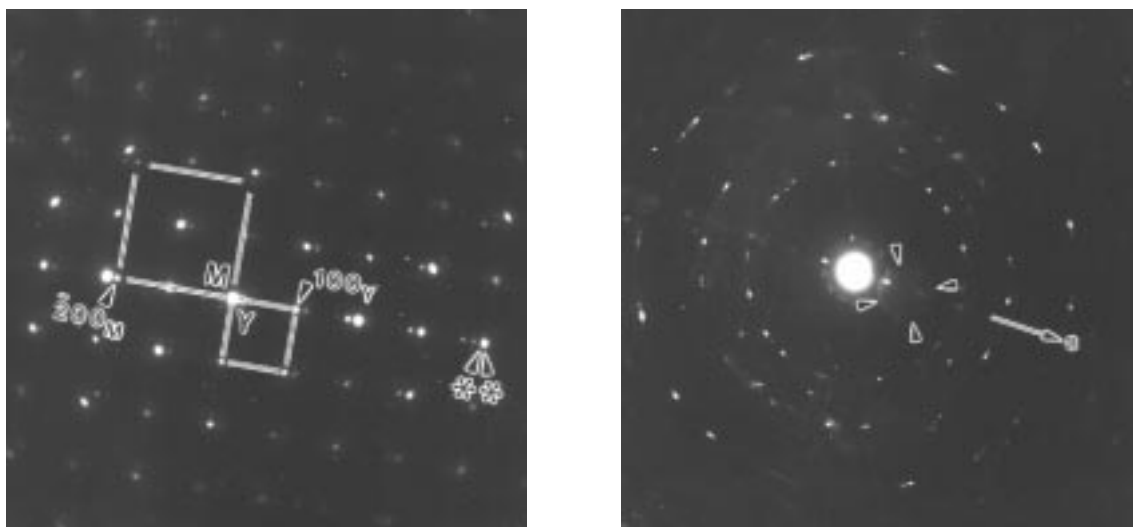


Figure 3.38: *LEFT:* Electron diffraction (ED) image of YBCO on MgO obtained in a TEM. In region '1' the two unit meshes of YBCO ('Y') and MgO ('M') are observed. Two reflections are labelled: YBCO(100) and MgO($\bar{2}00$). The two arrows with an asterisk demonstrate the orthorhombic splitting of the YBCO(400) reflex in YBCO(400) and YBCO(040) proving that only the superconducting phase of YBCO is present.

Figure 3.39: *RIGHT:* ED image of region '2' of the YBCO thin film. The spots are interpreted as YBCO in (100) orientation. The arrow depicts the c -direction. The four small arrows indicate the position of the contrast diaphragm.

A larger magnification of such a platelet is shown in figs. 3.40 (bright field image)⁴² and 3.41 (dark field image using the YBCO(100) and (200) reflections).⁴³ The dark field image has been generated by placing the contrast diaphragm to the position indicated by four small arrows in fig. 3.39. By this procedure diffraction spots can be related to objects in the image and it is possible to indicate the orientation of individual objects.

⁴²A TEM bright field image is generated if the zero-order spot in the electron diffraction image is selected. Areas where no matter is present are shown in white. Areas that are blocked by material give a smaller intensity on the image. The thicker a particle the more it absorbs the electrons and the darker it appears.

⁴³A dark field image is generated by selecting only individual higher-order spots in the electron diffraction image.

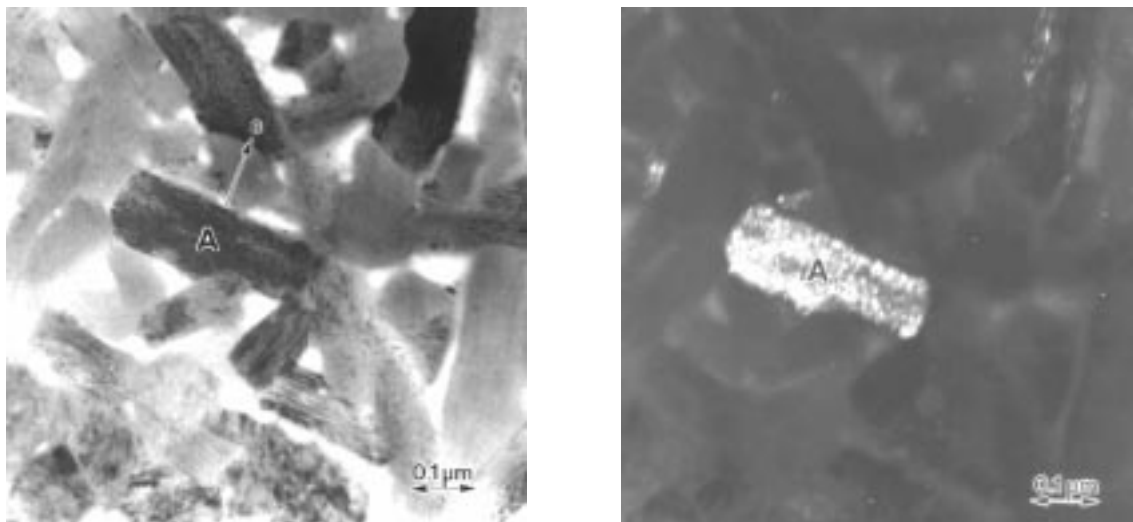


Figure 3.40: *LEFT:* Bright field TEM image showing (100)-oriented platelets. One of them is labelled by 'A' and its c-axis ([001] direction) is indicated. The respective c-axes of the other platelets are randomly oriented in the film plane.

Figure 3.41: *RIGHT:* Dark field TEM image of platelet 'A' generated by selecting certain YBCO(100) and (200) spots in the ED image. All other platelets do not appear bright since the selected diffraction conditions do not fit to them.

By selecting low order spots of the diffraction pattern for interference, high resolution electron microscopy (HREM) images with a resolution in atomic dimensions are obtained. Figure 3.42 shows a HREM image of YBCO 123 on MgO in planar geometry. The interatomic distance of 3.8 \AA between the atomic columns is clearly visible in the image. The arrows indicate the crystallographic a and b directions of YBCO. White lines mark the direction of the lattice planes. Please note that the HREM image is obtained by imaging both the YBCO 123 film and the MgO substrate simultaneously. Taking into account the comparatively poor point resolution capability of the Philips CM20T of 2.7 \AA ⁴⁴ the image quality is very good.

High resolution imaging of the boundary of one of the slabs having its c -axis in the film plane (like particle 'A' in fig. 3.40) lattice planes with the c -axis distance of YBCO 123 are revealed. They are shown in fig. 3.43 as stripe contrast. '1' denotes the (001)-oriented part of the YBCO 123 film with a and b axis in the film plane. '2' indicates the a -axis oriented particle exhibiting stripes with a distance of 11.7 \AA (c -distance in YBCO 123). The c -axis of platelet '2' is exactly parallel to the a/b -axis of the (001)-oriented part of the film. It is likely that individual a -axis oriented platelets are aligned epitaxially in the film, whereas bundles of a -axis oriented platelets (as region '2' in fig. 3.37) have

⁴⁴'Real' high resolution electron microscopes have a point resolution of 2 \AA or better. Such instruments are operated at 400 kV (shorter electron wave length) instead of 200 kV (like the Philips CM20T).

a random orientation in the plane.

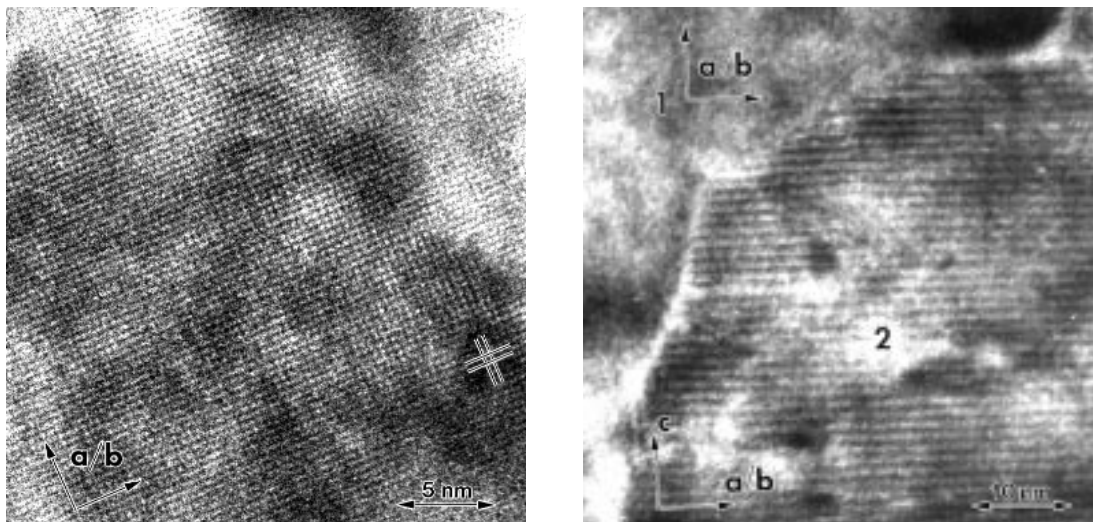


Figure 3.42: *LEFT:* HREM image of the c -axis oriented YBCO 123 matrix. The dots represent atomic columns and are separated by 3.8 Å. The crystallographic a - and b -axes are indicated. The white lines highlight the distance between the lattice planes.

Figure 3.43: *RIGHT:* HREM image of an individual a -axis oriented platelet ('2') embedded in the c -axis oriented YBCO 123 matrix ('1'). The lines are (001) lattice planes at a spacing of 11.7 Å. The corresponding a and b axes of the platelet are orthogonal to the a/b axes of the (001)-matrix which indicates epitaxial orientation.

A similar situation of a bundle of (100)-oriented platelets in a mainly (001) oriented YBCO film on MgO(100)⁴⁵ is encountered in the SEM images displayed in figs. 3.44 and 3.45. The area appearing brighter in fig. 3.44 is dominated by platelets embedded in a (001) oriented matrix⁴⁶ as shown in fig. 3.45. It is quite probable that by accident such an area has been observed in the TEM images above.

3.4.5 Thickness-gradient films

The half-shadow technique has been applied to grow thickness-gradient films at 675 and 700°C (samples TG-675 and TG-700). Maximum film thickness is about 210 and 280 nm, respectively. Figure 3.46a shows initial stages of growth of sample TG-675 comprising (001) terraces. In-plane misalignment of some terraces may be considered as a cause for the occurrence of screw dislocations at an advanced stage of growth. In fact, at larger

⁴⁵This may occur in case some part of the substrate is colder than the rest of the crystal platelet during the PLD process causing locally (100) growth instead of (001) growth.

⁴⁶XRD gives evidence of YBCO(001) growth with minor YBCO(100) content.

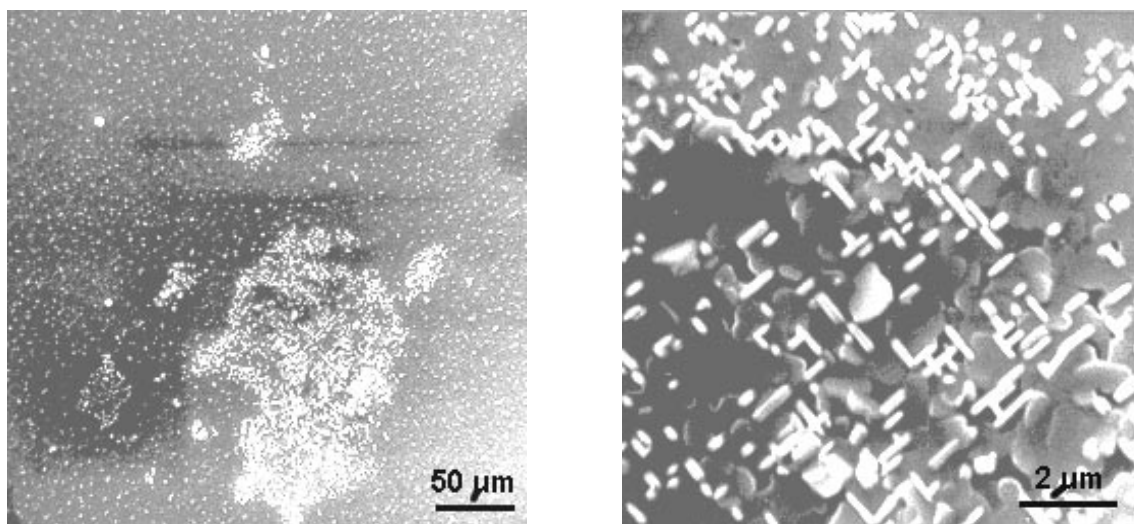


Figure 3.44: *LEFT:* Low resolution SEM image showing a presumably (100) oriented area (brighter) in a (001) oriented YBCO matrix.

Figure 3.45: *RIGHT:* Higher magnification by SEM of this area showing small platelets. They are aligned along two main directions and they are not tilted with respect to each other.

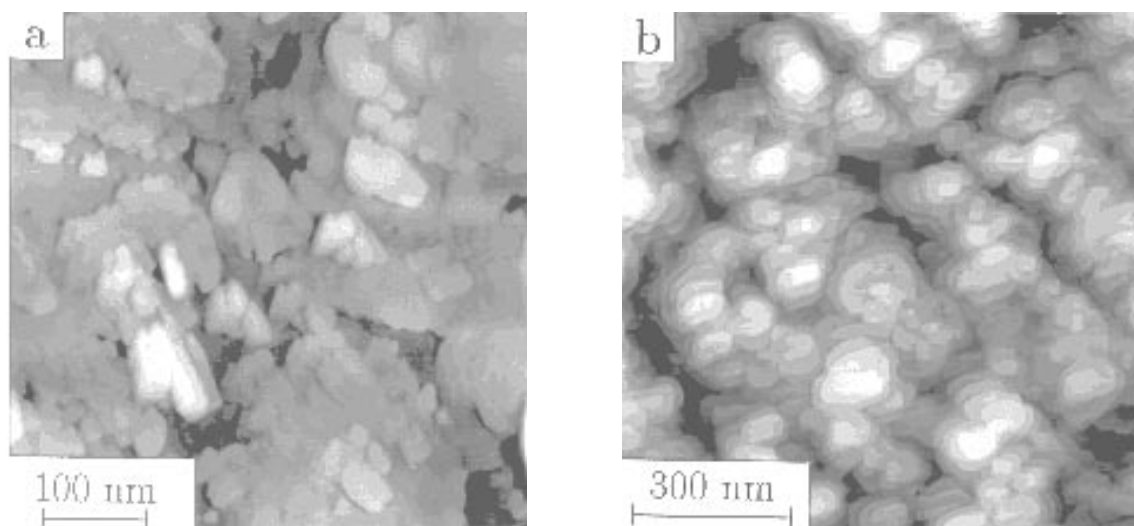


Figure 3.46: STM images of thickness-gradient sample TG-675. (a) Initial growth of (001) terraces; (b) continuous part of the thickness-gradient film showing growth hills with spiral step courses.

film thickness spiral growth step courses due to screw dislocations are observed (cf. fig. 3.46b).

Sample TG-700 exhibits by XRD both YBCO(100) and YBCO(001) orientations. Figure 3.47a shows the thin part of this sample. The well-aligned slabs correspond to (100)/(010) grains. Figure 3.47b shows that additional (001) growth – characterized by terraces – occurs at a larger film thickness.

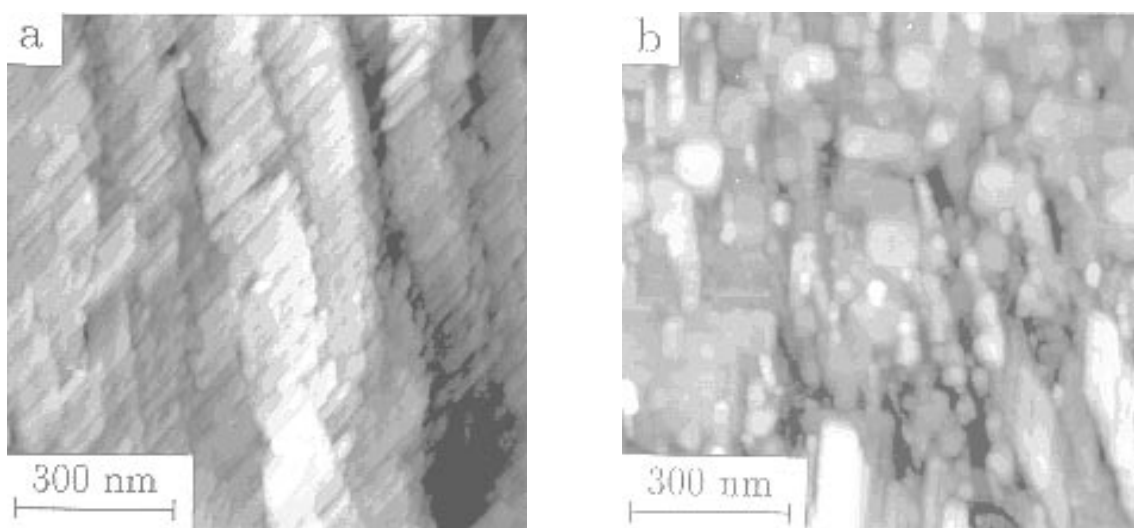


Figure 3.47: STM images of a thickness-gradient film prepared at 700°C (sample TG-700). (a) Early stages of growth comprising (100)/(010) oriented slabs; (b) (100) and (001) growth at an advanced stage demonstrated by slabs and growth hills.

3.4.6 Conclusion

Different orientations of YBCO films on MgO(001) have been observed both by XRD and scanning probe methods. Different grain shapes corresponding to different crystal orientations, such as (001), (100) and (110), have been recognized by comparison of XRD patterns with scanning probe images. The substrate temperature for optimized YBCO(001) growth on MgO is about 65° lower than on SrTiO₃. The half-shadow technique has been applied to grow thickness-gradient films, which combine different growth stages prepared under identical deposition conditions on a single substrate crystal. HRTEM images of the (001) and (100) lattice planes have been shown.

3.5 YBCO thin films by MOCVD

Due to the high growth rates used in pulsed laser deposition and the non-continuous flow of material⁴⁷ it might be suggested that this causes the vast number of screw dislocation type defects observed by STM in such films. To demonstrate that this is not the case films prepared by different methods have also been subject to investigations by STM and SFM.

3.5.1 Film preparation

A method by means of which continuous vaporization of material is possible, is chemical vapour deposition (CVD). To supply the metal atoms metalorganic compounds are used, i.e. Y, Ba and Cu with organic ligands (metalorganic chemical vapour deposition, MOCVD). One of the main advantages of MOCVD compared to genuine thermal evaporation methods is the use of Y, Ba and Cu in form of metalorganic (MO) compounds instead of pure metals which are more easily oxidized.⁴⁸ Conventional MOCVD yields high quality YBCO thin films with excellent crystallographic orientation and superconducting properties [3.47], but requires a carrier gas to transport the MO compounds. Using a special MOCVD technique developed by P. Häussler and B. Schulte⁴⁹ in collaboration with H. Adrian⁵⁰ high quality YBCO thin films can be deposited without a carrier gas [3.48, 3.49, 3.50]. As source materials 2,2,6,6-tetramethyl-3,5-heptandionates (THD) of Y, Ba and Cu are used. Both Y(THD)_3 and Cu(THD)_2 are volatile at relatively low temperatures and do not decompose thermally in an excessive way⁵¹, but Ba(THD)_2 which contains 0.5-1.6 molecules of water co-ordinated to each Ba atom [3.48] is more difficult to evaporate at a constant rate. Typical process data are $T_Y = 140^\circ\text{C}$, $T_{\text{Cu}} = 130^\circ\text{C}$ and $T_{\text{Ba}} = 264^\circ\text{C}$ with an O_2 flow rate of $200 \text{ cm}^3/\text{min}$. The three MO sources are directed through a chimney which is held at its upper end at a temperature of 270°C inducing the decomposition of the MO precursors and the reaction to the YBCO compound in presence of oxygen in close proximity of the substrate. The substrate is held at temperature of 800°C . Typical growth rates of $5 \text{ \AA}/\text{s}$ can be achieved. A in-situ post-annealing step at 500°C for 40 minutes in 1 bar of O_2 is necessary to obtain superconducting films. By variation of the rates of the MO precursor sources the film stoichiometry can be changed in a very controlled way [3.50]. The resulting film morphology has been studied by SEM [3.50]. A strong dependence of film morphology on the Ba/Cu ratio has been observed. Films with excess of Cu (relative to Ba) always show precipitates on the surface (presumably CuO). Copper-deficient films exhibit a surface with holes (growth pits) of different shape and orientation, especially at simultaneous yttria-deficiency. The authors suggest an island growth mechanism leading to these growth pits [3.50]. Barium-rich films and

⁴⁷Growth rates in PLD may be varied in a wide range from $0.05 \text{ nm}/\text{s}$ to $1 \text{ nm}/\text{s}$.

⁴⁸Since MOCVD does not require very pure vacuum conditions (as for thermal evaporation) it is suited very well for an industrial thin film preparation.

⁴⁹Hoechst AG, Central Research, Frankfurt, Germany

⁵⁰Institute of Solid State Physics, TH Darmstadt, Darmstadt, Germany

⁵¹For that reason Y(THD)_3 and Cu(THD)_2 yield constant evaporation rates on the time scale of hours.

films with an ideal Y:Ba:Cu = 1:2:3 stoichiometry show no particles and holes at all.

3.5.2 STM/SFM investigations

The scope of this investigation was to find out whether the surface structure of MOCVD films is similar to those of the PLD films or magnetron sputtered films of YBCO.

Here only some of the STM/SFM results will be discussed and compared to the YBCO film films prepared by PLD. MOCVD thin films of YBCO show by STM a similar surface structure as the PLD YBCO films. Both are dominated by a growth hill morphology with unit cell steps of YBCO and screw dislocations. Figure 3.48 is a STM image of the surface of a YBCO MOCVD film on MgO(100). Due to tip-geometry induced limitations in resolution the SFM image of the same MOCVD film (see fig. 3.49) does not show as many details as the STM image.

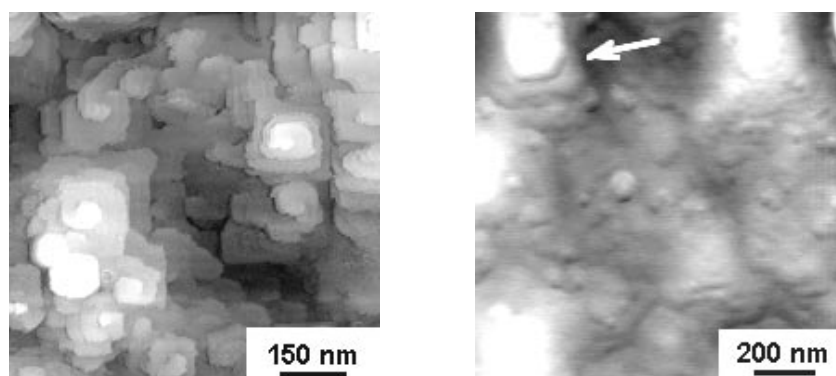


Figure 3.48: *LEFT:* STM image of the surface of a MOCVD YBCO thin film on MgO(100) showing the growth hill morphology with screw dislocations similar as observed on PLD YBCO films. The step height spacings are one unit cell in crystallographic c -direction.

Figure 3.49: *RIGHT:* SFM image acquired from the same MOCVD film. Due to the lower resolution capability of the SFM tip the image contrast is not as good as in the STM image. The white arrow indicates a growth step of one unit cell in height.

Depending on stoichiometry and substrate material the MOCVD films exhibit different surface structure [3.50]. This can be visualized by SFM on a micron scale. Figure 3.50 shows a MOCVD YBCO thin film on MgO(100). Its surface exhibits in addition to the growth hill structure displayed in figs. 3.48 and 3.49 some slab-like particles which are likely to be CuO needles. This matches well with the stoichiometry adjusted for this film. EDAX reveals that it is copper-rich.

A copper-deficient MOCVD YBCO film on a LaAlO₃ substrate is shown in the SFM image in figs. 3.51 and 3.52. Its surface structure is dominated by growth pits (holes **H**)

and some particulates. A closer view to the growth pits reveals that some needle-shaped particles are lying at the bottom of the growth pits. The orientation of the needles is along two directions perpendicular to each other. It is evident that these needles have impeded film growth at an initial stage. No complete YBCO terraces could be formed at locations where the needles were present. However, it remains unclear of what materials these needles are composed.⁵²

Very similar holes have been observed in STM images of PLD YBCO thin films on LaAlO_3 [3.42].

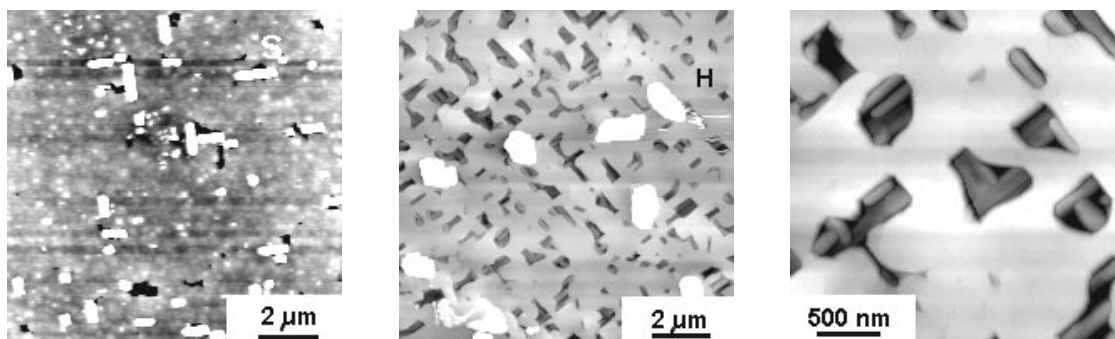


Figure 3.50: *LEFT:* SFM image of a copper-rich MOCVD YBCO thin film on MgO . Slab-like needles ('S') are found on the surface.

Figure 3.51: *MIDDLE:* SFM image of a copper-deficient MOCVD YBCO film on LaAlO_3 . Typical surface structures are particles and growth pits (holes **H**).

Figure 3.52: *RIGHT:* Detailed view of the holes in the same film by SFM. Each growth pit contains several needles (being aligned to two directions perpendicular to each other).

This growth pit morphology of copper-deficient MOCVD films is very similar to the one of PLD-grown YBCO films on LaAlO_3 . The STM images showed similar growth pits (section 3.2.3), but no needles were observed in the growth pits, presumably due to the fact that STM could not image the non-conducting needle material.

⁵²Probable suggestions would be that these needles consist of copper oxide or yttria.

3.6 YBCO thin films by thermal coevaporation (MBE)

Molecular beam epitaxy (MBE), or thermal coevaporation, is a further technique to prepare high quality films of various materials under well-defined preparation conditions. This technique has been applied even to very complex compounds such as YBCO 123.

The results presented in this chapter have been obtained by investigating thin film samples of YBCO prepared by thermal coevaporation at the Technical University of Munich (Germany) by F. Baudenbacher and K. Hirata from the research group of Prof. H. Kinder.

3.6.1 Film preparation

Films were deposited in a high vacuum evaporator using three resistively heated boats for Y, Ba and Cu metals [3.51, 3.52]. A quadrupol mass spectrometer measures the individual evaporation rates from the three boats and the output regulates a feedback connected to the boat heaters. A quartz crystal film thickness monitor oscillator is used to calibrate the quadrupol reading. Typical overall growth rates of the YBCO film is $2\text{\AA}/\text{s}$ yielding a thickness of 1200\AA . The substrate⁵³ is surrounded by an oven that heats the substrate by radiation. A typical substrate temperature is 650°C . A ring of small nozzles incorporated in the oven introduces molecular oxygen which is required to grow superconductive YBCO films. Differential pumping allows a pressure of $2\cdot 10^{-3}$ mbar at the substrate position and a base pressure of $2\cdot 10^{-5}$ mbar in the chamber. This allows the operation of a reflection high energy electron diffraction (RHEED) system for monitoring the film growth *in-situ*. Oxygenation of the film after deposition was done in 20 mbar of molecular oxygen.

3.6.2 Reflection high energy electron diffraction

The combination of MBE with reflection high energy electron diffraction (RHEED) is extremely powerful since the forward scattering geometry of RHEED permits measurement during the growth of the film. A fine beam of high energy electrons ($10 - 50\text{ keV}$)⁵⁴ is directed to the surface under investigation at a very small (grazing) angle of incidence in order to obtain a high surface sensitivity at a low penetration depth perpendicular to the surface. The cathode is on a negative high voltage potential, whereas the sample and the screen are on earth potential. The elastically scattered electrons are able to excite the screen without additional acceleration. The observed diffraction image is dominated by the elastically scattered electrons.⁵⁵ The intersection of the Ewald sphere with the screen determines the diffraction image. Figure 3.53 illustrates the RHEED setup: The incident electron beam is scattered elastically by the sample and generates a spot pattern

⁵³(100) faces of MgO or SrTiO₃ crystals.

⁵⁴Beam spot size is below 100 \AA .

⁵⁵Secondary electrons and inelastically scattered electrons have an energy too low to disturb the diffraction pattern on the screen.

on Laue circles⁵⁶ on the screen. The directly reflected spot is called specular beam and contributes the largest intensity.

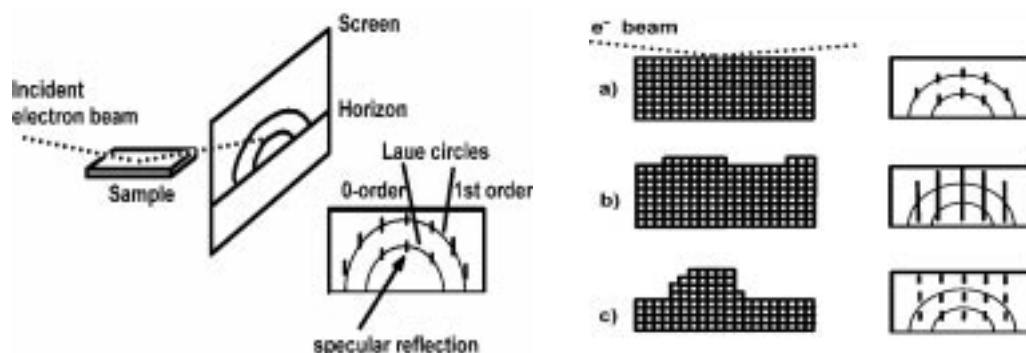


Figure 3.53: *LEFT:* Schematic of RHEED geometry: An electron beam is scattered elastically on a sample in grazing incidence. The diffracted intensity is recorded on a screen. For an ideally flat surface Laue spots are expected.

Figure 3.54: *RIGHT:* Different Laue patterns for different qualities of the surface: a) ideal flat surface yielding Laue spots, b) flat surface with monatomic steps or mosaic structure resulting in elongated spots or stripes, and c) surface with three-dimensional islands resulting in a transmission-type diffraction pattern

Only in case of a perfectly flat surface Laue spots are observed. In presence of a mosaic structure⁵⁷ within the excitation area of the electron beam the observed Laue spots are not circular but lengthy.⁵⁸ The same applies when the sample's surface is not atomically flat but shows unit cell steps on the surface. In case of three-dimensional islands on the sample's surface the diffraction pattern consists again of spots but they are not situated on the Laue circles expected for the (hk) reflections. Due to the increased roughness of the surface the intensity of the (hk) reflections is drastically reduced and the three-dimensional points in the reciprocal space dominate⁵⁹ and yield a diffraction image similar to one obtained by electron transmission of the sample. Figure 3.54 summarizes the three basic possibilities of RHEED patterns: a) ideal flat surface yielding Laue spots, b) flat surface with monatomic steps or mosaic structure resulting in elongated spots or stripes, and c) surface with three-dimensional islands resulting in a transmission-type

⁵⁶The Laue circles correspond to the section of planes of the reciprocal space with the screen. Due to the very special geometry of grazing incidence the information obtained on the direct space is more or less two-dimensional. Therefore only two-dimensional rods of the reciprocal space have to be taken into account (denoted (hk) reflections)

⁵⁷i.e. slightly tilted parts of the sample surface (fractions of a degree).

⁵⁸This is due to the finite thickness of the (hk) rods in the reciprocal space when intersected with the screen plane.

⁵⁹This is often also understood as transmission through the three-dimensional islands.

diffraction pattern [3.53].

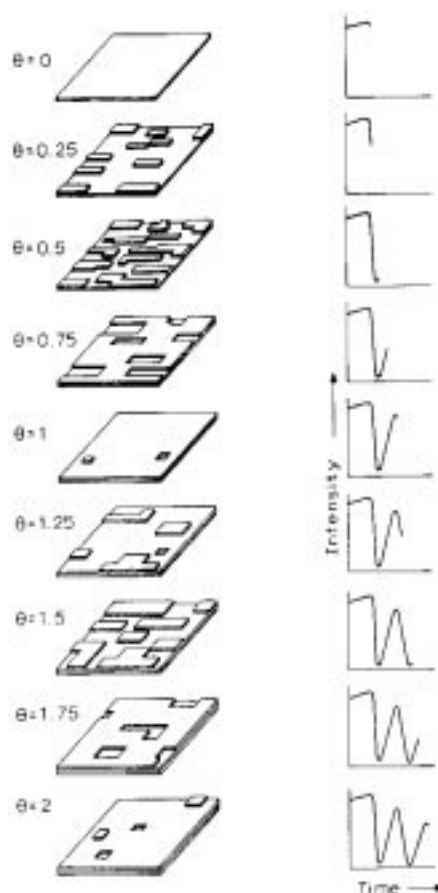


Figure 3.55: First-order growth model (two monolayers) in relation to the RHEED intensity behaviour (reproduced from the publication by *Joyce et al.*)

Due to its geometry the RHEED method can be performed during film growth giving direct insight into the growth mode.⁶⁰ By observation of the change of the intensity of the zero-order reflection (specular reflection) further information on growth is extracted. The fundamental paper by *Joyce et al.* [3.54] discusses this issue. The major aspects are summarized: Be assumed a perfect surface of a crystal: the RHEED pattern shows Laue spots. When growth commences two-dimensional nuclei are formed at random positions of the substrate's surface. The diffracted intensity (e.g. of the specular reflection) decreases due to an increase of diffuse scattering. In a single-scattering approximation⁶¹ this is reasonable since the De Broglie wavelength of the electrons is about 0.1 Å, which is

⁶⁰i.e. it can be determined directly whether the growth proceeds by the layer-by-layer mechanism or by the island growth mechanism. Transitions between the two modes may also be observed.

⁶¹Often also termed kinematic approximation.

well below of typical dimensions of steps on crystal surfaces (a few Ångstroms).⁶² Diffuse scattering is at a maximum at a half-layer coverage of the initially flat terrace. This yields to a minimum of the diffracted intensity. For a completed layer the diffracted intensity is at a maximum. This results in periodic oscillations of the diffracted intensity of the specular reflection with time. One period corresponds to the growth of a unit cell layer of material. Figure 3.55 illustrates the relation between monolayer coverage and intensity of the specular reflection [3.54].⁶³ The damping of the oscillations is understood as an gradual increase of monolayer roughness with increasing film thickness.⁶⁴

3.6.3 Scanning tunneling microscopy

3.6.3.1 YBCO thin film on MgO

RHEED oscillations have actually been observed by F. Baudenbacher, K. Hirata and H. Kinder from the Technical University of Munich in YBCO very thin films prepared by thermal co-evaporation [3.51, 3.52]. First the results obtained from a YBCO thin film on MgO with a thickness of 120 nm are presented [3.51, 3.55].

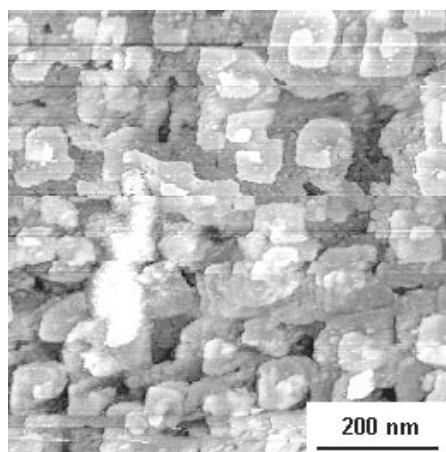


Figure 3.56: STM image of a YBCO thin film (120 nm) on MgO prepared by thermal co-evaporation showing a lot of growth hills with screw dislocations (about $10^{10}/\text{cm}^2$).

For the optimum stoichiometry of Y:Ba:Cu=1:2:3, the film appears to be totally smooth in SEM [3.55]. By STM the smooth surface is resolved to tiny growth hills with a screw dislocation located at the centre of each growth hill [3.55, 3.56]. The number density of screw dislocations is as high as $10^{10}/\text{cm}^2$ which is a decade more than the number

⁶²In case the wavelength is much smaller than the size of the scatterer, diffuse scattering is obtained.

⁶³A more detailed discussion would include diffraction as a multiple-scattering (dynamical) process. Please refer to the publication by Joyce for that issue.

⁶⁴For this reason the RHEED oscillations can only be observed up to a certain film thickness (for YBCO 10 monolayers, typically).

determined for the laser-deposited [3.21] or magnetron sputtered films [3.24]. Figure 3.56 demonstrates this high number density of screw dislocations observed.

3.6.3.2 YBCO ultrathin film on SrTiO₃

To take advantage of the RHEED facility ultrathin⁶⁵ films of YBCO have been grown on SrTiO₃ [3.56]. Figure 3.57 shows the RHEED pattern as photographed from the screen. The streaky nature of the pattern indicates that the surface of the YBCO film must be extremely smooth.⁶⁶ The intensity of the specular reflection (upper curve) and the background intensity (lower curve) versus time during the growth process is plotted in figure 3.58.

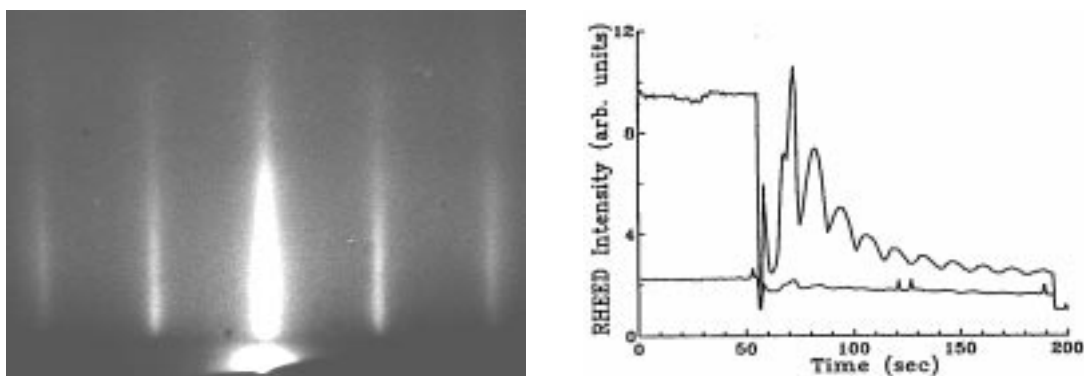


Figure 3.57: *LEFT:* Photograph of the RHEED screen showing a streaky pattern typical of two-dimensional layer-by-layer growth. The YBCO surface of this film sample is expected to show only small unit-cell-scale roughness.

Figure 3.58: *RIGHT:* Intensity of the specular reflection (upper curve) and background intensity (lower curve) as a function of time during the growth process of the YBCO film on SrTiO₃(100). Each of the oscillations corresponds to the formation of an additional monolayer. The growth was stopped after 10.5 monolayers. The oscillations are damped implying a weak, but gradual roughening of the surface.

This film is expected to exhibit flat terraces covered by a nominal half monolayer in form of monolayer islands. This is verified in the STM image acquired from this film (fig. 3.59). All steps in the image are of one unit cell height in crystallographic *c*-direction of YBCO. The brightness contrast (topographic height) reveals three levels of height. The darkest level is more or less covered totally by the next brighter level. Thus we tend to attribute the lowest level in the image to the RHEED oscillation number 9 which stands for the YBCO monolayer number 9. The almost complete terrace must be

⁶⁵'Ultrathin' shall mean in the following that the film thickness is only a few unit cells. This can be indicated very precisely since the growth is documented by the RHEED oscillations.

⁶⁶At least on the scale of the size of the electron beam which has only a diameter of 100 Ångstroms.

the one corresponding to the RHEED oscillation number 10. A half of a monolayer is characterized by the half RHEED oscillation number 11. The ratio of visible monolayers is most obviously demonstrated by looking at the (brightness/height distribution) histogram of the STM image. Two Gaussian peaks with almost equal areas under the peaks are observed in the histogram (fig. 3.60). This implies that the nominal coverage is 10 and a half monolayer (ML). Concluding the observed RHEED oscillations and the STM data give a consistent set of observations which clearly demonstrate the correctness of the interpretation of RHEED oscillations in YBCO films as growth of monolayer terraces.

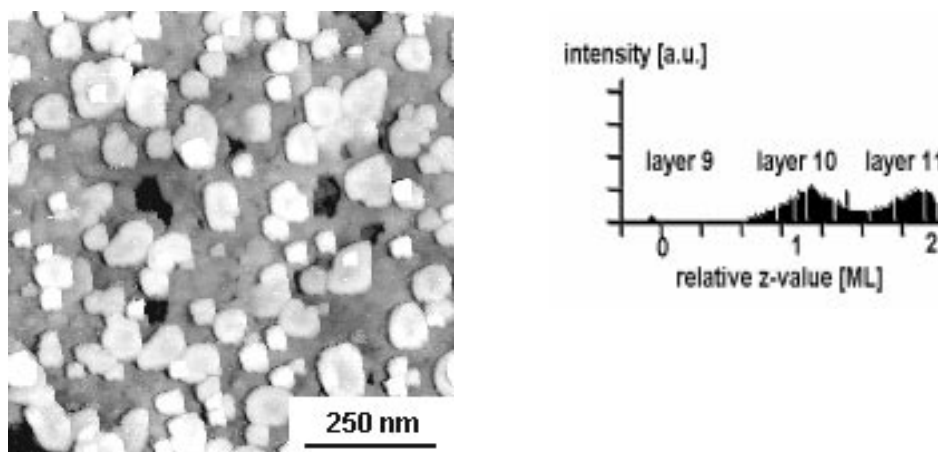


Figure 3.59: *LEFT:* STM image of the YBCO film on SrTiO_3 prepared by thermal co-evaporation as described above. The RHEED pattern and the RHEED oscillations shown above imply a nominal coverage of 10.5 ML. This is clearly observed in the STM image: the brighter (higher) layer (number 11) covers about 50 percent of the lower lying (darker) layer (number 10). All steps are unit cell steps (1.17 nm). Some holes in the terrace number 9 are observed.

Figure 3.60: *RIGHT:* Height (brightness) distribution in the STM image shown left. Two Gaussian peaks with almost the same areas under it represent the layers 10 and 11. Some intensity is due to the holes in layer number 9.

3.6.3.3 Influence of substrate tilt

Unfortunately things are more complicated. If the substrate is off-cut a certain angle it will exhibit a cascade of steps in the SPM images. A naive schematic view of this issue is shown in fig. 3.61. The miscut is assumed to be off the $\langle 100 \rangle$ directions. Over a lateral distance x , a height difference z occurs resulting in a stepped SrTiO_3 surface. The miscut angle is derived by $\alpha = \arctan(z/x)$. Buffered by some interface layer the YBCO film grows tilted by the same angle, but with an average terrace width that is three times larger than that of SrTiO_3 due to the tripled unit cell layer height of YBCO.

As an example fig. 3.62 demonstrates how a miscut substrate influences the growth of ultrathin YBCO films.⁶⁷

The image ($300 \text{ nm} \times 300 \text{ nm}$, i.e. $x = 300 \text{ nm}$) shows a cascade of 6 unit cell

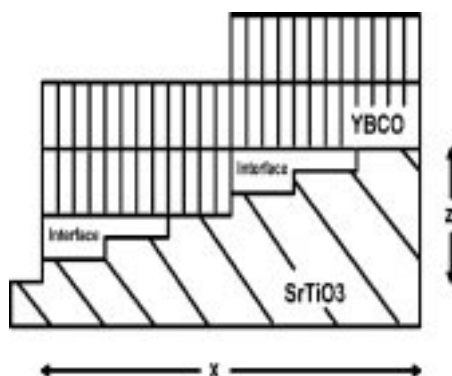


Figure 3.61: Model of the YBCO overgrowth on a miscut SrTiO_3 surface.

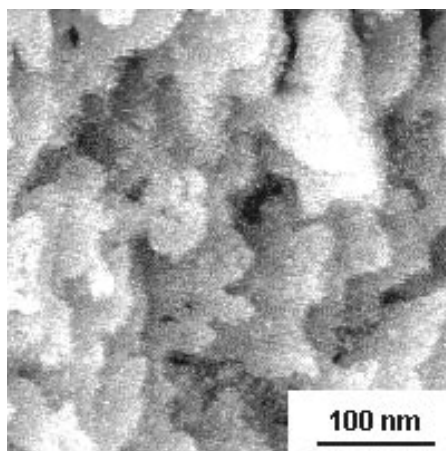


Figure 3.62: STM image of an ultrathin YBCO film on $\text{SrTiO}_3(100)$. The YBCO step cascade (6 unit cell steps or about 7 nm over a distance of 300 nm) implies a substrate miscut of 1.3° .

steps of YBCO (i.e. a height difference of about $z = 7 \text{ nm}$). This results in a miscut angle⁶⁸ $\alpha = \arctan(z/x) = 1.3^\circ$. This is to be compared to the specifications of the substrate manufacturers who indicate miscut angles of $0.5 - 1^\circ$ for the best substrates. Some substrates, of course, may be aligned more precisely to the (001) face. Concluding choice of substrates with excellent orientation is crucial for the study of the growth of ultrathin films by scanning force microscopy.

⁶⁷At a larger film thickness the substrate-induced tilt of the YBCO film is relaxed (probably by introducing defects like dislocations).

⁶⁸Assumed the substrate is only miscut along [100] or [010].

3.6.4 Comparing RHEED intensity with STM topography

By the use of specially selected⁶⁹ SrTiO₃ substrates with a very low miscut angle ultrathin YBCO films have been grown. The growth was monitored by observing the RHEED oscillations. Figure 3.63 shows a typical RHEED oscillation recording of YBCO growth on SrTiO₃. After opening the shutter that blocks the metal vapour beams some 'irregular' oscillations start followed by the regular oscillations related to YBCO unit cell growth. After 10 oscillations (or 10 YBCO layers) the shutter is closed again to stop the growth at the maximum of the RHEED intensity. After the shutter has been closed the RHEED intensity is increasing again due to thermal annealing of the YBCO film. The occurrence of irregular RHEED oscillations in the beginning of the YBCO growth process has been investigated by the Munich group [3.57] and is due to the growth of an interface consisting of Cu metal and CuO₂ particles which cause additional RHEED patterns. These patterns influence the recorded RHEED intensity and lead to the irregular oscillations.

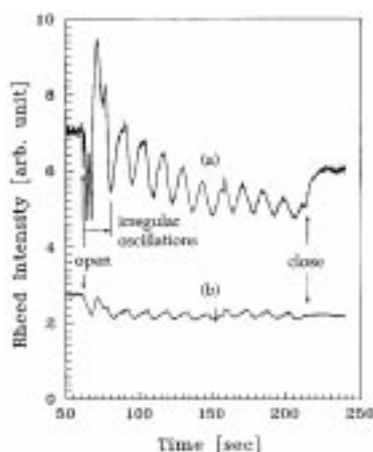


Figure 3.63: (a) Variation of the RHEED intensity of the specular beam with time during the growth of a YBCO ultrathin film on SrTiO₃ (upper curve). The growth was stopped at the maximum of the tenth oscillation. (b) The lower curve is the RHEED background intensity.

Two films of similar thickness (10 monolayers of YBCO) have been deposited on selected SrTiO₃ substrates having a very low miscut angle. The growth of one film has been stopped at a RHEED maximum to yield a nominally complete YBCO layer as film surface, the growth of the other film has been interrupted at a RHEED minimum in order to create a nominal coverage of a half monolayer on completed terraces. Scanning tunneling microscopy has been performed to demonstrate the difference in film morphology. Indeed, the STM image of the film preserved in the state of a RHEED maximum reveals a complete terrace (fig. 3.64), whereas the image of the film with a growth stop at a

⁶⁹X-ray diffraction in a four-circle diffractometer was used to select substrates with a miscut angle of below 0.15°.

RHEED minimum exhibits numerous small islands yielding a half monolayer coverage (fig. 3.65).

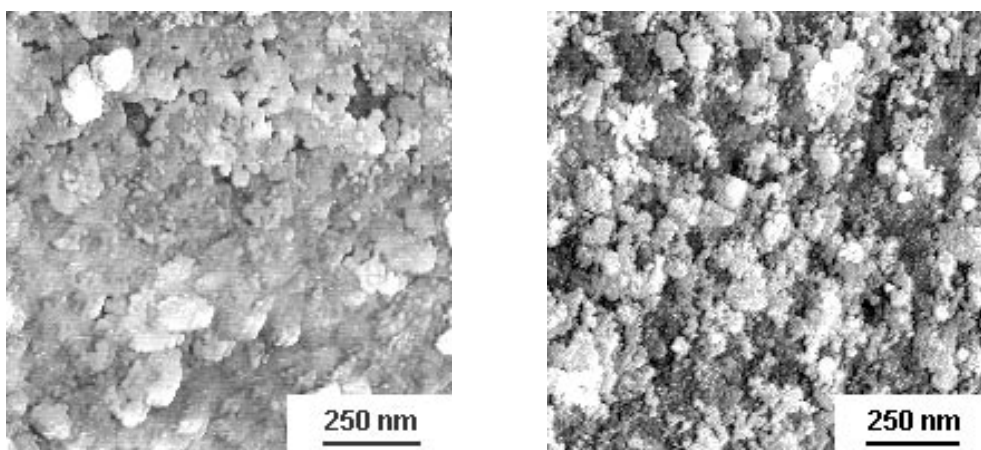


Figure 3.64: *LEFT:* STM image of a YBCO film on SrTiO₃ with growth stop at the maximum of a RHEED oscillation (complete layer).

Figure 3.65: *RIGHT:* STM image of a YBCO film on SrTiO₃ with a growth stop at a minimum of a RHEED oscillation (many small islands).

3.6.5 Conclusion

Thermal co-evaporation of Y, Ba and Cu metals and subsequent oxygenation is a method to grow high-quality YBCO thin films with accurate control of the growth rates of the individual components. Films of a thickness of about 120 nm show a similar morphology by STM as films prepared by magnetron-sputtering, pulsed laser deposition or metalorganic chemical vapour deposition: in all cases a typical growth hill morphology is found, sometimes with a screw dislocation at the centre of each growth hill. For the MBE films very tiny growth hills have been observed which may be related to the low growth temperature and growth rate in MBE. The simultaneous recording of the RHEED intensity during growth allows to characterize ultrathin films of only a few monolayers of YBCO in thickness. Intentional stop of growth of ultrathin films at a maximum or a minimum of the RHEED oscillation intensity results in films with completed terraces or half-covered terraces. The corresponding STM images verify the interpretation of RHEED oscillations as growth of individual monolayers of YBCO very impressively.

3.7 MXPS investigations of YBCO thin films

3.7.1 Atomic resolution on YBCO

In this section the atomic surface of YBCO is reconsidered. Early STM observations of an atomic lattice with a lattice constant of 0.38 nm have been reported by *L.E.C. van Leemput et al.* [3.58] in 1988 in YBCO 123 single crystals. Since the resolution was better in one direction he concluded to have imaged the CuO chain layer. The STM observation of two different, approximately square atomic lattices with lattice constants of 0.38 nm and 0.27 nm as presented in this thesis, has raised new questions concerning the interpretation of atomically resolved STM data on YBCO surfaces. Atomic lattices with lattice constants of 0.38 nm and 0.27 nm are observed for YBCO 123, 247 and 124 single crystals [3.59] and YBCO 123 thin films [3.60, 3.61]. As an example, atomically resolved YBCO 123 thin film surfaces are shown in fig. 3.66.

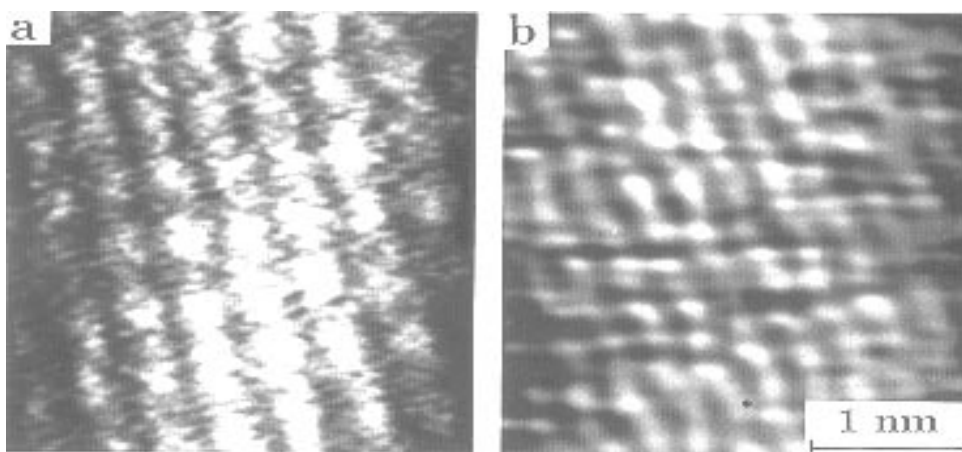


Figure 3.66: Atomic resolution STM images ($3 \times 3 \text{ nm}^2$) of a laser-deposited YBCO thin film. (a) Approximately square surface lattice with 0.38 nm spacings corresponding to *a*- or *b*-axis lengths of the YBCO unit cell. Corrugation amplitudes (peak to peak) between 0.04 and 0.1 nm. Tunneling current $I_t = 0.29 \text{ nA}$, tip bias voltage $U_s = +179 \text{ mV}$ (constant current image). (b) Atomic surface lattice with 0.27 nm spacings corresponding to the O(2)-O(3) distance. Tunneling current 0.9 nA, tip bias voltage +600 mV (constant height image).

For an interpretation the unit cell of YBCO 123 should be examined again (fig. 3.67). Some unit cells viewed from the [100] direction are shown in stereographic representation in fig. 3.68. The (001) surface which in being investigated here is displayed as a stereo image in fig. 3.69.

3.7.2 Interpretation based on STM data

Both atomic lattices can be imaged consecutively by variation of tunneling bias voltage. No surface damage was observed after atomic resolution imaging. Similar atomic ar-

rangements on surfaces of $Y_2Ba_4Cu_{6+n}O_{14+n}$, $n=0,1,2$, single crystals are observed [3.59].

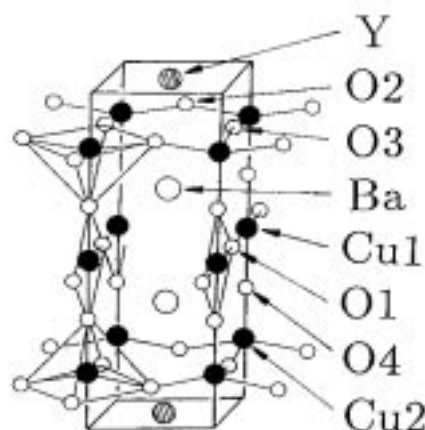


Figure 3.67: Model of the $Y_1Ba_2Cu_3O_7$ unit cell. The labels indicate atomic species.

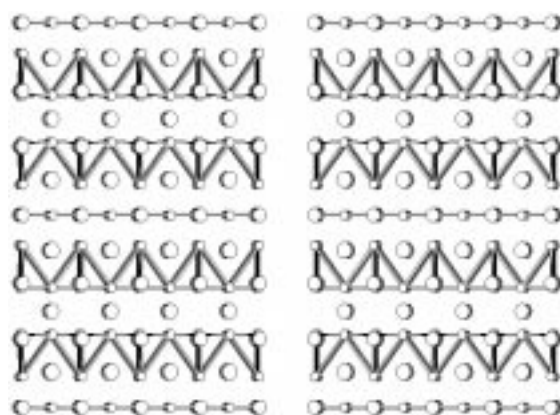


Figure 3.68: Stereographic projection of $4 \times 4 \times 2$ YBCO 123 unit cells (viewing direction along $[100]$). The layers are the following (from top to bottom): CuO chains, Ba-O, CuO_2 planes (pyramids), Y layer, CuO_2 planes (pyramids), Ba-O, CuO-chains, Ba-O, CuO_2 planes, Y layer, CuO_2 planes, Ba-O, CuO-chains. Oxygen atoms are displayed smaller than the metal atoms. Note the wiggled surface of the CuO_2 planes which is due to the shift of oxygen atoms off the plane of the Cu atoms (the shift about 0.3 \AA).

Up to now, atomic resolution has only been achieved in step-free areas⁷⁰ on the YBCO surface. Comparing the observed distances of 0.38 and 0.27 nm with the model of the unit cell of YBCO (fig. 3.67) it is possible to attribute the 0.38 nm spacing to several different atomic species: Y-Y in the yttrium layers, Cu(1)-Cu(1) and O(1)-O(1) in the Cu-O chains, Cu(2)-Cu(2) in the Cu- O_2 layers, or Ba-Ba and O(4)-O(4) in the Ba-O

⁷⁰Up to now, it was not possible to obtain atomic resolution across YBCO steps.

layers. However, the second square atomic arrangement with a spacing of 0.27 nm can be unambiguously attributed to the O(2)-O(3) spacing in the Cu-O₂ layers.⁷¹ Based on this definite assignment, the 0.38 nm spacing is likely to correspond to the Cu(2), Ba, O(4) or Y arrangement. However, reconstruction of the YBCO surface as suggested by *Frank et al.* [3.62] cannot be excluded. Their suggestion is based on a quantitative angle-resolved X-ray photoemission spectroscopy study in vacuum. They conclude that YBCO is terminated by an approximately 1 nm thick insulating layer containing a Ba-O layer and parts of the Cu-O chains.

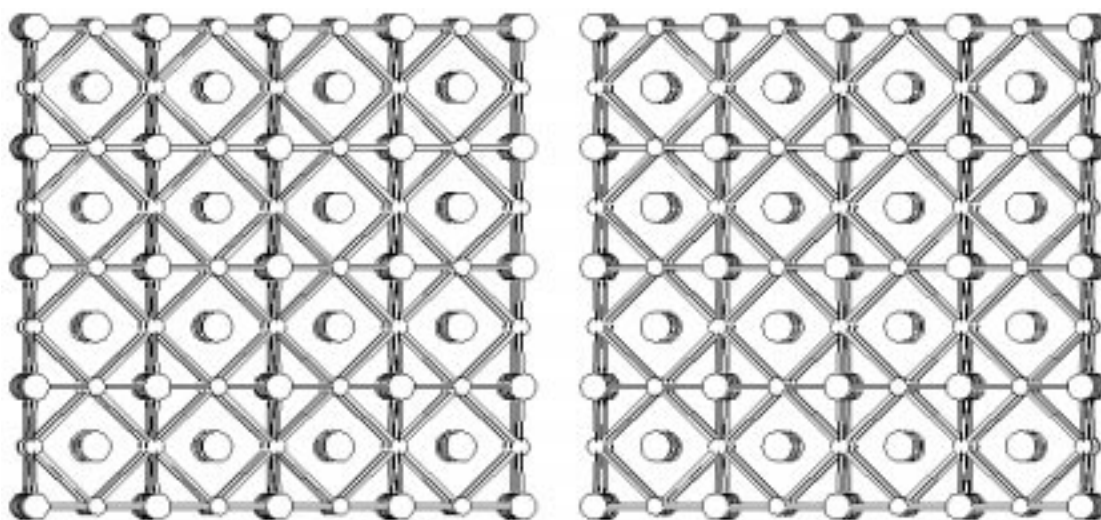


Figure 3.69: Stereo image of the (001) surface of YBCO 123: The mesh with a smaller lattice constant (0.27 nm) is built up of the CuO₂ pyramids. The lattice with a lattice constant of 0.38 nm consists of the *a*- and *b*-axis framework (metal atoms, oxygen atoms in the BaO plane).

The two observed atomic arrangements agree with the photoemission study [3.62], if it is assumed that the 0.27 nm spacing actually corresponds to the O(2)-O(3) distance in the Cu-O₂ layer and the 0.38 nm spacing is attributed - for reasons of similar tunneling probabilities from different oxygen states - to the O(4)-O(4) distance in the Ba-O layer. In addition, resonant tunneling processes [3.63] are a different possible explanation for the STM observation of atomic arrangements in YBCO. Proposed experiments required to clarify the question of the terminating layer of YBCO are for example inelastic ion scattering spectroscopy or high-accuracy quantitative X-ray photoelectron spectroscopy.

⁷¹It may be objected that for example the Ba-O plane contains the 0.27 nm distance as well. Although this is true, the 0.27 nm distance is the spacing between a barium and an oxygen atom. In STM barium and oxygen atoms exhibit a different density of states at the Fermi edge. This would imply a different appearance of the barium and oxygen atoms in STM images, which was not observed. For that reason the 0.27 nm lattice is expected to consist of one species of atoms. It should therefore be assigned to the O(2)-O(3) distance.

3.7.3 X-ray photoelectron spectroscopy

Angle-resolved X-ray photoelectron spectroscopy (AR-XPS) using monochromatized⁷² Al K_{α} radiation (energy: 1486.6 eV) was performed to obtain chemical information on the nature of the topmost layer of YBCO thin films. The experiments have been performed in the ESCALAB 210 spectrometer⁷³ of the Basel ESCA group.⁷⁴

The energy resolution of the instrument is 0.6 eV FWHM using a 150 mm (radius) hemispherical energy analyzer and a quartz crystal monochromator. The angular acceptance has been chosen $\pm 12^{\circ}$ for 0° incidence relative to the sample's surface normal and $\pm 3^{\circ}$ for 70° incidence. A multi-channel detection allows to acquire 5 energy channels simultaneously resulting in a reduction of measuring time by a factor of 5. To my knowledge this is the first angle resolved study of the surface on high quality YBCO thin films performed with monochromatized XPS.

3.7.4 Previous studies of YBCO by XPS

Several studies of the surface of YBCO are reported in literature by *Frank et al.* [3.64], *Aarnink et al.* [3.65] and *Behner et al.* [3.66]. In summary, most of the studies identify the Ba-O layer (with underlying Cu-O chain layer) as the surface layers of YBCO (see fig. 3.70). *Aarnink et al.* [3.65] can not exclude an amorphous surface layer of YBCO consisting of barium, copper, carbon and oxygen. A problem with the YBCO films used by *Frank et al.* [3.64] is the fact that the surface of the films is covered by 8-20 % by particles, outgrowths and droplets [3.64], which are not of the same chemical composition as the underlying YBCO film.⁷⁵ All films except those by *Behner et al.* [3.66] have been prepared outside the XPS-UHV chamber and are air-exposed. The films prepared *in-situ* by *Behner et al.* [3.66] show no traces of carbon at the surface. The aging process of the films upon exposure to the ambient for defined periods of time is clearly demonstrated in the publication by *Behner et al.* [3.66].

3.7.5 Angle-resolved photoemission

This section briefly introduces the technique of X-ray photoelectron spectroscopy (XPS). X-ray radiation from a X-ray tube is monochromatized by a quartz single crystal monochromator and directed to the sample (see fig. 3.71). A detector aligned at a well-defined

⁷²This is of special importance to avoid satellite peaks which may contribute up to 10 % of the signal. Using monochromatized radiation the background is much smaller and quantifying the spectra is much more reliable (accurate integration of peak area is possible).

⁷³Fisons, VG Instruments.

⁷⁴In this context I would like to thank H.-G. Boyen and P. Oelhafen for the realization of this study and the many helpful discussions.

⁷⁵The particles, outgrowths and droplets are reported to be richer in CuO compared to the YBCO matrix as determined by EDAX.

angle with respect to the sample's surface normal collects the photoelectrons being generated by the X-ray photons and analyzes the kinetic energy.

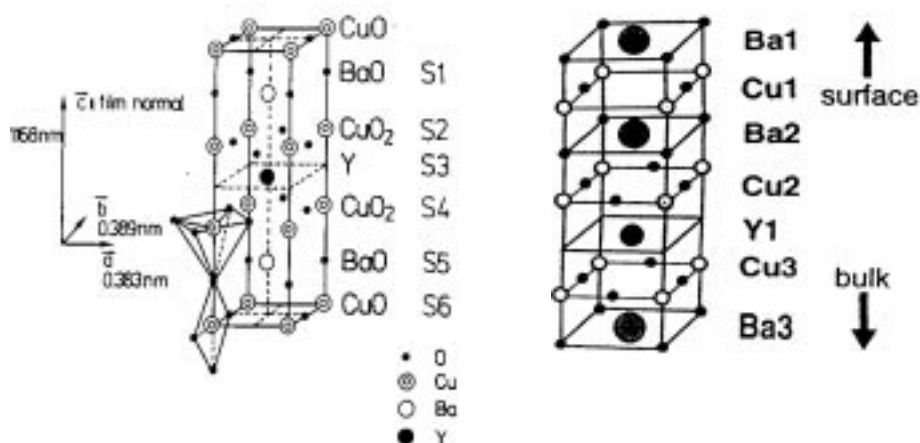


Figure 3.70: Unit cell models of $\text{YBa}_2\text{Cu}_3\text{O}_7$ summarizing the results of the XPS studies by *Frank et al.* (left) and *Behner et al.* (right).

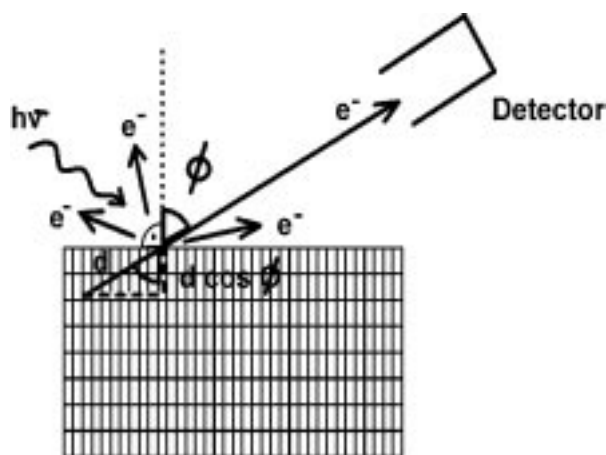


Figure 3.71: Schematic of the X-ray photoemission spectroscopy experiment (XPS): X-ray radiation with the energy $h\nu$ excites photoelectrons originating from a depth d of the sample. A detector collects the photoelectrons and analyzes them according to the kinetic energy. Tilting the sample off its surface normal by an angle Φ reduces the information depth to $d \cos \Phi$.

Although the penetration depth of the X-ray radiation is a few micrometre the photoelectrons are only able to pass a small part of the sample (only a few monolayers). For that reason the information obtained by XPS is based on the very topmost atomic surface layers. Under a detection direction normal to the sample's surface the information originates from a depth d . When enlarging the angle between the sample's surface normal

and the detector, the information depth is reduced to $d \cos \Phi$ (Φ being the angle between the sample's surface normal and the detector). This allows to investigate the chemical composition of the topmost surface layers of the sample. For that reason angle-resolved MXPS was chosen as a method to determine the nature of the topmost surface layer of YBCO. The setup of the angle-resolved XPS experiment is shown in fig. 3.72.

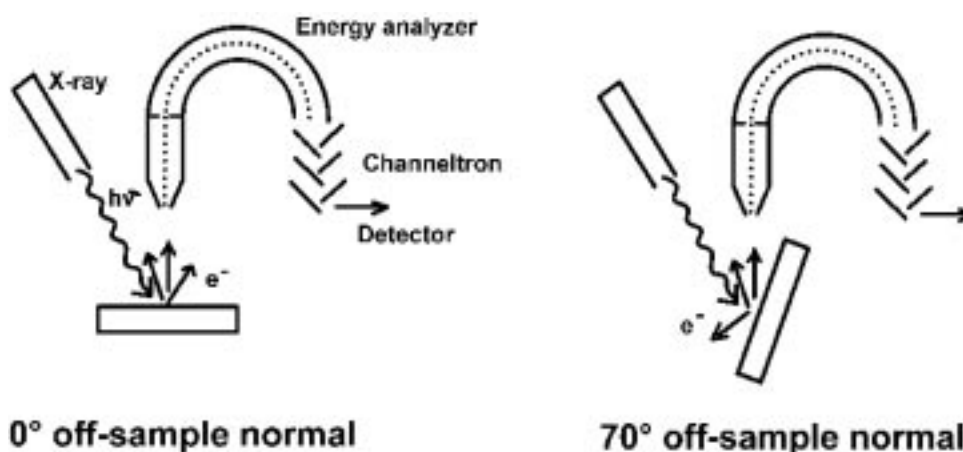


Figure 3.72: Schematic view of the angle resolved XPS experiment at two angles (0° and 70° off the sample's surface normal). The collected photoelectrons are analyzed in terms of the kinetic energy. Using the known X-ray radiation energy the binding energy of the atoms responsible for the photoelectron can be determined and therewith the elements involved in the surface.

The surface sensitivity of (angular-resolved) photoelectron spectroscopy has been accurately studied and modeled in a publication by Seah and Dench [3.68]. The information depth of most photoemission data follows a general curve displayed in fig. 3.73. Information from a specific elemental state is directly connected to a certain information depth λ . For inorganic compounds this relation is as follows:

$$\lambda = 2170/E^2 + 0.72\sqrt{aE}. \quad (3.3)$$

The information depth is in monolayers with a denoting the thickness of one monolayer, and E denoting the kinetic energy of the photoelectrons. The given example assumes a monolayer thickness $a = 0.2$ nm which is the typical thickness of an atomic layer in YBCO.⁷⁶ The bold lines indicate the elements present in the YBCO compound and the corresponding kinetic energies. The majority of the photoelectrons is emitted from a layer of a thickness of about 10 nm. At an angle of 70° between detection direction and sample's surface normal the information depth is below 2 nm allowing the discussion of the chemical nature of the YBCO surface layer.

⁷⁶Six such layers form the unit of YBCO: BaO, CuO₂, Y, CuO₂, BaO, CuO.

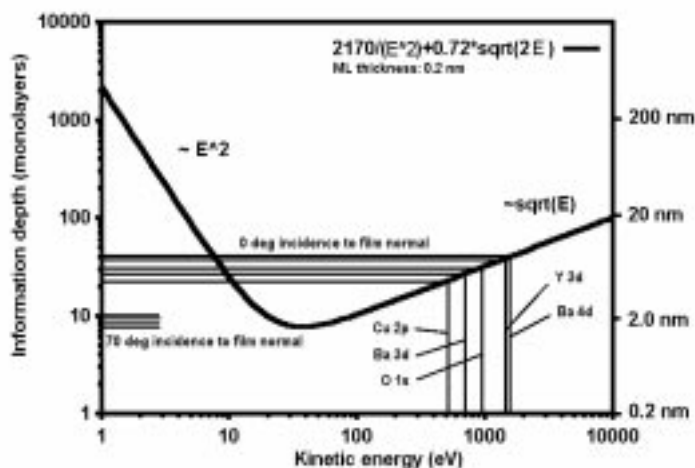


Figure 3.73: Double logarithmic Seah-Dench plot calculated for a monolayer thickness of 0.2 nm. According to the kinetic energy of the electrons the information originates from different depths (typical information depths of the elements in question are indicated). At 70° incidence to the film normal the surface sensitivity is about 10 times higher.

3.7.6 Two YBCO thin films for MXPS investigations

This section presents two YBCO thin film samples of a different quality. The first sample, 'Y1', has been stored for several months in an argon filled glass tube without desiccative

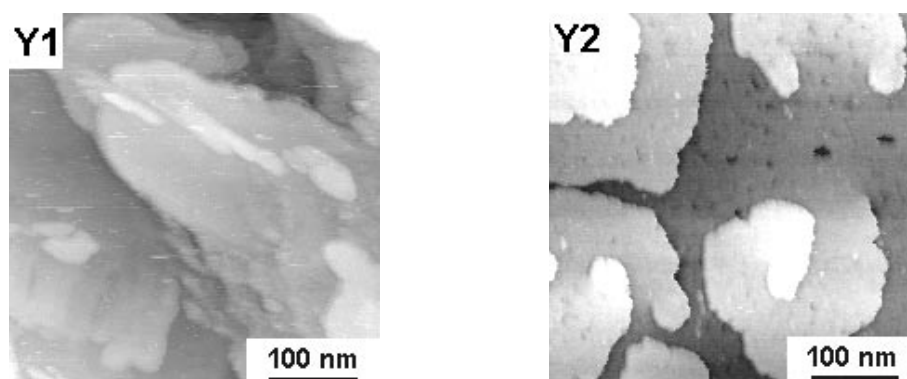


Figure 3.74: *LEFT:* STM image of an aged YBCO film ('Y1') investigated to demonstrate deterioration effects. The investigation by XPS will show that this is due to a contamination layer of hydrocarbons and barium carbonate. *RIGHT:* STM image of a fresh YBCO thin film ('Y2') showing clear step patterns. The XPS investigation will show that almost no barium carbonate contamination layer is present.

material. The other sample, 'Y2', is freshly prepared and protected by silica gel. Both samples have been subjected to an investigation by STM. Even if sample 'Y1' exhibits step patterns the surface seems to be contaminated. The step edges are not resolved clearly and appear fuzzy (see fig. 3.74, left). Sample 'Y2', on the other hand, exhibits clear step patterns and screw dislocations (see fig. 3.74, right).

Monochromatic XPS in UHV reveals the presence of Y, Ba, Cu, O and C on the surface of sample 'Y2'. The survey spectrum at a detector angle of 0° with respect to the sample's surface normal is shown in fig. 3.75. In the following high resolution spectra (resolution about 0.6 eV) of the individual photoemission peaks of both samples 'Y1' and 'Y2' will be discussed.

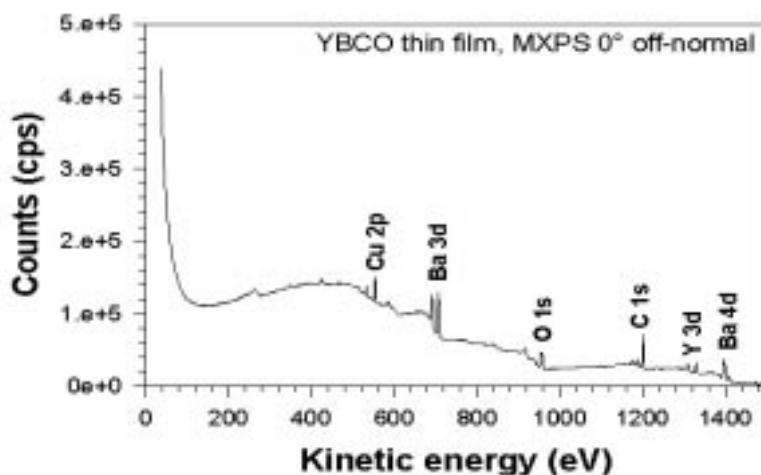


Figure 3.75: MXPS Al K_α spectrum (energy of the radiation: 1486.6 eV) of sample 'Y2'. The presence of several peaks allows the chemical analysis of the sample's surface. Peaks of Cu 2p, Ba 3d, O 1s, C 1s, Y 3d and Ba 4d are labelled.

High resolution MXPS spectra — at $\Phi = 0^\circ$ relative to the sample's surface normal — of the Ba 3d and Ba 4d states are shown in figs. 3.76 and 3.77. The cleaner sample 'Y2' shows two barium components distinguished by a difference in binding energies. The contaminated sample 'Y1' is dominated by a single barium component. The interpretation is simplified by studying the corresponding C 1s spectra of the two samples (fig. 3.78). Whereas the contaminated sample 'Y1' shows carbon peaks at two different binding energies the cleaner sample 'Y2' exhibits mainly one component. A comparison with literature (e.g. *Behner et al.* [3.66]) suggests that the component at a higher binding energy⁷⁷ is due to carbonate formation, and the component of lower binding energy

⁷⁷Since the binding energy is the energy of the radiation (1486.6 eV) minus the kinetic energy, the binding energy is at the left end of the abscissa. The spectra of kinetic and binding energy look the same but the axes are labelled differently.

(i.e. the right component) is attributed to pure carbon or, more probably, a layer of hydrocarbons since hydrogen can not be detected in photoemission spectroscopy. This means the aged sample ('Y1') has suffered from a contamination layer formed by barium carbonate and by a layer of hydrocarbons. Direct comparison of the integrated peak intensities of the barium and carbon peaks by assuming a barium surface covered by a hydrocarbon layer has shown that the hydrocarbon contamination layer must be as thick as approximately 20 monolayers of carbon. This sounds quite a lot, but it should be kept in mind that all air-exposed samples will be immediately covered by a hydrocarbon layer. Removing this layer in UHV by heating and ion-sputtering is possible, but preferential sputtering of the YBCO surface may occur and affect the analysis of the topmost layer of YBCO. In STM this non-conducting hydrocarbon layer does not seem to disturb strongly the images, probably it is simply pushed away while scanning. In photoemission, however, this hydrocarbon layer just reduces the measured peak intensities of the other elements by acting as a transparent layer with an extinction coefficient. This does implicitly *not* affect the elemental ratios of Y:Ba:Cu at the surface of the YBCO film.

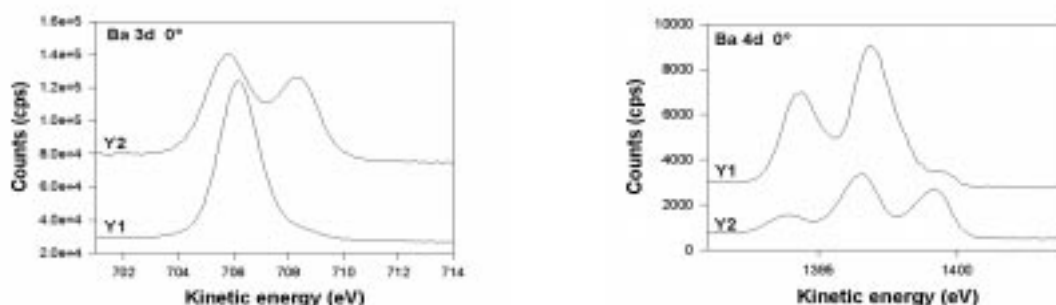


Figure 3.76: *LEFT:* High resolution MXPS spectrum of the Ba 3d 5/2 peak at $\Phi = 0^\circ$. Whereas the contaminated sample 'Y1' mainly shows a single barium component, the clean sample exhibits two different barium components. This finding is in agreement with other authors, e.g. *Behner et al.*

Figure 3.77: *RIGHT:* MXPS of the Ba 4d 3/2 (left) and 5/2 (right) doublet. Again, sample 'Y2' exhibits two barium components (each a doublet) with different binding energies implying barium in two different chemical environments. Sample 'Y1' however, solely shows one strong doublet component.

Analysis of the Cu 2p 3/2 states shows (see fig. 3.79) very similar MXPS spectra of both the aged and clean samples implying that surface reactions do not proceed via formation of different carbon compounds. The Cu 2p 3/2 state is splitted into two components (a weak and broad feature at lower kinetic energy and a sharp and clear feature at higher kinetic energy). The left component has been assigned to the copper in the Cu-O chains (see for example: *Frank et al.*, [3.64]), whereas the other is interpreted as the copper state in the superconductive Cu-O₂ planes. The presence of both components

at normal incidence reflects the bulk of YBCO.

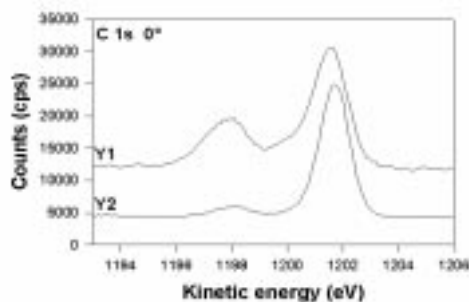


Figure 3.78: MXPS spectra of C 1s in samples 'Y1' and 'Y2'. The aged sample 'Y1' exhibits two carbon components. A component at higher binding energy (lower kinetic energy, left peak) typical of carbonates, and a component of lower binding energy (right peak) attributed to pure carbon or hydrocarbons. The cleaner sample 'Y2' exhibits mostly the hydrocarbon component.

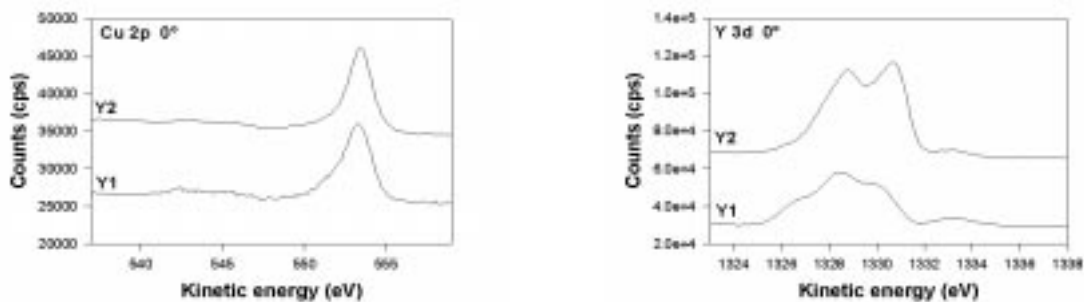


Figure 3.79: *LEFT:* High resolution MXPS spectrum of the Cu 2p 3/2 peak at $\Phi = 0^\circ$. Two components are observed: a broad and weak peak (left) being caused by the copper in the Cu-O chains, and a intense peak originating from the copper in the CuO₂ planes. The aged ('Y1') and the clean ('Y2') sample do not differ very much.

Figure 3.80: *RIGHT:* MXPS of the Y 3d 3/2 (left) and 5/2 (right) doublet. Slight differences between the aged and the clean film are observed implying some reactive Y interface.

The Y 3d states which are a doublet of Y 3d 3/2 and Y 3d 5/2 is found to change slightly by comparing the spectra obtained from the aged and the clean sample. This might imply some reactive Y at the interface to the contamination layer (see fig. 3.80).

The last element to be discussed is oxygen. The MXPS spectrum reveals two O 1s

components (two chemical sites) in the cleaner sample 'Y2', whereas one component is dominating in case of the aged sample 'Y1' (see fig. 3.81). Summarizing the observations of differences between the aged and the clean sample, it can be stated that reactions involve mainly the elements barium, carbon and oxygen. This is compatible with the general observation of barium carbonate and barium hydroxide formation at the surface of YBCO on being exposed to humid air.

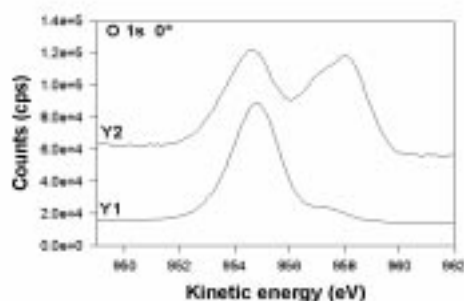


Figure 3.81: MXPS spectra of O 1s. The fresh sample 'Y2' shows two oxygen components whereas one of them is strongly suppressed in the aged sample 'Y1'. Thus the reactive interface involves oxygen as well.

3.7.7 Determination of the YBCO toplayer

This last section discusses the results obtained by angle-resolved photoemission spectroscopy in order to interpret the STM observation of two different surface lattices with lattice constants of 0.38 nm and 0.27 nm.

First, the MXPS spectra of the Ba 3d 5/2 (fig. 3.82) and Ba 4d 3/2, 5/2 states (fig. 3.83) are shown.

Since from the two components of the Ba 3d 5/2 spectrum observed at $\Phi = 0^\circ$ only one component is found at $\Phi = 70^\circ$, the peaks may be separated in bulk components 'b' and surface components 's'. The peaks are fitted to a Gaussian shape using the background subtraction method introduced by Shirley [3.67]. If a surface component is observed at $\Phi = 70^\circ$, this element is part of the topmost surface layers of YBCO. The same behaviour is also found on analyzing the Ba 4d 5/2, 3/2 doublet (see fig. 3.83). As conclusion from the barium spectra it is evident that barium is part of the surface layer.

The Y 3d 5/2, 3/2 doublet is shown in fig. 3.84. One component seems to be sufficient to explain the spectrum at $\Phi = 0^\circ$. At the surface-sensitive angle $\Phi = 70^\circ$ no appreciable yttrium intensity is found indicating that yttrium is *not* part of the topmost surface layer of YBCO.

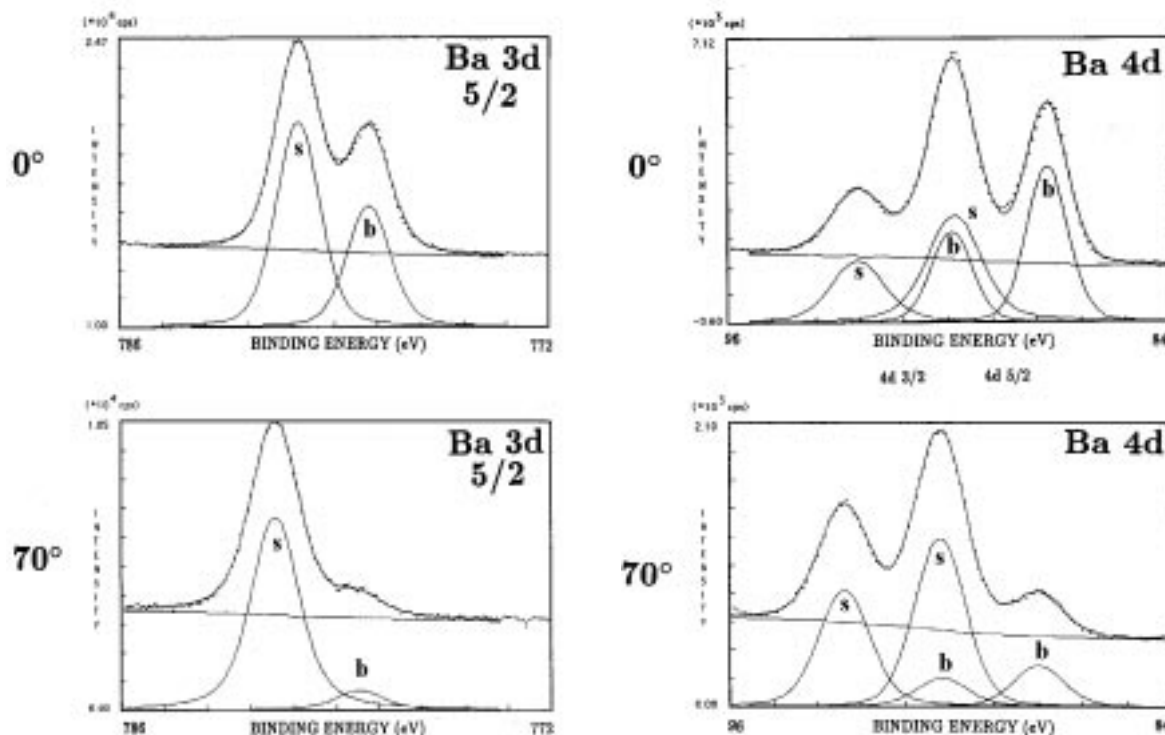


Figure 3.82: *LEFT:* High resolution MXPS spectrum of the Ba 3d 5/2 peak at $\Phi = 0^\circ$ (upper spectrum) and $\Phi = 70^\circ$ (lower spectrum). The spectrum is fitted using two barium components (labelled 's' and 'b'). At $\Phi = 70^\circ$ the bulk component 'b' vanishes implying the existence of a barium surface component 's'. This implies barium is present in the topmost layers of YBCO.

Figure 3.83: *RIGHT:* Ba 4d 3/2 (higher binding energy) and 5/2 (lower binding energy) doublet. Both surface and a bulk components are observed.

The Cu 2p 3/2 state is split up (as previously mentioned) in a copper peak originating from the copper oxide chains (left, broad peak in fig. 3.85) and a peak caused by the CuO₂ planes (right, sharp peak). Both peaks are observed in the $\Phi = 0^\circ$ spectrum, but the Cu-O chain feature is absent in the $\Phi = 70^\circ$ spectrum. This observation indicates that the surface layer of YBCO incorporates the CuO₂ plane layer and *not the Cu-O chain layer*, as it has been suggested in previous studies by others ([3.64] – [3.66]).

This result is of special importance since it is fully compatible with the observation of two atomic surface lattices with lattice constants of 0.38 nm and 0.27 nm by STM. Thus the interpretation of the STM data with the help of the AR-MXPS data is as following:

- The 0.27 nm square atomic lattice is the oxygen arrangement of O(2)-O(3) in the CuO_2 plane.
- The 0.38 nm square atomic lattice is the O(4) arrangement of the Ba atom arrangement in the Ba-O plane.

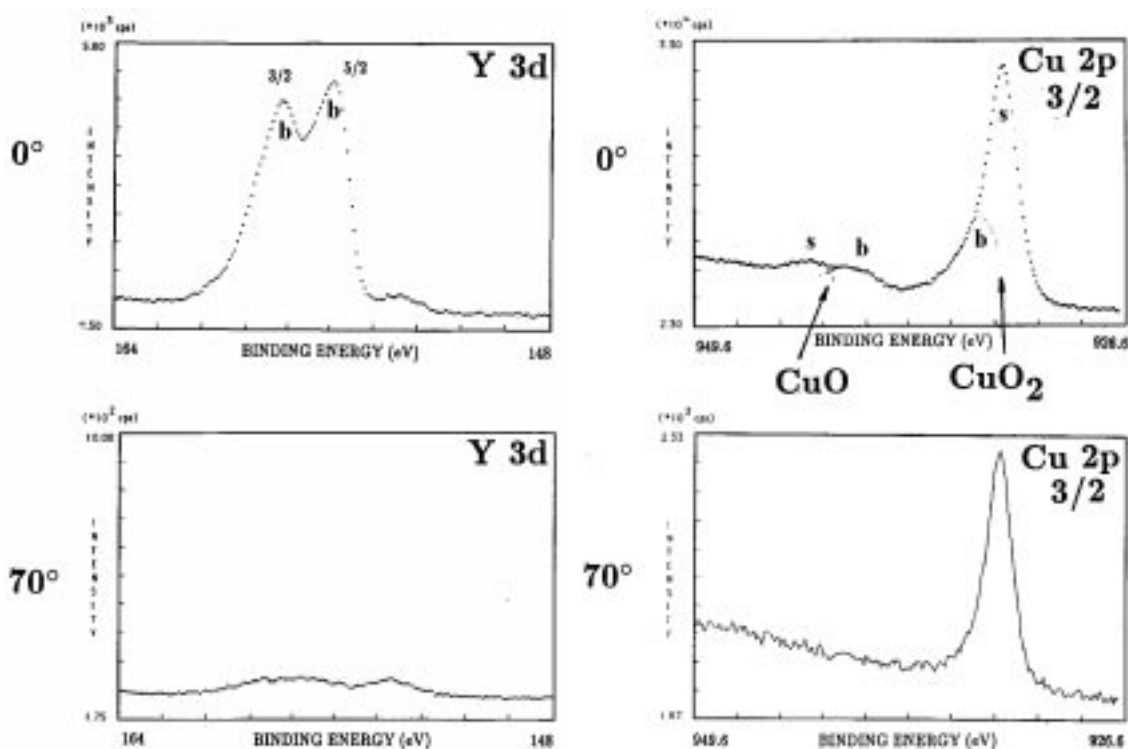


Figure 3.84: *LEFT:* High resolution MXPS spectrum of the Y 3d 3/2 (left peak) and 5/2 (right peak) doublet. Since both peaks vanish in the $\Phi = 70^\circ$ spectrum yttrium is not part of the surface.

Figure 3.85: *RIGHT:* High resolution MXPS spectrum of the Cu 2p 3/2 states. At $\Phi = 0^\circ$ (upper spectrum) a Cu-O chain component (left) and a CuO_2 plane component are observed (right). At $\Phi = 70^\circ$, however, only the component attributed to CuO_2 plane is present implying the absence of Cu-O chain features at the surface of particle-free YBCO films.

The suggested layer sequence of YBCO is displayed in fig. 3.86. The YBCO surface is terminated by a CuO_2 and a Ba-O layer.

To complete this section the O 1s and C 1s spectra are shown in figs. 3.87 and 3.88. The O 1s data exhibits at $\Phi = 0^\circ$ four components attributed to surface and bulk peaks of two oxygen species. At $\Phi = 70^\circ$ one oxygen species is suppressed. It should be added that the relative intensity of the individual peaks has changed implying a more complex situation in case of the oxygen distribution.

The C 1s spectrum shows at $\Phi = 0^\circ$ two components previously attributed to the carbonate contribution (left peak) and the hydrocarbon contribution (right peak). At $\Phi = 70^\circ$ only the hydrocarbon peak is left implying carbonate formation is a bulk effect.

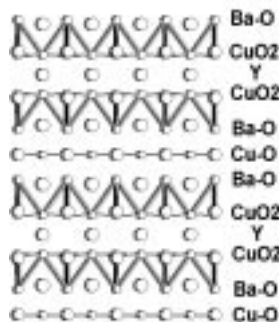


Figure 3.86: Suggested layer sequence of YBCO based on scanning tunneling microscopy and angle-resolved X-ray photoelectron spectroscopy.

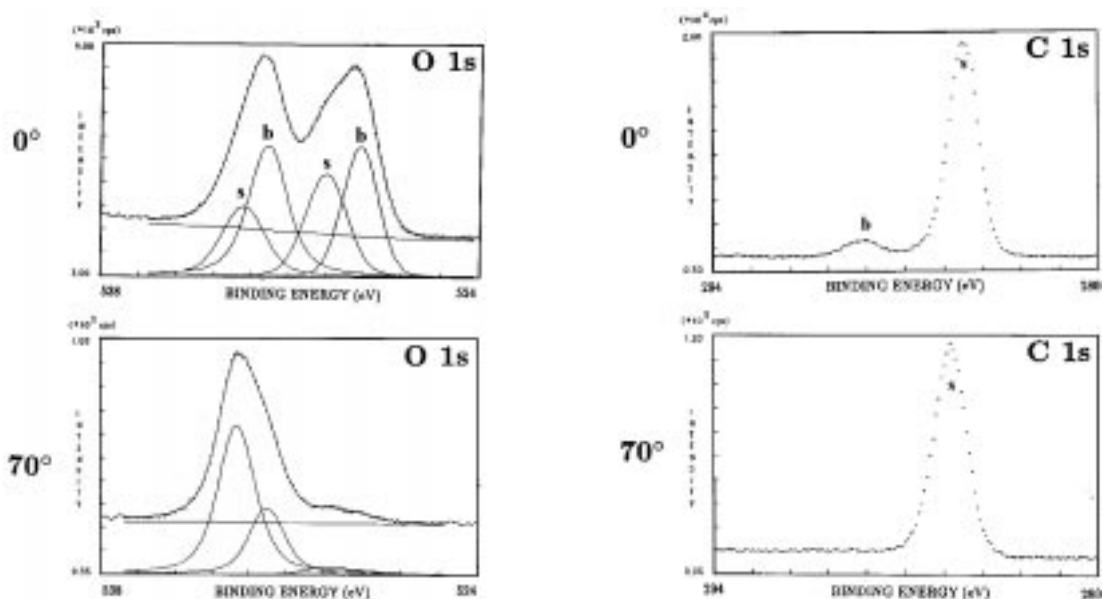


Figure 3.87: *LEFT:* High resolution AR-MXPS spectra of the O 1s state. Four peaks are revealed at $\Phi = 0^\circ$ which change the relative intensity ratio at $\Phi = 70^\circ$.

Figure 3.88: *RIGHT:* C 1s spectra showing at $\Phi = 0^\circ$ both a carbonate contribution (left peak) and a hydrocarbon peak (right peak). At $\Phi = 70^\circ$ the carbonate peak has disappeared indicating that carbonate formation might be a bulk phenomena.

3.8 YBCO thin films by LPE

Liquid-phase epitaxy is in contrast to the previously described vapour-growth methods a technique which is related closer to the growth of single crystals from a flux or a melt. Film thicknesses of several μm can be obtained within a few minutes. The growth occurs very near to equilibrium. Surface diffusion allows interstep distances of several μm . Epitaxial growth occurs at very low supersaturation ($>1000\times$ smaller than in PVD or CVD).

3.8.1 Film preparation

YBCO films by LPE [3.70, 3.71, 3.72] have been grown by C. Klemenz and H.J. Scheel.⁷⁸ The constituents BaO_2 , CuO and Y_2O_3 corresponding to 5 weight % YBCO in a flux solvent of $\text{BaCuO}_2\text{-CuO}$ at 31 mol % BaO were molten in a conical yttria crucible by heating to 1010°C during 9 hours. After soaking for 7 hours the temperature was increased to 1040°C and reduced to 1000°C within 90 mins. A $\text{NdGaO}_3(110)$ substrate was then vertically dipped into the solution at 995°C and rotated at 16 rpm. After very slow cooling in 9h50min. to 993.6°C the substrate with the YBCO layer was slowly lifted out of the melt (23 min.) and then removed from the furnace.

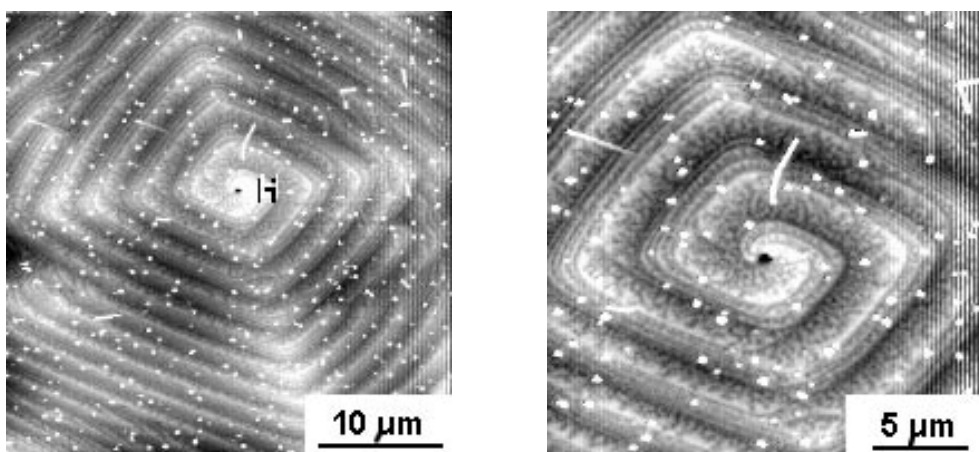


Figure 3.89: Two different SFM magnifications of a LPE-grown YBCO film on $\text{NdGaO}_3(110)$ showing a spiral growth hill with a Burgers vector component of 4-5 YBCO(001) spacings perpendicular to the film surface. The hollow core in the centre of the growth hill is labeled with **H**.

⁷⁸Cristallogene, Institute of Micro- and Optoelectronics, EPFL Lausanne, Switzerland.

3.8.2 SFM investigations

SFM investigations on these YBCO samples are performed at ambient temperature and pressure. The films exhibits large growth spirals with wide terraces ($\approx 2\mu\text{m}$) and step heights of 4-5 unit cell steps of YBCO. In all spirals imaged a hollow core is found in the centre of the growth spiral (see fig. 3.89).

Hollow cores might be very important for effective flux pinning in YBCO. By irradiation of YBCO crystals with heavy ions it has been observed that amorphous tracks are produced (columnar defects) in the crystal [3.73], which enhance flux pinning in YBCO. The number density of growth hills (and hollow cores) varies locally between $5 \times 10^2 \text{cm}^{-2}$ and 10^4cm^{-2} . A line section through the hollow core gives a diameter of 600 nm and a depth of at least 125 nm. This is to be compared to the diameter of a columnar defect created by ion irradiation (1 nm).

A further example of a spiral growth hill with a hollow core **H** is shown in fig. 3.90. Additionally a pinning centre for steps **P** is observed. Some impurity in the crystal has impeded step flow and produced these bunched steps.

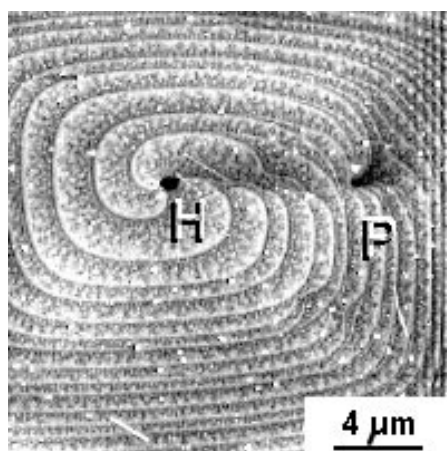


Figure 3.90: SFM image of a spiral growth hill with a hollow core **H**. A pinning centre for steps **P** (probably an impurity) leads to bunching of steps.

If it succeeds to grow superconducting LPE films with YBCO monosteps and terrace widths beyond $10\mu\text{m}$, the LPE method will be a key technique for the growth of very smooth YBCO films and to the realization of reliable planar Josephson junctions and SQUIDs made of YBCO.

3.9 ErBaCuO 124 thin films

3.9.1 ErBa₂Cu₄O₈ ceramics and thin films

The high T_c superconductor YBa₂Cu₄O₈ (Y 124) is thermodynamically more stable [3.74] than the non-stoichiometric YBa₂Cu₃O_{7- δ} (Y 123) favoring Y 124 for applications. The Y 124 synthesis requires a heat treatment in high oxygen pressure (kbar range) yielding bulk material and small single crystals (see Chapter 2). By substitution of Y by Er it is possible to prepare bulk material under ambient pressure [3.75]. This ceramic has been used as a target for pulsed laser deposition to grow ErBa₂Cu₄O₈ (Er 124) thin films (thickness: 200 nm) on SrTiO₃(100) and MgO(100) substrates using a KrF excimer laser ($\lambda = 248$ nm, energy density on the target: 2.5 J/cm²). The oxygen pressure during deposition was 27 Pa and the substrate temperature was 690°C, followed by cooling to 600°C in oxygen (4×10^4 Pa) at a rate of 4 K/min. After switching off the heater the film was cooled to room temperature.

3.9.2 Structural investigations

The phase purity of the Er 124 ceramic was verified by inductive and resistive T_c determination ($T_c = 80$ K), x-ray diffraction, high resolution transmission electron microscopy (HRTEM) using a JEOL 4000 EX microscope (400 kV, 1.9 Å point resolution, defocus conditions near Scherzer focus) and by electron diffraction (ED).⁷⁹ Figure 3.91 shows an ED pattern and a HRTEM image of a ceramic Er 124 sample. The ED pattern is compatible with the structure of Er 124 (*Ammm*, No. 65, $a=0.3847$ nm, $b=0.3872$ nm, $c=2.7278$ nm) [3.75].

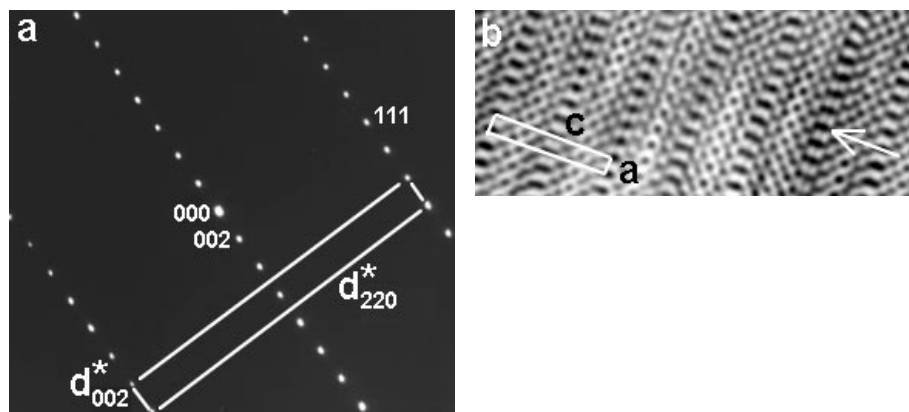


Figure 3.91: Er 124 ceramics: (a) ED pattern along $[1\bar{1}0]$. (b) Lattice image viewed along $[010]$.

⁷⁹The TEM investigations have been performed by N.D. Zakharov and D. Hesse, Max-Planck-Institute for Microstructure Physics, D-06120 Halle/Saale, Germany.

The lattice image shows the elongated slabs (arrow) typical of the double Cu–O chains present in Er 124 and compares well with simulations and previous HRTEM observations [3.76]. Similar data is obtained from the Er 124 thin film on SrTiO_3 . The cross-section HRTEM image in figure 3.92 shows the SrTiO_3 substrate and the epitaxially grown Er 124 (001) film.

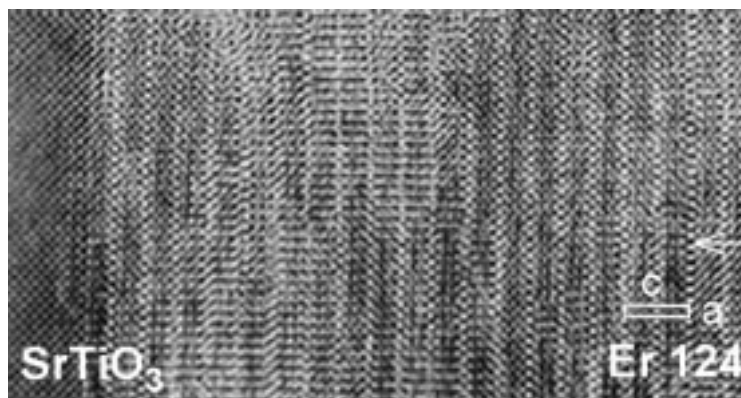


Figure 3.92: Er 124 thin film on $\text{SrTiO}_3(100)$: cross-section HRTEM image viewed along [010]. A unit cell is marked. The arrow indicates the double Cu–O chains.

The surface morphology of the Er 124 thin films has been studied with a scanning tunneling microscope (STM) in air at room temperature using a Nanoscope II STM with a $\text{Pt}_{90}\text{Ir}_{10}$ tip. Figure 3.93 shows a constant current STM image of an Er 124 thin film on $\text{MgO}(100)$. Growth hills of a diameter of about 100 nm dominate the surface topography similar to previous STM data obtained from Y 123 (001) thin films [3.12, 3.13]. The line section (fig. 3.93b) demonstrates that steps observed are all 2.7 nm in height corresponding to one [001] spacing of Er 124. This implies that the full crystallographic unit cell of Er 124 is the stable growth unit, i.e. the growth unit comprises two $\text{ErBa}_2\text{Cu}_4\text{O}_8$ units as expected from a crystal chemistry point of view. Contrary to Y 123 (001) thin films screw dislocations are observed very rarely in Er 124 thin films. A screw dislocation is labelled by "s" in figure 3.93a. The maximum height difference in the STM image is 4 unit cells (10.8 nm) over an area of $0.25 \mu\text{m}^2$ which is about three times smaller than in Y 123 thin films grown under optimized conditions (maximized T_c , minimized x-ray rocking curve widths) [3.44]. By further optimization of Er 124 thin film growth it should be possible to grow even smoother films.

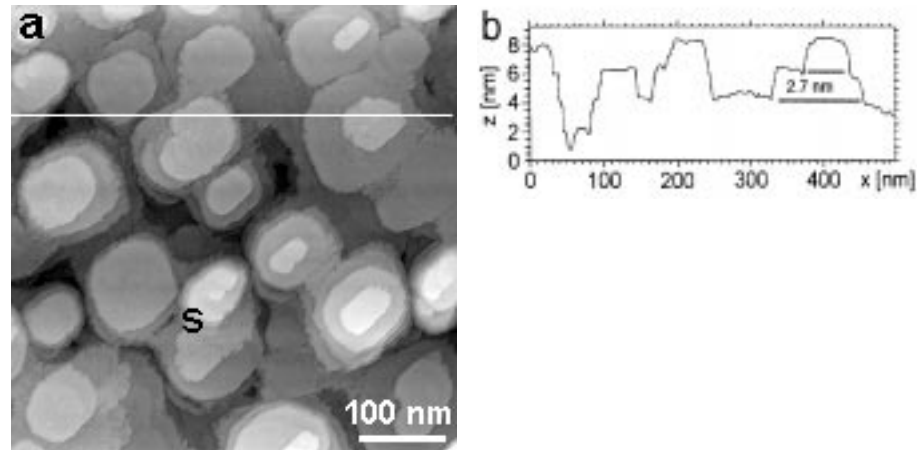


Figure 3.93: Er 124 thin film: (a) STM topview image showing growth hills with steps of 2.7 nm in height (c -axis parameter of Er 124). A topography section (white line) is shown in (b). Tunneling current: 0.3nA, sample bias voltage: -1V.

3.9.3 Conclusion

$\text{ErBa}_2\text{Cu}_4\text{O}_8(001)$ (Er 124) thin films have been prepared by pulsed laser deposition from ceramic Er 124. Transmission electron microscopy and electron diffraction is used to identify the Er 124 phase in both ceramics and thin films. Scanning tunneling microscopy images of the film samples show growth hills with steps having a height of 2.7 nm. This implies that the growth unit is the full crystallographic cell with two $\text{ErBa}_2\text{Cu}_4\text{O}_8$ units.

3.10 Summary

YBCO thin films prepared by various methods and on different substrates seem to have some morphological aspects in common such as the presence of growth hills and step patterns with the height of a single unit cell in crystallographic [001] direction. Screw dislocation defects often occur in the films but the question could not yet be definitely answered whether these dislocations affect or improve the superconducting properties of the films as it was suggested in publications by *Gerber et al.* [3.12] and *Schlom et al.* [3.24]. Even if screw dislocations act to some extent as pinning centres for flux lines, it remains to be cleared why YBCO thin films on SrTiO_3 prepared by pulsed laser deposition (section 3.3) do not exhibit screw dislocations but show similar high critical current densities as films having screw dislocations [3.44]. Due to the growth hill morphology — which is also 'ideal' in terms of the structural X-ray data [3.44] — YBCO thin films contain the same number of valleys between the growth hills as growth hills, and it may be suggested that the flux lines stick to these valleys. A reduction of the length of a flux line implies a reduction of energy. In fact, recent MFM experiments by *H. Hug and A. Moser* [3.69], University of Basel, suggest that flux lines are actually pinned in the valleys. This finding would explain the fact why films without screw dislocations exhibit similar values of the critical current density as films with screw dislocations. The occurrence of screw dislocations may also be related to the miscut of the substrate or to the substrate lattice constants.

Different deposition techniques such as MO-CVD (section 3.5) and thermal co-evaporation (section 3.6) allow a direct monitoring of vaporization and growth rates using quartz oscillators and quadrupole mass spectrometers. The RHEED technique allows the direct observation of the growth mode, but due to the very small spot size of the electron beam only spatially limited information is available. The combination of RHEED growth pattern with STM images has demonstrated that the layer-by-layer growth model suggested by the observation of RHEED oscillations is basically correct but does not hold on a micron scale which is relevant for technical applications using superconducting quantum effect devices.

STM has visualized the surface of YBCO both on a micrometre as well as on an atomic scale. With the help of angular resolved X-ray photoelectron spectroscopy two square atomic surface lattices of 0.38 nm and 0.27 nm spacings as observed by STM could be interpreted in a consistent way as O(4) and O(2)/O(3) arrangements in the BaO and CuO_2 planes of YBCO (section 3.7).

Section 3.8 demonstrates that liquid phase epitaxy as a non-vapour-growth method is capable to produce quite smooth films with terrace widths of a few μm which is relevant for applications.

In section 3.9 the successful growth of $\text{ErBa}_2\text{Cu}_4\text{O}_8(001)$ thin films by PLD is reported and illustrated by STM and TEM images. $\text{ErBa}_2\text{Cu}_4\text{O}_8$ has advantages compared to $\text{YBa}_2\text{Cu}_3\text{O}_{7-\delta}$, mainly concerning the higher thermodynamic stability and the absence of a structural phase transition, which complicates the growth of YBCO 123.

References

- [3.1] M. Schieber, *J. Cryst. Growth* 109 (1991) 401.
- [3.2] T. Terashima, K. Iijima, K. Yamamoto, Y. Bando and H. Mazaki, *Jpn. J. Appl. Phys.* 27 (1988) L91.
- [3.3] H.C. Li, G. Linker, F. Ratzel, R. Smithey and J. Geerk, *Appl. Phys. Lett.* 52 (1988) 1098.
- [3.4] R.L. Sandstrom, W.J. Gallagher, T.R. Dinger and R.H. Koch, *Appl. Phys. Lett.* 53 (1988) 444.
- [3.5] D. Dijkamp, T. Venkatesan, X.D. Wu, S.A. Shaheen, N. Jisrawi, Y.H. Min-Lee, W.L. McLean and M. Croft, *Appl. Phys. Lett.* 51 (1987) 619.
- [3.6] C.B. Eom, J.Z. Sun, B.M. Lairson, S.K. Streiffer, A.F. Marshall, K. Yamamoto, S.M. Anlage, J.C. Bravman and T.H. Geballe, *Physica C* 171 (1990) 354.
- [3.7] P.H. Kes and J. van den Berg, in *Studies of High Temperature Superconductors, Vol. 5*, ed. A. Narlikar (NOVA Science Publishers, New York, 1990), p.83.
- [3.8] E.J. Kramer, *Phil. Mag.* 33 (1976) 331.
- [3.9] C.S. Pande, *Appl. Phys. Lett.* 28 (1976) 462.
- [3.10] C.J. van der Beek and P.H. Kes, *Phys. Rev. B* 43 (1991) 13032.
- [3.11] J. Kulik, *J. Appl. Phys.* 70 (1991) 4398.
- [3.12] C. Gerber, D. Anselmetti, J.G. Bednorz, J. Mannhart and D. G. Schlom, *Nature* 350 (1991) 279.
- [3.13] M. Hawley, I.D. Raistrick, J.G. Beery and R.J. Houlton, *Science* 251 (1991) 1587.
- [3.14] T. Terashima, Y. Bando, K. Iijima, K. Yamamoto, K. Hirata, K. Hayashi, K. Kamigaki and H. Terauchi, *Phys. Rev. Lett.* 65 (1990) 2684.
- [3.15] F. Baudenbacher, K. Hirata, P. Berberich, H. Kinder, W. Assmann and H.P. Lang, *Physica C* 185-189 (1991) 2177.
- [3.16] M.G. Norton and C.B. Carter, *J. Cryst. Growth* 110 (1991) 641.

- [3.17] S.K. Streiffer, B.M. Lairson, C.B. Eom, B.M. Clemens, J.C. Bravman and T.H. Geballe, *Phys. Rev. B* 43 (1991) 13007.
- [3.18] G. Binnig and H. Rohrer, *Helv. Phys. Acta* 55 (1982) 726.
- [3.19] M.D. Kirk, J. Nogami, A.A. Baski, D.B. Mitzi, A. Kapitulnik, T.H. Geballe and C.F. Quate, *Science* 242 (1988) 1673.
- [3.20] X.L. Wu, C.M. Lieber, D.S. Ginley and R.J. Baughmann, *Appl. Phys. Lett.* 55 (1989) 2129.
- [3.21] H.P. Lang, T. Frey and H.-J. Güntherodt, *Europhys. Lett.* 15 (1991) 667.
- [3.22] H.P. Lang, T. Frey, R. Sum and H.-J. Güntherodt, in *High T_c Superconductor Thin Films*, ed. L. Corraera, Elsevier Science Publishers B.V. (1992) 789.
- [3.23] H.P. Lang, H. Haefke, G. Leemann and H.-J. Güntherodt, *Le vide, les Couches Minces - Supplément au n° 259* (1991) 38.
- [3.24] D.G. Schlom, D. Anselmetti, J.G. Bednorz, R. Broom, A. Catana, T. Frey, Ch. Gerber, H.-J. Güntherodt, H.P. Lang and J. Mannhart, *Z. Phys. B* 68 (1992) 163.
- [3.25] M. A. Harmer, C. R. Fincher and B. A. Parkinson, *J. Appl. Phys.* 70 (1991) 2760.
- [3.26] H.U. Krebs, Ch. Krauns, X. Yang and U. Geyer, *Appl. Phys. Lett.* 59 (1991) 2180.
- [3.27] D.P. Norton, D.H. Lowndes, X.-Y. Zheng, S. Zhu and R.J. Warmack, *Phys. Rev. B* 44 (1991) 9760.
- [3.28] J. Moreland, P. Rice, S.E. Russek, B. Jeanneret, A. Roshko, R.H. Ono and D.A. Rudman, *Appl. Phys. Lett.* 59 (1991) 3039.
- [3.29] I.D. Raistrick, M. Hawley, J.G. Beery, F.H. Garzon and R.J. Houlton, *Appl. Phys. Lett.* 59 (1991) 3177.
- [3.30] I. Maggio-Aprile, A.D. Kent, Ph. Niedermann, Ch. Renner, L. Antognazza, L. Miéville, O. Brunner, J.-M. Triscone, and Ø. Fischer, *Ultramicroscopy* 44 (1992) 728.
- [3.31] H. Olin, G. Brorsson, P. Davidsson, Z.G. Ivanov, P.-Å. Nilsson, T. Cleason, *Ultramicroscopy* 44 (1992) 734.
- [3.32] J.P. Zheng, Q.Y. Ying, S. Witanachchi, Z.Q. Huang, D.T. Shaw, and H.S. Kwok, *Appl. Phys. Lett.* 54 (1989) 954.
- [3.33] R.K. Singh, L. Ganapathi, P. Tiwari, and J. Narayan, *Appl. Phys. Lett.* 55 (1989) 2351.
- [3.34] R. Sum, R. Lüthi, H.P. Lang, and H.-J. Güntherodt, *Helv. Phys. Acta* 66 (1994) 883.
- [3.35] H.P. Lang, H. Haefke, G. Leemann and H.-J. Güntherodt, *Helv. Phys. Acta* 65 (1992) 864.

- [3.36] W.K. Burton, N. Cabrera and F.C. Frank, *Phil. Trans. R. Soc. A* 243 (1951) 299.
- [3.37] J.W. Matthews, in *Epitaxial Growth, Part B*, ed. J.W. Matthews, Academic Press, New York (1975), p. 559.
- [3.38] L.J. Griffin, *Phil. Mag.* 41 (1950) 196.
- [3.39] A. R. Verma, *Phil. Mag.* 42 (1951) 1005.
- [3.40] F. C. Frank, *Adv. Physics* 1 (1952) 91.
- [3.41] A. J. Forty, *Adv. Physics* 3 (1954) 1.
- [3.42] H.P. Lang, H. Haefke, G. Leemann and H.-J. Güntherodt, *Physica C* 194 (1992) 81.
- [3.43] H. Haefke, H.P. Lang, G. Leemann and H.-J. Güntherodt, *Appl. Phys. Lett.* 60 (1992) 3054.
- [3.44] H.P. Lang, R. Sum, H. Haefke and H.-J. Güntherodt, *Jour. Alloys and Compounds* 195 (1993) 97.
- [3.45] D.G. Schlom, D. Anselmetti, J.G. Bednorz, Ch. Gerber and J. Mannhart, *Mat. Res. Soc. Symp. Proc. Vol. 280* (1993) 341.
- [3.46] H.P. Lang, R. Sum, J.-P. Ramseyer, H. Haefke and H.-J. Güntherodt, *Proceedings ICMAS-92, Paris (21-22 Oct. 92)*, p.209.
- [3.47] H. Yamane, H. Masumoto, T. Hirai, H. Iwasaki, K. Watanabe, N. Kobayashi and Y. Muto, *Appl. Phys. Lett.* 53 (1988) 1548.
- [3.48] B. Schulte, M. Maul, W. Becker, H.G. Schlosser, S. Elschner, P. Häussler and H. Adrian, *Appl. Phys. Lett.* 59 (1991) 869.
- [3.49] B. Schulte, M. Maul, W. Becker, S. Elschner, H.G. Schlosser, P. Häussler and H. Adrian, in *High T_c Superconductor Thin Films*, ed. L. Corraera, Elsevier Science Publishers B.V. (1992) 325.
- [3.50] B. Schulte, M. Maul, P. Häussler, W. Becker, M. Schmelz, M. Steins and H. Adrian, *Jour. Alloys and Compounds*, 195 (1993) 299.
- [3.51] F. Baudenbacher, K. Hirata, P. Berberich, H. Kinder and W. Assmann, in *High T_c Superconductor Thin Films*, ed. L. Corraera, Elsevier Science Publishers B.V. (1992) 365.
- [3.52] F. Baudenbacher, H. Karl, P. Berberich, H. Kinder, *J. Less.-Comm. Metals*, 164-165 (1990) 269.
- [3.53] M. Henzler, W. Göpel, in: *Oberflächenphysik des Festkörpers*, B.G. Teubner Verlag, Stuttgart (1991).

- [3.54] B.A. Joyce, P.J. Dobson, J.H. Neave, K. Woodbridge, J. Zhang, P.K. Larsen and B. Bölger, *Surface Science* 168 (1986) 423.
- [3.55] F. Baudenbacher, K. Hirata, P. Berberich, H. Kinder, W. Assmann and H.P. Lang, *Physica C* 185-189 (1991) 2177.
- [3.56] H. Kinder, F. Baudenbacher, P. Berberich, S. Corsepius, O. Eibl, H.J. Güntherodt, K. Hirata, H.P. Lang, W. Prusseit, and M. Zwerger, in: *Electronic properties of High- T_c superconductors*, ed. H. Kuzmany, M. Mehring, J. Fink, Springer Series in Solid State Sciences, Vol. 113 (1993) 45.
- [3.57] K. Hirata, F. Baudenbacher, H.P. Lang, H.-J. Güntherodt and H. Kinder, *Jour. Alloys and Compounds*, 165 (1993) 105.
- [3.58] L.E.C. van Leemput, P.J.M. van Bentum, L.W.M. Schreurs and H. van Kempen, *Physica C* 152 (1988) 99.
- [3.59] H.P. Lang, J.P. Ramseyer, D. Brodbeck, T. Frey, J. Karpinski, E. Kaldis and T.H. Wolf, *Ultramicroscopy* 42-44 (1992) 715.
- [3.60] H.P. Lang, T. Frey and H.-J. Güntherodt, *Europhys. Lett.* 15 (1991) 667.
- [3.61] H.P. Lang, H. Haefke, G. Leemann and H.-J. Güntherodt, *Physica C* 194 (1992) 81.
- [3.62] G. Frank, Ch. Ziegler and W. Göpel, *Phys. Rev. B* 43 (1991) 2828.
- [3.63] R. Berthe and J. Halbritter, *Phys. Rev. B* 43 (1991) 6880.
- [3.64] G. Frank, Ch. Ziegler and W. Göpel, *Phys. Rev. B* 43 (1991) 2828.
- [3.65] W.A.M. Aarnink, J. Gao, H. Rogalla and A. van Silfhout, in *High T_c Superconductor Thin Films*, ed. L. Correria, Elsevier Science Publishers B.V. (1992) 777.
- [3.66] H. Behner, K. Rührnschopf, G. Wedler and W. Rauch, *Physica C* 208 (1993) 419.
- [3.67] D.A. Shirley, *Phys. Rev. B* 5 (1972) 4709.
- [3.68] M.P. Seah and W.A. Dench, *Surface and Interface Analysis* 1 (1979) 2.
- [3.69] H. Hug, private communication.
- [3.70] H.J. Scheel, in *Advances in Superconduct. VI*, Springer/Tokyo 1994.
- [3.71] H.J. Scheel, *Appl. Phys. Lett.* 37 (1980) 70.
- [3.72] C. Klemenz and H.J. Scheel, *J. Cryst. Growth* 129 (1993) 421.
- [3.73] L. Civale, A.D. Marwick, T.K. Worthington, M.A. Kirk, J.R. Thompson, L. Krusin-Elbaum, Y. Sun, J.R. Clem and F. Holtzberg, *Phys. Rev. Lett.* 67 (1991) 648.
- [3.74] J.Karpinski, E.Kaldis, *Nature* 331 (1988) 242.

- [3.75] R.J. Cava, J.J. Krajewski, W.F. Peck Jr., B. Batlogg, L.W. Rupp Jr., *Physica C* 159 (1989) 372.
- [3.76] H.W. Zandbergen, R.J. Cava, J.J. Krajewski and W.F. Peck Jr., *Physica C* 179 (1991) 227.

Chapter 5

Fullerenes

5.1 Introduction

The discovery [5.1, 5.2] of the third ordered form of carbon has its roots in the investigation of molecule clouds in the universe. *H.W. Kroto* (Univ. of Sussex, U.K.) studied in the 80's 'complex' molecules like ethanol, NH_3 , H_2O or HCO^+ in interstellar clouds by radioastronomy. The light of the stars lying behind such clouds is being absorbed partially in a way specific to the molecules present in the interstellar cloud. *Kroto's* new method to identify molecular species in interstellar clouds was it to synthesize special molecules exhibiting carbon chains such as HC_3N , HC_7N and HC_9N in the laboratory. The absorption spectrum acquired in laboratory was then compared to spectra obtained by μ -wave spectroscopy from interstellar clouds. The presence of these molecules was related to the understanding of energy production processes in red giant carbon stars.¹ *Kroto's* new approach was it to perform carbon vaporization experiments in the laboratory and to compare the measured absorption spectra to those obtained by radioastronomy.

R.F. Curl and R.E. Smalley from Rice University, Texas, U.S.A., did in 1985 laser vaporization experiments using rotating disks of different materials. Vaporized particles were studied using a mass spectrometer. *Kroto* suggested an experiment with a rotating graphite disk. At the 4th of September in 1985 [5.2] a mass spectrum was obtained showing a clear peak for a species with a mass number of 720 corresponding to a molecule built up of 60 carbon atoms. An earlier graphite vaporization experiment by the Exxon Research group (*Rohlfing et al.*) [5.3] was later found also to contain a peak in the mass spectra at 720 (C_{60}) and 840 (C_{70}), but was not interpreted properly at that time. From symmetry arguments *Kroto* suggested a possible structure for this molecule: a closed-cage molecule having a truncated icosahedron structure (the structure of a soccer ball). Such a highly symmetric molecule was expected to show well-predictable properties:

- structure built up of 12 carbon pentagons and 20 carbon hexagons,
- $60 \times 3 - 6 = 174$ degrees of freedom,

¹Red giant carbon stars do not show hydrogen emission lines but carbon lines. The standard model for energy production in a star by fusion of hydrogen to helium (followed by more complicated fusion processes) is not applicable to this type of star.

- only 4 IR active modes,
- 10 Raman active modes,
- a single ^{13}C nuclear magnetic resonance (NMR) line (all carbon atoms are equivalent).

At that time it seemed not to be possible to confirm these predictions since this new material was not available in sufficient amounts to perform solid state experiments.

The mass spectra showed some special features: in a mass range equivalent to 1–35 carbon atoms all integer peaks were observed implying the presence of all sorts of carbon chain fragments. In a mass range from 36 to over 110 carbon atom masses only the even *carbon mass numbers* were observed. This was later found to be a genuine property of this new class of closed-cage molecules.

The idea of a soccer-ball-shaped molecule made *Kroto* think of the dome-like architecture by Buckminster Fuller² and he suggested the name *Fullerenes* or *Buckyballs* for the new closed-cage molecules.

To understand the geometry of the most abundant representative of the fullerenes, C_{60} , the net of the truncated icosahedron is discussed (see fig. 5.1):

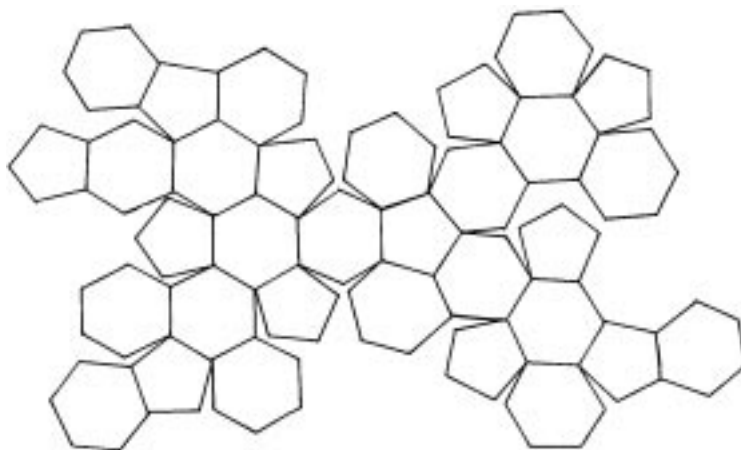


Figure 5.1: Net of the truncated icosahedron. The closed-cage structure consists of 12 pentagons and 20 hexagons. Pentagon edges never touch (isolated pentagon rule).

The truncated icosahedron (icosahedral symmetry group I_h) is one of the Archimedean bodies. Thus the *Euler's rule* is applicable:

$$faces + vertices = edges + 2 \quad (5.1)$$

in short:

$$f + v = e + 2 \quad (5.2)$$

²Buckminster Fuller built geodesic domes for the world exposition (EXPO) 1966 in Montreal.

The number of faces f is the sum of the numbers of hexagons h and pentagons p . Each hexagon has 6 edges and each pentagon has 5 edges. Each edge is part of two faces and each vortex in common to three edges, thus the following equations are valid:

$$2e = 5p + 6h \quad (5.3)$$

$$3v = 5p + 6h \quad (5.4)$$

On inserting e and v in *Euler's rule* the following relation is obtained:

$$5e + 6e + \frac{5p + 6h}{3} = \frac{5p + 6h}{2} + 2 \quad (5.5)$$

or simplified:

$$p = 12 \quad (5.6)$$

Concluding, a closed cage structure of pentagons and hexagons must consist of *twelve pentagons*, the number of hexagons is *arbitrary*. If in addition it is required that no neighbouring pentagons occur³ (isolated pentagon rule) the smallest closed-cage structure is a truncated icosahedron having 20 hexagons. This structure has according to *Euler's rule* 60 vortices and 90 edges, and is identical to the C₆₀ fullerene (see fig. 5.2).

By adding an additional hexagon to the structure the condition that three edges have one common vortex must be respected. This results in the addition of 2 carbon atoms per added hexagon⁴ and is the reason for the occurrence of only even numbered members of the fullerenes. Note that the pentagons are required to curve the surface.⁵

By optimization of the conditions during the graphite vaporization process (mainly the helium pressure used to generate the supersonic gas jet to extract the fullerenes) *Kroto, Curl and Smalley* could influence the ratio of the different fullerenes detected in the mass spectrometer. The most abundant fullerene was C₆₀. With smaller abundance C₇₀, C₈₄, C₇₆ and C₇₈ were observed.

In the late 80's astrophysicist *W. Krätschmer* (Max-Planck-Institute for nuclear physics in Heidelberg, Germany) was working on an explanation of interstellar absorption by carbon soot particles. He measured absorption spectra from carbon soot generated in laboratory using an arc. A high voltage applied to two electrodes shaped as graphite rods in a vacuum chamber generates an arc. A helium pressure of some mbar ascertains good thermal contact due to the large heat capacity of helium. After production the carbon soot particles condense at the wall of the chamber.

IR and UV-vis spectra from the soot prepared in 130 mbar He showed four characteristic absorption lines, which are evidence of a highly symmetric structure. A comparison has brought up the result that these four lines are the predicted IR modes of C₆₀. The advantage of *Krätschmer's* preparation method [5.4] is the facile synthesis of macroscopic

³This yields a higher symmetry and — for chemical reasons — a higher stability since the sp^2/sp^3 coordination of the carbon atoms favours six-membered rings.

⁴Pentagons cannot be added due to *Euler's rule*.

⁵The theoretical claim for negatively curved carbon atom surfaces by introduction of carbon heptagons into a graphitic (hexagon) sheet has not yet been proved experimentally.

amounts of fullerenes. The fullerene solid can be dissolved in toluene or benzene yielding a red solution. Non-fullerene fractions of the soot are not dissolved and can be removed by filtering. The dissolved fullerene mixture is purified by chromatography using an Al_2O_3 column.

The predicted single ^{13}C NMR line was found soon by *Taylor et al.* [5.5] using a benzene solution of C_{60} . The narrowness of the ^{13}C NMR line of C_{60} was interpreted as a very fast rotation of the C_{60} molecule on the NMR time scale (rotation frequency: $\approx 10^{10}$ Hz). The broadening of the ^{13}C NMR line with decreasing temperature implies the freezing of this rotation. This effect is studied in the work by *Yannoni et al.* [5.6] in the temperature range between 295 and 77 K.

The electronic structure of the molecule was determined using Hückel calculations

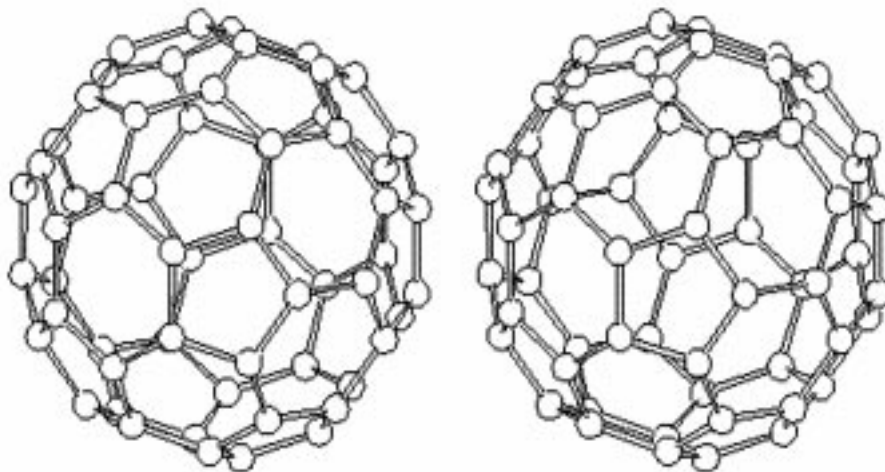


Figure 5.2: Stereographic view of the C_{60} fullerene molecule.

by *Haddon et al.* in 1986 [5.7]. The result is shown in fig. 5.3.

The carbon atoms in the C_{60} molecule show hybridization similar to diamond and graphite. The sp^x -hybridized orbitals seem to be closer to the graphitic case (sp^2) than to the diamond case (sp^3). Three hybridized orbitals constitute the bonds between carbon atoms and a fourth orbital (p_z) is standing perpendicular on the fullerene ball surface. A computer simulation of the electron distribution of a C_{60} molecule at 1000 K is shown in fig. 5.4.⁶ Only the bonds between carbon atoms are shown.

The transition from the energy levels of the C_{60} molecule to the C_{60} solid is shown in fig. 5.5 and discussed by *Saito et al.* [5.8]. Solid C_{60} shows a band-gap between the highest occupied molecular orbital (HOMO) and the lowest unoccupied molecular orbital (LUMO) of about 1.5 eV making the solid to an insulator or a semiconductor with a large band-gap.

⁶Photo by *J. Bernholc et al.*, North Carolina State University / Science Photo Library, published in *Physics world*, April 1992 issue, p.1)

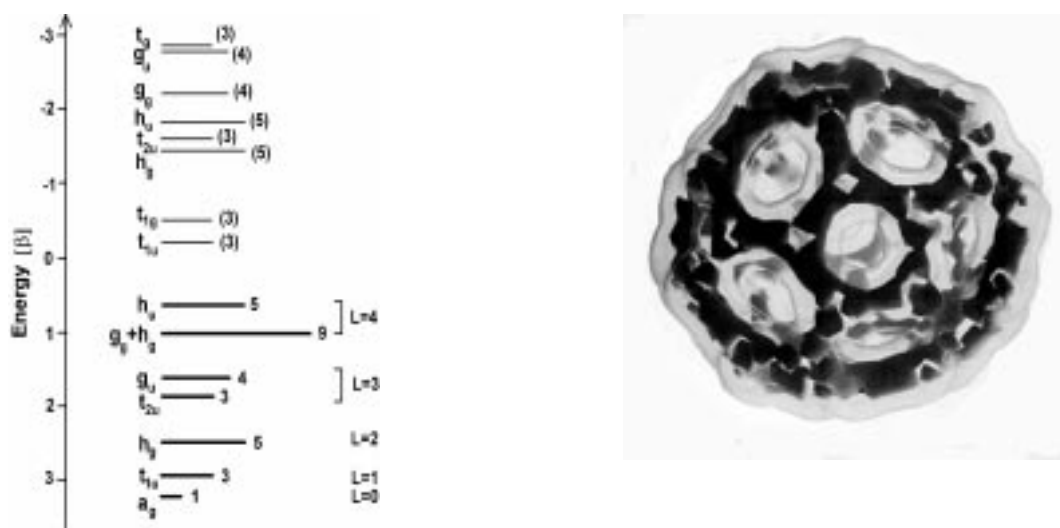


Figure 5.3: *LEFT:* Hückel molecular orbital calculation after *Haddon et al.* [5.7]. The bold lines represent occupied states. The length of the lines is a measure for the number of electrons present (shown on the right). The angular momentum quantum numbers L are indicated. The thin lines represent unoccupied states. The degeneracy is indicated in parentheses. The states are labelled on the left side.

Figure 5.4: *RIGHT:* π -orbital skeleton of the fullerene C_{60} molecule. Computer simulation of the electron distribution at 1000 K by *J. Bernholc et al.*

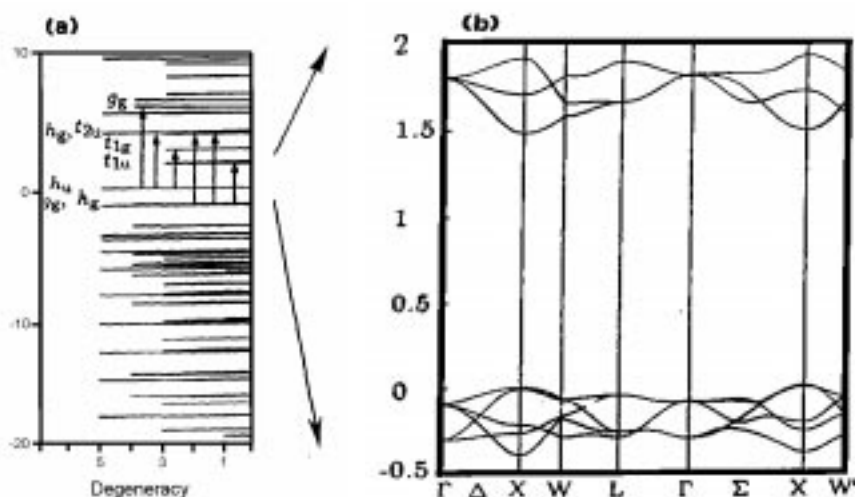


Figure 5.5: (a) Electronic energy levels of an isolated C_{60} molecule and the energy bands of solid *fcc* C_{60} (b). The valence-band top at the X point is defined as the zero energy. The optically allowed transitions with excitation energies less than 6 eV are indicated by arrows. Figure and figure caption by *Saito et al.* [5.8].

The C_{60} solid has been found to form under ambient conditions a face-centred cubic lattice with a lattice constant of 1.416 nm. The densest lattice plane is the (111) plane with a nearest-neighbour distance of 1 nm (see fig. 5.6). Bulk structure refinement has been performed using X-ray diffraction (XRD) [5.9, 5.10], neutron scattering [5.11] and electron diffraction [5.4].

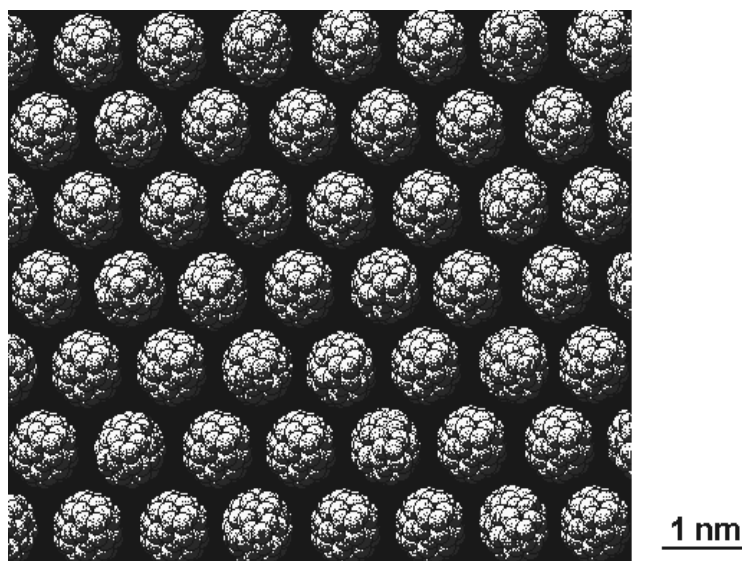


Figure 5.6: $C_{60}(111)$ plane exhibiting the densest packing of C_{60} molecules.

Growth of fullerene single crystals [5.12] and highly-ordered thin-film samples by sublimation permits more detailed investigations of the structural properties of fullerenes. Local imaging methods such as TEM [5.13, 5.14] and STM [5.15]–[5.18] allow a more detailed understanding of the local structure and morphology of bulk and surface, respectively. STM has been successfully applied to image surfaces of thin fullerene films obtained by sublimation of fullerene powders onto conductive substrates [5.15, 5.16]. The characterization of thin fullerene films on different substrates is discussed in the following sections.

5.2 Fullerene films on HOPG and Pt substrates

5.2.1 Film casting

Due to the insulator bulk properties of C_{60} it is necessary to grow thin fullerene films in order to be able to do experiments with a STM. As direct and inverse photoemission experiments show [5.17], at a coverage of 1-2 monolayers of C_{60} on $Ag(110)$ ⁷ the HOMO and LUMO are observed to shift towards E_F by 0.2 eV respectively by 0.9 eV. The first monolayer of C_{60} behaves *metallically*.

A very easy method to prepare thin fullerene films is *film casting*. In this procedure C_{60} powder is dissolved in a solvent — toluene or benzene — and a drop of the solution is being put onto a substrate and allowed to dry slowly. Figure 5.7 shows an optical micrograph of such a sample obtained from a C_{60} solution in toluene and applied on a glass substrate. Here — similar to the results obtained by *Krätschmer et al.* [5.4] — even some fullerene crystals appeared. By adding more solvent it is possible to grow very thin films on conductive substrates as will be discussed in the following.

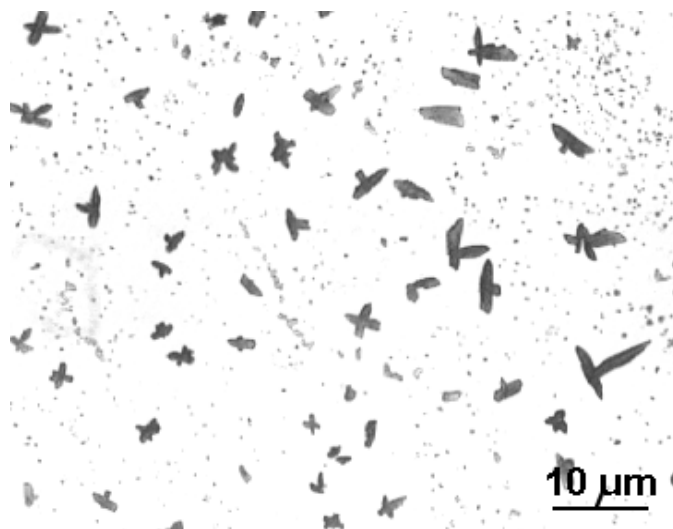


Figure 5.7: Tiny fullerene crystals grown by allowing to dry a drop of C_{60} solution in toluene on a glass substrate.

5.2.2 Fullerene films on HOPG

HOPG is a substrate with structural properties very similar to fullerenes due to the six-membered carbon ring structure. Since HOPG is conductive it is a good choice as a substrate for STM investigations. Unfortunately, the high electric field caused by the STM tip and/or the similar chemical natures of HOPG and fullerenes make HOPG an

⁷This is valid for gold substrates, too.

inappropriate substrate for C_{60} . The fullerene molecules preferentially stick to graphite steps and lead to a distortion of the electronic structure of HOPG. Figure 5.8 depicts an example of the phenomenon: a fullerene molecule 'F' on a graphite plane 'G' induces changes of the in-plane lattice constant of more than 80 percent. The undisturbed HOPG lattice with a nearest-neighbour distance of 0.25 nm is imaged close to the label 'G'.

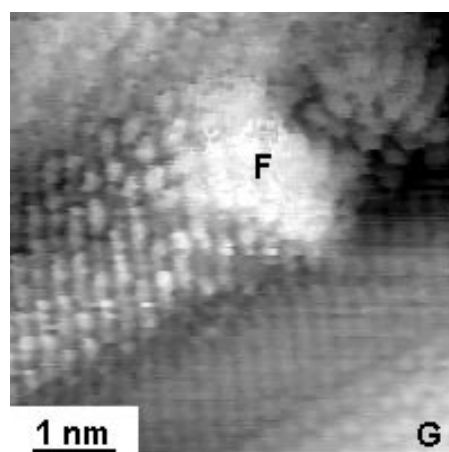


Figure 5.8: A fullerene molecule 'F' on graphite 'G' leads to electronic distortions of the atomic lattice of HOPG (STM image).

5.2.3 Fullerene films on polycrystalline platinum

Due to the inadequacy of graphite substrates other materials had to be tested. Various substrates were used to support the C_{60} for STM investigations such as polished Si(100) and GaAs(100) wafers, optically polished and ultrasonically cleaned gold, silver, palladium, rhodium and platinum foils. Si(100) and GaAs(100) were also coated with a 2 nm thick Pt-C layer by electron-beam evaporation to provide surfaces appropriate for STM experiments in air. Among the different substrates used, platinum was found to stabilize the fullerene molecules best, whereas considerable mobility of the C_{60} molecules was observed on the other substrates. Therefore the focus is on the STM results obtained from C_{60} films deposited on platinum foils [5.19].

5.2.3.1 Experimental

Polycrystalline C_{60} starting material was produced according to the *Krättschmer* method by *A. Zahab and P. Bernier*⁸. The C_{60} powder, purified by soxhlet extraction with toluene, was dissolved in toluene and deposited by film casting on a polycrystalline Pt substrate for the images presented in this section. The scanning tunneling microscope was operated at room temperature in air. Various mechanically prepared Pt₉₀Ir₁₀ tips were used on each sample to exclude tip-geometry induced artifacts. All images are recorded in the

⁸G.D.P.C.–U.S.T.L., Montpellier (France)

constant current mode and therefore give height information.

5.2.3.2 STM results

C_{60} films on platinum exhibit quite a flat surface for STM experiments. Fig. 5.9 shows molecularly flat terraces of C_{60} molecules separated by a monomolecular step. The step height is about 0.5 ± 0.1 nm.

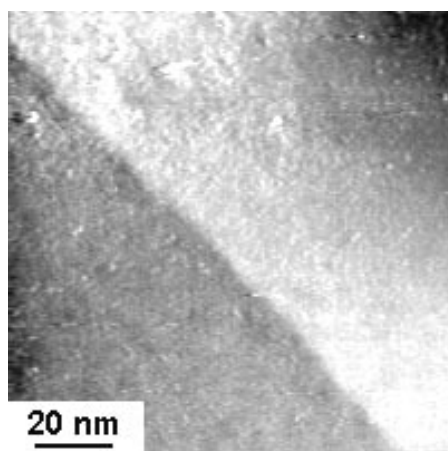


Figure 5.9: Constant current STM image of a C_{60} thin film on a platinum foil showing a monomolecular step of C_{60} . Tunneling current $I_t = 0.4$ nA, sample bias voltage $U_s = -8$ mV.

Larger magnifications of the film sample show individual C_{60} molecules with an apparent average diameter of about 0.8 nm, in agreement with structural models. In contrast to the other substrates used for C_{60} molecules, platinum enables stable imaging of the C_{60} molecules by STM. Fig. 5.10 shows individual ball-shaped molecules with apparent corrugations of 0.4 to 0.7 nm. The figure also reveals distinct internal features of the buckminster fullerene molecules. Each molecule exhibits about 10 smaller spherical features of about 0.1 nm diameter and about 0.05 nm apparent corrugation. It is not yet clear whether these features may be attributed to the carbon atoms of the C_{60} icosahedron (see also fig. 5.12 for comparison) or to other features such as bonds or rings. Submolecular features of the C_{60} molecules have been observed on several C_{60} films on platinum with different tips in both imaging modes of the scanning tunneling microscope (topographic constant current mode and constant height mode). The submolecular features are basically independent of scanning speed, sample bias voltage (within a range of ≈ 50 mV) and tunneling current (typically below 2 nA). Since different C_{60} molecules show different geometrical arrangements of the submolecular features, imaging of tip geometry can be ruled out. Furthermore, submolecular features of C_{60} molecules are favourably observed on randomly arranged, isolated C_{60} molecules. Therefore instrumental artifacts are considered unlikely as an explanation for these features.

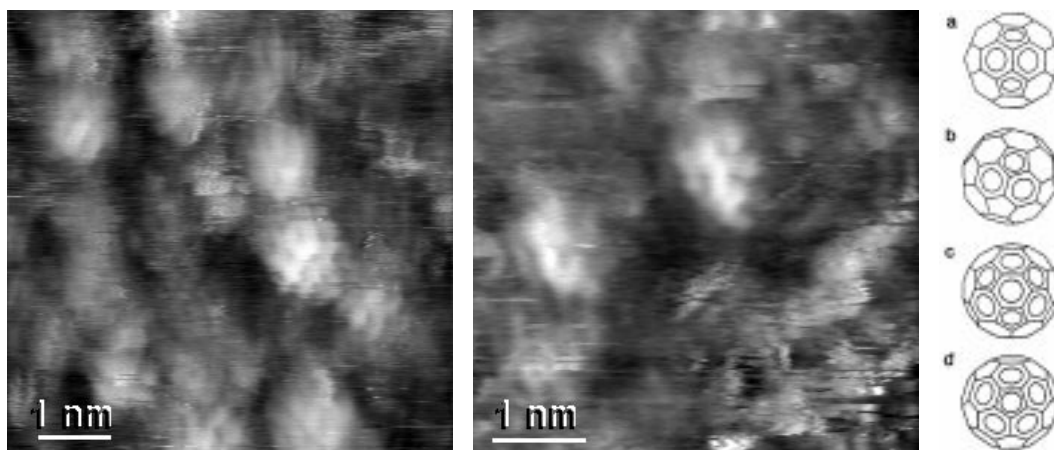


Figure 5.10: Constant current STM images showing in greater detail the individual ball-like molecules (apparent corrugations ≈ 0.6 nm) with intramolecular features (apparent corrugations ca. 0.05 nm). Tunneling current $I_t = 1.6$ nA, sample bias voltage $U_s = -17$ mV.

Figure 5.11: Wire frame model in different orientations (a) – (d) for comparison with the STM images of fullerene molecules.

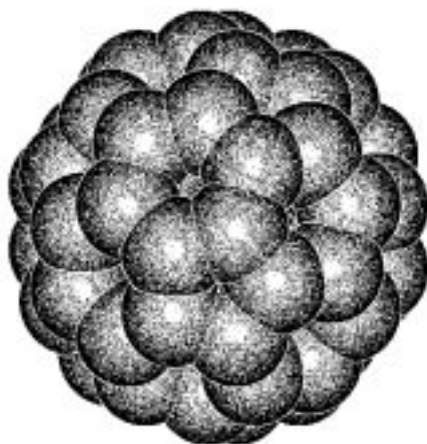


Figure 5.12: Van-der-Waals radii model showing the C_{60} molecule.

An analysis of the STM images by means of a comparison with the structural model gives in most of the cases consistent results concerning identification of feature positions with carbon atom sites in the C_{60} molecule (see fig. 5.11 for a comparison with a wire frame model of C_{60}). A van-der-Waals radii representation of C_{60} is shown in fig. 5.12. STM studies by *Chen et al.* [5.21, 5.22] have shown similar internal features of C_{60} molecules deposited on gold.

Previous studies have shown that C_{60} molecules exhibit a high reactivity with catalytic Pt^0 in a $(Ph_3P)_2Pt(\eta^2 - C_{60}) \cdot C_4H_8O$ complex along the so-called 6:6 bonds, the common bonds between two hexagon faces [5.11]. This might possibly be an explanation of the observed immobilization of the C_{60} molecules on the platinum foil. It can also happen that a C_{60} molecule is picked up by the Pt-Ir STM tip and gets immobilized there. In this case, the internal features of the C_{60} molecule as seen in the STM images would have to be attributed to the C_{60} molecule bonded to the tip.

In summary, it turned out from a comparison of several substrates that platinum is clearly a favorable choice to immobilize the fullerenes for STM investigations.

Further theoretical work, especially concerning the $Pt^0 - C_{60}$ interaction, has to be done to understand this issue better.

A better-defined approach to ultrathin fullerene films on single-crystalline substrates is the sublimation process. The C_{60} solid (*fullerite*) does not undergo a melting transition on heating, but *sublimes*, i.e. the solid phase directly transforms to a vapour phase. The sublimation process⁹ may also be used to grow small fullerene crystals, as demonstrated by the AFM image in fig. 5.13.¹⁰

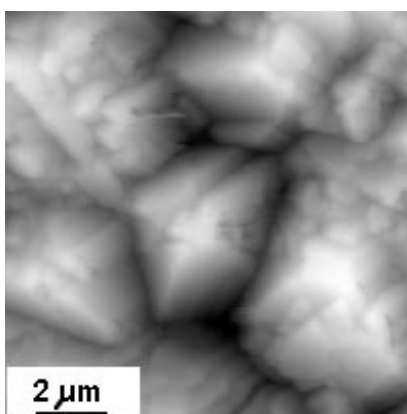


Figure 5.13: AFM image of sublimed C_{60} crystals. The sample is non-conductive.

⁹Fullerenes only need to be heated in a vacuum to sublime. The molecules can be condensed on a substrate kept at a lower temperature than that used for sublimation to prepare a fullerene thin film.

¹⁰Sample by P. Häussler/HOECHST AG, Frankfurt (Germany).

5.3 Fullerene films on monocrystalline Au substrates

This section is devoted to STM investigations of fullerene thin films on Au(111) substrates on a mica support. This type of substrate allows epitaxial growth of the fullerene layer and is ideal to study basic types of defects in the films under ambient conditions.

5.3.1 Experimental

5.3.1.1 Sample sources

Two sources of $C_{60/70}$ mixtures have been used. They have been prepared independently in private¹¹ and commercial laboratories¹² by a technique similar to those described by *Krätschmer et al.* [5.4]. The mixtures from these two sources are defined as mixture 1 (Montpellier) and 2 (MER). Pure (99.999 %) C_{60} and almost pure C_{70} (93 %), used as a control, has been obtained from a private laboratory.¹³ It was extracted from the fullerene soot by the soxhlet method using xylene under exclusion of air and separated from the higher fullerenes by column-chromatography (using hexane/xylene and modified Al_2O_3 as stationary phase). The purity has been characterized by quantitative UV-VIS photometry (using standard addition for quantification). This analysis detects traces of C_{70} and higher fullerenes in C_{60} , but yields only about 90 % purity of higher fullerenes due to band overlaps. By High Pressure Liquid Chromatography (HPLC) no traces of C_{70} have been found in the pure C_{60} . The C_{70} control has been supplied by the same group. By HPLC, the C_{70} powder has been found to contain 6 - 8 % C_{60} .

5.3.1.2 Preparation of Au(111) films on mica

Epitaxial Au(111) films on mica are prepared by two different evaporation methods. The first method involves thermal evaporation in a high vacuum chamber (10^{-3} Pa). To improve the adherence of the Au film, an approximately 1 nm thick Cr buffer-layer is evaporated onto a freshly cleaved mica substrate prior to the deposition of the 100 nm thick Au film. The deposition rate for the Au film is 0.5 nm/s. The Au film is then carefully heated in a butane-propane flame of a micro-torch until it turns red. Quenching the hot Au film in ultrapure H_2O (Millipore) results in a clean, flat (111)-oriented Au film. The widths of the (111) terraces are a few hundred nanometres as determined by STM.

The second method involves evaporation of Au from a resistively heated graphite crucible in a high vacuum (10^{-4} Pa) directly onto a mica substrate that has been cleaved in vacuum. Careful thermal shielding avoids the exposure of the substrate to the hot

¹¹P. Bernier and A. Zahab, G.D.P.C.-U.S.T.L. F-34095 Montpellier Cedex 05, France.

¹²Materials and Electrochemical Research (MER) Corp., 7960 South Kolb Road, Tucson, Arizona 85706, U.S.A.

¹³H. Werner and R. Schlögl, J.W. Goethe University, Institute of Inorganic Chemistry, Niederurseler Hang, W-6000 Frankfurt 50, Germany.

graphite crucible. A gold film thickness of 40 nm results from a deposition rate of 0.04 nm/s and a substrate temperature of 300°C. Both methods yield clean Au(111) substrates of similar quality for subsequent STM studies.

5.3.1.3 Fullerene film preparation

Thin fullerene films are prepared by sublimation of fullerene powder mixtures onto thin Au(111) substrate layers on mica. A sublimation apparatus with two chambers (substrate heating stage and fullerene heating chamber) is used. A schematic drawing of the sublimation apparatus is shown in fig. 5.14.

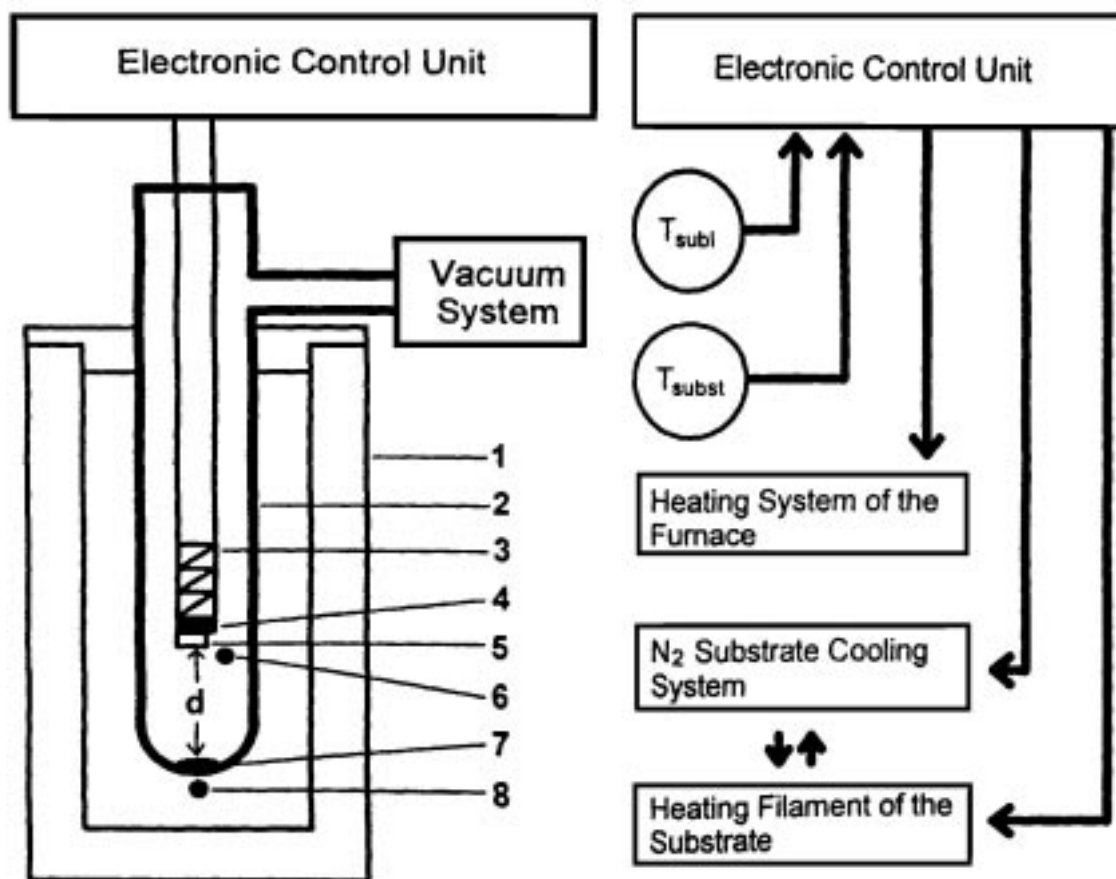


Figure 5.14: Schematic setup of the sublimation vessel with a movable substrate stage (*LEFT*) and the setup for temperature control (*RIGHT*). (1) External furnace, (2) sublimation chamber, (3) inner tube, (4) copper block substrate stage, (5) Au(111) substrate on mica, (6) chromel-alumel thermocouple for measuring T_{subst} , (7) fullerene powder, (8) chromel-alumel thermocouple for T_{subl} . The sublimation distance d is indicated by arrows.

The sublimation vessel consists of a chamber (2) containing the fullerene powder (7)

and of a tube (3) with the Au(111)/mica substrate (5). The substrate is mounted with silver paint on a copper block (4) at the tube's end. The chamber and the tube can be maintained at different temperatures to an accuracy of 1-2 °C. The chamber is evacuated by means of a diffusion pump system to a pressure of 10^{-3} Pa prior to film preparation. The substrate is preheated to the deposition temperature (T_{substr}) by a resistance heating system to ensure a defined substrate temperature during the whole sublimation process. The process is started by placing the vessel in an external furnace (1). Its temperature (T_{subl}) is monitored by a chromel-alumel thermocouple (8). A cooling system using nitrogen gas flow maintains T_{substr} being measured by a chromel-alumel thermocouple (6). The sublimation distance d (distance between the fullerene powder and the Au(111)/mica substrate) is indicated in fig. 5.14. After the process of sublimation the vessel is removed from the external furnace, cooled down to room temperature and taken into an argon-filled glove box. In this glove box the gold-supported fullerene film is removed from the copper plate for STM investigations. Typical parameters used for preparation of thin fullerene films are $T_{subl} = 350 - 370^{\circ}\text{C}$ and $T_{substr} = 220 - 230^{\circ}\text{C}$ for a heating time $t_h = 30 - 40$ min (at a sublimation distance of $d = 2.9$ cm between fullerene powder and Au(111) substrate). The different possibilities to change the deposition conditions (sublimation and substrate temperatures) and the sublimation distance are schematically shown in fig. 5.14 on the right.

Further experiments have been performed using a sublimation vessel with a movable substrate stage for the variation of d in the range of 3 to 15 cm. A vessel with a similar geometry but with a fixed substrate stage (at $d = 3.0$ cm) was employed for the variation of T_{substr} in the range of 200 to 275 °C. In both experiments T_{subl} was kept at a constant value of 360 °C.

5.3.1.4 Thermogravimetric and differential thermal analyses

In order to study the sublimation process in more detail, fullerene powder has been subjected to an investigation in a combined thermogravimetric analysis (TGA) and differential thermal analysis (DTA) apparatus (Mettler TA-1). With this apparatus, weight losses of a sample on heating, and thermal phase transitions can be recorded simultaneously as a function of temperature. The sample crucible containing a small amount of fullerene powder (40 mg of $\text{C}_{60/70}$ mixture **2**) and a reference crucible containing fine grained Al_2O_3 is heated to 600°C at a rate of 4 K/min. The weight loss (TGA) and the temperature difference with respect to the reference crucible (DTA) are measured simultaneously as the temperature is ramped up from room temperature to 600°C. The measurements have been performed both under flowing Ar gas and at a pressure of 5 Pa.

5.3.1.5 UV-VIS Spectroscopy

The absorption of light in the range of wavelengths from 200–600 nm is measured for *n*-hexane solutions of pure C_{60} , pure C_{70} , and mixtures **1** and **2** of C_{60} and C_{70} . The

concentration of solutions is chosen for complete solubility of the powders (0.5 mg / 10 ml). A two-beam optical spectrophotometer (Uvikon 810) and *n*-hexane reference are used.

5.3.1.6 High pressure liquid chromatography

High pressure liquid chromatography (HPLC) has been performed on hexane solutions of pure C₆₀, pure C₇₀, and mixtures **1** and **2**. The C₆₀ and C₇₀ samples are prepared as saturated solutions. An analytical HPLC column, 4.6 × 250 mm i.d., packed with a covalently bound chiral dinitrobenzamide phenylglycine stationary support, is used to achieve efficient separation of the two fullerenes [5.23, 5.24]. The column is eluted with *n*-hexane (HPLC grade) at a flow of 1 ml / min. Spectroscopic (UV) detection is performed at 280 nm. Retention times for the two fullerenes under these elution conditions are 11.6 min for C₆₀ and 20.6 min for C₇₀.

	HPLC ^a (hexane solutions)	¹³ C NMR ^b (solid state)	STM ^c (film)
Mixture 1	23.3 % (19.4 %)	25.0 ± 0.2 %	15.3 ± 2.1 %
Mixture 2	21.9 % (18.2 %)	– ^d	16.6 ± 3.7 %

^a Determined directly from peak integration (without correction). Number in parentheses corrected for relative molar absorptivities of C₇₀ and C₆₀, $\epsilon(C_{70})/\epsilon(C_{60}) = 1.2$ at 280 nm [5.23].

^b A. Zahab, Ph. D. Thesis, Univ. Montpellier.

^c Determined by counting C₇₀ molecules in the STM images averaged over several STM images acquired from 5 different regions of the sample. Uncertainty calculated by standard deviation.

^d not available.

Table 5.1: Determination of the C₇₀ content of different fullerene mixtures.

5.3.1.7 ¹³C Nuclear magnetic resonance

Solid state ¹³C nuclear magnetic resonance (NMR) has been used with mixture **1** to determine the C₇₀/C₆₀ ratio in the fullerene powder prior to sublimation [5.20]. The NMR samples are comprised of 50 mg of the fullerene mixture in the form of powders. The ¹³C NMR measurements have been performed using a CXB200 Bruker spectrometer, operating at 50.3 MHz and at room temperature. Magic angle spinning has been used to increase the resolution of the spectra. Pulsing sequences have been optimized to take into account the relaxation times of the fullerenes. The width of the ¹³C line at 143.6

ppm (relative to tetramethylsilane) corresponding to the C_{60} molecules is typically on the order of 3 – 5 Hz wide. For the C_{70} molecules, the five inequivalent carbon sites yield five NMR lines which are collectively integrated to give the C_{70} content. Comparison of this collective integration of the five C_{70} peaks with the integration of the single C_{60} peak provides the C_{70}/C_{60} ratio data in Table 5.1.

5.3.1.8 Scanning tunneling microscopy

Scanning tunneling microscopy (STM) is performed in air at room temperature using a commercially available instrument (Nanoscope II). Several mechanically prepared $Pt_{90}Ir_{10}$ tips have been used on every sample to avoid tip-geometry induced artifacts in the images. Applied tunneling currents lie between 0.5 and 1 nA, and tip bias voltages are in the range of 100 - 500 mV. All images are recorded in the constant current mode and therefore give topographic height information, which is encoded to a grey-scale (a brighter grey-value in the STM image corresponds to higher features).

5.3.2 Results

5.3.2.1 Study of the sublimation process

Simultaneous thermogravimetric and differential thermal analyses (TGA/DTA) have been used to investigate the sublimation process for a mixture of C_{60} and C_{70} in order to determine optimum sublimation temperatures. The commercial $C_{60/70}$ source (mixture 2) has been used for this experiment. Figure 5.15 shows the TGA and DTA curves obtained at two different pressures: (a) in an argon gas flow (10^5 Pa) and (b) under a moderate vacuum (5 Pa). Both data sets are corrected to a baseline linear with temperature (Archimedian buoyancy effects, thermal drift). Mass losses observed in the TGA signal due to sublimation can be correlated to endotherms in the DTA curve. Fig. 5.15a shows that in a Ar gas flow, considerable sublimation occurs between 300 and 600°C. Fig. 5.15b shows TGA/DTA curves obtained at a pressure of 5 Pa. Although mass loss proceeds similarly to the measurement in flowing argon (fig. 5.15a), endothermal processes occur in two distinct stages, 200 to 450°C and 450 to 600°C. This two-step process might be related to sublimation and combustion of the fullerenes. The stage at a lower temperature should be basically split up into two steps since two different energies exist to sublime C_{60} and C_{70} . An observation of different sublimation yields of C_{60} and C_{70} has already been reported in literature [5.4]. A different explanation for the first step of weight loss might be the desorption of impurities (e.g. co-crystallized solvents, oxygen or nitrogen) from the C_{60} material. Such desorption processes have been observed by mass-spectroscopy to occur in the temperature range of the first weight loss [5.25]. The temperatures chosen for the thin film preparation (350-370°C) lie within the range of endotherms (sublimation) observed in the DTA curves.

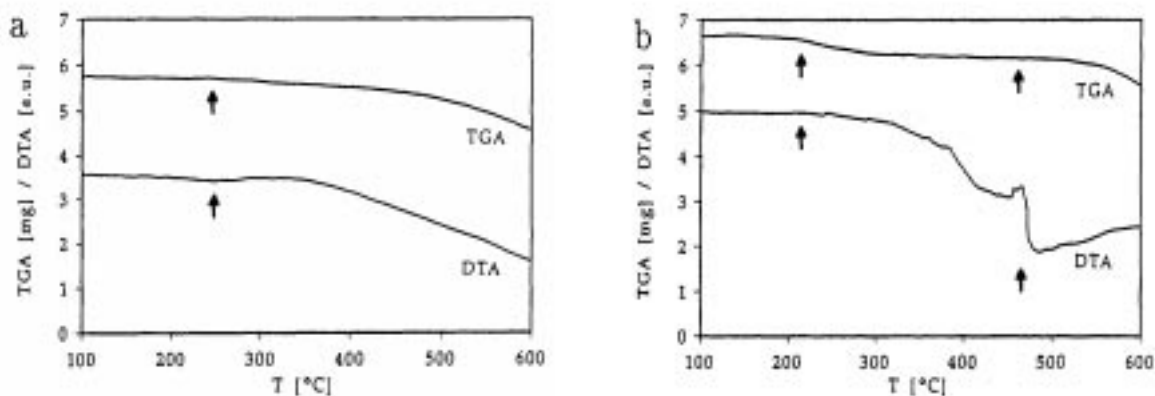


Figure 5.15: Thermogravimetric analysis and differential thermal analysis curves (corrected for a baseline linear with temperature). (a) Fullerene mixture **2** heated in an Ar gas flow. The arrow marks the beginning of the sublimation process, indicated by a mass loss and endothermic drop in the TGA and DTA signals, respectively. (b) Fullerene mixture **2** heated in a moderate vacuum of 5 Pa. Mass loss and endothermic processes occur in at least two steps (arrows).

5.3.2.2 UV-VIS spectroscopy of fullerene powder solutions

Qualitative information on the ratio of C_{60} and C_{70} in fullerene mixtures in solution can be obtained from optical absorption spectra [5.5],[5.26]–[5.28]. Figure 5.16 shows absorption spectra (wavelengths between 200 and 600 nm) of different fullerene solutions and standards in *n*-hexane as measured by two-beam optical absorption spectroscopy (using *n*-hexane as a reference). The fullerene solutions analyzed are pure C_{60} (Fig. 5.16a), 'pure' C_{70} (Fig. 5.16b) and the two different $C_{60/70}$ mixtures (mixtures **1** and **2**, figs. 5.16c and 5.16d). C_{60} in *n*-hexane exhibits four characteristic absorption peaks that arise from interband transitions among the π orbitals [5.27]. One of these is a distinct absorption feature in the range of 400 to 410 nm (see arrow in fig. 5.16a), whereas C_{70} shows a characteristic absorption feature between 370 and 390 nm (see open arrow in fig. 5.16b). Both features are present in absorption spectra of solutions of fullerene mixtures **1** and **2** (arrows in figs. 5.16c and 5.16d), in addition to peaks common to both species. Although figs. 5.16c and 5.16d confirm the presence of fullerene mixtures, no accurate quantitative information concerning the C_{70}/C_{60} ratio can be obtained from these spectra.

5.3.2.3 High-pressure liquid chromatography

High pressure liquid chromatography (HPLC) has been used to determine the C_{70}/C_{60} ratios in the mixed powders prior to sublimation. Analyses¹⁴ are performed on hexane

¹⁴The HPLC work has been done by M. Felder and C. Bolm, Organic Chemistry Institute, University of Basel, St. Johanns-Ring 19, CH-4056 Basel (Switzerland).

solutions of *thoroughly* dissolved fullerene mixtures to assure analysis of *total* fullerene content. In addition, HPLC analysis has been performed on samples of pure C_{60} and 'pure' C_{70} , the latter of which was found to contain 6-8% C_{60} in these HPLC measurements.

The results of the HPLC measurements are compiled in Table 5.1. Values for the percentage of C_{70} in the mixtures are reported both as a direct integration of peak area, and corrected for differences in extinction coefficients of C_{60} and C_{70} at 280 nm (by a factor of 1.2 [5.23]). Both powder mixtures **1** and **2** contain roughly 1 : 4, $C_{70} : C_{60}$. Mixture **1** contains a slightly higher percentage of C_{70} than mixture **2**.

Comparison of these C_{70}/C_{60} ratios in fullerene powders to those determined by STM on sublimed fullerene films (section 5.3.5) provides an indication of the transfer ratio of the two species in the sublimation process.

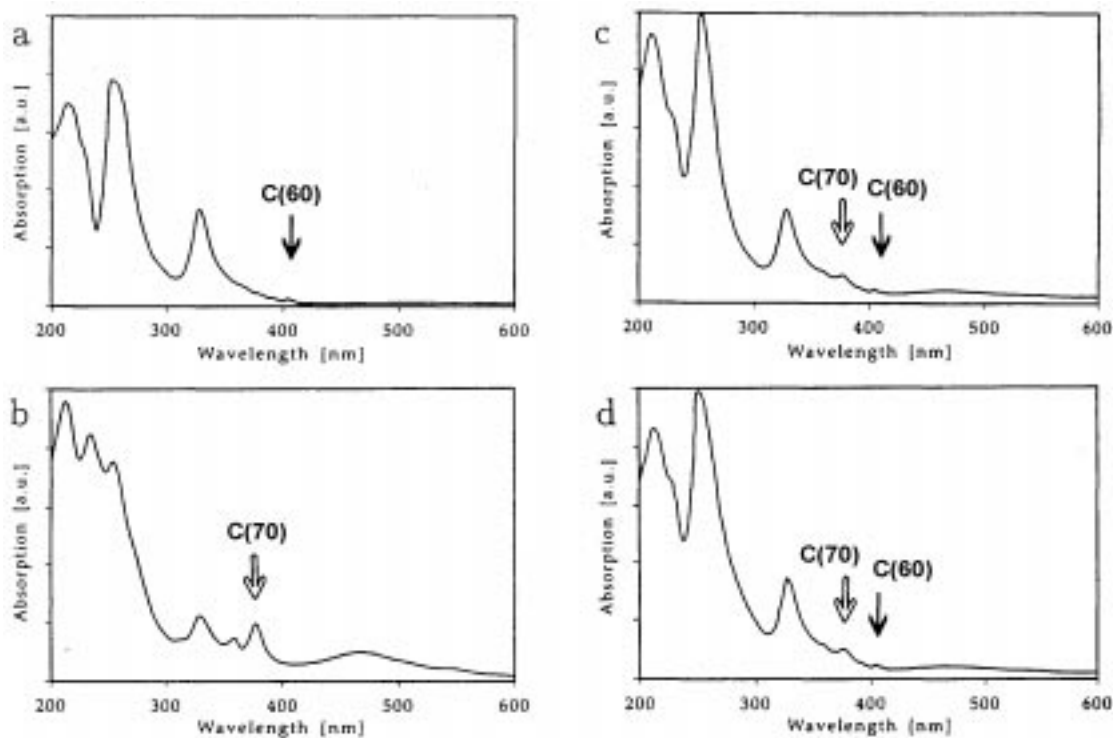


Figure 5.16: Optical absorption spectra of fullerene solutions in *n*-hexane. Characteristic features are marked by arrows. (a) pure C_{60} , (b) pure C_{70} , (c) $C_{60/70}$ mixture **1**, (d) $C_{60/70}$ mixture **2**.

5.3.3 STM images of Au(111) substrates

Gold thin films in (111) orientation on mica exhibit by STM flat terraces of often triangular shape due to gliding planes generated by the rapid cooling in water during production of the films. The terrace width may be as large as half a micron, but is often smaller. Figure 5.17 shows STM images of quenched Au(111) films. The (111) orientation of the films is evidenced by the XRD pattern in fig. 5.18.

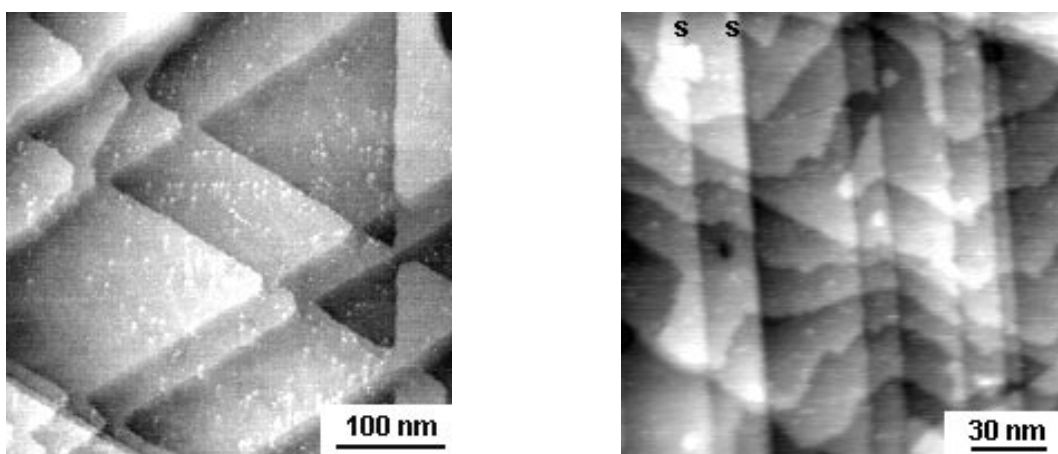


Figure 5.17: STM images of Au(111) surfaces with triangular terraces. Gliding planes cause parallel steps 's' visible in the picture on the right.

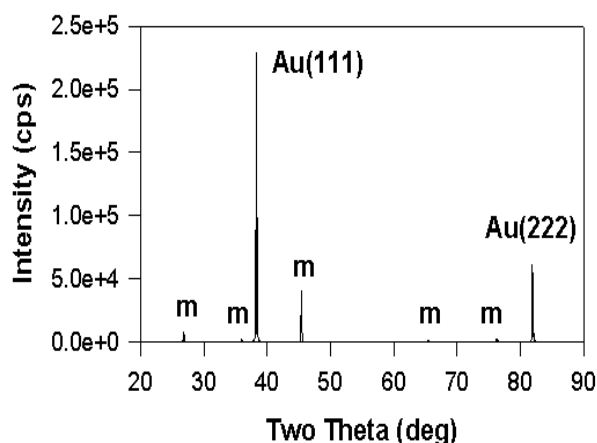


Figure 5.18: Cu K_{α} XRD pattern of a Au(111) film on mica. Mica substrate peaks are labelled 'm'.

5.3.4 Step structure of fullerene films

The surfaces of fullerene thin films on Au(111) substrates obtained by the sublimation process described above have been imaged by scanning tunneling microscopy (STM).

STM reveals that the $C_{60/70}$ thin film samples consist of crystalline $C_{60/70}(111)$ do-

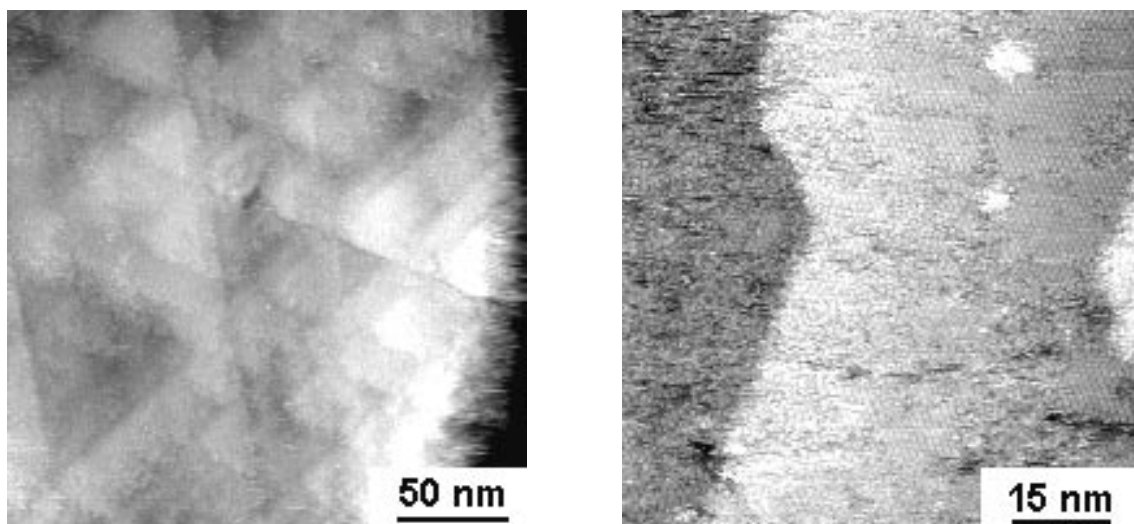


Figure 5.19: *LEFT:* Large scale view of a fullerene film on Au(111). The triangular shape of the gold terraces is still clearly visible. *RIGHT:* More detailed view of the fullerene terraces.

mains with a lateral extent of a few hundred nanometres, an area consistent with the average size of the Au(111) terraces (see fig. 5.19). The observation of the hexagonal $C_{60/70}(111)$ pattern over large areas suggests epitaxial growth of $C_{60/70}$ on Au(111).

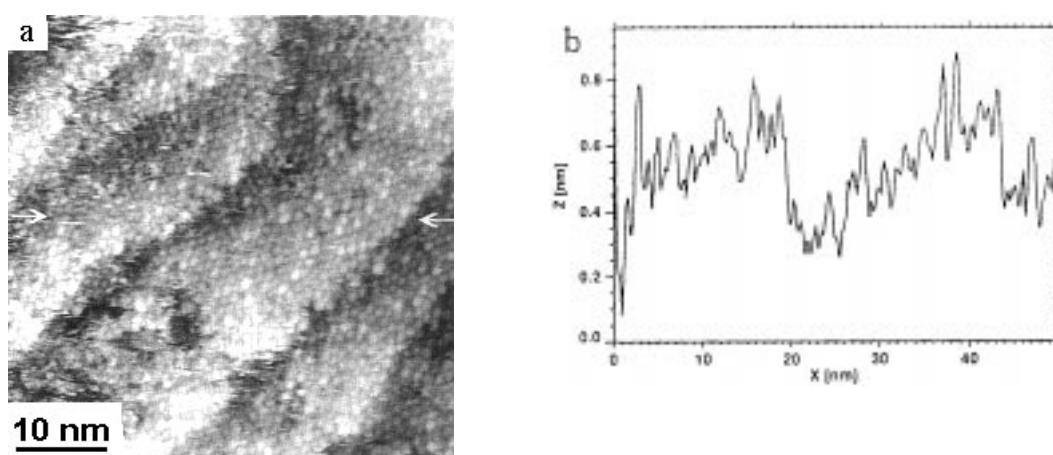


Figure 5.20: (a) Terrace and step structure of a fullerene thin film on Au(111) prepared from fullerene mixture 1. A scanline (between arrows) is displayed in (b). Step heights observed are about 0.25 to 0.5 nm and correspond to single and double gold steps in the Au[111] direction.

Figure 5.20a shows a STM image of an area of $50\text{ nm} \times 50\text{ nm}$ of the surface of a $\text{C}_{60/70}$ thin film on Au(111) (fullerene mixture 1). The terrace and step structure in this image is due to the terraced step structure of the Au(111) substrate as can be inferred from the line section in fig. 5.20b. The step heights of about 0.25 to 0.5 nm correspond to a single or double step height of gold in the Au[111] direction (0.2355 nm). The edges of the fullerene terraces can be resolved into individual molecules demonstrating the presence of kinks (fig. 5.21).

The observation of steps with heights of single or multiple substrate steps instead of fullerene step heights, and the fact that no STM images can be obtained from thick fullerene films (not conductive) leads to the conclusion that the actual thickness of these films is only 1–2 monolayers. As will be discussed later, films prepared with a slightly reduced deposition time show coverages of less than one monolayer by STM.

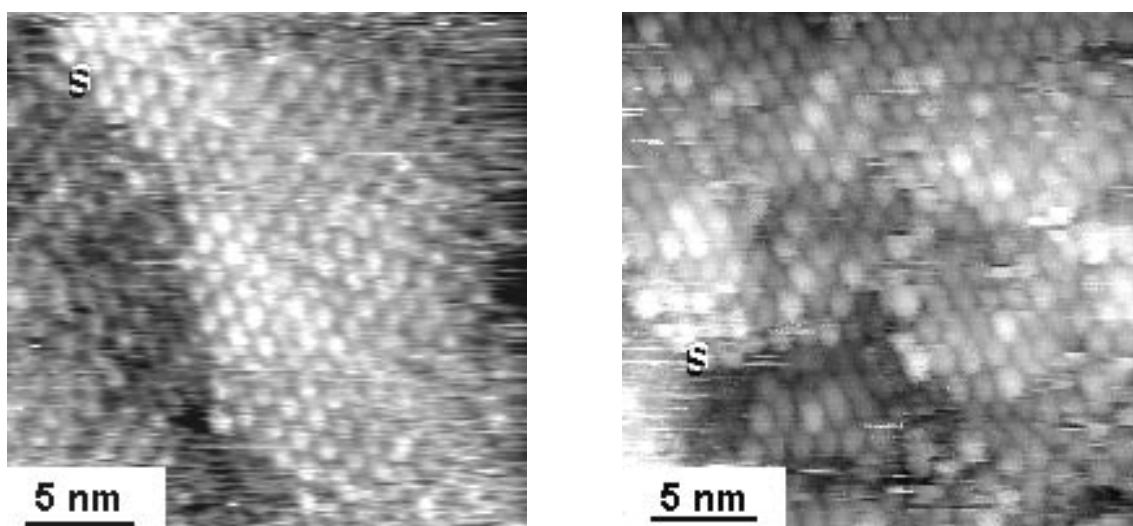


Figure 5.21: Detailed view of fullerene terrace edges. The heights of the steps 's' are identical to those of Au(111) monosteps.

5.3.5 Fullerene films of pure C(60) and mixtures C(60)/C(70)

Figure 5.22 shows three STM images of fullerene thin films differing in C_{70} content. Fig. 5.22a displays the molecularly resolved surface of a fullerene film prepared from pure C_{60} starting material. The ball-shaped molecular units are interpreted to be C_{60} molecules. They have a uniform shape. The molecules form a pattern of hexagonal symmetry ((111) face of the fcc lattice) with a nearest-neighbour-distance of 1 nm. The molecules have an apparent diameter of 0.7 nm and show molecular corrugations (peak to peak) of about 0.2 nm. They appear smooth due to the fast rotation at room temperature.

However, films prepared from fullerene mixtures exhibit a molecular pattern of hexagonal symmetry consisting of two different kinds of molecules (figs. 5.22b and 5.22c):

molecules having an apparent diameter of 0.7 nm and a corrugation (peak to peak) of about 0.2 nm, and molecules having an apparent diameter of 0.8 nm and a corrugation of 0.3 nm. The three images shown in fig. 5.22 are representative of a series of images obtained from each sample. The molecules with a larger diameter and corrugation are assigned to C_{70} molecules and the smaller ones to C_{60} molecules. The C_{70}/C_{60} ratio has been determined from the STM image by counting the numbers of smaller and larger molecules.

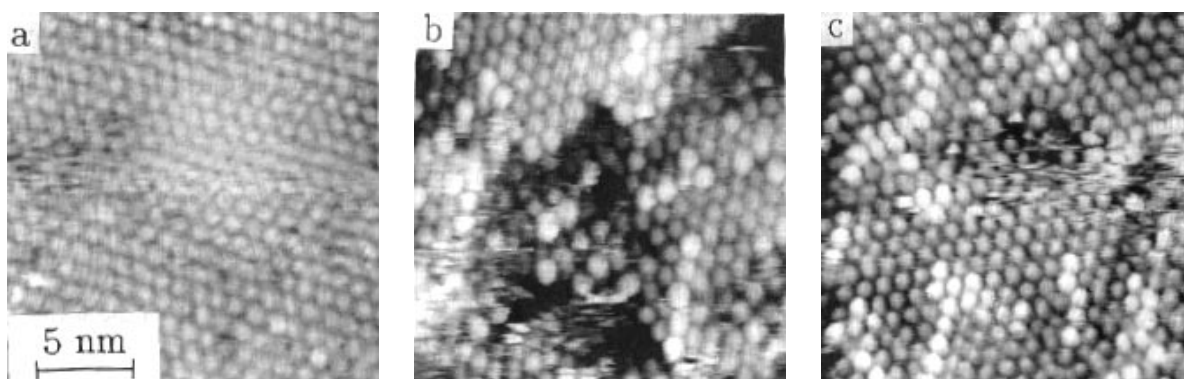


Figure 5.22: STM images of thin fullerene films on Au(111) prepared by sublimation from different fullerene powders. (a) pure C_{60} . The ball-shaped features correspond to C_{60} molecules (apparent diameter: 0.7 nm) arranged in a hexagonal lattice (nearest-neighbour-distance: 1 nm). (b) C_{60}/C_{70} mixture 1. The molecules appearing brighter in the STM image have a larger corrugation than the C_{60} molecules and are interpreted as C_{70} molecules. (c) C_{60}/C_{70} mixture 2.

A three-dimensional rendition of a STM image of a mixed C_{60}/C_{70} film is shown in fig. 5.23a. Compare to the wire models of C_{60} and C_{70} displayed in fig. 5.23b.

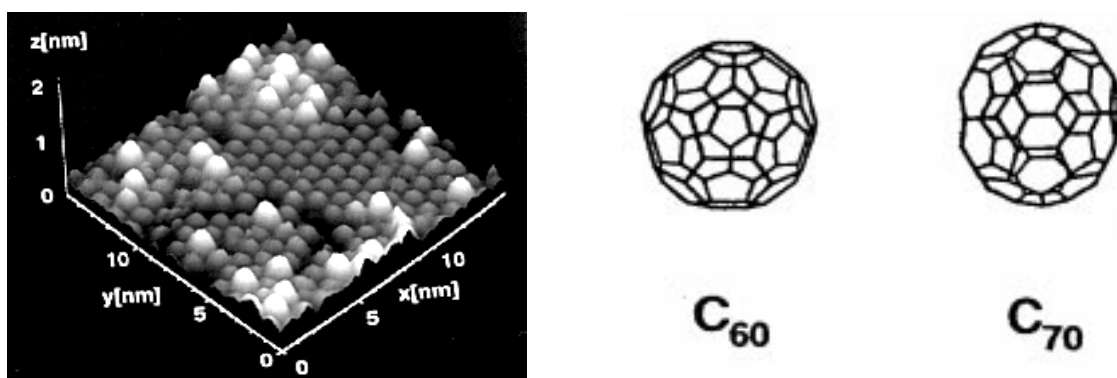


Figure 5.23: (a) Three-dimensional representation of an area of $15 \times 15 \text{ nm}^2$ of the surface of a C_{60}/C_{70} film on Au(111). The molecules appearing brighter are C_{70} molecules, the darker ones are C_{60} molecules. (b) Wire-models of C_{60} and C_{70} fullerene molecules.

The prolate shape of the C_{70} fullerene is clearly different from the purely spherical shape of the C_{60} fullerene. The longest axis of the C_{70} fullerene is also the favoured rotation axis. Thus it is not surprising that the C_{70} fullerenes in the $C_{60/70}$ film are oriented with their longest axis perpendicular to the Au(111) surface.

Table 5.1 (p. 185) gives a summary of the results obtained from a statistical analysis of STM images acquired from 5 regions of each sample. The results are to be compared to those obtained by HPLC (see 5.3.1.6) in solutions of the unsublimed powders. In both mixtures **1** and **2**, the C_{70} content of the films is considerably lower than in the corresponding powder prior to sublimation. Surprisingly, the HPLC results indicate a slightly higher percentage of C_{70} in mixture **1** than in **2**, whereas the STM results show the reverse ordering. This is possibly due to the fact that the ratio determined by STM is obtained from a very small area of the sample and the statistical uncertainty is of a few percent. The observed differences between HPLC and STM ratio might be explained by differences in sublimation rates of the two species. It is important to keep in mind that the C_{70}/C_{60} ratio in films depends on various preparation parameters, such as the distance between fullerene powder and substrate in the sublimation apparatus and the temperature-gradient applied. These issues are treated in the following sections.

5.3.6 Variation of sublimation parameters

As demonstrated above the quantitative evaluation of STM images of $C_{60/70}$ thin films by counting C_{70} and C_{60} molecules yields a local value of the C_{70}/C_{60} ratio. In the following this ratio is studied as a function of sublimation distance and substrate temperature.¹⁵ This values are compared to those determined by UV-VIS spectroscopy on dissolving the fullerene films in *n*-hexane.

In most cases more than 20 images acquired from different areas of the film surface were evaluated and the C_{70}/C_{60} ratio determined. The values for the C_{70}/C_{60} ratios given in this work represent the average values. The corresponding standard deviation of the individual values is a measure for the error.

C_{70} content histograms for two films prepared at different substrate temperatures (200°C and 275°C), but at the same sublimation distance ($d = 3$ cm) are shown in fig. 5.24. The abscissa is the C_{70} content and the ordinate is the number of occurrence of a certain C_{70} content interval (2 percent). Typical STM images obtained from the two samples are shown in fig. 5.25 in a three-dimensional rendition. It is obvious from the image that the C_{70} content is larger in the film prepared at a higher substrate temperature.

The C_{70}/C_{60} ratio cannot only be determined from STM images by *counting the molecules*, but also by *integration of the brightness distribution*. The brightness distribution in a STM image is identical to the height distribution of the topography. Since

¹⁵The C_{70}/C_{60} ratio of the sublimed powder was constant for each series of experiments: $C_{70}/C_{60} = 0.236$ for the experiment of varying the sublimation distance and $C_{70}/C_{60} = 0.182$ for variation of substrate temperature.

only C_{70} molecules provide the big height values it should be possible — in principle — to obtain back the C_{70}/C_{60} ratio from the height distribution (see fig. 5.26 for explanation). The hollow sites of the C_{60} matrix have to be considered, too. This method actually works, but suffers from a large inaccuracy ($C_{70}/C_{60} = 0.2 \pm 0.05$). For that reason this idea will no longer be pursued.

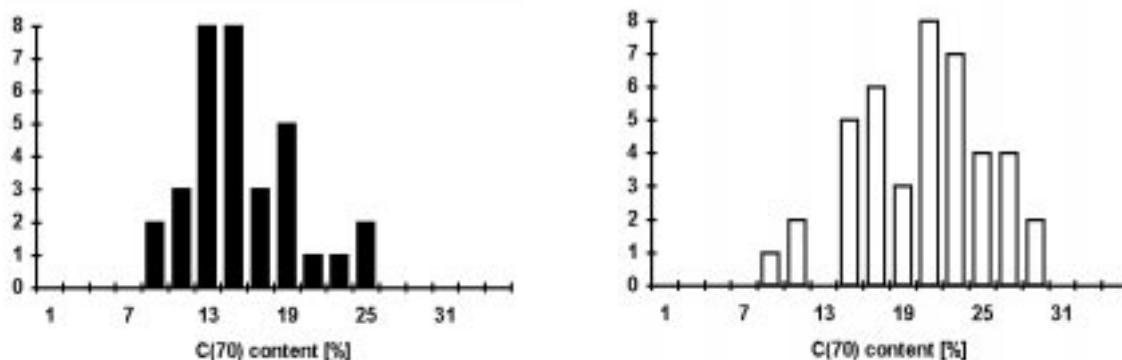


Figure 5.24: *LEFT:* C_{70} content histogram for a $C_{60/70}$ film prepared at 200°C. *RIGHT:* C_{70} content histogram for a film grown at 275°C.

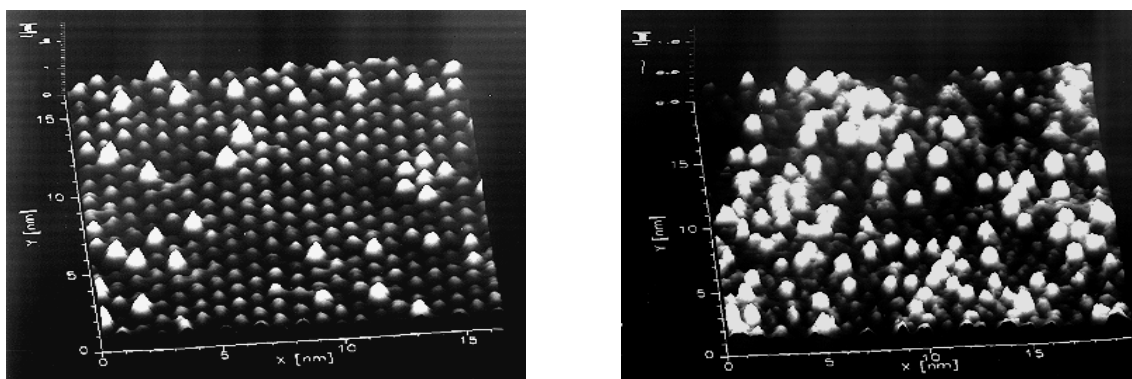


Figure 5.25: *LEFT:* 3D-STM image of a $C_{60/70}$ film showing a small C_{70} content ($T_{substr} = 200^\circ\text{C}$). *RIGHT:* 3D-STM image of a film with a large C_{70} content ($T_{substr} = 275^\circ\text{C}$).

In order to test the method of determining the C_{70}/C_{60} ratio by counting C_{60} and C_{70} molecules on STM images of the film surface and relate the result to UV-VIS spectroscopy data, fullerene thin films from pure C_{60} and pure C_{70} have been prepared. The sublimation conditions were as follows: $T_{subl} = 360^\circ\text{C}$, $T_{substr} = 225^\circ\text{C}$, and $d = 3\text{ cm}$.

Figure 5.27 shows typical STM images obtained from such films. Figure 5.27a shows the surface of a pure C_{60} film consisting of ball-shaped molecules arranged in an array with threefold symmetry ($C_{60}(111)$ face). A similar situation is encountered for a film prepared from pure C_{70} (fig. 5.27b): Only one species of molecules is observed. $C_{70}(111)$

faces do not seem to be as smooth as $C_{60}(111)$ faces. The reason for the poorer image quality may be due to the prolate shape of C_{70} .

UV-VIS absorption spectroscopy is a reliable method to trace C_{60} and C_{70} in solu-

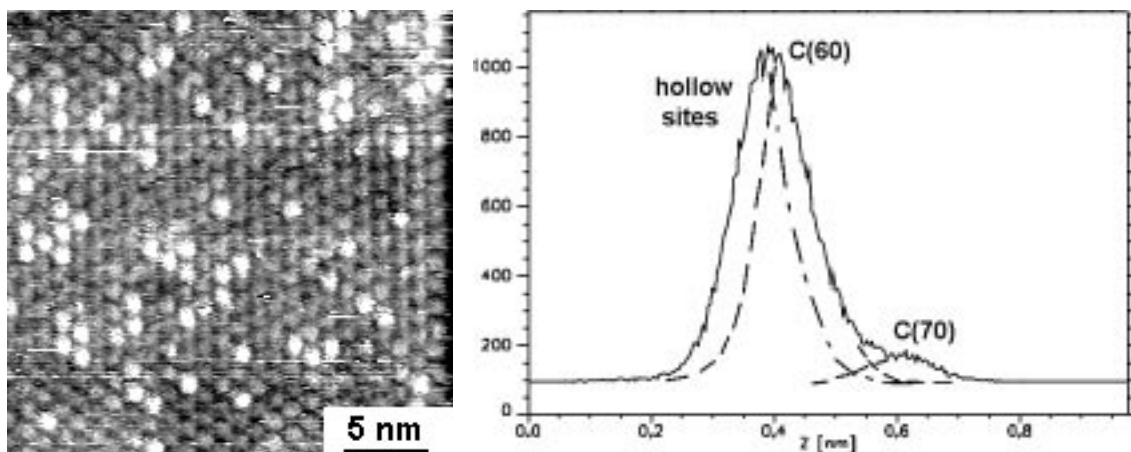
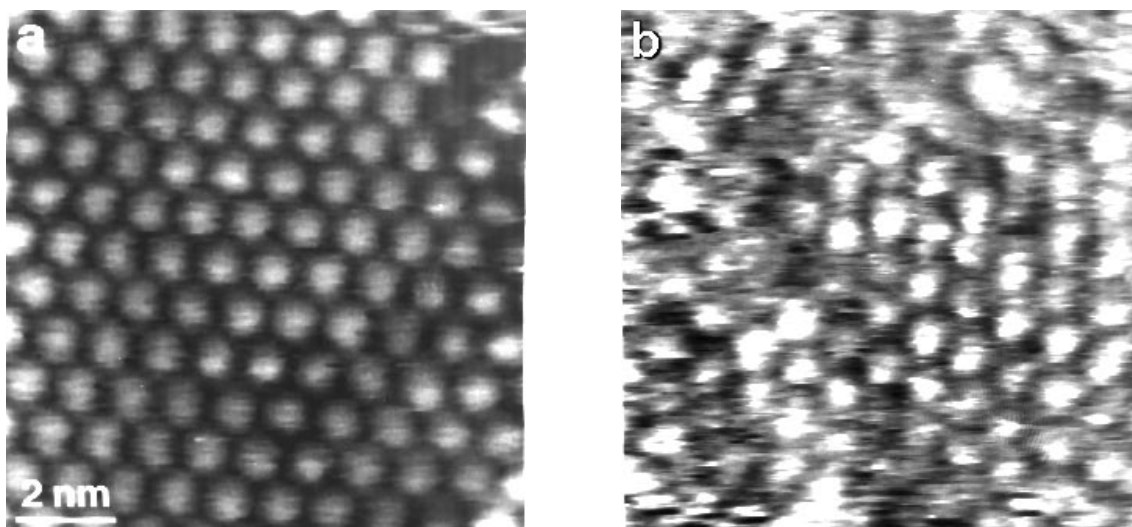


Figure 5.26: *LEFT:* STM topview image of a $C_{60/70}$ film. *RIGHT:* The brightness (height) distribution histogram is composed of three peaks attributed to C_{60} , C_{70} (dashed lines) and the hollow sites of the matrix (dash-dotted line). By integrating the three peak areas a C_{70}/C_{60} ratio may be determined in principle ($C_{70} : C_{60} = 0.2 \pm 0.05$).

tions [5.26]. Due to the high symmetry of the C_{60} and C_{70} molecules, the UV-VIS spectra can be predicted very accurately [5.29, 5.30].



(continued on following page)

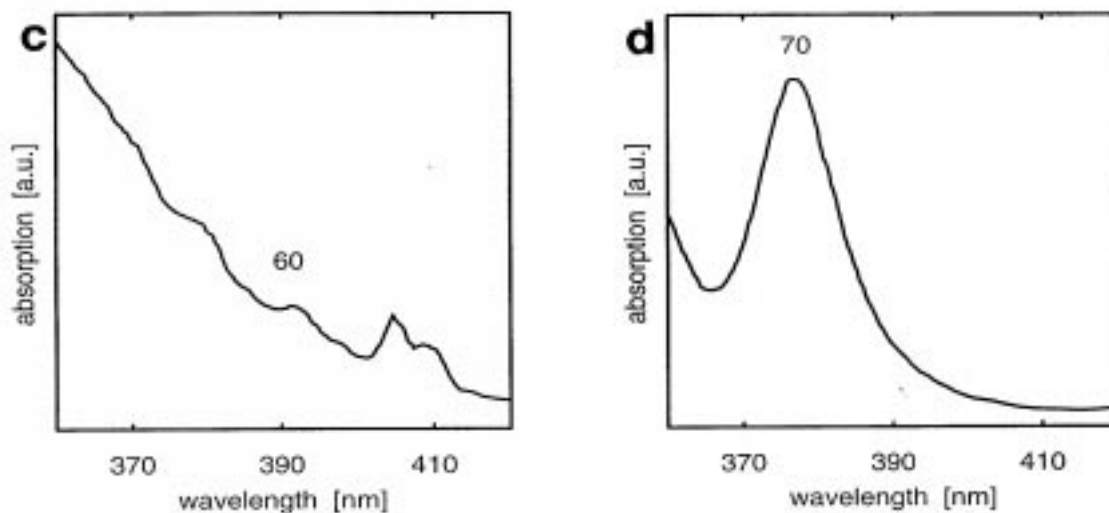


Figure 5.27: (a) STM image of the surface of a fullerene thin film prepared from pure C₆₀. (b) STM image of a thin film prepared from pure C₇₀. (c) Part of a UV-VIS absorption spectrum of a *n*-hexane solution of the pure C₆₀ film shown in (a) with an absorption feature close to 390 nm typical of C₆₀ (labeled by '60'). (d) UV-VIS spectrum of a *n*-hexane solution of the C₇₀ film shown in (b) with a characteristic absorption feature close to 375 nm (labeled by '70').

The UV-VIS absorption spectra of *n*-hexane solutions obtained from C₆₀ and C₇₀ films show optical absorption features typical of C₆₀ (the feature close to $\lambda = 390$ nm is labeled with '60' in fig. 5.27c) and C₇₀ (a peak close to $\lambda = 375$ nm is marked with '70' in fig. 5.27d). Although these features are comparatively weak they ensure an unambiguous identification of C₆₀ and C₇₀. More intense absorption features in the range of wavelengths between 200 and 350 nm cannot be used for a clear identification of the two fullerene species because the peaks overlap (see also fig. 5.16c and d). These STM images and UV-VIS spectra of pure C₆₀ and C₇₀ are used as a reference standard for the investigation of fullerene films prepared from mixtures of C₆₀ and C₇₀ with varying parameters for film growth like T_{substr} and d .

5.3.7 Variation of sublimation distance

The separation of fullerenes by the sublimation of C_{60/70} powder in the temperature gradient of a furnace is an effective method to obtain purified C₆₀ and C₇₀. This issue was studied in a sublimation experiment by Cox *et al.* [5.31] using UV-VIS spectroscopy. The C₇₀/C₆₀ ratio of deposits obtained by the sublimation in a temperature gradient (600 °C along 45 cm) was found to vary as a function of the sublimation distance. The sublimes enriched in C₇₀ are observed in the hot part of the sublimation tube (short sublimation distance) whereas the deposits with a low C₇₀ content are condensed at the colder end of the tube (long sublimation distance).

To study this issue on a molecular scale the effects of the substrate temperature T_{substr} as well as of the sublimation distance d have to be considered.¹⁶ A calculation based on vapour pressure data of C_{60} and C_{70} [5.32, 5.33] has shown that the ratio of the vapour pressures of C_{60} and C_{70} is almost constant in the range of T_{substr} in question (200 - 275 °C) so that the C_{70}/C_{60} ratio is not significantly affected by the different vapour pressures of the two fullerene species.

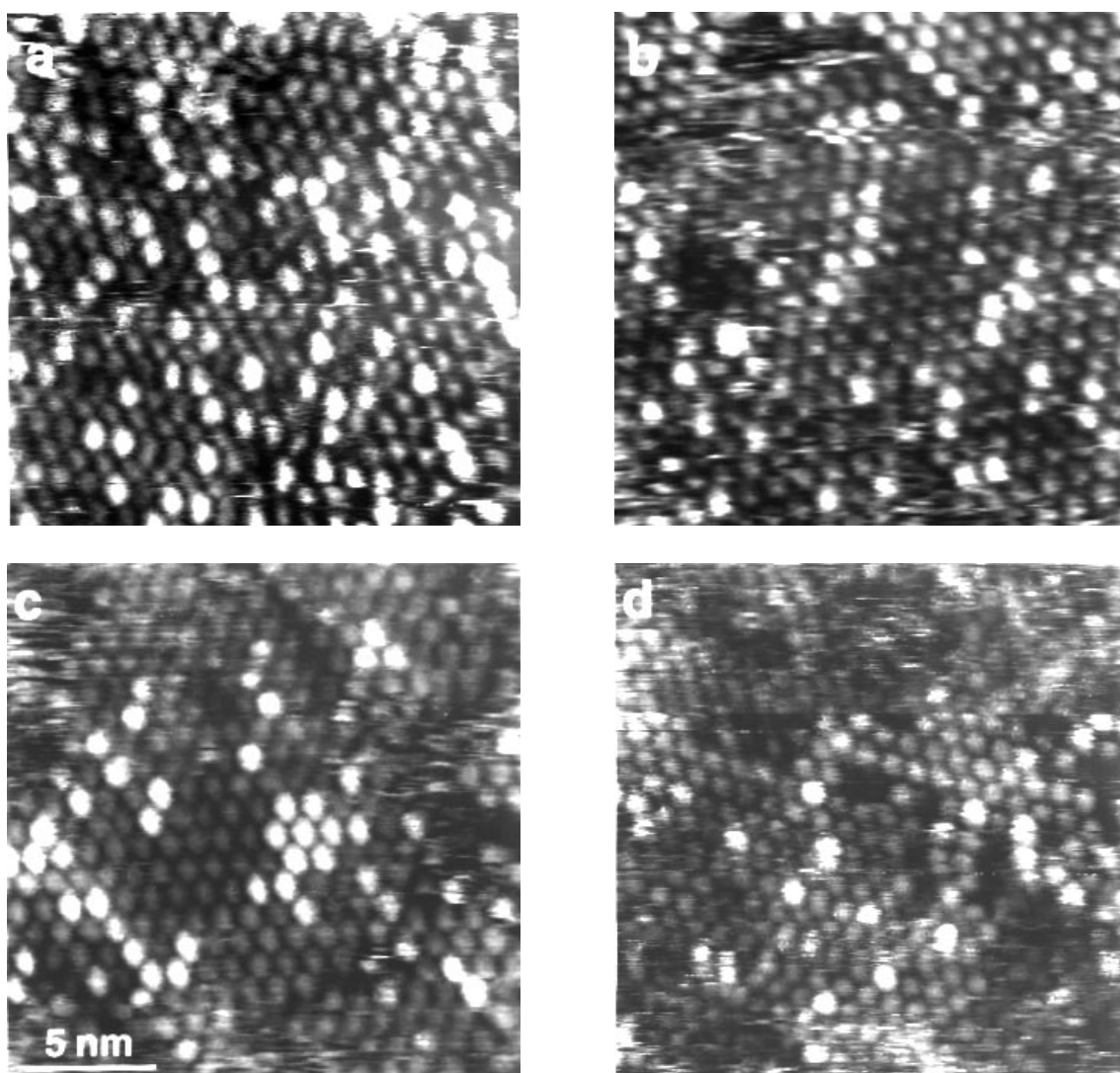


Figure 5.28: Series of four STM topview images showing the dependence of the sublimation distance d on the C_{70}/C_{60} ratio: (a) $d = 3$ cm, (b) $d = 5$ cm, (c) $d = 10$ cm, (d) $d = 15$ cm. The C_{70} content in the films decreases with increasing sublimation distance.

¹⁶These experiments have been performed by K.M. Heeger, summer student from St. Edmund Hall, University of Oxford, OX1 4AR (Great Britain), during a stay at the Physics Institute at Basel University.

The sublimation distance d was varied in the range of 3 to 15 cm with intermediate values at 5 and 10 cm. The temperature homogeneity range in the sublimation vessel is only provided up to a distance d of about 15 cm. Distances smaller than 3 cm are excluded because of geometrical restrictions.

Figure 5.28 shows four STM topview images of fullerene thin films prepared at $T_{substr} = 225$ °C and $T_{subl} = 360$ °C from a $C_{60/70}$ source with a C_{70}/C_{60} ratio of 0.236 (HPLC). The sublimation distance was increased from (a) 3 cm, (b) 5 cm, (c) 10 cm to (d) 15 cm. Counting the C_{70} and C_{60} molecules yields a decrease of the C_{70} content with increasing sublimation distance d . This issue is quantified in the graph shown in fig. 5.29b. The error bars represent the standard deviation of the individual C_{70}/C_{60} ratios (determined by counting of molecules) from the average value. The same dependence of the C_{70}/C_{60} ratio on d is observed by UV-VIS spectroscopy (fig. 5.29a). The intensity of the C_{70} peak is diminishing with increasing sublimation distance ('A' to 'D') whereas the C_{60} feature is growing.

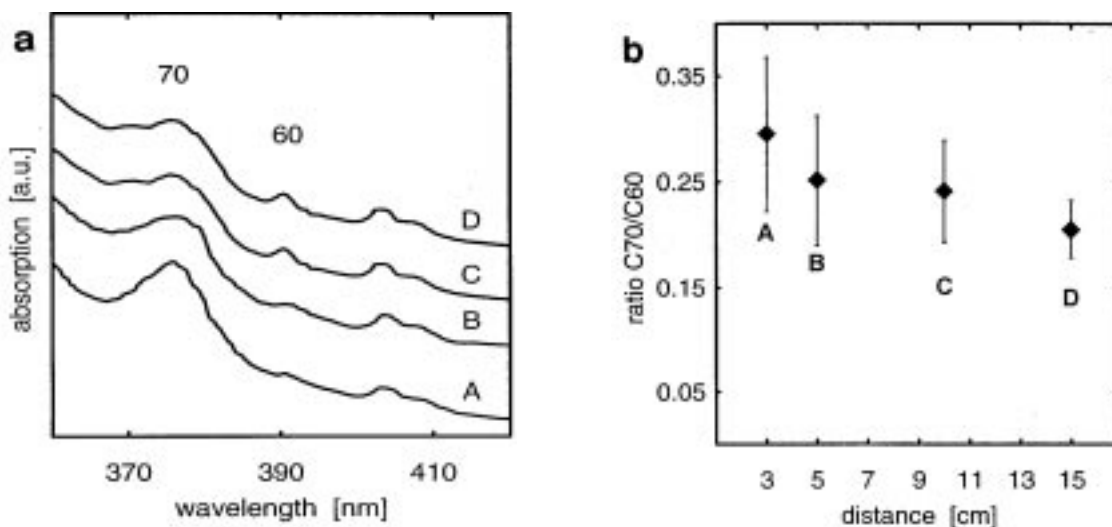


Figure 5.29: (a) UV-VIS spectra of the fullerene solutions in n -hexane obtained from the films shown above. The labels '60' and '70' indicate the location of absorption features typical of C_{60} and C_{70} , respectively. The letters 'A', 'B', 'C' and 'D' refer to the films prepared at $d = 3$ cm, 5 cm, 10 cm and 15 cm. The intensity of the feature labeled '70' decreases with increasing sublimation distance d implying a decrease of the C_{70} content. The intensity of the feature labeled '60' is increasing with d . (b) C_{70}/C_{60} ratios by counting the two species of molecules in STM images of films prepared at different sublimation distances d . The diamond symbols represent the average of the ratios determined from several images. The error bar is the standard deviation from the average value.

5.3.8 Variation of substrate temperature

The substrate temperature T_{substr} was varied in the range of 200 to 275 °C, in steps of 25 °C. Lower substrate temperatures have been found to yield preferably disordered films which could not be used for a clear determination of the C_{70}/C_{60} ratio using the method of counting the molecules. Higher T_{substr} leads to an incomplete coverage of the substrate surface due to the smaller sticking probability of the fullerene molecules at elevated temperatures being comparable to T_{subl} .

Figure 5.30 shows four STM topview images of films prepared at $d = 3$ cm and $T_{subl} =$

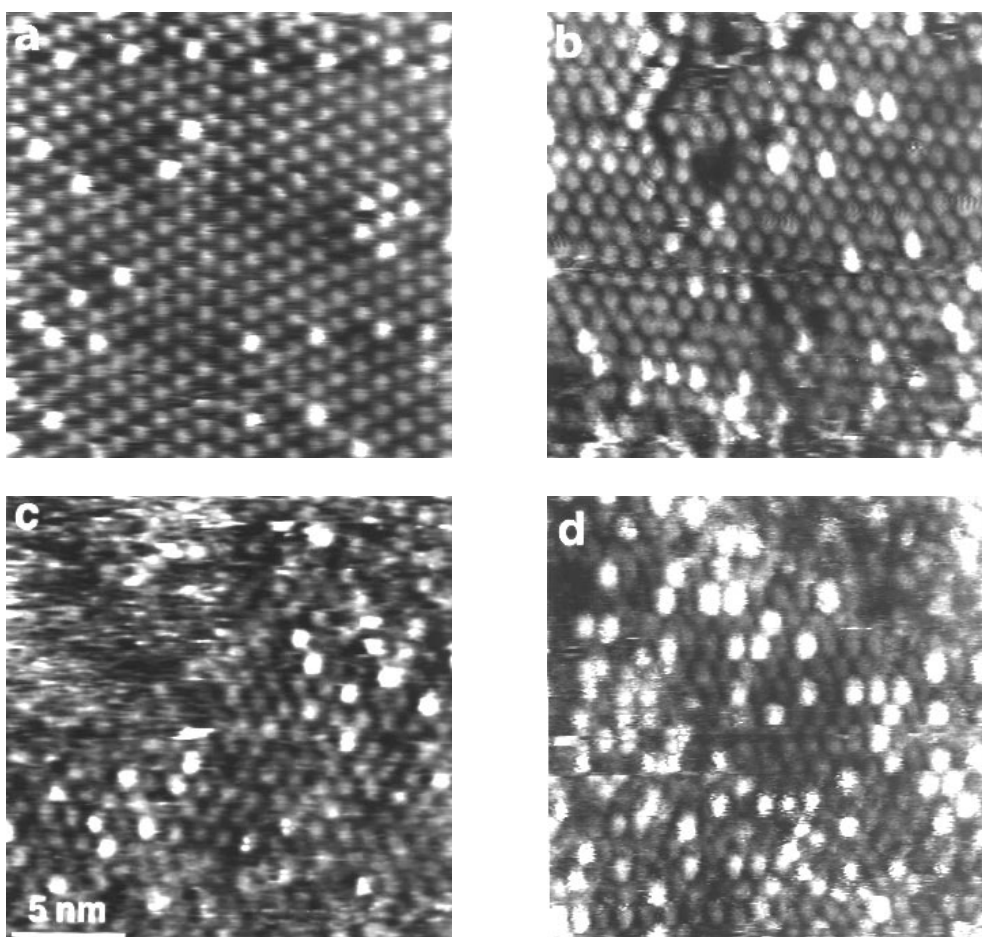


Figure 5.30: Series of four STM topview images showing the dependence of the substrate temperature T_{substr} on the C_{70}/C_{60} ratio: (a) $T_{substr} = 200$ °C, (b) $T_{substr} = 225$ °C, (c) $T_{substr} = 250$ °C, (d) $T_{substr} = 275$ °C. The C_{70} content in the films increases with increasing substrate temperature.

360 °C. A $C_{60/70}$ source was used with a C_{70}/C_{60} ratio of 0.182 (determined by HPLC). With increasing substrate temperature (images (a) 200 °C, (b) 225 °C, (c) 250 °C, (d) 275 °C) the C_{70}/C_{60} ratio is observed to increase. The same tendency is found in the UV-VIS spectra of *n*-hexane solutions of the fullerene sublimates (fig. 5.31a). Figure 5.31b

shows the dependence of the C_{70}/C_{60} ratio on the substrate temperature as determined by counting C_{60} and C_{70} molecules imaged by STM.

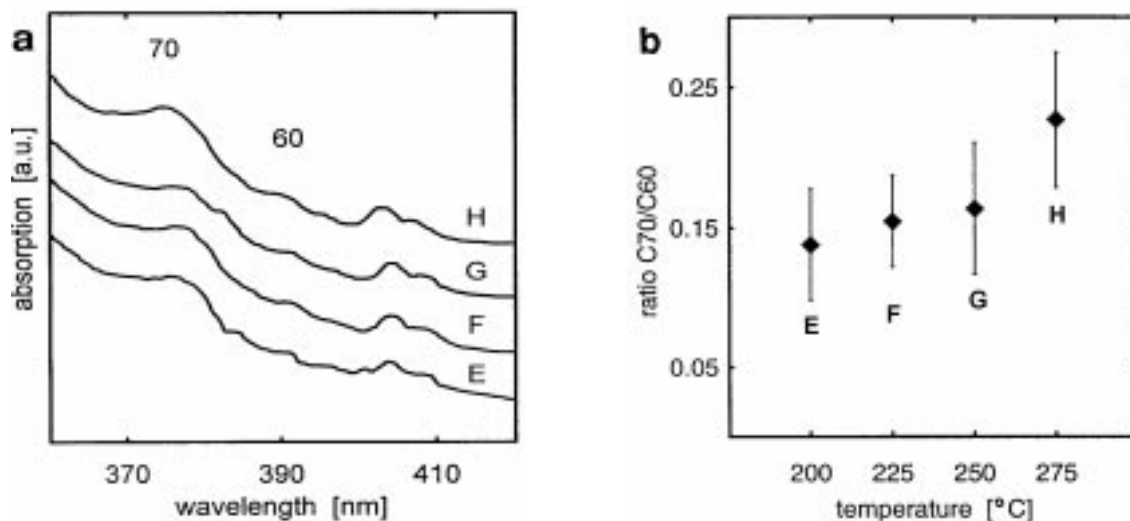


Figure 5.31: (a) UV-VIS spectra of the fullerene solutions in *n*-hexane obtained from the films shown above. The labels '60' and '70' indicate absorption features typical of C_{60} and C_{70} , respectively. The letters 'E', 'F', 'G' and 'H' identify the films prepared at $T_{substr} = 200$ °C, 225 °C, 250 °C and 275 °C. The intensity of the feature labeled '70' increases with increasing substrate temperature T_{substr} implying an increase of the C_{70} content. The intensity of the feature labeled '60' is decreasing with T_{substr} . (b) C_{70}/C_{60} ratios by counting the two species of molecules in STM images of films prepared at different substrate temperatures T_{substr} . The diamond symbols represent the average of the ratios determined in several images. The error bar is the standard deviation from the average value.

5.3.9 Dynamic processes

In fullerene films obtained from mixtures of C_{60} and C_{70} , dynamic rearrangement processes of the surface have been observed by monitoring the relative positions of the C_{70} molecules in successively recorded STM images. The following STM images can also be found in [5.34]–[5.36]. Figure 5.32 shows a set of 6 STM images (fig. 5.32a – 5.32f) recorded at time intervals of 15 seconds. Position changes of individual C_{70} molecules (indicated by small arrows) in the $C_{60}(111)$ host lattice can be easily pursued in figs. 5.32a - 5.32f. In particular, the rearrangement processes can be studied in the example of a 'f'-shaped feature in the STM images (marked by an open arrow in fig. 5.32a). Such rearrangement processes might possibly be induced by the high electric field (about 10^6 V/m) present between tip and sample or by tip-molecule interactions.

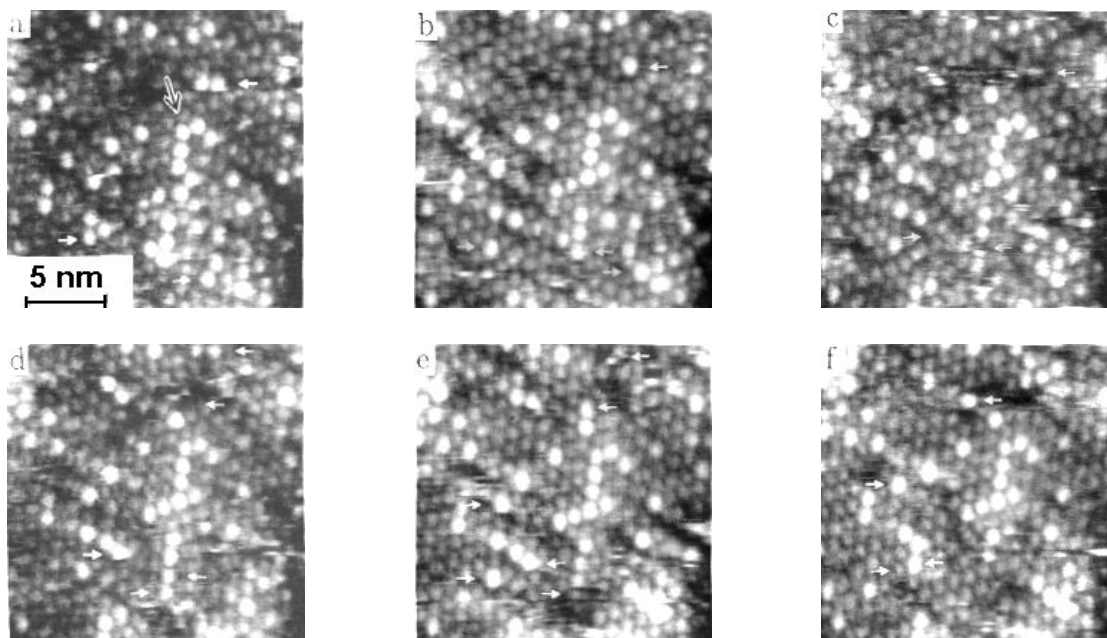


Figure 5.32: (a) – (f) STM images taken at intervals of 15 seconds. Dynamic rearrangements can be monitored by observing the relative positions of C_{70} molecules in successive images. Relative positions of particular C_{70} molecules in successive images are marked by small arrows. Note the evolution of the 'f' – shaped C_{70} feature (indicated by an open arrow) with time.

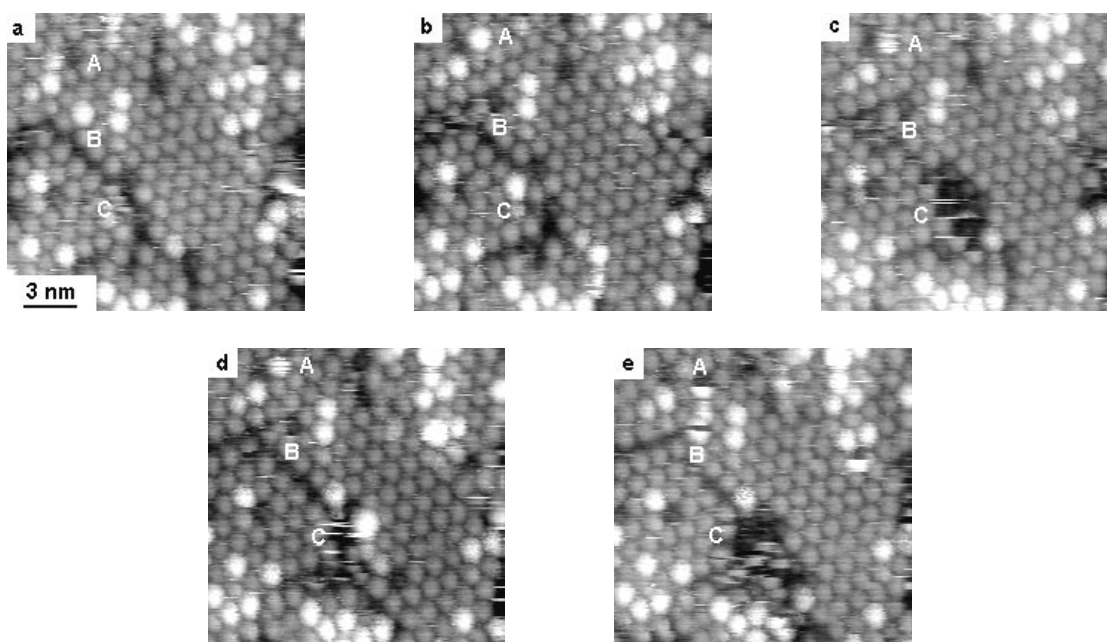


Figure 5.33: (a)–(e) Position changes of C_{70} molecules observed as a function of time. Acquisition time for each image in this sequence: 15 s.

On the other hand, thermally activated diffusion could be operative here. A further example of movement of C_{70} molecules is shown in fig. 5.33. Note the movement of C_{70} molecules in the upper left corner of the images. The time interval between successive images is 15 seconds. The vacancy 'A' in fig. 5.33a is occupied by a C_{70} molecule in fig. 5.33b. A C_{70} molecule at 'B' in fig. 5.33a is no longer on this lattice site in fig. 5.33b. Probably it diffused to site 'C', which was unoccupied before. Further C_{70} displacements can be followed in fig. 5.33a-f.

5.3.10 Variation of coverage

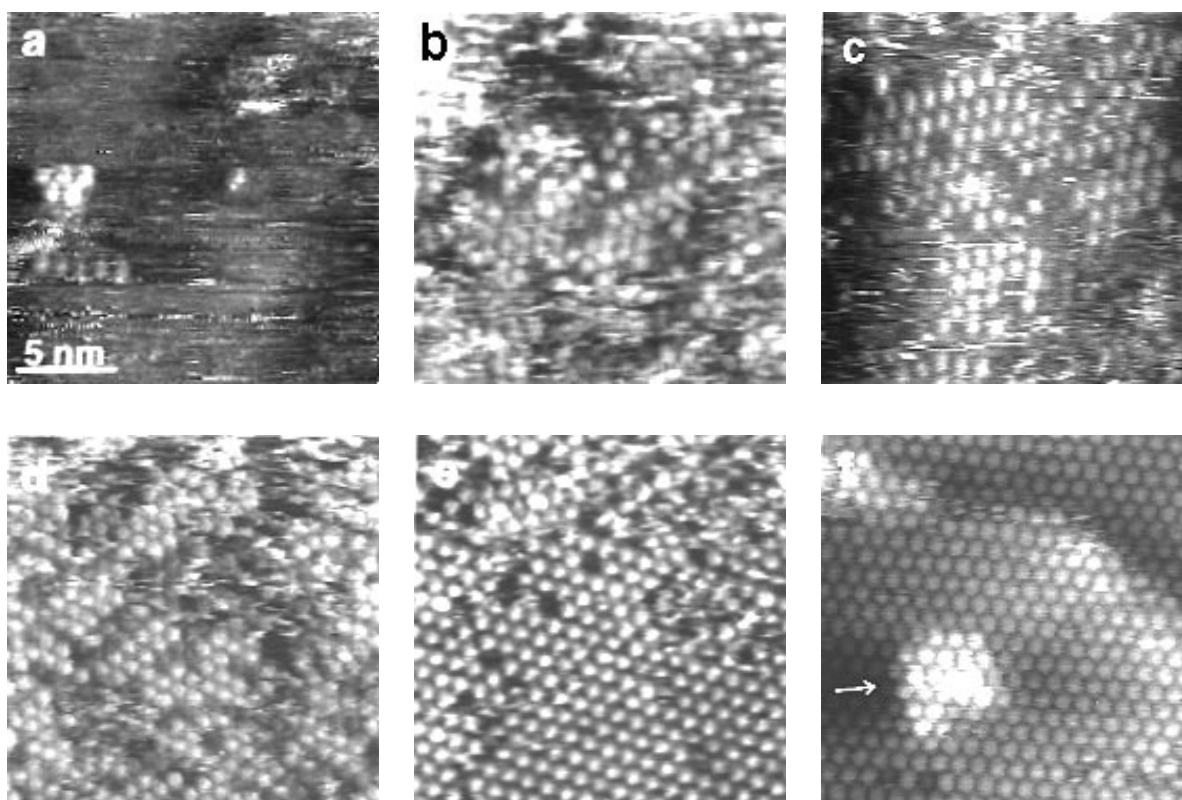


Figure 5.34: (a) – (f) STM images of C_{60} films at different coverages (initial islands to complete layer and growth of a second layer).

Figure 5.34 shows STM images of six C_{60} films prepared with different sublimation times, and hence with different coverages. Films a-e (figs. 5.34a-e) show a coverage of less than one monolayer (ML) of C_{60} , whereas a second layer (arrow) is observed for film f (fig. 5.34f). The sublimation times and coverages (determined by counting the C_{60} molecules in the STM images) are shown in fig. 5.35. The substrate temperature during sublimation is 220-230 °C.

As can be seen in the STM images, the fullerene molecules can also condense at seemingly random positions on flat Au(111) terraces. The nucleation of C_{60} at step edges has recently been investigated in detail under vacuum conditions by *Altman et al.* [5.37]. The layer formation leading to the $C_{60}(111)$ face with a hexagonal symmetry is observed (fig. 5.34a): a unit consisting of 5 molecules, although individual molecules are also observed with a relatively strong bonding to the Au(111) substrate compared with tip-molecule interaction.

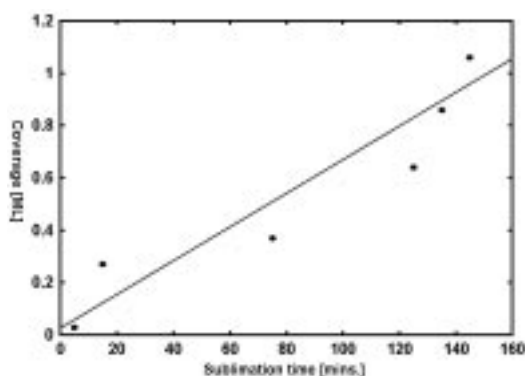


Figure 5.35: Preparation times and resulting coverage for submonolayer films. The line is a linear least-square fit. The correlation coefficient is 0.94.

In films prepared from a $C_{60/70}$ mixture similar islands are found to form. The C_{70} molecules are randomly distributed in the C_{60} layer (see fig. 5.36).

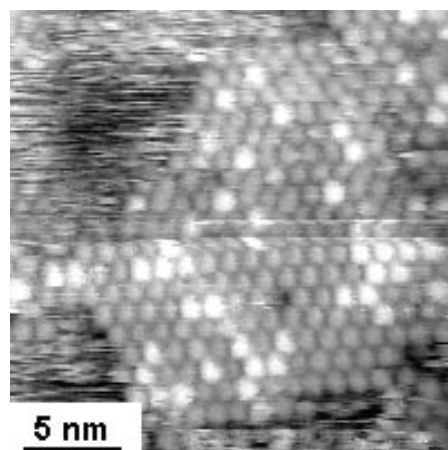


Figure 5.36: STM image of a $C_{60/70}$ island. No preferential sites for the C_{70} molecules are observed.

5.3.11 Lattice defects

5.3.11.1 Point defects

Surfaces of fullerene thin films exhibit a large number of defects such as vacancies and boundaries. Fig. 5.37 and 5.38 show STM images demonstrating two types of lattice point defects. Fig. 5.37a shows a perfect fcc $C_{60}(111)$ lattice with four vacancies (indicated by arrows). The STM line section (between arrows) in fig. 5.37b shows that one C_{60} molecule in the row is suppressed or missing (arrow and label 'V').

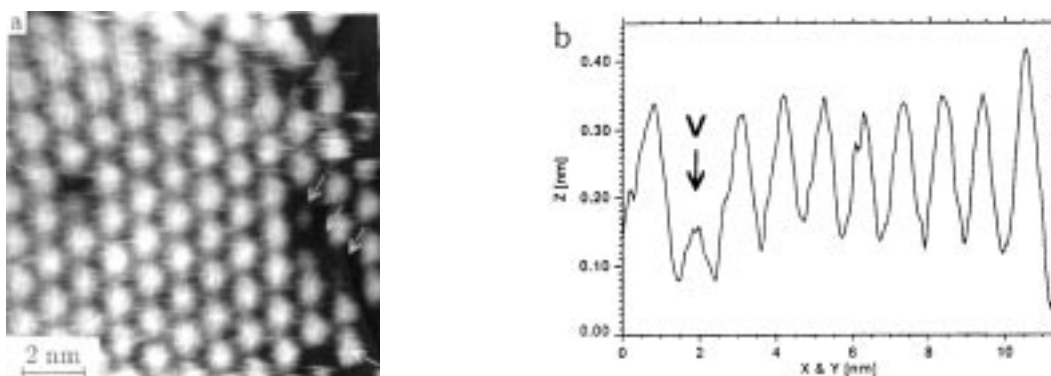


Figure 5.37: STM images and line sections of a fullerene thin film having lattice point defects. (a) Vacancies (indicated by arrows) in the fcc(111) face of a film prepared from pure C_{60} . The line section indicated by 2 arrows in (a) is displayed in (b). The vacancy is marked by an arrow.

Figure 5.38 is a sequence of 6 STM images recorded at intervals of 15 seconds: a vacancy (close to letter 'V' in fig. 5.38b) and an interstitial (in the centre of the black circle in fig. 5.38b). Interstitials in a fcc lattice are in most cases *split interstitials*, i.e. two molecules occupy a single regular lattice site. The long axis of a split interstitial is parallel to $\langle 100 \rangle$. Note that this interstitial is present and stable in the whole series of STM images in fig. 5.38. A line section crossing the vacancy and the interstitial is displayed in fig. 5.39. A schematic of a split interstitial is given in the same figure. Again, the molecules appearing brighter are C_{70} molecules. Dynamic rearrangement of C_{70} molecules is observed with time. A C_{60} molecule close to the position marked with 1 in fig. 5.38a is replaced by a C_{70} molecule in fig. 5.38b. In fig. 5.38a and 5.38c, a C_{70} molecule is observed close to position 2, whereas this lattice site is occupied by a C_{60} in fig. 5.38b.

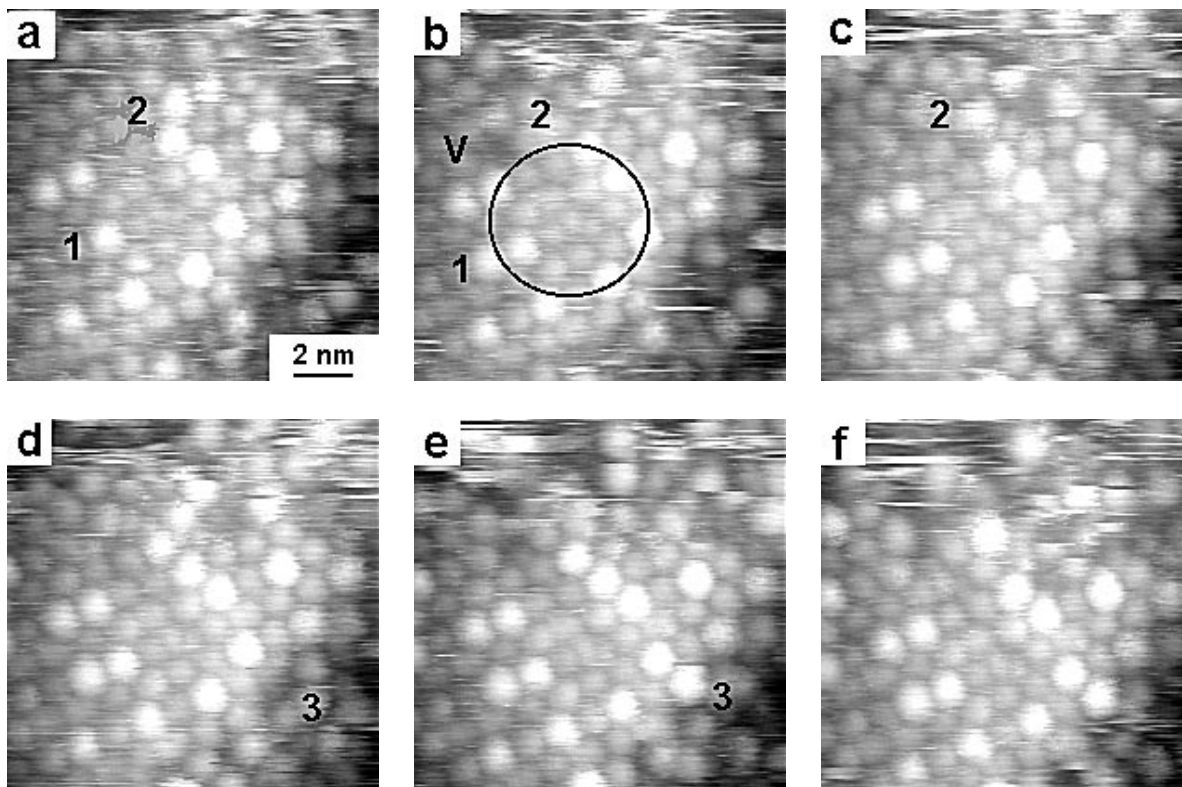


Figure 5.38: (a) – (f) Sequence of 6 STM images recorded at time intervals of 15 s showing rearrangement of C_{70} molecules and vacancies (marked by 1,2 and 3). Two types of lattice point defects are indicated in (b): a vacancy V and a split interstitial (centre of the circle).

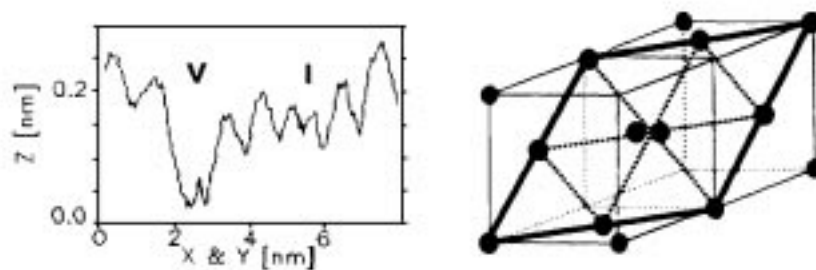


Figure 5.39: Line section crossing the vacancy site V and the interstitial site I. Model of a split interstitial in a fcc lattice. The (111) plane is highlighted.

5.3.11.2 Boundaries

In fig. 5.40 a boundary (marked by an open arrow) between two domains of the $C_{60}(111)$ face can be detected. Such boundaries occur when different layer stackings (ABC and CBA) co-exist on a fcc(111) face and two differently stacked domains meet (see schematics in fig. 5.41). The existence of such boundaries is a further evidence for the epitaxial growth of $C_{60/70}$ on Au(111), implying a well-defined growth relationship between Au(111) and $C_{60/70}(111)$. The STM line section (fig. 5.40b) across this boundary displays a row of C_{60} molecules including some C_{70} molecules (having 0.3 nm corrugation instead of 0.1 nm of the C_{60} molecules). The groove (open arrow) that represents the boundary appears with a depth of 0.1 nm.

A further type of boundary is shown in fig. 5.42. The two domains shown in the image

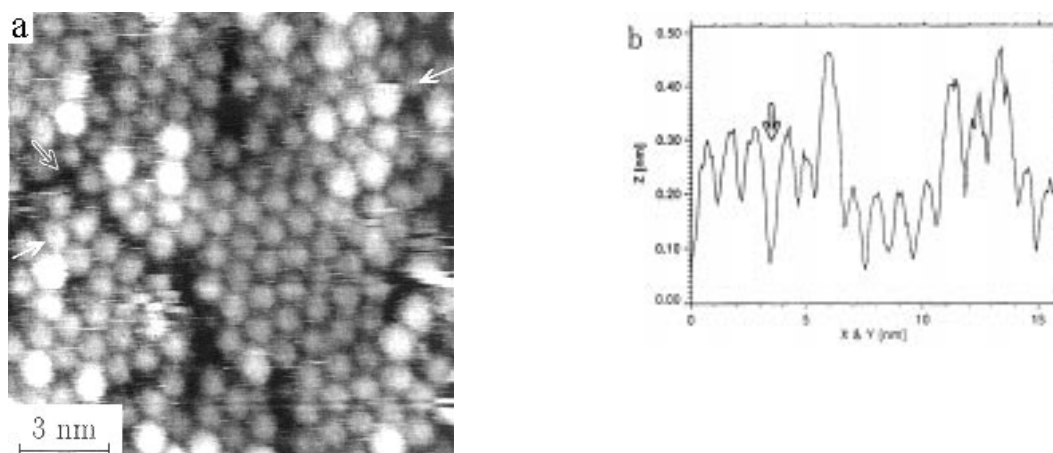


Figure 5.40: (a) A domain boundary in a $C_{60/70}$ film (open arrow). A section (indicated between arrows) is shown in (b). The boundary (open arrow) separates two fullerene domains having different stacking order (ABC and CBA). C_{70} molecules show a larger corrugation than C_{60} molecules as can be seen in the line section.

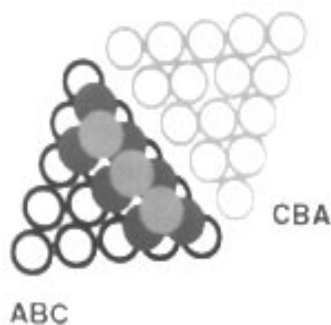


Figure 5.41: Model for a stacking domain boundary. (A-layer: black, B-layer: dark grey, C-layer: light grey).

are separated by a twin boundary. The white lines indicate one of the $\langle 110 \rangle$ directions in the two lattices. The acute angle between the lines is close to the value of 30 degrees expected for a twin boundary. The occurrence of such boundaries is further evidence for epitaxial growth of the fullerene layer.

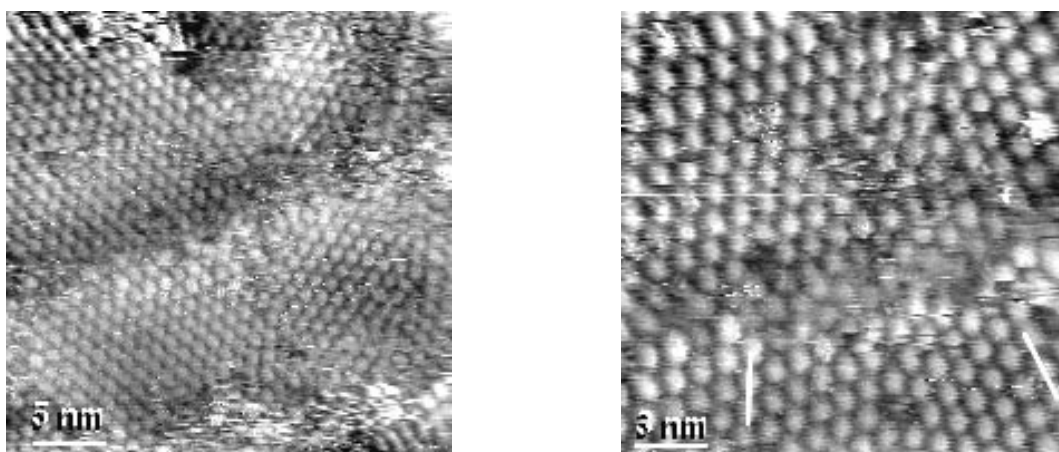


Figure 5.42: Twin boundary in a C_{60} thin film. The white lines in the detail image indicate $\langle 110 \rangle$ directions of the two lattices.

5.3.12 C_{70} films

C_{70} films can be prepared under similar conditions as C_{60} films. On a large scale C_{70} layers fully cover the gold substrate terraces (fig. 5.43 left). On a molecular scale the hexagonal arrangement of molecules seemed to be often disturbed (fig. 5.43 right). This might be in relation with the ellipsoidal shape of the C_{70} molecules. Their long axis may be aligned perpendicular to the film's surface (fig. 5.43 middle) or not (fig. 5.43 right).

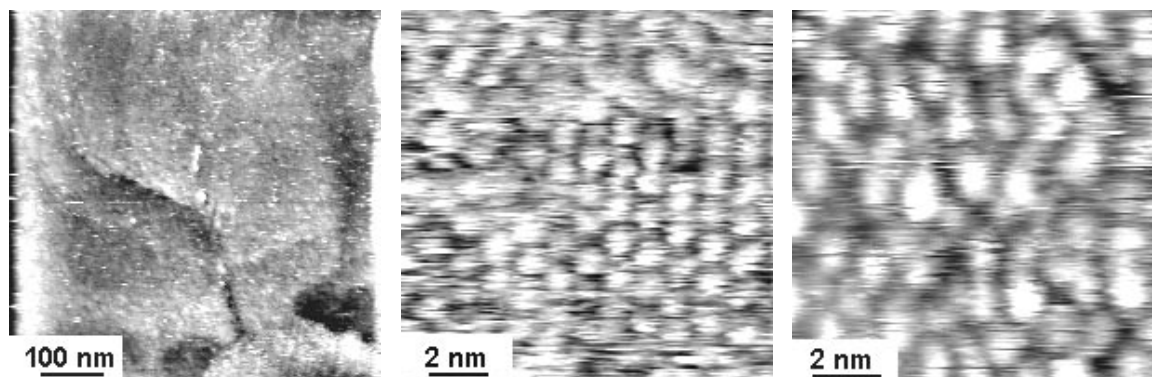


Figure 5.43: C_{70} fullerene films. *LEFT:* Survey. *MIDDLE:* Ordered hexagonal array. *RIGHT:* Disordered molecule array.

5.3.13 Intramolecular contrast

In certain cases intramolecular features of individual C_{60} molecules have been observed by STM. Although it has been found by NMR in bulk samples that C_{60} molecules rotate at a high frequency at ambient temperatures [5.6, 5.38], in a film configuration immobilization of the molecules on a substrate could impede such motion. Fig. 5.44 shows two STM images in which features within a C_{60} molecule are resolved. STM evidence of intramolecular contrast is reported in literature [5.21, 5.22]. Fig. 5.44a contains several such examples (indicated by arrows). In fig. 5.44b an individual C_{60} molecule close to a defect ('D') in the $C_{60}(111)$ lattice is singled out for its evidence of substructure (intramolecular contrast 'IC'). The symmetry of this substructure (one corrugation maximum surrounded by 6 others) is probably related to pentagon and hexagon ring features. The distance between corrugation maxima matches well the distance between carbon rings. This symmetry does not occur in the atomic lattice of the fullerene molecule supporting the interpretation of the corrugation maxima in terms of carbon ring centres. The observation that the apparent topographic maxima appear in the centre of the hexagon or pentagon is possibly due either to the actual local density of states of this particular molecule as influenced by the lattice defect, or, alternatively, due to a tip inhomogeneity. The latter explanation would be consistent with calculations that predict that the apparent topographic maxima for HOPG can actually occur in the centre of the graphite hexagon depending on the effective tip radius and the tip-to-sample distance [5.39]. Recent calculations by *Chavy et al.* [5.40] predict similar structures of intramolecular STM-contrast of C_{60} . The structures observed here are identical to those observed by *Behler et al.* at 4.5 K [5.41].

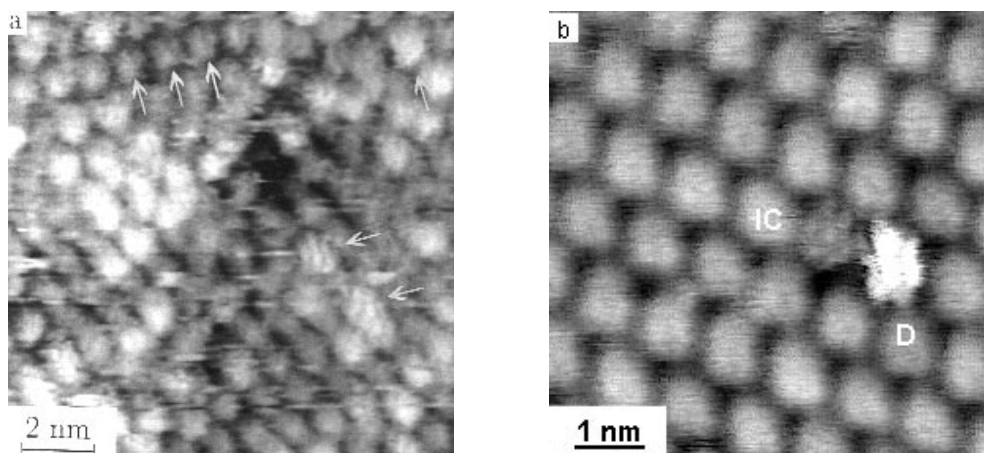


Figure 5.44: STM images showing contrast within individual C_{60} molecules. (a) Several C_{60} molecules (some of them indicated by arrows) show intramolecular contrast at spacings of about 0.3 nm. (b) Individual C_{60} molecule within the $C_{60}(111)$ surface showing distinct intramolecular features. The observation of intramolecular contrast (IC) in this particular C_{60} molecule is possibly related to the lattice defect (D) in its vicinity.

Figure 5.45 shows the observation of intramolecular contrast in almost every C_{60} molecule. This sample has been exposed to ambient air for several days. Reaction of the fullerenes with molecules of the ambient (oxygen) might possibly have enabled the observation of intramolecular contrast in this case.

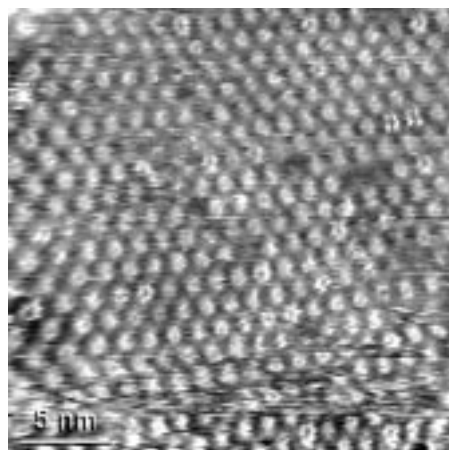


Figure 5.45: Plenty of C_{60} molecules in this STM image exhibit submolecular contrast.

5.3.14 Conclusion

Fullerene thin films on Au(111)/mica prepared under defined sublimation conditions have been investigated by STM and UV-VIS spectroscopy in dependence on preparation parameters like the initial C_{70}/C_{60} ratio, the sublimation distance, the substrate temperature and the sublimation time. The sublimation process has been investigated by combined TGA/DTA to facilitate the choice of sublimation temperatures. Optical absorption spectra of solutions of the powders reveal absorption features characteristic of C_{60} and C_{70} . STM images with molecular resolution of fullerene thin films sublimed from these mixtures show a hexagonal lattice (fcc(111) surface) consisting of two different molecular species which are assigned to C_{60} and C_{70} . By counting the two species in STM images, a direct assessment of the C_{70}/C_{60} ratio in films is possible. Evaluation of C_{70}/C_{60} ratios confirm the applicability of the sublimation method for fullerene separation and purification of $C_{60/70}$ mixtures even on a molecular scale. An increase of the sublimation distance is found to lead to a decrease of the C_{70}/C_{60} ratio, and an increase of the substrate temperature causes an increase of the ratio. These changes in the C_{70}/C_{60} ratio are visualized on a molecular scale.

The hexagonal lattice occasionally exhibits defects such as vacancies and boundaries in the STM images. Dynamic rearrangement processes have been observed by monitoring the relative positions of C_{70} molecules in the C_{60} host lattice. In films having a coverage of less than one monolayer of C_{60} molecules, nucleated C_{60} molecules on free Au(111) terraces have been imaged. In some cases intramolecular features within the C_{60} molecules in the fcc(111) hexagonal pattern have been observed.

5.4 Collapsed fullerite

5.4.1 Introduction

Despite of being a very stable chemical species fullerenes have been found to undergo structural transformations into different carbon phases under high pressure. Recently, it has been found that the simple-cubic (*sc*) to face-centred-cubic (*fcc*) ordering transition temperature ($T_c \approx 250$ K) of solid C_{60} increases with pressure and that the applied pressure greatly reduces orientational fluctuations of the C_{60} molecules in the ordered low-temperature *sc*-phase [5.42, 5.43]. At room temperature, the *fcc* structure remains the stable phase up to about 20 GPa [5.44]. Under extreme pressure conditions, several transformations of solid C_{60} into different structural states of carbon were reported (see fig. 5.46 for a compilation), e.g. a transition above 20 GPa from solid C_{60} into a more insulating covalent solid [5.45], and a transformation at about 18 GPa of solid C_{60} into hexagonal graphite under shock compression [5.46]. More recently, *Moshary et al.* [5.47] have reported on an irreversible transition of solid C_{60} to a new phase of carbon at pressures in the 17-25 GPa range. Raman scattering of the depressurized sample showed no trace of C_{60} , diamond, or graphite, indicating that the transition involved the collapse of C_{60} molecules into a new structure of carbon. This *collapsed fullerite (CF)* phase was proposed to represent a new amorphous structure different from amorphous graphite or amorphous carbon [5.47].

Reference	Observation
Samarra et al. PRL 67, 3135 (1991)	sc/fcc ordering temperature rises with pressure
Lu et al. PRL 68, 1551 (1992)	theoretical models for phase transitions in C_{60}
Duclos et al. Nature 351, 380 (1991)	fcc C_{60} is stable up to 200 kbar
Nunez-Regueiro et al. Nature 354, 289 (1991)	above 200 kbar: transition from C_{60} to insulating covalent solid
Yoo et al. Science 254, 1489 (1991)	at 180 kbar: C_{60} to hexag. graphite under shock compression
Moshary et al. PRL 69, 466 (1992)	170-250 kbar: C_{60} irreversible to new amorphous carbon phase Raman: no C_{60} , no diamond, no graphite

Figure 5.46: References for high pressure structural transformations of solid C_{60} into different forms of carbon.

Here, a scanning tunneling microscope (STM) has been used to locally transform C_{60} molecules of a C_{60} fullerite thin film on Au(111) into a new amorphous form of carbon by application of a pressure in the GPa range.

5.4.2 Experimental procedure

The effect of pressure on solid C_{60} is usually studied by using a conventional diamond-anvil cell. For surface-sensitive STM studies this experimental procedure would inherently suffer from two major drawbacks:

- Residual small particles and contamination on the surface of the pressurized sample originating from the cell walls can not be excluded.
- It is almost impossible to find the same surface area by STM before and after pressurization of the sample *ex-situ* in a diamond-anvil cell.

Therefore, a novel experimental procedure is presented in which pressure is locally applied *in-situ* on the multilayer C_{60} film by means of the STM tip itself. This can be achieved by increasing the tunnel current and decreasing the applied bias voltage, thereby increasing the tip-sample interaction strength considerably. It has already been found in earlier STM studies of graphite surfaces that even under 'normal' operation conditions (tunnel current of typically 1 nA, bias voltage of about 50 mV), a tip-sample interaction force as high as 10^{-6} N is present [5.48, 5.49]. Since the force is distributed over a relatively small area of typically 10^5 - 10^6 Å², a local pressure on the order of 0.1-1 GPa is easily reached [5.48]. By operating the STM under extreme tunneling conditions (tunnel current of several ten nA, sample bias near 0 mV), a sufficiently large pressure can locally be exerted on the multilayer C_{60} film that leads to a collapse of the C_{60} molecules underneath the STM tip. A schematic of the procedure is shown in fig. 5.47.

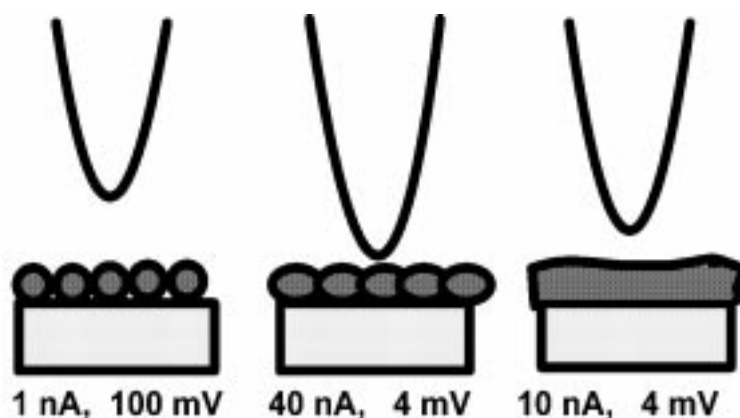


Figure 5.47: Application of pressure under extreme tunneling conditions leads to collapse of C_{60} fullerite.

Figure 5.48 shows the pressure effects related to 'extreme' tunneling conditions in more detail.

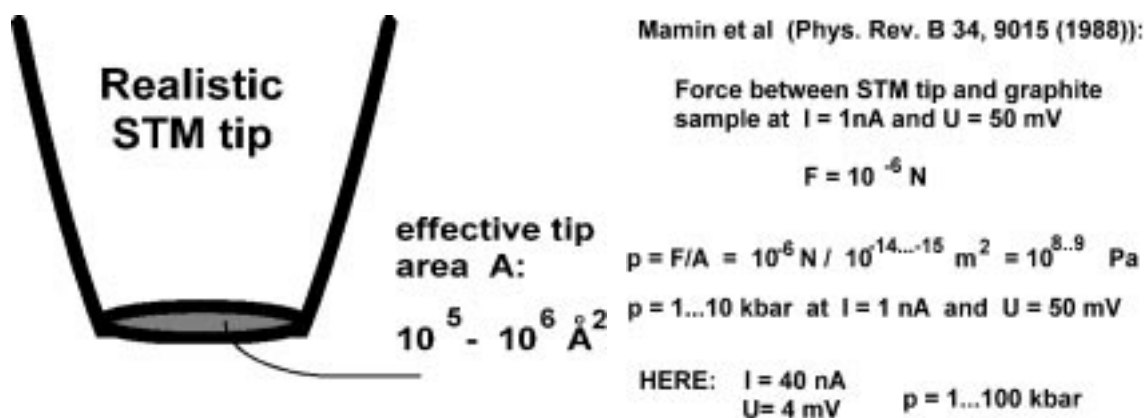


Figure 5.48: Effects of pressure application by 'extreme' tunneling conditions.

5.4.3 Results

The STM tip excursion (z -level movement) during pressurization of the multilayer C_{60} film has been recorded and is shown in fig. 5.49. As the tunnel current is increased from 1 nA to 40 nA at a sample bias voltage of close to 0 mV, the STM tip appears to move into the direction of the sample by about 17 Å.

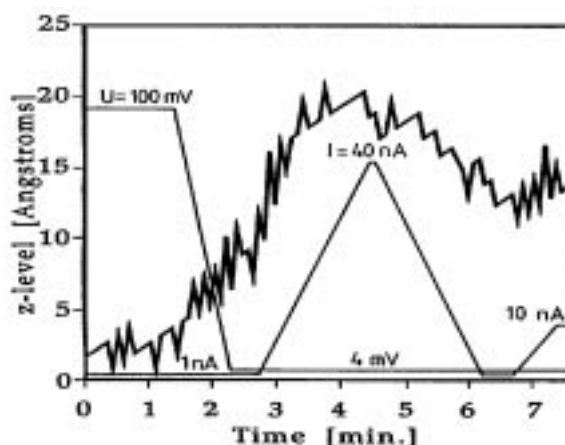


Figure 5.49: STM tip excursion as a function of time during local pressurization of the multilayer C_{60} film. The data is corrected for thermal drift and sample tilt. The tunnel current and the bias voltage at different times are indicated.

Upon decreasing the tunnel current to the previous value of 1 nA, the STM tip does not reach the initial z -level. The difference between the new z -level upon pressurization and the previous z -level before pressurization (with the same tunneling parameters) can be attributed to a collapse of C_{60} molecules in the localized region between tip and substrate. The z -level change amounts to about 10 Å, suggesting that a two-layer thick C_{60} film has locally collapsed. Subsequent STM imaging of the pressurized region was performed with a tunnel current of 10 nA and a sample bias voltage of -4 mV. When the same pressurization procedure is applied on an uncoated Au(111) substrate, no damage of the gold surface is observed.

In fig. 5.50a a typical STM topograph ($200 \text{ Å} \times 200 \text{ Å}$) of a multilayer C_{60} film is shown obtained with a constant tunnel current of 1 nA and a sample bias voltage of -100 mV. The protrusions (bright spots) in the image correspond to individual C_{60} molecules which are arranged in a triangular lattice with a lattice constant of 10 Å in agreement with literature values [5.15, 5.16, 5.21, 5.34].

In fig. 5.50b the same surface region ($200 \text{ Å} \times 200 \text{ Å}$) as in fig. 5.50a is presented after local pressurization of the C_{60} film. Obviously, C_{60} molecules are no longer visible. Instead, a step-and-terrace structure appears with a typical step-height value of about $(2.7 \pm 0.1) \text{ Å}$. This value is significantly larger than the monatomic step-height value of the Au(111) substrate (2.35 Å). Therefore, it is likely that the measured step-height value rather corresponds to the thickness of an individual carbon layer. When zooming out to an image area of $5000 \text{ Å} \times 5000 \text{ Å}$, the modified area was actually found to be $7 \cdot 10^5 \text{ Å}^2$ in size (see fig. 5.51). Beyond this area, C_{60} molecules are still observed providing evidence for the local nature of the modification experiment.

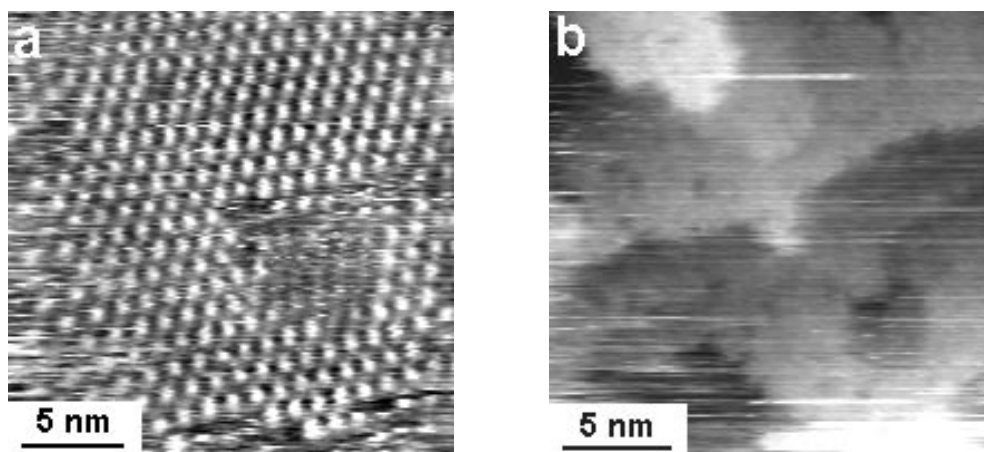


Figure 5.50: (a) STM image of a C_{60} thin film on Au(111) imaged at $U_t = 100 \text{ mV}$ and $I_t = 1 \text{ nA}$. (b) STM image of the same film after local pressurization (increase of the tunneling current to 40 nA and decrease of the bias voltage to 4 mV). The fullerene molecules are no longer observed.

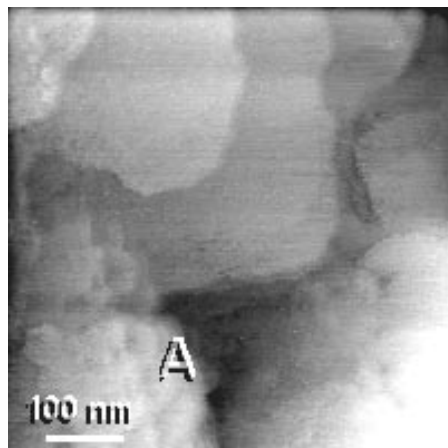


Figure 5.51: Large scale STM image showing the modified area (labelled 'A').

A detailed view of the modified area by STM yields different atomic structures. In some cases rather regular atomic arrangements are observed as shown in fig. 5.52.

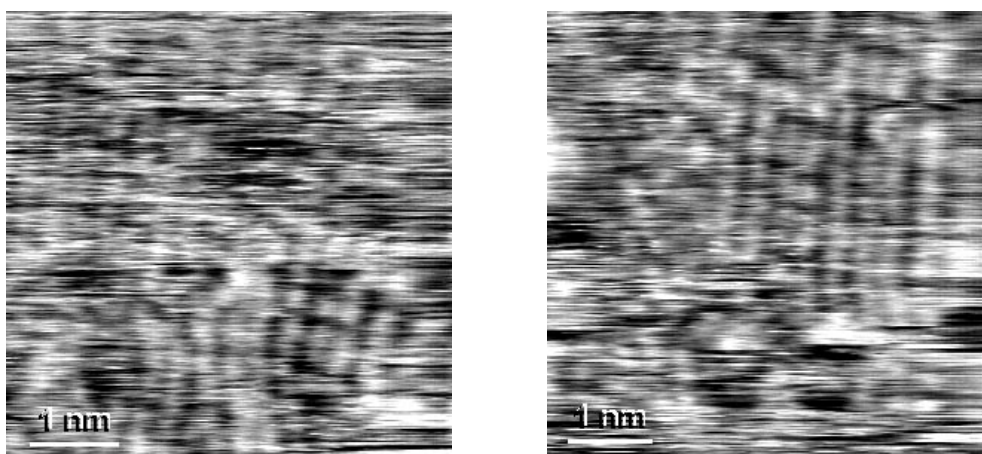


Figure 5.52: Rather regular atomic structure observed after the modification experiment.

In some experiments a disordered surface structure appears in the real-space images as shown in fig. 5.53 with the bright spots having typical interatomic distances between 2.5 and 3 Å. The lack of order is also reflected by the absence of sharp spots in the corresponding 2D power spectrum (see fig. 5.54). Instead, ring-like features are visible in this 2D power spectrum as typical for of amorphous structure.

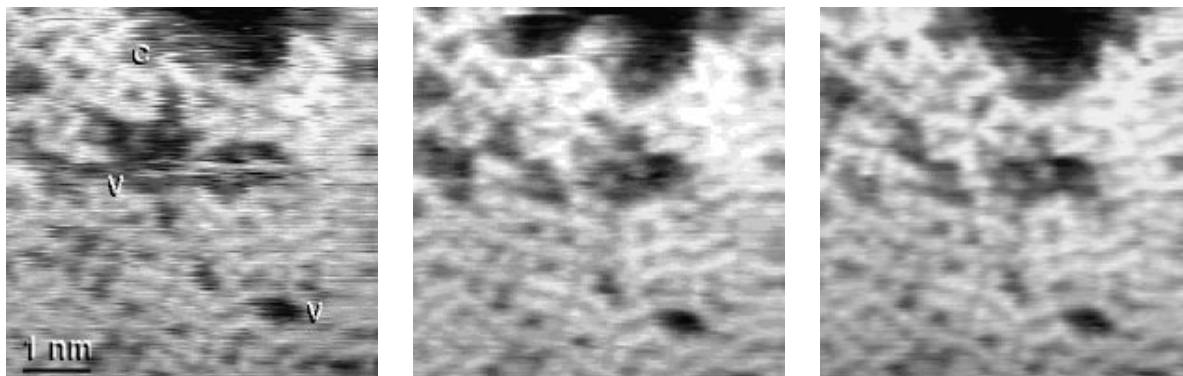


Figure 5.53: Three topographic atomic-resolution STM images of the collapsed fullerite structure and 2D power spectrum of the third image. Time interval between subsequent images is 15 s. The STM images reveal an amorphous structure. 'V' labels voids and 'c' indicates chain structures. Note the dynamic rearrangement of atomic chain fragments with time (probably induced by the scanning process).

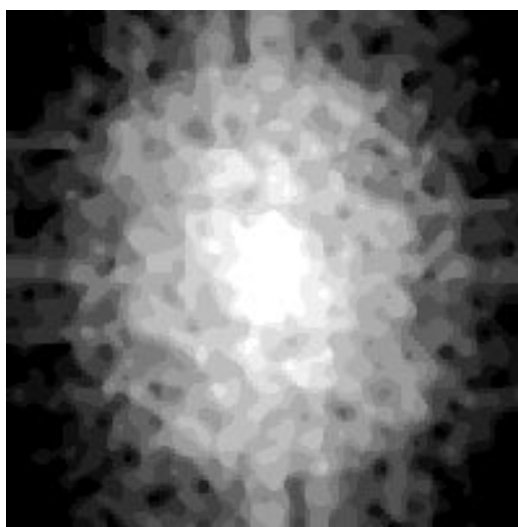


Figure 5.54: 2D power spectrum of the amorphous structure shown above. No peaks, but ring-like features typical of an amorphous structure are observed.

5.4.4 Pair correlation function

Upon parameterization of the real-space STM image, a radial distribution function (pair correlation function) has been derived using the procedure shown in fig. 5.55. The parameterized data-set and the pair correlation function are presented in fig. 5.56.

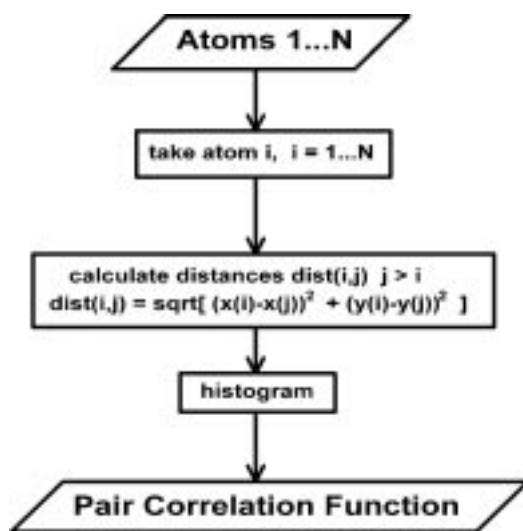


Figure 5.55: Flux diagram to determine a radial distribution function (pair correlation function).

The pair correlation function has the characteristic appearance of an amorphous structure with a nearest-neighbour peak at about $(2.7 \pm 0.1) \text{ \AA}$ and a second-nearest-neighbour peak at about $(3.5 \pm 0.1) \text{ \AA}$. Please note that the probability to observe interatomic distances between the nearest-neighbour distance and the second-nearest-neighbour distance is *different from zero* in contrast to crystalline structures. In order to demonstrate this fact the pair correlation function of a data-set obtained from a regular (crystalline) atomic arrangement is shown in fig. 5.57. These atomic positions are extracted from the STM image of the fullerene layer before modification (fig. 5.50).

The STM data of the pressurized multilayer C_{60} film is similar to earlier STM data of amorphous carbon films [5.50]. This implies that the transformation observed locally in real-space by means of STM corresponds closely to the transition of solid C_{60} into an amorphous carbon structure as proposed by *Moshary et al.* [5.47]. These authors concluded that the new structure of carbon obtained by the collapse of solid C_{60} is dissimilar from diamond and graphite. The real-space STM data as well as the corresponding pair correlation function yields a nearest-neighbour distance of $(2.7 \pm 0.1) \text{ \AA}$ which is close to the second-nearest neighbour distance of 2.6 \AA obtained by local density approximation (LDA) calculations [5.51] for the liquid state of carbon, but slightly larger than the interatomic distance on the (111) surface of diamond (2.52 \AA), the distance between *B*-type sites on the graphite (0001) basal plane (2.46 \AA), or the values for the second-nearest neighbour distance (2.5 \AA) in amorphous carbon [5.52]. The nearest-neighbour-distances

and the second-nearest-neighbour distances are compiled in fig. 5.58.

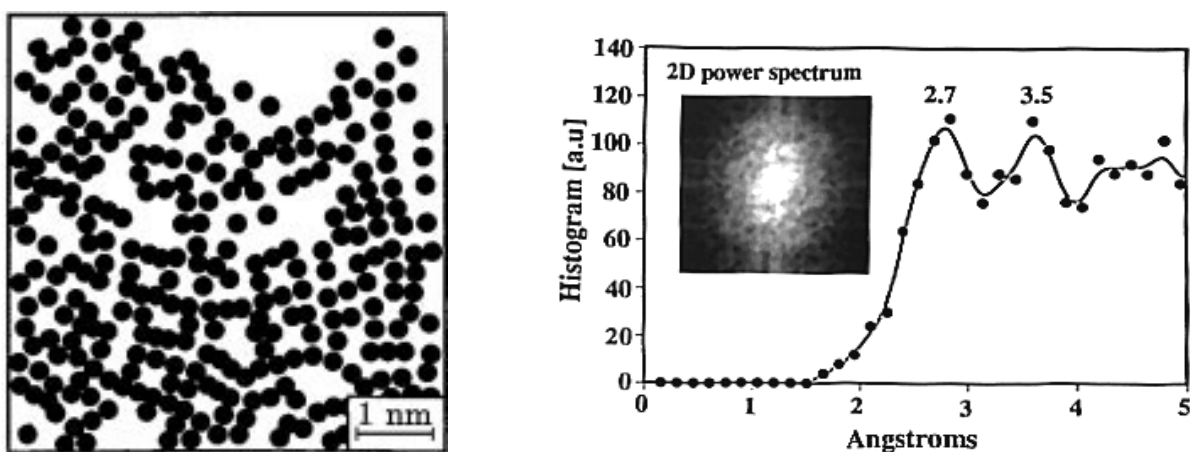


Figure 5.56: *LEFT:* Parameterized data-set of the amorphous collapsed fullerite structure. *RIGHT:* Pair correlation function based on these atom positions. The observed interatomic distances are classified with a resolution of 0.15 \AA and displayed in a histogram (filled dots). The curve is an approximation to the histogram data and serves as a guide to the eye. The inset shows the 2D power spectrum of the STM data. The rings correspond to the nearest-neighbour and second-nearest neighbour distances in the real space image.

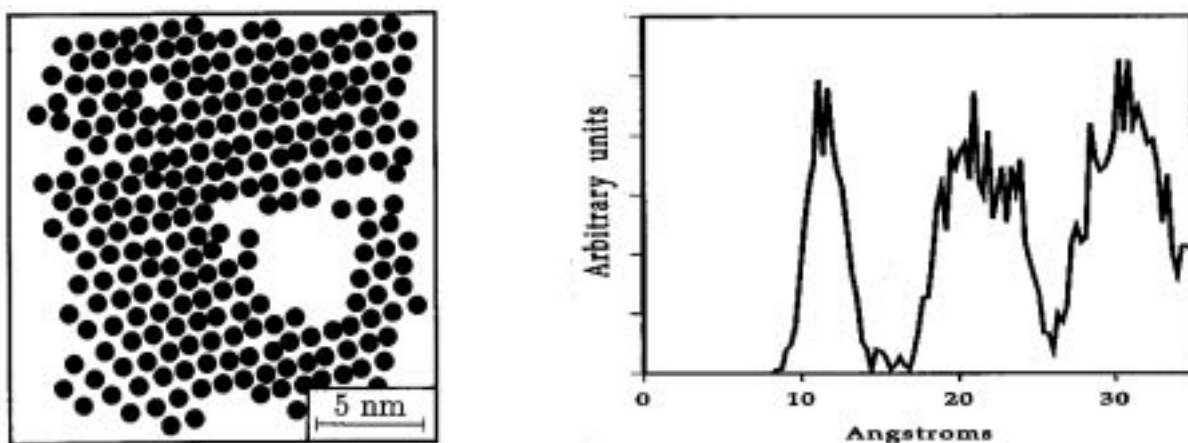

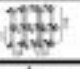

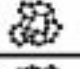
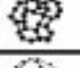



Figure 5.57: *LEFT:* Parameterized atomic positions of the STM image of a fullerene layer. *RIGHT:* Pair correlation function of this data. The nearest neighbour distance is about 10 \AA .

		Nearest-neighbour \AA	Second-nearest neighbours \AA
	Collapsed Fullerite	---	2.7
	Graphite	1.42	2.46
	Diamond	1.55	2.52
	Liquid Carbon	1.35	2.6 ^{a)}
	a-C:H	1.52	2.5 ^{b)}
	Fullerenes	1.36 - 1.44	2.4

a) Galli et al (LDA calculation), Phys. Rev. Lett. 63, 988 (1989)
 b) Gaskell et al (neutron scattering), Phil. Mag. B 66, 155 (1992)

Figure 5.58: Nearest-neighbour and next-nearest neighbour distances for different allotropes of carbon.

5.4.5 Angular distribution function

A different method to characterize order and disorder in a structure is the determination of the *angular distribution function*. It displays the distribution of angles between vectors of interatomic distances within a range of absolute interatomic distances, e.g. from zero to the nearest-neighbour distance. The angle distribution function has been determined using the procedure displayed in fig. 5.59.

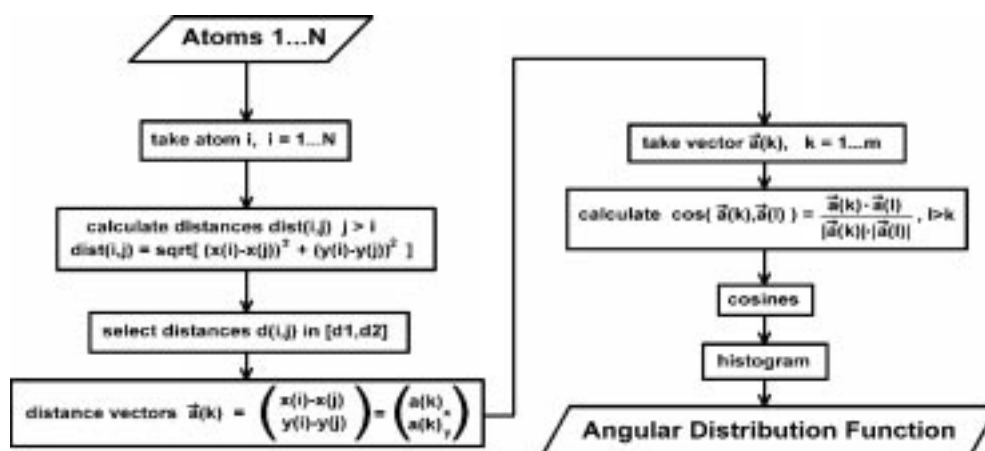


Figure 5.59: Flux diagram to evaluate the angle distribution function.

The following example demonstrates the information extracted from an angle distribution function when applied to a crystalline structure such as HOPG. Fig. 5.60 shows a STM image of HOPG. Each atom has nearest neighbours in directions with an intermediate angle of 0° , 60° , 120° , 180° , 240° and 300° . These values correspond to cosine values of -1 , -0.5 , $+0.5$ and $+1$. The angular distribution function exactly shows peaks at these cosine values (see fig. 5.61) and zero intensity between the peaks.

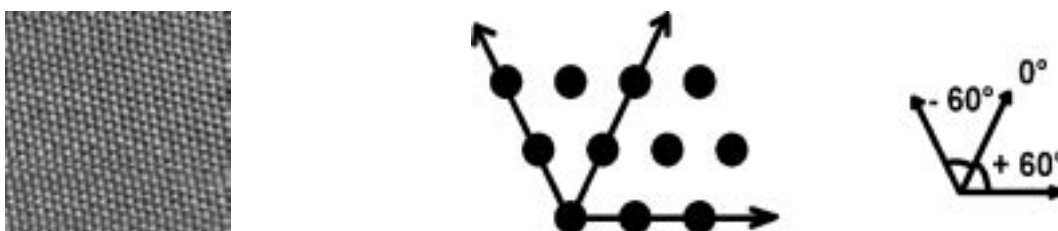


Figure 5.60: *LEFT:* STM image of a crystalline structure (HOPG). *RIGHT:* Possible angles between directions of nearest neighbours.

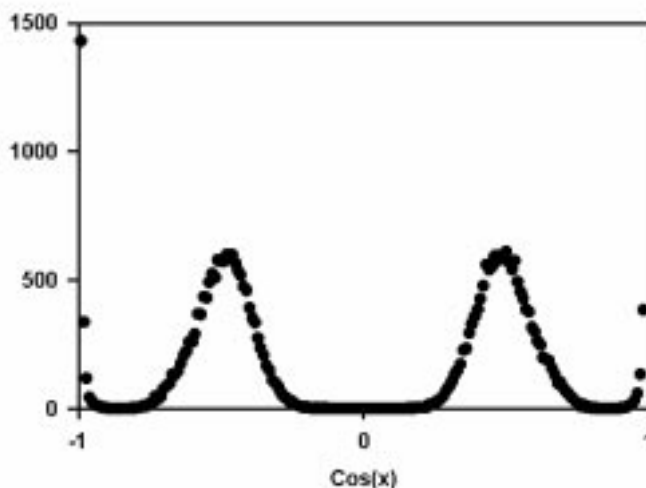


Figure 5.61: Angle distribution function of HOPG (using distances between 0 and 3 \AA including the nearest-neighbour distance).

An amorphous structure, however, is expected to show only peaks at cosine values equal to ± 1 of the intermediate angle between directions of nearest-neighbour distances. All other angles should be distributed randomly and give a non-vanishing, constant intensity in the angle distribution function. This is actually the case if fig. 5.62 is considered.

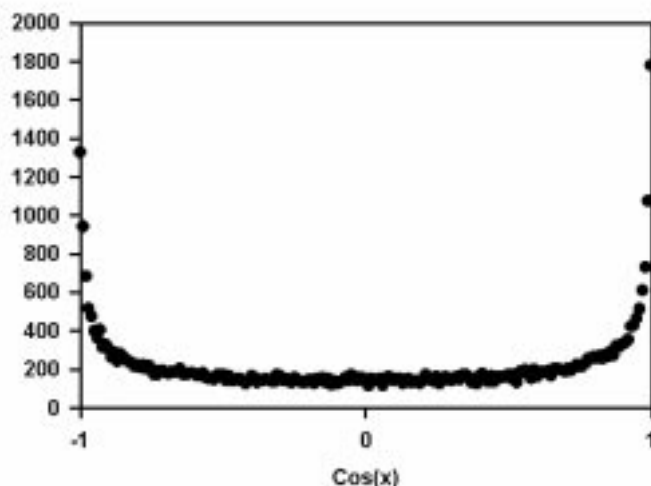


Figure 5.62: Angle distribution function of collapsed fullerite (distances between 0 and 3 Å).

5.4.6 Bonding-type distribution

Several different amorphous and glassy states of carbon can be distinguished, e.g. by their sp^2 -to- sp^3 bonding ratio. Additional corrugation between the atomic features in fig. 5.63 suggests the presence of electronic density of states between the corrugation maxima in certain directions. A statistical analysis of the nature of such 'in-plane-bonds' shows that 50.2 % of the atomic features have an in-plane-bond to one other atom in the plane, and 40.9 % exhibit in-plane-bonds to two other atoms provided that the corrugation maxima can actually be interpreted as atomic sites. All other atoms show no in-plane-bonds. The distribution of in-plane-bonds in the STM image might be related to the actual hybridization type of bonding. *Ab initio* molecular dynamics [5.53] and tight-binding molecular dynamics simulations [5.54] as well as ^{13}C nuclear magnetic resonance (NMR) experiments on amorphous carbon [5.55] give percentages of 1.5 - 12 % for 2-fold, 71 - 93.6 % for 3-fold and 4.9 - 22.5 % for 4-fold coordination of the carbon atoms. Assumed that the three types of in-plane-bond patterns (see fig. 5.63) can be identified with the three different coordination types of carbon, a carbon coordination number for collapsed fullerite can be extracted from the STM data (fig. 5.53 and 5.63). Provided the number of bonds of each atom equals the number of visible 'in-plane-bonds' plus two 'invisible' bonds (to the underlying atomic layer and in direction to the tip) and that the corrugation maxima actually correspond to atomic sites, 50.2 % of the atoms would be 3-fold coordinated (graphite-like sp^2 bonding), 40.9 % would be 4-fold coordinated (diamond-like sp^3 bonding) and the remaining ones (8.9 %) would be 2-fold coordinated. This results in an averaged coordination number of approximately 3.3. Figure 5.64 sum-

marizes bonding-type distributions of collapsed fullerite and of amorphous carbon data in literature.

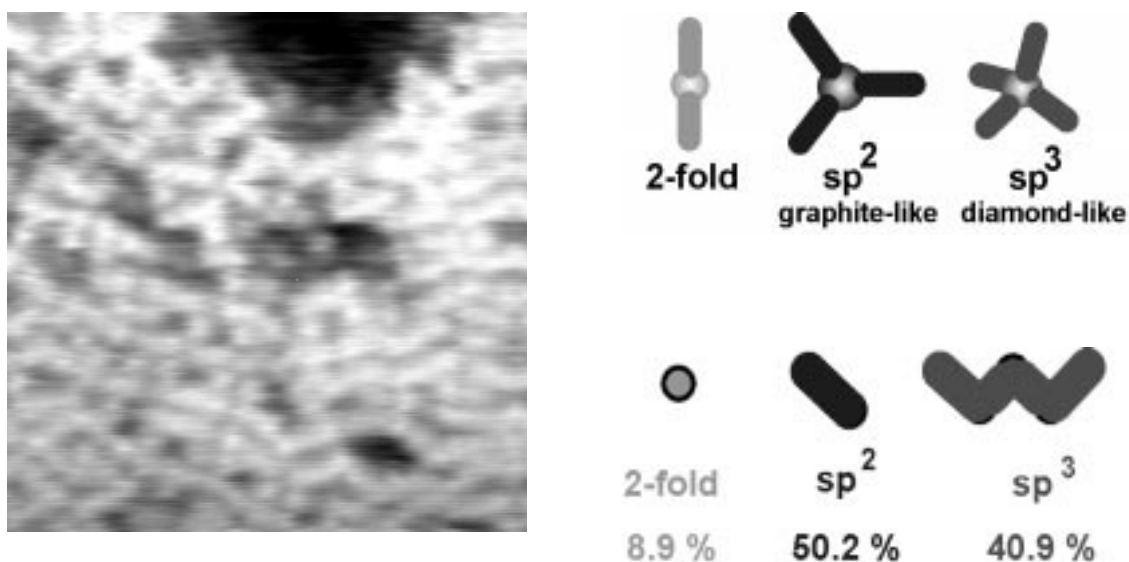


Figure 5.63: *LEFT:* STM image of collapsed fullerite. *RIGHT:* Bonding-types of carbon and their suggested appearance in the STM image of collapsed fullerite.

Method/Experiment	Density	2-fold %	3-fold %	4-fold %	Coord. number
ab initio MD Galli et al, PRL 62, 555	2.0	--	85	15	3.15
Tight Binding Molecular Dynamics Wang et al, PRL 73, 611	2.2	12.0	80.6	7.4	2.96
	2.44	5.8	80.0	14.2	3.08
	2.69	6.5	71.0	22.5	3.16
¹³ C NMR Pai et al, PRB 44, 6741	2.0-2.44	1.5	93.6	4.9	3.03
STM, Collapsed Fullerite	?	8.9	50.2	40.9	3.32

Figure 5.64: Compilation of bonding-type distribution of carbon in amorphous carbon (simulations) and collapsed fullerite (derived from STM data).

5.4.7 Conclusion

In summary, it has been shown that a multilayer C₆₀ film can locally be transformed into an amorphous carbon structure upon *in-situ* pressurization in a scanning tunnel-

ing microscope by a collapse of C_{60} molecules in the region between tip and substrate. The amorphous structure obtained is locally different from diamond and graphite. From the vertical tip movement during the transformation process, the local collapse of two monolayers of C_{60} is inferred. Based on atomically resolved STM-images of this 'collapsed fullerite' (CF) structure, a pair correlation function is presented characteristic of an amorphous structure with a nearest-neighbour peak at 2.7 Å. The two-dimensional power spectrum of the real-space data exhibits no spots but rings, which are attributed to first and second nearest-neighbour distances of the CF structure. An analysis of the number of nearest-neighbours of each atomic feature shows that about 50 % of the atoms have in-plane-bonds to one other atom, and 40 % have bonds to two other atoms.

5.5 Doped/intercalated fullerenes

5.5.1 Introduction

Doping of C_{60} films with alkali metals has been found to result in electrical conductivities comparable to doped polyacetylene [5.56]. K_3C_{60} contains a superconducting phase with a transition temperature T_c of 18 K (onset) [5.57], which is rather high compared to a T_c of 0.55 K of the corresponding stage-1 potassium graphite intercalation compound [5.58]. The room-temperature structure of K_3C_{60} has been determined to be face-centred cubic, but with a slightly enlarged lattice constant compared to the undoped material [5.59] (see fig. 5.65). Superconductivity at higher temperatures was found in Rb-doped (28 K) [5.60], and (Cs,Rb)-doped C_{60} (33 K) [5.61]. A monotonic increase of T_c with the fcc lattice parameter was confirmed for several alkali metal doped C_{60} compounds [5.62].

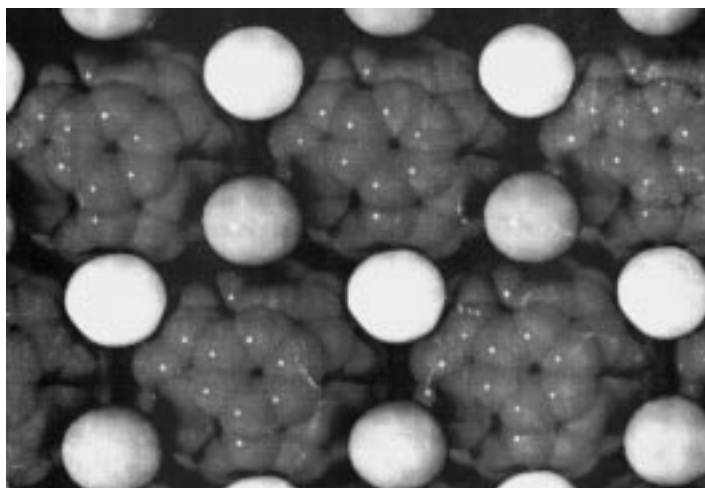


Figure 5.65: The (111) surface of M_3C_{60} (M = alkali metal). Reproduced from Nature, cover page of issue no. 6328, June 20, 1991.

The alkali-metal dopant atoms occupy two different sites in the fcc lattice of C_{60} : 2 smaller tetrahedral sites (3.3 Å) and 1 larger (3.7 Å) octahedral site (see fig 5.66). On larger doping level the compound M_xC_{60} is body-centred-tetragonal ($x=4$) or body centred cubic ($x=6$). Only the M_3C_{60} compound is superconducting.

Further fullerene compounds are reported to be superconductive (in chronological order). A result obtained by *Z. Iqbal et al* [5.63] of a $T_c = 48$ K in $Rb_{2.7}Tl_{2.2}C_{60}$, however, was later found to be due to a malfunction of the superconductive quantum interferometer device (SQUID) magnetometer [5.64]. $(K,Tl)C_{60}$ [5.65] and $(Rb,Tl)C_{60}$ [5.66] compounds were observed to show solely the T_c values of K_3C_{60} (18 K) and Rb_3C_{60} (28 K). A proposal by *R. Lal et al.* [5.67] on possible T_c enhancement in fulleride superconductors by halogen doping has given rise to the synthesis of iodine-doped C_{60} in Japan. A report of a T_c of 57 K for this compound [5.68] was later also found to be due to instrumental artifacts and the claim of superconductivity was withdrawn [5.69]. Confirmed reports on

superconductivity exist for $\text{Na}_2\text{MC}_{60}$ ($\text{M}=\text{K},\text{Rb}$; $T_c = 2.5$ K) and $\text{A}_2\text{CsC}_{60}$ ($\text{A}=\text{Na},\text{Li}$; $T_c = 12$ K) [5.70, 5.71]. *A.R. Kortan et al* have found that Ca_5C_{60} is a superconductor below 8.4 K [5.72]. *L.W. Song et al.* have observed a diamagnetic magnetization anomaly in ICl-C_{60} below 65 K [5.73]. The compound $\text{Na}_{3+x}\text{N}_y\text{C}_{60}$ shows a superconducting transition at 12 K [5.74], $(\text{NH}_3)_4\text{Na}_2\text{CsC}_{60}$ is superconducting below 29.6 K [5.75]. In a Sn-doped sample a Chinese group has observed a magnetization anomaly below 40 K [5.76].

Fullerene superconductors are BCS-type superconductors¹⁷ with a high density of states near the Fermi level $N(E_F)$ [5.62] which explains the high values of T_c .¹⁸ Since T_c (and therewith the phonon frequencies) depend on the atomic mass, isotope effect is expected. It has been observed in ^{13}C enriched Rb_3C_{60} samples [5.77, 5.78]. The following table (5.2) summarizes the superconducting properties of K_3C_{60} and Rb_3C_{60} granular samples (after *Sparn et al.* [5.79]):

Parameter	Rb_3C_{60}	K_3C_{60}
T_c (K)	29.6	19.3
H_{c1} (mT)	26	13
H_{c2} (T)	78	49
J_c (10^6 Acm ⁻²)	1.5	0.12
Coherence length ξ_0 (nm)	2-3	2.6-3.5
London penetration depth λ_0 (nm)	168-440	240-480
$\kappa = \lambda_0/\xi_0$	84	92

Table 5.2: Superconducting properties of alkali metal doped fullerenes.

In-situ doping experiments of C_{60} films with Rb by *T. Takahashi et al.* [5.80] have shown the gradual occurrence of states near the Fermi level showing a metallic behaviour at Rb_3C_{60} . This metallic band results from a full charge transfer from the alkali metal atom to the C_{60} . It was observed by photoemission [5.81] and electron energy loss spectroscopy [5.82]. Since the states near the Fermi level originate from states localizes at the C_{60} it is to be expected that STM images of K- or Rb-doped fullerene samples will exhibit a molecular structure very similar to that of undoped samples. In particular, it is not possible to observe by STM the intercalated alkali metal atoms [5.83].

In the following only granular Rb_3C_{60} and KTl/RbTl -doped fullerene samples will be discussed.

¹⁷BCS = Bardeen-Cooper-Schrieffer. These three physicists have suggested in the late fifties a theory on superconductivity based on electron pair formation (Cooper pairs) using a phonon mediated interaction. This theory is today the standard microscopic theory of superconductivity.

¹⁸ $k_B T_c \propto 1.14 (h/2\pi) \omega_q \exp(-1/N(E_F) \times U_0)$, ω_q is a typical phonon frequency (10^{12} Hz), $N(E_F) \times U_0 \approx 0.5$.

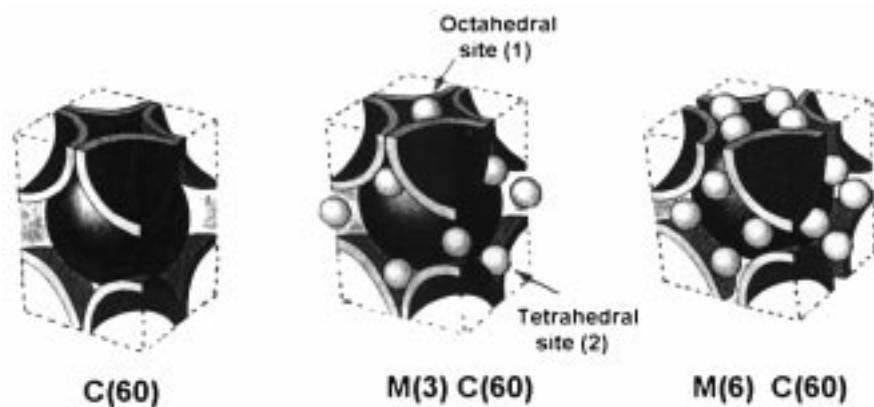


Figure 5.66: Different dopant levels of M_xC_{60} . Figure reproduced from A.F. Hebard, *Physics Today* 45 (1992) 26.

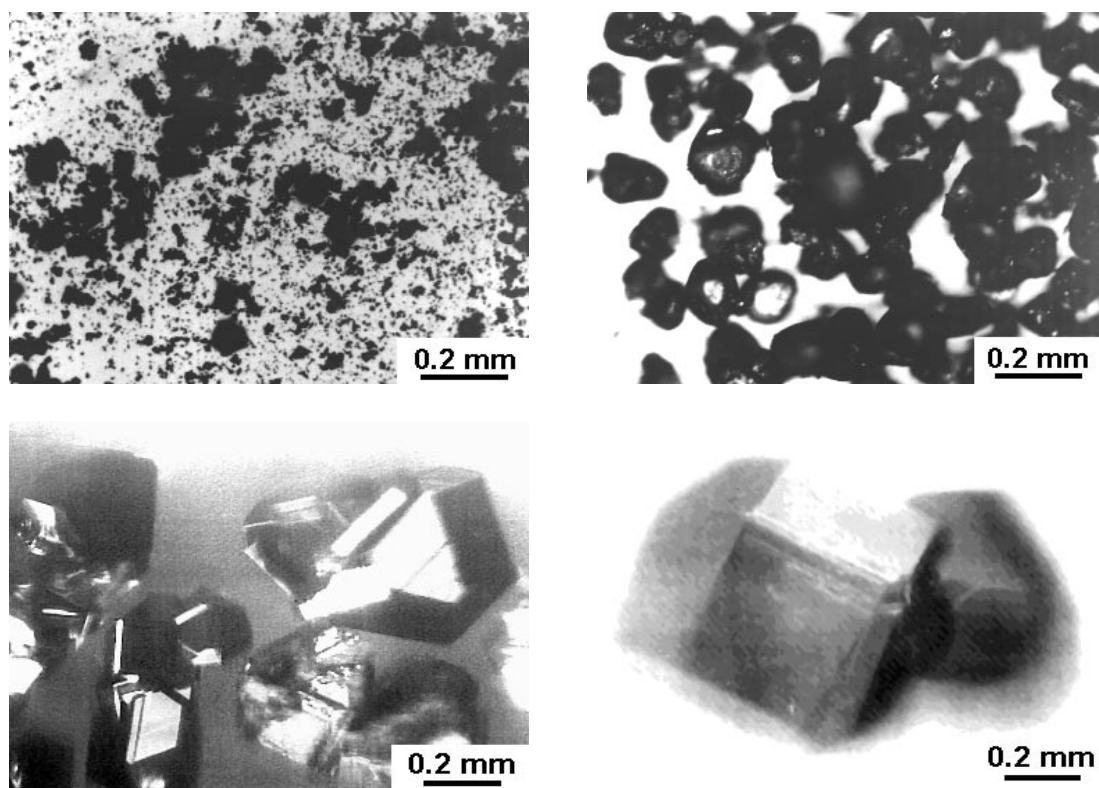


Figure 5.67: *TOP LEFT:* Granular $C_{60/70}$, *TOP RIGHT:* Granular C_{60} . *BOTTOM:* C_{60} single crystals. Note the different 'grain size' of the materials.

5.5.2 Materials

The choice of fullerene source materials determines the superconducting properties to a large extent. This is demonstrated using granular $C_{60/70}$ (with approx. 20 % C_{70}), granular C_{60} (C_{70} content below 0.05 %) and single crystals of C_{60} (C_{70} content below 0.01 %) as starting material for the doping with metallic rubidium in the ratio 1:3. Figure 5.67 shows optical micrographs of the fullerene materials. These fullerene source materials and corresponding amounts of Rb in the molar ratio 1:3 are heated typically in a pure argon atmosphere at 450 °C for 40 h (Rb_3C_{60}). The powders are sealed under vacuum and characterized within the sealed glass tubes by DC SQUID magnetometry. The temperature scans (Zero-Field-Cooled (ZFC) and Field-Cooled (FC) in a magnetic field of 10.6 Gauss) are shown in fig. 5.68. These DC SQUID data have been acquired by R. Schauwecker¹⁹ [5.84].

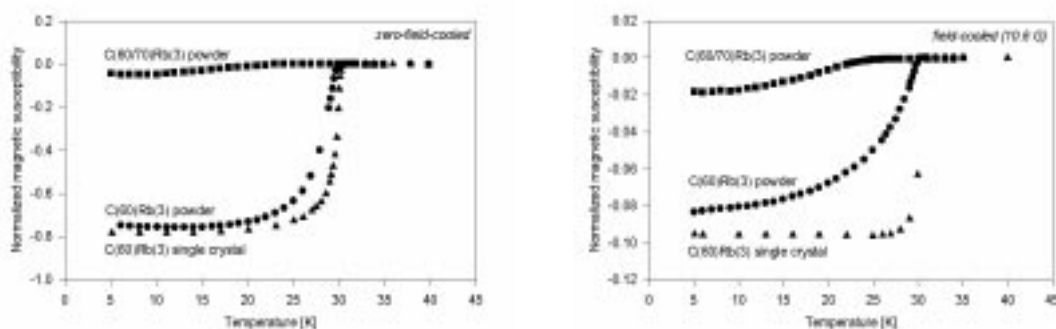


Figure 5.68: *LEFT:* Zero-field-cooled temperature scan of magnetization for granular $Rb_3C_{60/70}$, granular Rb_3C_{60} and single crystalline Rb_3C_{60} . *RIGHT:* Field-cooled temperature scan (10.6 Gauss). The magnetization increases with increasing grain size.

The SQUID signal decreases with decreasing grain size and the transition broadens. This is in contrast to cuprate based superconductor epitaxial films which show a very sharp transition. Geometrical size effects influence the superconducting properties of granular fulleride superconductors to a large extent, since the penetration depth of the magnetic field is comparable to the grain size. Grains being smaller or of a size comparable to the penetration depth will not or only very little contribute to the magnetic signal observed in a SQUID magnetometer. This explains the observed increase of magnetic signal with grain size (see fig. 5.68).

5.5.3 STM results on granular Rb_3C_{60}

Granular material does not seem to be suitable for STM experiments since no flat surface is present. At the time when these STM experiments were performed, only granular

¹⁹University of Zürich (Switzerland).

intercalated fullerenes were available. Pressing pellets at moderate pressure from Rb_3C_{60} powders under argon without exposure to air and moisture in a stainless-steel glove box is the procedure pursued here to prepare comparatively flat samples. For the STM experiments in the argon-filled glove box at room temperature, these pellets are mechanically cleaved to remove any contaminations introduced to the surface layers during compaction.

Pressed pellets of Rb_3C_{60} ($T_c = 27$ K) exhibit by STM on a large scale a surface dominated by grains of a size of a few hundred nanometres (see fig. 5.69). This granularity is responsible for the low diamagnetic shielding observed in that sample. *J.R. Clem and V.G. Kogan* [5.85] have calculated the effects of the finite grain size upon the temperature dependence of magnetization of a sample consisting of spherical grains. Grains with sizes R that are comparable to the magnetic field penetration depth $\lambda(T \rightarrow 0)$ give only small contributions (magnetic suppression factor $P=0.2$ for $R/\lambda(0) = 2$) to the signal observed in a magnetization experiment. A typical value for the magnetic field penetration depth $\lambda(T \rightarrow 0)$ in Rb_3C_{60} is 247 nm [5.79]. This often leads to an underestimation of the superconducting volume fractions of doped fullerite superconductor powders if the fraction is determined from zero-field-cooling magnetization experiments without grain size corrections.

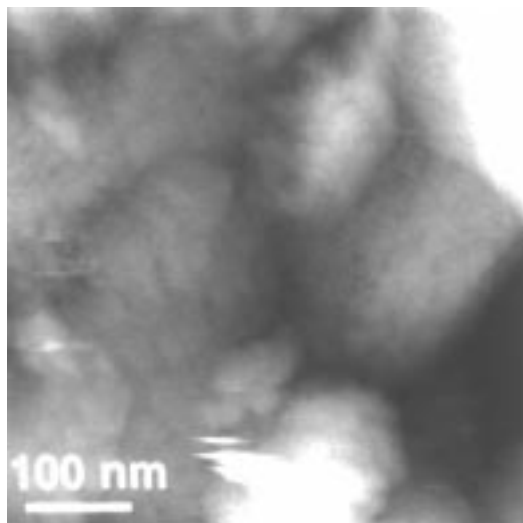


Figure 5.69: Large scale STM image of Rb_3C_{60} showing grains with typical sizes of a few hundred nanometres.

Molecularly resolved STM images of Rb_3C_{60} grains show ball-shaped features with an apparent diameter of 0.7 nm. These features have to be attributed to individual C_{60} molecules. Different crystallographic faces are observed (see fig. 5.70). Figure 5.70a shows the (111) face with a hexagonal arrangement of fullerene molecules with a nearest-neighbour-distance of 1 nm. A schematic view of the (111) plane in the fcc lattice is displayed in fig. 5.70b. Figure 5.70c shows an oblique lattice ($a = 1$ nm, $b = 1.7$ nm),

which is interpreted as the fcc(311) face (see for comparison the schematic view of the fcc(311) plane in fig. 5.70d).

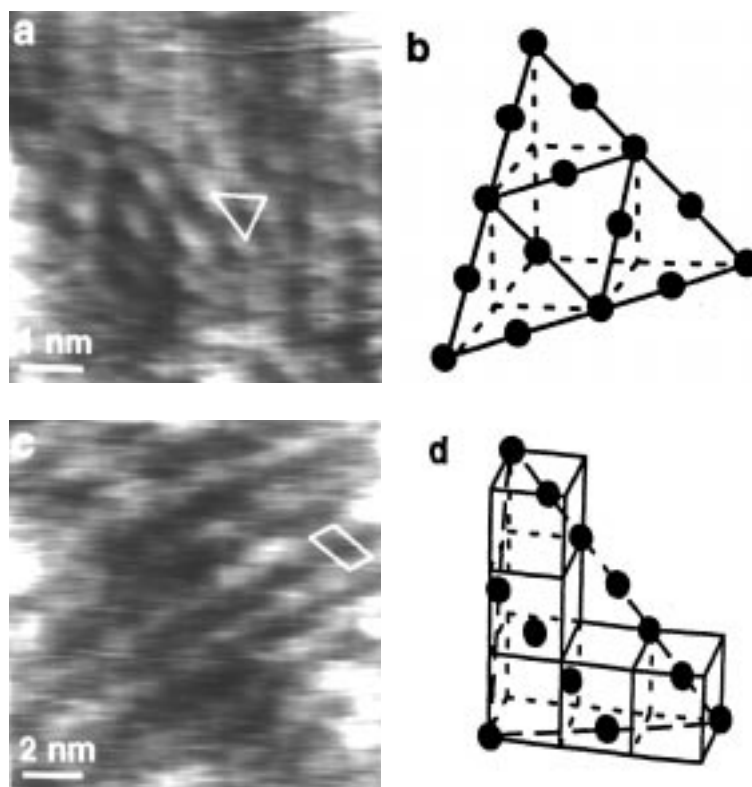


Figure 5.70: Molecular resolution STM images of a Rb_3C_{60} grain. (a) (111) facet with a hexagonal arrangement of C_{60} molecules. The nearest-neighbour-distance is about 1 nm, the apparent size of the molecules is 0.7 nm. The white triangle is the (111) mesh unit. (b) Schematic view of the fcc(111) plane. (c) (311) facet showing an oblique C_{60} lattice ($a = 1$ nm, $b = 1.7$ nm). (d) Schematic view of the fcc(311) plane. The white parallelogram is the (311) mesh unit.

5.5.4 STM results on KTI- and RbTI-doped C(60)

Polycrystalline $\text{C}_{60/70}$ and the respective dopants ($\text{KTl}_{1.5}$ and $\text{RbTl}_{1.5}$) in the molar ratio 1:3 were heated in a pure argon atmosphere at 340 °C for 62 h ($(\text{KTl}_{1.5})_3\text{C}_{60}$) and 450 °C for 18 h ($(\text{RbTl}_{1.5})_3\text{C}_{60}$). After pressing pellets STM investigations were performed in argon environment. The synthesis of the KTI- and RbTI-codoped samples goes back to previous results obtained from other doped materials such as graphite intercalation compounds (GIC's). Among the GIC's with the highest critical temperatures to superconductivity T_c are $\text{KTl}_{1.5}\text{C}_4$ (2.7 K) and $\text{KTl}_{1.5}\text{C}_8$ (2.45 K) [5.86]. C_{60} fullerenes doped with thallium-alkali metal alloys also show superconductivity [5.65, 5.66]. Their T_c 's,

however, coincide in most cases with those of the non-thallium-containing K- and Rb-doped fullerites. Regarding the similar T_c 's of the Tl-containing and non-Tl-containing K- and Rb-fullerites, it is rather straightforward to assume that the Tl-metal has little or no influence on superconductivity in these compounds. A recent report [5.87] has proved the presence of metallic Tl in $(\text{RbTl}_{1.5})_3\text{C}_{60}$. The STM images shown here support the presence of Tl-metal in doped fullerites with the nominal composition $(\text{MTl}_{1.5})_3\text{C}_{60}$ ($M = \text{K}, \text{Rb}$).

AC-susceptibility as a function of temperature provides evidence for the presence of

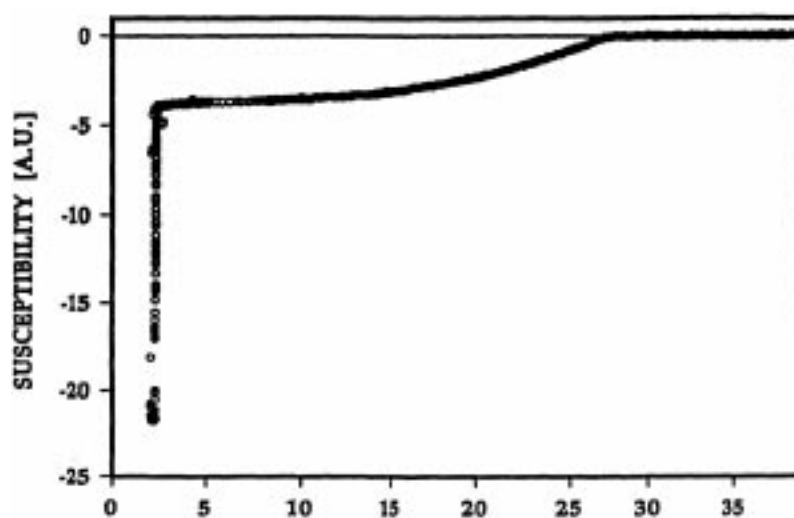


Figure 5.71: Temperature-dependent AC susceptibility data for a $(\text{RbTl}_{1.5})_3\text{C}_{60}$ powder sample. T_c (onset) is at 27.5 K. A second transition assigned to metallic thallium is observed at 2.4 K.

metallic Tl in the samples. $(\text{KTl}_{1.5})_3\text{C}_{60}$ ($T_c = 17.6$ K) and $(\text{RbTl}_{1.5})_3\text{C}_{60}$ ($T_c = 27.5$ K) exhibit at 2.4 K a second transition which coincides with the T_c of metallic thallium. The shielding fraction of the Tl indicates that approximately 90 % of the Tl used for preparation of the $(\text{RbTl}_{1.5})_3\text{C}_{60}$ sample contributes to the diamagnetic signal. Figure 5.71 shows the temperature dependence of the AC-susceptibility at $\nu = 107$ Hz of $(\text{RbTl}_{1.5})_3\text{C}_{60}$ powder sample (data by *M. Baenitz*²⁰). The T_c (27.5 K) is very similar to that of Rb_3C_{60} ($T_c = 28$ K). X-ray diffraction of RbTl-doped C_{60} samples shows, in addition to the Rb_3C_{60} reflections, peaks for both hexagonal and simple cubic thallium [5.87]. This implies that the initially homogeneous $\text{RbTl}_{1.5}$ alloy has separated into its components during the preparation of $(\text{RbTl}_{1.5})_3\text{C}_{60}$, and mainly Rb_3C_{60} is formed. Consequently, the Rb_3C_{60} powder contains metallic thallium.

A synthesis of Rb_3C_{60} using binary alloys can still be useful since the binary alloys are handled more easily (grinding, weighing) and processed at lower reaction temperatures.

²⁰Freie Universität Berlin, Berlin (Germany).

Zhang *et al.* [5.88] have used RbHg alloy to prepare Rb_3C_{60} at 200 °C.

STM images of the Tl-containing compounds show similar grain sizes as the non-Tl-containing compounds (see the large scale STM image of $(\text{RbTl}_{1.5})_3\text{C}_{60}$ in fig. 5.72a). However, a clear difference from the non-Tl-containing compounds is observed on a molecular scale. Figure 5.72b displays a STM image of $(\text{KTl}_{1.5})_3\text{C}_{60}$ showing ball-shaped features of an apparent diameter of 1.7 nm. This value is significantly larger than that of a single C_{60} molecule (0.7 nm).

These larger units have to be interpreted as aggregates of C_{60} and the intercalant metals. Actually, a rough estimate of the diameter of a $(\text{KTl}_{1.5})_3\text{C}_{60}$ complex as composed of metal atoms and a C_{60} molecule in a close-packed-arrangement of hard spheres with the respective van-der-Waals radii gives a diameter of about 1.5 nm [5.89].

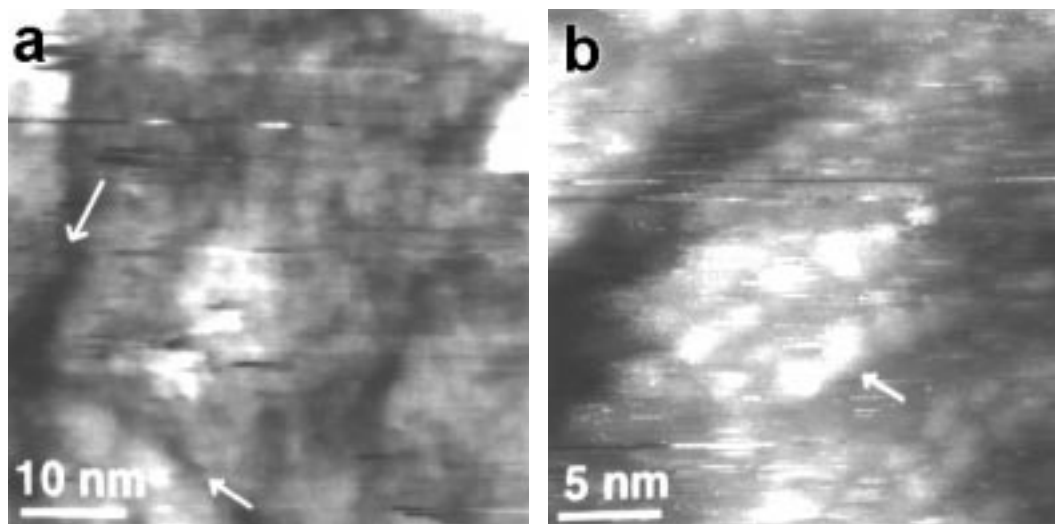


Figure 5.72: (a) STM image of $(\text{RbTl}_{1.5})_3\text{C}_{60}$ showing grain boundaries (marked by arrows). (b) Molecular resolution STM image of $(\text{KTl}_{1.5})_3\text{C}_{60}$. The apparent diameter of the ball-shaped features (arrow) is significantly larger (1.7 nm) than that of a C_{60} molecule (0.7 nm). This might be explained by assigning the balls to a complex of C_{60} and the intercalant and/or electronic structure effects.

Since STM measures the local density of states at the Fermi level, the electronic structure of $(\text{KTl}_{1.5})_3\text{C}_{60}$ may also influence the size and shape of the spherical features in fig. 5.72b. No structure which could be assigned to metal intercalant atoms has been resolved within the ball-shaped units.

5.5.5 Conclusion

In summary, large scale STM images of alkali metal doped fullerite powder samples show grain sizes of several hundred nanometres. This small size which is comparable to the magnetic field penetration depth may account for the observed small shielding fractions in magnetization experiments. Molecular scale STM images of Rb_3C_{60} reveal (111) and (311) arrangements of fullerene molecules, but no indications of the Rb intercalant are found since there is no intercalant density of states near the Fermi energy. In $(\text{KTl}_{1.5})_3\text{C}_{60}$, however, the significantly larger molecular units can be explained by the AC susceptibility and X-ray diffraction evidence of metallic thallium in the thallium-alkali metal doped fullerites.

5.5.6 Outlook

Doped fullerene-based superconductor compounds as well as cuprate superconductors do not seem to be 'ideal' materials for the application of high temperature superconductivity. Up to now (1994) only very few application areas of these materials have been established. On the RF-application panel Tl-Ba-Ca-Cu-O thin film based devices allow the construction of *microwave filters, antennas and resonators* which have the same figures of merit as copper based devices, but are of a much smaller size, which is an advantage for space applications. Examples in the high power branch are *current leads* made from ceramic YBCO to feed in high currents to conventional superconducting magnets operated at liquid helium temperatures. The thermal and electrical losses of HTSC current leads are much smaller than those of copper leads. A further application is a *current limiter*: if the current in an electricity network exceeds the critical current of a HTSC element incorporated in the network, the loss of superconductivity limits the current. Despite of some BSCCO powder-in-tube-type 'wires' HTSC cannot be handled as usual Cu wires due to the brittleness of these materials.

The recent discovery of RE(Ni/Pt)BC (RE=rare earth) superconductors [5.90, 5.91, 5.92] might provide promising candidates for applications since these materials are less brittle and behave similar to metals regarding their mechanical properties. $\text{YNi}_4\text{BC}_{0.2}$ ($T_c = 12.5$ K), $\text{YNi}_2\text{B}_3\text{C}_{0.2}$ ($T_c = 13.5$ K) [5.91], $\text{YPd}_5\text{B}_3\text{C}_{0.3}$ ($T_c = 22.6$ K) [5.92] and $\text{RENi}_2\text{B}_2\text{C}$ (RE = Y, Tm, Er, Ho, Lu) ($T_c = 16.6$ K) [5.93] are typical representatives of this class of superconductors. The crystal structure of $\text{LuNi}_2\text{B}_2\text{C}$ has been determined to space group $I4/mmm$, $a = 3.4639\text{\AA}$, $c = 10.6313\text{\AA}$ and consists of alternating LuC and buckled $\text{Ni}_2\text{B}_2\text{-C}$ layers [5.94]. T_c is up to now comparable with technically relevant superconductors like Nb_3Sn ($T_c = 18.0$ K), but possibly systems with even higher T_c will be found.

References

- [5.1] H.W. Kroto, J.R. Heath, S.C. O'Brian, R.F. Curl, R.E. Smalley, *Nature* 318 (1985) 162.
- [5.2] H.W. Kroto, *Angew. Chem.* 104 (1992) 113.
- [5.3] E.A. Rohlfing, D. Cox, A. Kaldor, *J. Chem. Phys.* 81 (1984) 3322.
- [5.4] W. Krätschmer, L.D. Lamb, K. Fostiropoulos, R. Huffman, *Nature* 347 (1990) 354.
- [5.5] R. Taylor, J.P. Hare, A.K. Abdul-Sada, H.W. Kroto, *Chem. Commun.* 20 (1990) 1423.
- [5.6] C.S. Yannoni, M.E. Johnson, G. Meijer, D.S. Bethune, J.R. Salem, *Jour. Phys. Chem.* 95 (1991) 9.
- [5.7] R.C. Haddon, L.E. Brus, K. Raghavachari, *Chem. Phys. Lett.* 125 (1986) 459.
- [5.8] S. Saito, A. Oshiyama, *Phys. Rev. Lett.* 66 (1991) 2637.
- [5.9] J.E. Fischer, P.A. Heiney, A.R. McGhie, W.J. Romanov, A.M. Denenstein, J.P. McCauley Jr., and A.B. Smith III, *Science* 252 (1991) 1288.
- [5.10] P.A. Heiney, J.E. Fischer, A.R. McGhie, W.J. Romanow, A.M. Denenstein, J.P. McCauley Jr., A.B. Smith III, and D.E. Cox, *Phys. Rev. Lett.* 66 (1991) 2911.
- [5.11] W.I.F. David, R.M. Ibberson, J.C. Matthewman, K. Prassides, T.J.S. Dennis, J.P. Hare, H.W. Kroto, R. Taylor and D.R.M. Walton, *Nature* 353 (1991) 147.
- [5.12] R.M. Fleming, B. Hessen, A.R. Kortan, T. Siegrist, P. Marsh, D.W. Murphy, R.C. Haddon, R. Tycko, G. Dabbagh, A.M. Muzsca, M.L. Kaplan, S.M. Zahurak, *Mater. Res. Soc. Symp. Proc.* 206 (1991) 691.
- [5.13] Y. Saito, N. Suzuki, H. Shinohara, T. Hayashi, and M. Tomita, *Ultramicroscopy* 41 (1992) 1.
- [5.14] W. Krakow, N.M. Rivera, R.A. Roy, R.S. Ruoff, and J.J. Cuomo, *J. Mater. Res.* 7 (1992) 784.
- [5.15] R.J. Wilson, G. Meijer, D.S. Bethune, R.D. Johnson, D.D. Chambliss, M.S. de Vries, H.E. Hunziker and H.R. Wendt, *Nature* 348 (1990) 621.
- [5.16] J.L. Wragg, J.E. Chamberlain, H.W. White, W. Krätschmer and D.R. Huffman, *Nature* 348 (1990) 623.

- [5.17] D. Purdie, IBM Research Division, Zürich Research Lab., Rüschlikon (Switzerland), private communication.
- [5.18] Y.Z. Li, J.C. Patrin, M. Chander, J.H. Weaver, L.P.F. Chibante, and R.E. Smalley, *Science* 252 (1991) 547, *idem Science* 253 (1991) 429.
- [5.19] H.P. Lang, V. Thommen-Geiser, J. Frommer, A. Zahab, P. Bernier and H.-J. Güntherodt, *Europhys. Lett.* 18 (1992) 29.
- [5.20] A. Zahab, J.L. Sauvajol, L. Firlej, R. Aznar, P. Bernier: *J. Phys. I (France)* 2 (1992) 7.
- [5.21] T. Chen, S. Howells, M. Gallagher, L. Yi, D. Sarid, D.L. Lichtenberger, K.W. Nebesny and C.D. Ray, *J. Vac. Sci. Technol. B* 9 (1991) 2461.
- [5.22] D. Sarid, T. Chen, S. Howells, M. Gallagher, L. Yi, D.L. Lichtenberger, K.W. Nebesny and C.D. Ray, D.R. Huffman and L.D. Lamb, *Ultramicroscopy* 42-44 (1992) 610.
- [5.23] J.M. Hawkins, T.A. Lewis, S.D. Loren, A. Meyer, J.R. Heath, Y. Shibato, and R.J. Saykally, *J. Org. Chem.* 55 (1990) 6250.
- [5.24] W.H. Pirkle, C.J. Welch, *J. Org. Chem.* 56 (1991) 6973, *idem J. Chromatogr.* 609 (1992) 89.
- [5.25] H. Werner, D. Bublak, U. Göbel, B. Henschke, W. Bensch, and R. Schlögl, *Angew. Chem. Int. Ed. Engl.* 31 (1992) 868.
- [5.26] J. P. Hare, H. W. Kroto, R. Taylor, *Chem. Phys. Lett.* 177 (1991) 394.
- [5.27] H. Ajie, M.M. Alvarez, S.J. Anz, R.D. Beck, F. Diederich, K. Fostiropoulos, D.R. Huffman, W. Krätschmer, Y. Rubin, K.E. Schriver, D. Sensharma, and R.L. Whetten, *J. Phys. Chem.* 94 (1990) 8630.
- [5.28] P.-M. Allemand, A. Koch, F. Wudl, Y. Rubin, F. Diederich, M. M. Alvarez, S. J. Anz, R. L. Whetten, *J. Am. Chem. Soc.* 113 (1991) 1050.
- [5.29] F. Negri, G. Orlandi and F. Zerbetto, *Chem. Phys. Lett.* 144 (1988) 31.
- [5.30] I. László and L. Udvardi, *Chem. Phys. Lett.* 136 (1987) 418.
- [5.31] D.M. Cox, R.D. Sherwood, P. Tindall, K.M. Creegan, W. Anderson and D.J. Martella, in: *Fullerenes*, Hammond, G., (Editor), American Chemical Society Symposium Series 481, Washington, DC, U.S.A., pp. 117-125 (1992).
- [5.32] J. Abrefah, D.R. Olander, M. Balooch and W.J. Siekhaus, *Appl. Phys. Lett.* 60 (1992) 1313.
- [5.33] C.K. Mathews, P.R. Vasudeva Rao, T.G. Srinivasan, V. Ganesan, N. Sivaraman, T.S. Lakshmi Narasimhan, I. Kaliappan, K. Chandran and R. Dhamodaran, *Current Science* 61 (1991) 834.

- [5.34] H.P. Lang, V. Thommen-Geiser, C. Bolm, M. Felder, J. Frommer, R. Wiesendanger, R. Schlögl, A. Zahab, P. Bernier, G. Gerth, D. Anselmetti, and H.-J. Güntherodt, *Appl. Phys. A* 56 (1993) 197.
- [5.35] H.P. Lang, V. Thommen-Geiser, R. Hofer and H.-J. Güntherodt, in *Electronic Properties of Fullerenes*, Springer Series in Solid-State Sciences 117 (ed. H. Kuzmany, J. Fink, M. Mehring, S. Roth, 228 (1994).
- [5.36] H.P. Lang, V. Thommen-Geiser and H.-J. Güntherodt, *J. liq. molec. cryst.* (1994).
- [5.37] E.I. Altman, R.J. Colton, *Surf. Sci.* 279 (1992) 49.
- [5.38] R. Tycko, R.C. Haddon, G. Dabbagh, S.H. Clarum, D.C. Douglass, A.M. Mujسع, *J. Phys. Chem.* 95 (1991) 518.
- [5.39] C. Horie and H. Miyazaki, *Jpn. J. Appl. Phys.* 26 (1987) L995.
- [5.40] C. Chavy, C. Joachim and A. Alibelli, *Chem. Phys. Lett.* 214 (1993) 569.
- [5.41] S. Behler, H.P. Lang, S. Pan, V. Thommen-Geiser and H.-J. Güntherodt, *Z. Phys. B* 91 (1993) 1.
- [5.42] G.A. Samara, J.E. Schirber, B. Morosin, L.V. Hansen, D. Loy, and A.P. Sylwester, *Phys. Rev. Lett.* 67 (1991) 3136.
- [5.43] J.P. Lu, X.-P. Li, and R.M. Martin, *Phys. Rev. Lett.* 68 (1992) 1551.
- [5.44] S.J. Duclos, K. Brister, R.C. Haddon, A.R. Kortan, and F.A. Thiel, *Nature* 351 (1991) 380.
- [5.45] M. Núñez-Regueiro, P. Monceau, A. Rassat, P. Bernier, and A. Zahab, *Nature* 354 (1991) 289.
- [5.46] C.S. Yoo and W.J. Nellis, *Science* 254 (1991) 1489.
- [5.47] F. Moshary, N.H. Chen, I.F. Silvera, C.A. Brown, H.C. Dorn, M.S. de Vries, and D.S. Bethune, *Phys. Rev. Lett.* 69 (1992) 466.
- [5.48] H.J. Mamin, E. Ganz, D.W. Abraham, R.E. Thomson, and J. Clarke, *Phys. Rev. B* 34 (1986) 9015.
- [5.49] C.M. Mate, R. Erlandsson, G.M. McClelland, and S. Chiang, *Surf. Sci.* 208 (1989) 473.
- [5.50] B. Marchon, M. Salmeron, and W. Siekhaus, *Phys. Rev. B* 39 (1989) 12907.
- [5.51] G. Galli, R.M. Martin, R. Car, and M. Parrinello, *Phys. Rev. Lett.* 63 (1989) 988.
- [5.52] P.H. Gaskell, A. Saeed, P. Chieux, and D.R. McKenzie, *Phil. Mag. B* 66 (1992) 155.
- [5.53] G. Galli, R.M. Martin, R. Car, and M. Parrinello, *Phys. Rev. Lett.* 62 (1989) 555.
- [5.54] C.Z. Wang, K.M. Ho, and C.T. Chan, *Phys. Rev. Lett.* 70 (1993) 611.

- [5.55] H. Pan, M. Pruski, B.C. Gerstein, F. Li, and J.S. Lannin, *Phys. Rev. B* 44 (1991) 6741.
- [5.56] R.C. Haddon, A.F. Hebard, M.J. Rosseinsky, D.W. Murphy, S.J. Duclos, K.B. Lyons, B. Miller, J.M. Rosamilia, R.M. Fleming, A.R. Kortan, S.H. Glarum, A.V. Makhija, A.J. Muller, R.H. Eick, S.M. Zahurak, R. Tycko, G. Dabbagh and F.A. Thiel, *Nature* 350 (1991) 320.
- [5.57] A.F. Hebard, M.J. Rosseinsky, R.C. Haddon, D.W. Murphy, S.H. Glarum, T.T.M. Palstra, A.P. Ramirez and A.R. Kortan, *Nature* 350 (1991) 600.
- [5.58] N.B. Hannay, T.H. Geballe, B.T. Matthias, K. Andres, P. Schmidt and D. MacNair, *Phys. Rev. Lett.* 14 (1965) 225.
- [5.59] O. Zhou, J.E. Fischer, N. Coustel, S. Kycia, Q. Zhu, A.R. McGhie, W.J. Romanow, J.P. McCauley Jr, A.B. Smith and D.E. Cox, *Nature* 351 (1991) 462.
- [5.60] M.J. Rosseinsky, A.P. Ramirez, S.H. Glarum, D.W. Murphy, R.C. Haddon, A.F. Hebard, T.T.M. Palstra, A.R. Kortan, S.M. Zahurak and A.V. Makhija, *Phys. Rev. Lett.* 66 (1991) 2830.
- [5.61] K. Tanigaki, T.W. Ebbesen, S. Saito, J. Mizuki, J.S. Tsai, Y. Kubo and S. Kuroshima, *Nature* 352 (1991) 222.
- [5.62] R.M. Fleming, A.P. Ramirez, M.J. Rosseinsky, D.W. Murphy, R.C. Haddon, S.M. Zahurak and A.V. Makhija, *Nature* 352 (1991) 787.
- [5.63] Z. Iqbal, R.H. Baughman, B.L. Ramakrishna, S. Khare, N.S. Murphy, H.J. Bornemann, D.E. Morris, *Science* 254 (1991) 826.
- [5.64] Z. Iqbal, R.H. Baughman, S. Khare, N.S. Murphy, B.L. Ramakrishna, H.J. Bornemann, D.E. Morris, *Science* 256 (1992) 950.
- [5.65] M. Kraus, J. Freytag, S. Gärtner, H.M. Vieth, W. Krätschmer and K. Lüders, *Z. Phys. B* 85 (1991) 1.
- [5.66] M. Kraus, S. Gärtner, M. Baenitz, M. Kanowski, H.M. Vieth, C.T. Simmons, W. Krätschmer, V. Thommen, H.P. Lang, H.-J. Güntherodt and K. Lüders, *Europhys. Lett.* 17 (1992) 419.
- [5.67] R. Lal and S.K. Joshi, *Solid State Comm.* 80 (1991) 725.
- [5.68] *Nature* 352 (1991) 749.
- [5.69] Comment by D. Swinbanks, *Nature* 353 (1991) 377.
- [5.70] K. Tanigaki, I. Hirose, T.W. Ebbesen, J. Mizuki, Y. Shimakawa, Y. Kubo, J.S. Tsai and S. Kuroshima, *Nature* 256 (1992) 419.
- [5.71] K. Tanigaki, T.W. Ebbesen, J.S. Tsai, I. Hirose and J. Mizuki, *Europhys. Lett.* 23 (1993) 57.

- [5.72] A.R. Kortan, N. Kopylov, S.H. Glarum, E.M. Gyorgy, A.P. Ramirez, R.M. Fleming, F.A. Thiel and R.C. Haddon, *Nature* 355 (1992) 529.
- [5.73] L.W. Song, K.T. Fredette, D.D.L. Chung and Y.H. Kao, *Solid State Comm.* 87 (1993) 387.
- [5.74] K. Imaeda, I.I. Khairullin, K. Yakushi, M. Nagata, N. Mizutani, H. Kitagawa and H. Inokuchi, *Solid State Comm.* 87 (1993) 375.
- [5.75] O. Zhou, R.M. Fleming, D.W. Murphy, M.J. Rosseinsky, A.P. Ramirez, R.B. Dover and R.C. Haddon, *Nature* 362 (1993) 433.
- [5.76] G. Zhennan, Q. Jiusin, J. Zhaoxia, Z. Xihuang, F. Sunqi, Z. Wensheng and Z. Xing, *Solid State Comm.* 82 (1992) 167.
- [5.77] T.W. Ebbesen, J.S Tsai, K. Tanigaki, J. Tabuchi, Y. Shimakawa, Y. Kubo, I. Hirose and J. Mizuki, *Nature* 355 (1992) 620.
- [5.78] A.P. Ramirez, A.R. Kortan, M.J. Rosseinsky, S.J. Duclos, A.M. Muzsca, R.C. Haddon, D.W. Murphy, A.V. Makhija, S.M. Zahurak, K.B. Lyons, *Phys. Rev. Lett.* 68 (1991) 1058.
- [5.79] G. Sparr, J.D. Thompson, R.L. Whetten, S.M. Huang, R.B. Kaner, F.N. Diederich, G. Gruner, K. Holczer, *Physical Review Letters* 68 (1992) 1228.
- [5.80] T. Takahashi, T. Morikawa, S. Hasegawa, K. Kamiya, H. Fujimoto, S. Hino, K. Seki, H. Katayama-Yoshida, H. Inokuchi, K. Kikuchi, S. Suzuki, K. Ikemoto, and Y. Achiba, *Physica C* 190 (1992) 205.
- [5.81] P.J. Benning, J.L. Martins, J.H. Weaver, L.P.F. Chibante, and R.E. Smalley, *Science* 252 (1991) 1417.
- [5.82] L.Q. Jiang and B.E. Koel, *Phys. Rev. Lett.* 72 (1994) 140.
- [5.83] J.H. Weaver, D.M. Poirier, and Y.B. Zhao, in *Electronic Properties of Fullerenes*, Eds. H. Kuzmany, J. Fink, M. Mehring and S. Roth, Springer-Verlag Berlin Heidelberg (1993), p. 146.
- [5.84] R. Schauwecker: *Magnetische Eigenschaften des supraleitenden Zustands von Rb₃C₆₀*, Diplomarbeit, Physikinstitut der Universität Zürich (1994).
- [5.85] J.R. Clem and V.G. Kogan, *Jpn. J. Appl. Phys.*, 26 (1987) 1161.
- [5.86] R.A. Wachnik, L.A. Pendry, F.L. Vogel and P. Lagrange, *Solid State Comm.* 43 (1982) 5.
- [5.87] M. Kraus, M. Baenitz, S. Gärtner, H.M. Vieth, H. Werner, R. Schlögl, W. Krätschmer, M. Kanowski, V. Thommen, H.-J. Güntherodt and K. Lüders, in: *Novel Forms of Carbon* (Materials Research Society, Pittsburgh, 1992), MRS Symposium Proceedings, Volume 270, p. 135.

- [5.88] Z. Zhang, C.-C. Chen, S.P. Kelty, H. Dai and C.M. Lieber, *Nature* 353 (1991) 333.
- [5.89] H.P. Lang, K. Lüders, R. Wiesendanger, M. Kraus, S. Gärtner, W. Krätschmer and H.-J. Güntherodt, *Physica B* 182 (1992) 223.
- [5.90] C. Mazumdar, R. Nagarajan, C. Godart, L.C. Gupta, M. Latroche, S.K. Dhar, C. Levy-Clement, B.D. Padalia and R. Vijayaraghavan, *Solid State Commun.* 87 (1993) 413.
- [5.91] R. Nagarajan, C. Mazumdar, Z. Hossain, S.K. Dhar, K.V. Gopalakrishnan, L.C. Gupta, C. Godart, B.D. Padalia and R. Vijayaraghavan, *Phys. Rev. Lett.* 72 (1994) 274.
- [5.92] R.J. Cava, H. Takagi, H.W. Zandbergen, J.J. Krajewski, W.F. Peck Jr., R.B. van Dover, R.J. Felder, T. Siegrist, K. Mizuhashi, J.O. Lee, H. Eisaki, S.A. Carter and S. Uchida, *Nature* 367 (1994) 146.
- [5.93] R.J. Cava, H. Takagi, B. Batlogg, H.W. Zandbergen, J.J. Krajewski, W.F. Peck Jr., T. Siegrist, B. Batlogg, R.B. van Dover, R.J. Felder, K. Mizuhashi, J.O. Lee, H. Eisaki and S. Uchida, *Nature* 367 (1994) 252.
- [5.94] T. Siegrist, H.W. Zandbergen, R.J. Cava, J.J. Krajewski, W.F. Peck Jr., *Nature* 367 (1994) 254.

Chapter 4

Traditional carbon allotropes and GIC's

The second range of topics deals with traditional carbon allotropes like graphite and diamond. Although graphite has only little in common with the HTSC discussed in chapters 2 and 3, it is also a layered material that can be manipulated to a large extent by changing its electronic structure by doping with metals. These so-called Graphite Intercalation Compounds (GIC's) exhibit a large structural variety which is accessible to investigations with a scanning tunneling microscope. In contrast to the HTSC most of these GIC's are very unstable when stored in the ambient air so that special precautions have to be taken, for example investigation by STM in a glove box filled with high purity argon gas. Some GIC's are even superconductors¹ but this will not be discussed here. Structural aspects will dominate the chapter on carbon allotropes.

The second 'classic' allotrope of carbon is diamond with a three-dimensional cubic structure being very different from the layered materials discussed so far. Even diamond can be doped by boron or arsenic resulting in appreciable conductivity at room temperature. Such doped homoepitaxial diamond films on diamond substrates have been subject to STM investigations as well.

4.1 Graphite

The first section discusses graphite. Even if large single crystals of hexagonal graphite are not available a textured form with micrometre-sized single crystalline domains is available: Highly Oriented Pyrolytic Graphite (HOPG). The [0001] direction of HOPG is perpendicular to the surface of the shiny HOPG platelets. Figure 4.1 displays the atomic structure of graphite. The graphite sheets (graphene layers) show an *AB* stacking sequence with the *B* layers shifted with respect to the *A* layers. The carbon atoms in the graphite allotrope have a sp^2 hybridization giving rise to strong in-plane bonds and weak bonds between planes. The *AB* stacking causes the so-called *carbon site asymmetry*: two inequivalent sites are observed in graphene layers. The α -sites are located above and below carbon atoms in the neighbouring graphene layers, whereas the β -sites are situated above and below carbon ring centres (hollow sites) of adjacent graphene layers. This asymmetry affects the electronic structure of graphite, especially at its surface. Cal-

¹At very low temperatures like 0.55 K in case of a K-GIC.

culations by *Batra et al.* [4.1] and *Tománek et al.* [4.2, 4.3] have shown that the Local Density of States (LDOS) close to the Fermi level is different for the two carbon sites.

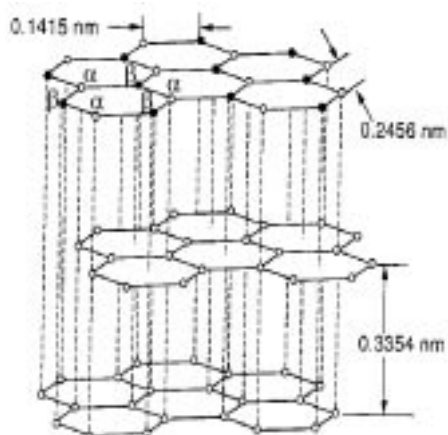


Figure 4.1: Structure of highly oriented pyrolytic graphite (HOPG). The interatomic distance in the graphitic planes (graphene layers) with honeycomb symmetry is 0.1415 nm. Two inequivalent sites are found: α -sites having a carbon atom in the second layer and β -sites located over a carbon ring centre in the second layer. The distance between site-equivalent atoms is 0.2456 nm. The interlayer spacing between graphene planes is 0.3354 nm.

Graphite and especially HOPG has become an established calibration standard for scanning tunneling microscopy due to the facile preparation of a clean surface by cleaving it.² The first investigations of graphite by *Binnig et al.* [4.4] clearly demonstrated the atomic resolution capability of the STM, but also showed that the information obtained is electronic structure of the surface. Assumed a tunneling voltage V is applied, only the states in the energy window $E_F \pm eV$ contribute to the tunnel current. Due to the carbon site asymmetry the LDOS of the two different sites is different [4.1]–[4.3] and leads to a hexagonal atom pattern with a lattice constant of 0.25 nm instead of a honeycomb structure with an interatomic distance of 0.14 nm (see fig. 4.3). This implies that only one type of carbon sites is imaged at a given bias voltage. Figure 4.2 shows a typical STM image of graphite in a three-dimensional rendition. The hillocks spaced by a distance of 0.25 nm represent β -sites of the carbon (0001) surface.

²Cleaving of HOPG may be done by using a piece of adhesive tape, glueing it to the HOPG surface and tearing it off. Some HOPG material sticks to the tape and a fresh HOPG surface is exposed. A different method is cleaving HOPG by using a razor blade.

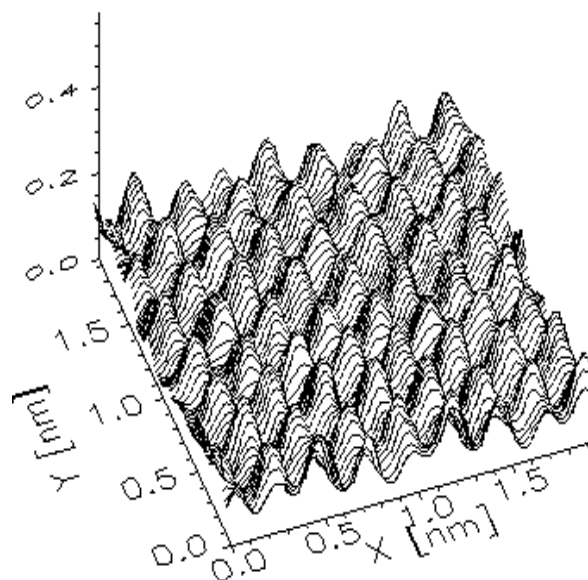


Figure 4.2: Three-dimensional rendition of a STM image of a HOPG surface. The hillocks represent β -sites of the carbon (0001) surface spaced by 0.25 nm.

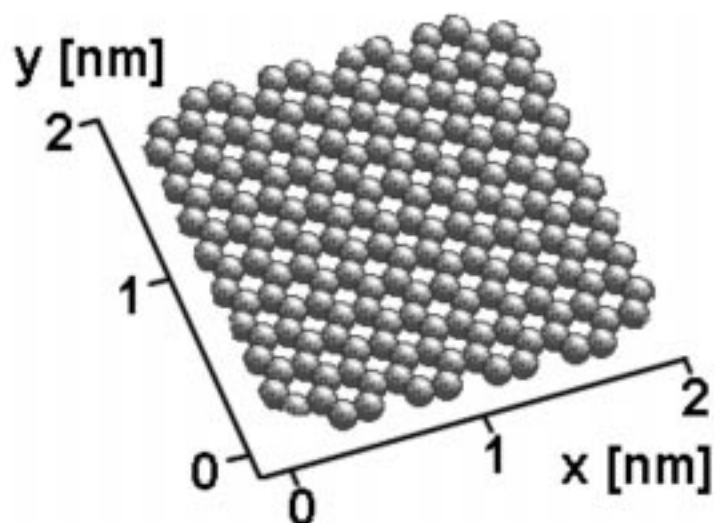


Figure 4.3: Graphite (0001) surface. The nearest distance between carbon atoms in the honeycomb structure is 0.14 nm.

4.2 Graphite intercalation compounds

4.2.1 Introduction

Graphite Intercalation Compounds (GIC's) [4.5] have been of interest for a long time, both from a theoretical as well as from an experimental point of view. They provide model compounds for quasi-two-dimensional systems where the electronic and magnetic properties can be tailored to a large extent by choosing an appropriate intercalant. The insertion of intercalant layers between graphene sheets leads to an enlargement of the c-axis parameter in GIC's compared to pristine HOPG. Figure 4.4 schematically shows the stacking sequence in a *stage-1 GIC*: an alternating sequence of graphene sheets and intercalant layers. Figure 4.5 shows a three-dimensional model of a stage-1 GIC with a 2×2 intercalant superstructure³ in the galleries.⁴ Four different intercalant sites are observed denoted by α, β, γ and δ . Figure 4.6 illustrates the different stages of GIC's.

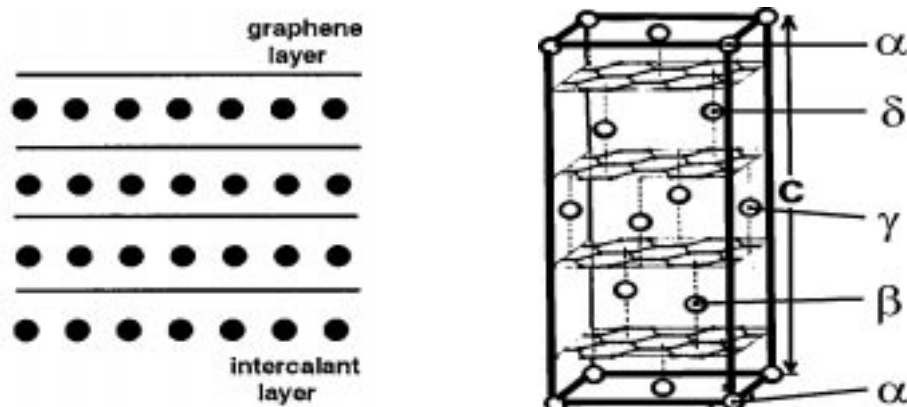


Figure 4.4: *LEFT:* Schematic side view of a stage-1 GIC. The stage indicates the number of graphene layers between intercalant layers.

Figure 4.5: *RIGHT:* Three-dimensional model of a stage-1 GIC with a 2×2 intercalant superstructure. Although the graphite does not show *AB* stacking four different intercalant sites are observed indicated by α, β, γ and δ .

In addition, the interesting transport, optical, catalytical, and tribological properties of GIC's open up a variety of applications. For some of these applications, such as in catalysis and tribology, the surface atomic and electronic structure plays a major role. It is therefore desirable to investigate the surface structure of GIC's in more detail, whereas earlier experimental investigations of GIC's have mainly focused on bulk properties. It

³With respect to the graphite honeycomb lattice. The sum formula of a stage-1 GIC with a 2×2 superstructure is C_8M with M denoting the (alkali) metal intercalant.

⁴The space between graphene sheets available for the insertion of the intercalant species is often called *gallery*.

was only recently that microscopic techniques such as high-resolution scanning-ion microscopy [4.6, 4.7] with about 20 nm lateral resolution and scanning tunneling microscopy (STM) [4.8]–[4.20] with atomic-resolution capability were applied to study the surface structure of GIC's from a submicrometre down to the atomic scale. Interesting superlattice structures have been found on the surfaces of GIC's by atomic-resolution STM studies. Here, STM data is presented obtained on the whole series of binary alkali-metal-graphite intercalation compounds (AM-GIC's) including Li-, K-, Rb-, and Cs-GIC's of stage-1. In addition the ternary AM-GIC's K₂Rb-, K₂Cs-, and RbCs-GIC's of stage-1 have been studied. The STM results obtained on a submicrometre scale indicate the presence of an inhomogeneous distribution of the intercalant, which seems to be an intrinsic property of GIC's. Atomic-resolution STM studies of binary AM-GIC's confirm earlier observations of hexagonal as well as nonhexagonal superlattices. The nonhexagonal one-dimensional superlattices observed by STM at the surface of binary heavy alkali-metal GIC's [4.15, 4.16] are also observed at the surface of ternary AM-GIC's. In addition, rectangular superlattices are found on the surfaces of binary and ternary AM-GIC's. It will be argued that the presence of a surface-driven charge-density wave (CDW) is the most likely explanation for these rectangular superlattice structures.

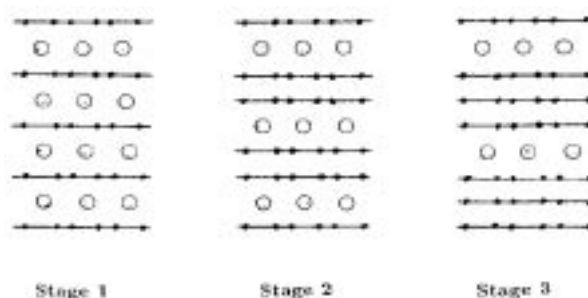


Figure 4.6: GIC's of different stage. The stage denotes the number of graphene layers between intercalant layers.

4.2.2 Experimental conditions

4.2.2.1 Preparation of GIC's

The following comments apply to the preparation of alkali-metal GIC's only since solely this type of GIC's has been studied in the present work. Due to the high reactivity of the alkali metals with oxygen⁵ special precautions have to be taken for a successful preparation of GIC's. In Basel sample handling is performed⁶ in a stainless steel glove box filled with high purity argon gas. Basically two methods are used for preparation of GIC's: the liquid phase reaction and the gas phase reaction. For the gas phase reaction an evacuated glass tube with several chambers is used (see fig. 4.7). The intercalant

⁵Lithium shows in addition a high reactivity with nitrogen.

⁶All GIC samples studied here have been prepared and characterized by Verena Thommen-Geiser.

(alkali metal) is located in the chamber shown on the left end of the tube. This chamber is directly connected to a second chamber containing the HOPG graphite. By placing the vessel in a furnace with a temperature gradient⁷ the alkali metal vaporizes and is being transferred to the chamber containing the HOPG. The vapour condenses in the colder chamber and is intercalating the HOPG. After intercalation and cooling the vessel to room temperature a small glass tube at the right end of the vessel can be broken by means of a steel rod (hammer) to transfer the intercalated samples to a sample holder, which is sealed afterwards. All these steps have to be executed without exposure to air. In fact, the whole procedure is done even without exposing the sample to argon.

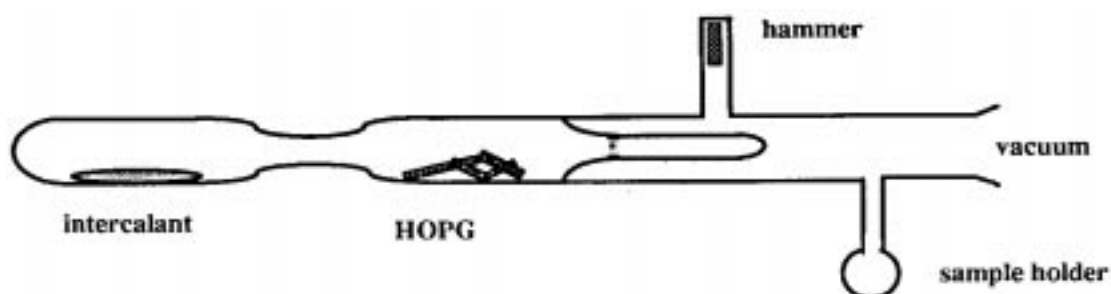


Figure 4.7: Vessel for preparation of GIC's by the vapour reaction method.

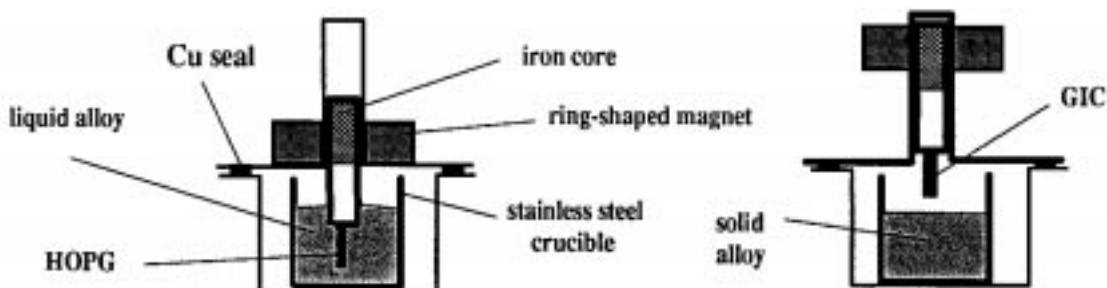


Figure 4.8: High temperature crucible for intercalation using the liquid phase reaction method.

The second method is the liquid phase reaction method (see fig. 4.8) where the HOPG platelet is in direct contact with the alkali metal. The easiest realization of this method is immersing the HOPG platelet in a crucible filled with molten alkali metal (on a heater plate) in the argon glovebox. A special type of crucible is shown in fig. 4.8 which is especially suited for intercalation at temperatures up to 600°C. The HOPG platelet being immersed into the intercalant is fixed to a stick with an iron core. By moving upwards a ring-shaped magnet the sample can be pulled out of the liquid alloy before the alloy solidifies.

⁷The alkali metal is situated at the hotter end.

Both methods are described in detail in previous PhD thesis work by *Pfluger* and *Gubler* [4.21, 4.22] or in literature [4.23]–[4.25].

The stage-1 Li-, K-, and ternary GIC samples were obtained by liquid-phase reaction of HOPG with the molten alkali metals (reaction temperatures between 100 and 250°C, exposure times between 4 h and 16 d). The stage-1 Rb- and Cs-GIC samples were prepared by the two-zone gas-phase reaction from HOPG (reaction temperatures of 200–280°C, exposure times of 1–3 d). The stage of all samples was checked by X-ray diffraction. As an example fig. 4.9 shows the X-ray diffraction spectrum of a K-GIC of stage-1 and that of pristine graphite.

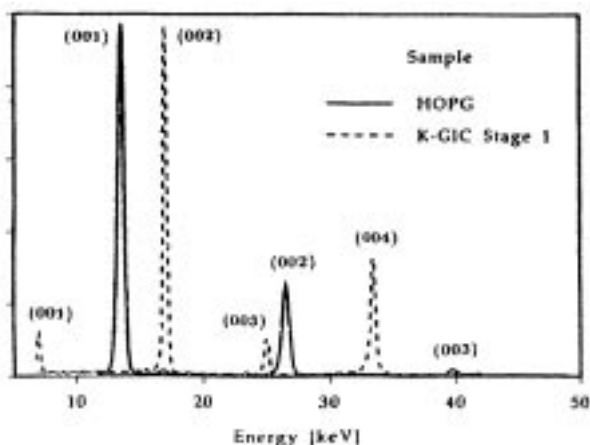


Figure 4.9: X-ray diffraction pattern of a K stage-1 GIC and pristine graphite. Note the enlargement of the layer spacing due to the potassium intercalation.

4.2.2.2 STM in high purity argon environment

The STM used for the investigation of the surface structure of GIC's is a commercially available instrument⁸ that is operated at room temperature in a stainless-steel glove box containing a high-purity Ar atmosphere (1 bar). A gas purification system lowers the O₂, N₂ and H₂O impurity levels beyond the detection limit of 1 ppm. The GIC samples were transferred into the glove box in sealed glass tubes through a fast-entry air lock. Thus, the GIC samples were never exposed to air. After breaking the glass tubes *in situ* inside the glove box, the samples were mechanically fixed on the sample holder stage of the STM unit. Prior to each series of STM measurements, the samples were freshly cleaved. Depending on the degree of surface reactivity of the different compounds, STM experiments could be performed on clean surfaces for time periods between half an hour and several hours in the described environment. After that time period a graphitic surface structure was visible only, without any superimposed superlattices. Mechanically prepared Pt-Ir tips were used for the STM measurements. To exclude artifacts originating from tip asymmetries or multiple tip imaging, several different tips were used for each kind of

⁸Nanoscope II, Digital Instruments Inc., Santa Barbara, CA.

sample. STM measurements were performed both in the constant-current as well as in the constant-height mode. The constant-current mode is particularly useful for getting quantitatively the measured corrugation amplitudes, whereas the constant-height mode offers the advantage of excluding corrugation enhancement effects due to forces acting between tip and sample [4.26].

4.2.3 STM on binary alkali metal GIC's

Prior to discussing the STM results on binary alkali metal GIC's (AM-GIC's) some remarks should be given on superstructures superimposed onto the graphite honeycomb lattice. In fig. 4.10 the graphite honeycomb lattice is shown. Choosing the reference hexagon (origin) in the left bottom corner of fig. 4.10 (labelled by '0') the distances of the other hexagons are indicated by numbers (the distances are measured in units of the smallest spacing between two hexagons). By this method superstructures can be easily described, i.e. the regular occupation of some hexagon sites. If all hexagon sites are occupied by an intercalant atom a 1×1 'superstructure' would result. In that case, however, it can not be distinguished between a 1×1 'superstructure' and a STM image of pristine graphite. In other cases like 2×2 or $\sqrt{3} \times \sqrt{3}$ superstructures the STM image of such a surface will be different from that of pristine graphite.

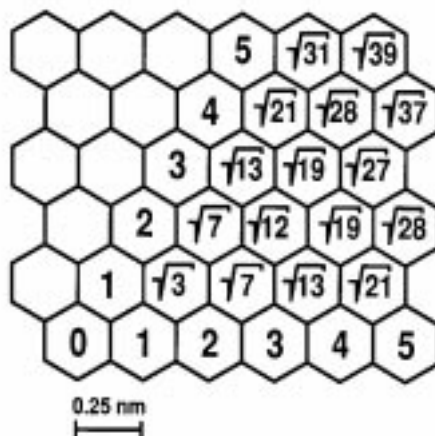


Figure 4.10: Several possible superstructures on the graphitic honeycomb lattice. For explanation see text.

4.2.3.1 Li-GIC's

Stage-1 Li-GIC's have been studied from a submicrometre down to the atomic scale using STM. Large-scale STM images typically show extended (> 100 nm), atomically flat terraces separated by steps, mainly of monatomic height ((0001) spacing after intercalation:

$I_c = 0.37$ nm), or grain boundaries originating from the HOPG host (see fig. 4.11). In addition, island-like structures were often found defined by an apparently reduced topographic height (see arrow). These islands typically have a lateral dimension of 50-200 nm and do not terminate at steps or grain boundaries. The apparent topographic depth of the islands observed in fig. 4.11 is about 2-3 nm, but can also be smaller. The measured depth was found to be independent of the applied bias voltage within a range of 0.05-1.0 V and also independent of the tunneling current within a range of 1-10 nA. These regions of apparently reduced topographic height may originate from locally missing intercalated lithium most likely in subsurface parts of the sample. However the observed islands do not necessarily represent topographic surface structure only. It is also possible that the islands represent surface regions of increased local work function leading to an increased local tunneling barrier height and therefore to an apparent decrease of the measured height in topographic STM images according to the tunneling formula

$$I \propto \exp(-A\sqrt{\Phi}s) \quad (4.1)$$

where

- $A = 1.025 \text{ eV}^{-1/2} \text{ \AA}^{-1}$,
- Φ is the local tunneling barrier height,
- s is the distance between the tip and the sample surface,
- and I is the tunneling current, which was kept constant during this STM measurement.

The relative change of the local tunneling barrier height is then given by

$$\Delta\Phi/\Phi_h = \frac{\Phi_h - \Phi_l}{\Phi_h} = 1 - \left(\frac{1}{1 + \Delta/s(\Phi_h)}\right)^2 \quad (4.2)$$

where

- Φ_h (Φ_l) is the higher (lower) value of the local tunneling barrier height,
- $s(\Phi_h)$ the distance between the tip and the sample surface corresponding to the higher local work-function region,
- and Δ is the apparent change of the topographic height.

Regardless of the interpretation of the STM image contrast in this case, the observed islands clearly indicate inhomogeneities in the spatial distribution of the lithium. It is interesting to make a comparison with the observation of islands of similar size in stage-4 SbCl_5 -GIC's [4.27]. In this case, Sb-rich islands of lateral dimension 50-100 nm have

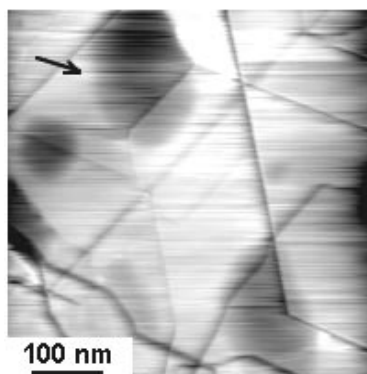


Figure 4.11: STM image of the surface of a stage-1 Li-GIC sample. Islands of apparently reduced topographic height can be seen clearly (arrow). These islands are not affected by monatomic steps running through the islands.

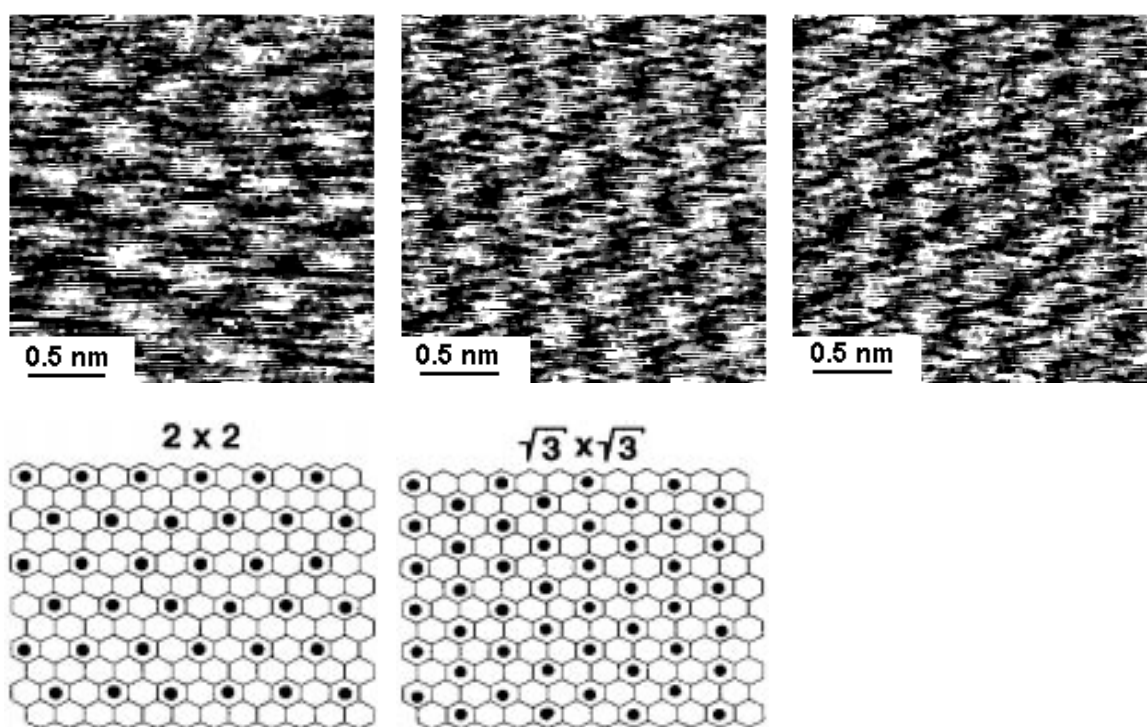


Figure 4.12: Atomic resolution STM images showing different hexagonal superlattices: 2×2 ($I_t = 10$ nA, $U_s = -162$ mV), *MIDDLE*: $\sqrt{3} \times \sqrt{3}$ ($I_t = 2.7$ nA, $U_s = -272$ mV), *RIGHT*: incommensurate superlattice with a lattice constant 0.35 nm ($I_t = 2.7$ nA, $U_s = -272$ mV). Models of 2×2 and $\sqrt{3} \times \sqrt{3}$ superstructures are shown in the lower row.

been identified by means of analytical electron microscope measurements, again indicating inhomogeneities in the distribution of the intercalated material in a completely different, acceptor GIC sample. It seems that such inhomogeneities are intrinsically present in GIC's, since they are observed in a variety of different compounds obtained by different preparation conditions.

Atomic-resolution STM measurements on the stage-1 Li-GIC's confirm earlier STM observations [4.11, 4.12] of three different hexagonal superlattices corresponding to 2×2 , $\sqrt{3} \times \sqrt{3}$ and an incommensurate hexagonal superlattice with lattice constants of 0.49 ± 0.02 nm, 0.43 ± 0.02 nm, and 0.35 ± 0.02 nm, respectively (fig. 4.12). These superlattices originate from the ordered arrangement of lithium at the surface of the stage-1 Li-GIC's. Bias-dependent STM measurements did not reveal a dependence of the observed superlattices on the applied sample-bias voltage within a bias range of ± 300 mV. Finally, it should be noted that nonhexagonal, one-dimensional superlattices such as those observed at the surface of heavier alkali-metal GIC's (see below) have never been observed at the surface of Li-GIC's.

4.2.3.2 K-GIC's

K-GIC's were found to be the most difficult system from the binary AM-GIC's series for STM studies, mainly because of their extremely high surface reactivity.

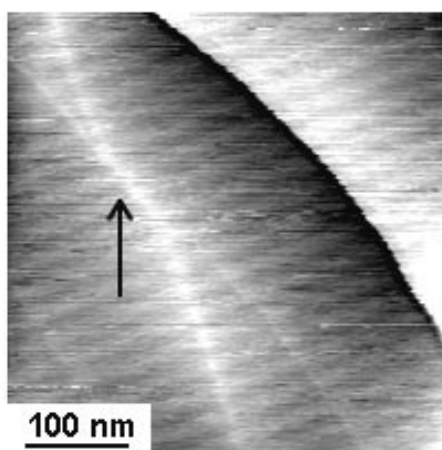


Figure 4.13: STM image of a stage-1 K-GIC sample. An arrow indicates a line-shaped feature of apparently increased topographic height.

In an earlier STM study by *Anselmetti et al.* [4.10, 4.12] of K-GIC's only a graphitic surface structure could be observed. More recently performed STM studies of this system also reveal a variety of superlattice structures that are, however, observable only within a very limited time period after freshly cleaving the sample. The observation of superlattice structures at the surface of stage-1 K-GIC's was possible due to a different sample preparation procedure which was based on a liquid-phase reaction, in contrast to earlier STM studies [4.10, 4.12] where samples obtained by the two-zone gas-phase reaction were

used.

K-GIC samples exhibit by STM (see fig. 4.13) on a large scale flat terraces with unit cell steps (0.6 nm in height, $I_c = 0.54$ nm). Again, line shaped regions of apparently increased topographic height (+ 0.2 nm) are observed (see arrow in fig. 4.13).

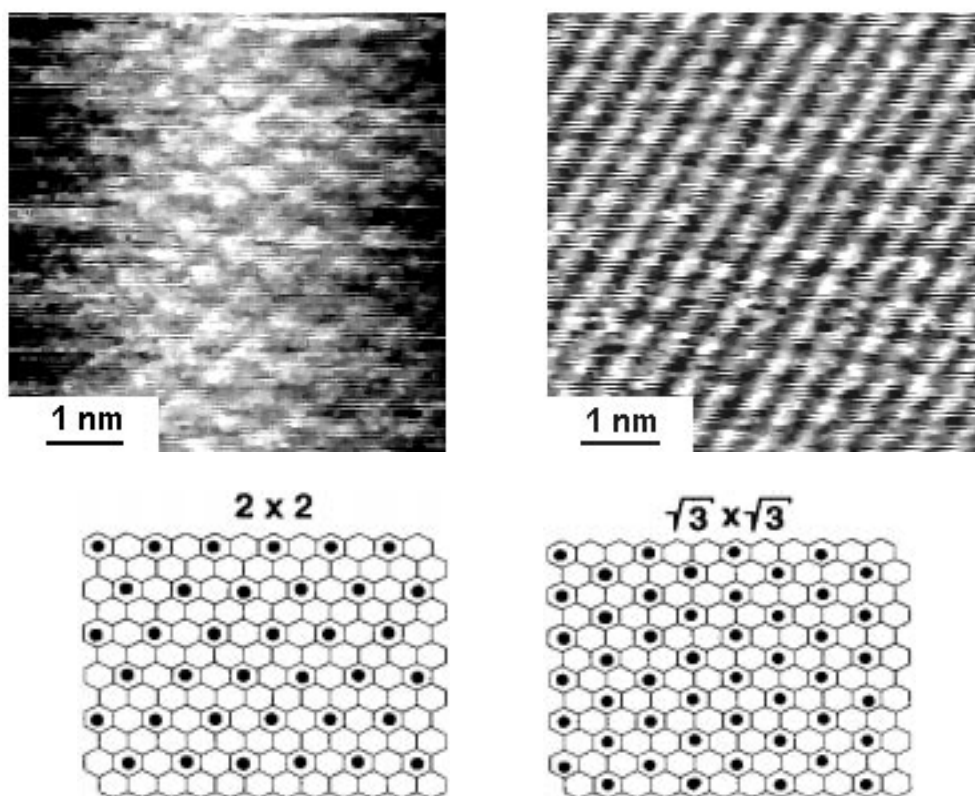


Figure 4.14: *LEFT:* Atomic resolution STM image of C₈K (2×2 superstructure). ($I_t = 3.5$ nA, $U_s = -20$ mV).

Figure 4.15: *RIGHT:* STM image of C₆K ($\sqrt{3} \times \sqrt{3}$ superstructure). ($I_t = 5$ nA, $U_s = -50$ mV). The lower row displays models for the observed superstructures.

In fig. 4.14 a STM image is given of a stage-1 K-GIC sample showing a 2×2 superlattice structure. This STM observation is consistent with earlier STM studies of stage-1 K-GIC's by another STM group [4.13, 4.14]. In addition, a novel $\sqrt{3} \times \sqrt{3}$ superlattice at the surface of stage-1 K-GIC's (fig. 4.15) is shown that has not been observed previously. The possible existence of the $\sqrt{3} \times \sqrt{3}$ superlattice period in stage-1 K-GIC's has recently been theoretically predicted on the basis of *ab initio* calculations within the density-functional formalism [4.28]. Indications for the presence of a $\sqrt{3} \times \sqrt{3}$ superlattice at the surface of stage-1 Cs-GIC's have been found experimentally by means of angle-resolved photoemission spectroscopy [4.29]. This $\sqrt{3} \times \sqrt{3}$ surface superlattice is also in contrast to the 2×2 superlattice as observed in the bulk of stage-1 Cs-GIC's.

In addition, a nonhexagonal, one-dimensional superlattice structure ($\sqrt{3} \times \sqrt{27}$) is also observed at the surface of stage-1 K-GIC's (see fig. 4.16). Such structure was previously found at the surface of heavy alkali-metal GIC's [4.15, 4.16]. Finally, a novel nonhexagonal rectangular superlattice has been found (fig. 4.17) with a periodicity of 0.95 ± 0.1 nm.

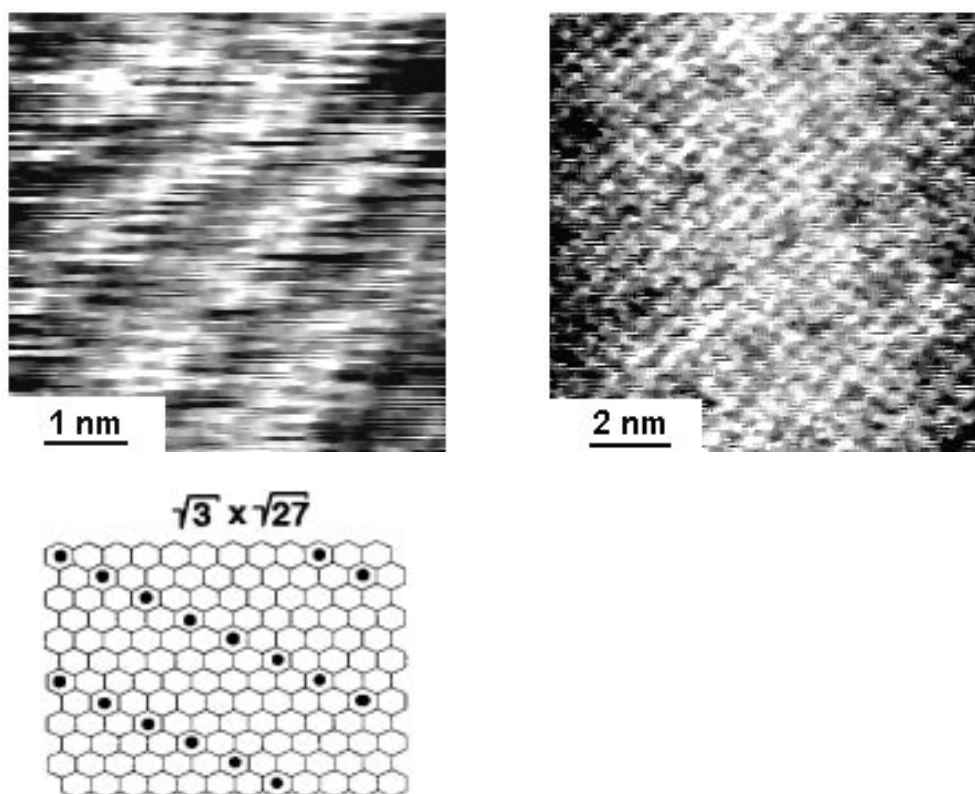


Figure 4.16: *LEFT:* Atomic resolution STM image showing a $\sqrt{3} \times \sqrt{27}$ superstructure. The model is shown below.

Figure 4.17: *RIGHT:* Novel rectangular superlattice of 0.95 nm period, which is simultaneously observed together with the underlying K 2×2 lattice ($I_t = 3.5$ nA, $U_s = -20$ mV).

4.2.3.3 Cs- and Rb-GIC's

C_8Rb and C_8Cs exhibit large terraces with 0.6 nm steps ($I_{c,Rb} = 0.56$ nm, $I_{c,Cs} = 0.59$ nm). Figure 4.18 shows a STM image of the surface of a C_8Cs sample. The "brighter" lines are possibly boundaries between different intercalated domains. Figure 4.19 shows the C_8Cs 2×2 superlattice and fig. 4.20 displays the C_8Rb 2×2 superlattice. Note the vacancy (bold arrow) and adatom defect (open arrow) in fig. 4.20. During the course of STM imaging, various one-dimensional superstructures have been observed. Two differ-

ent spacings between linear structures can be observed in fig. 4.21, left, (Cs-GIC). The smaller spacing corresponds to a $\sqrt{3} \times 3$ superlattice. The larger one is a $\sqrt{3} \times 4$ structure. At even larger depletion of the first gallery of C_8Cs , linear $\sqrt{3} \times \sqrt{21}$ (fig. 4.21, middle) or linear superstructures with two different spacings ($\sqrt{3} \times \sqrt{21}/\sqrt{3} \times \sqrt{28}$) (fig. 4.21, right) are observed simultaneously with the graphite host lattice.

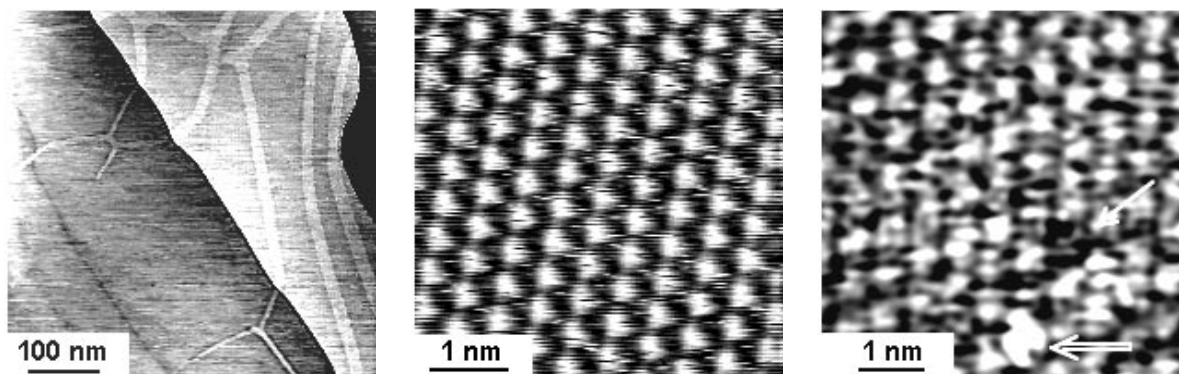


Figure 4.18: *LEFT:* STM survey image of the surface of a stage-1 Cs-GIC showing terraces and steps. Narrow bright bands might be interpreted as domain boundaries.

Figure 4.19: *MIDDLE:* C_8Cs exhibiting a 2×2 superlattice ($I_t = 2.9$ nA, $U_s = -72$ mV).

Figure 4.20: *RIGHT:* C_8Rb 2×2 superlattice showing two point defects: a vacancy is indicated by an open arrow and an adatom site is marked by a bold arrow ($I_t = 5.1$ nA, $U_s = -53$ mV).

4.2.4 STM on ternary alkali metal GIC's

4.2.4.1 KCs-GIC's of stage-1

For the first time ternary AM-GIC's have been studied as an extension of the investigations of binary AM-GIC's. Similar characteristic features have been observed in STM images of ternary AM-GIC's as at the surface of the binary AM-GIC's. In fig. 4.22 a large-scale STM image of the surface of stage-1 KCs-GIC's is presented. Besides step and other defect structures, islands of various sizes and shapes, already observed on stage-1 Li-GIC's (fig. 4.11), are visible. These islands have an extent of 50-200 nm, typically. In contrast to the observation of islands at the surface of stage-1 Li-GIC's, the islands on stage-1 KCs-GIC's exhibit apparently increased topographic height. Again, the observation of such islands is attributed to an inhomogeneous distribution of the intercalant. For ternary GIC's such inhomogeneities can either result from a deficiency of one component only [4.27], or, less likely, of both components of the intercalant.

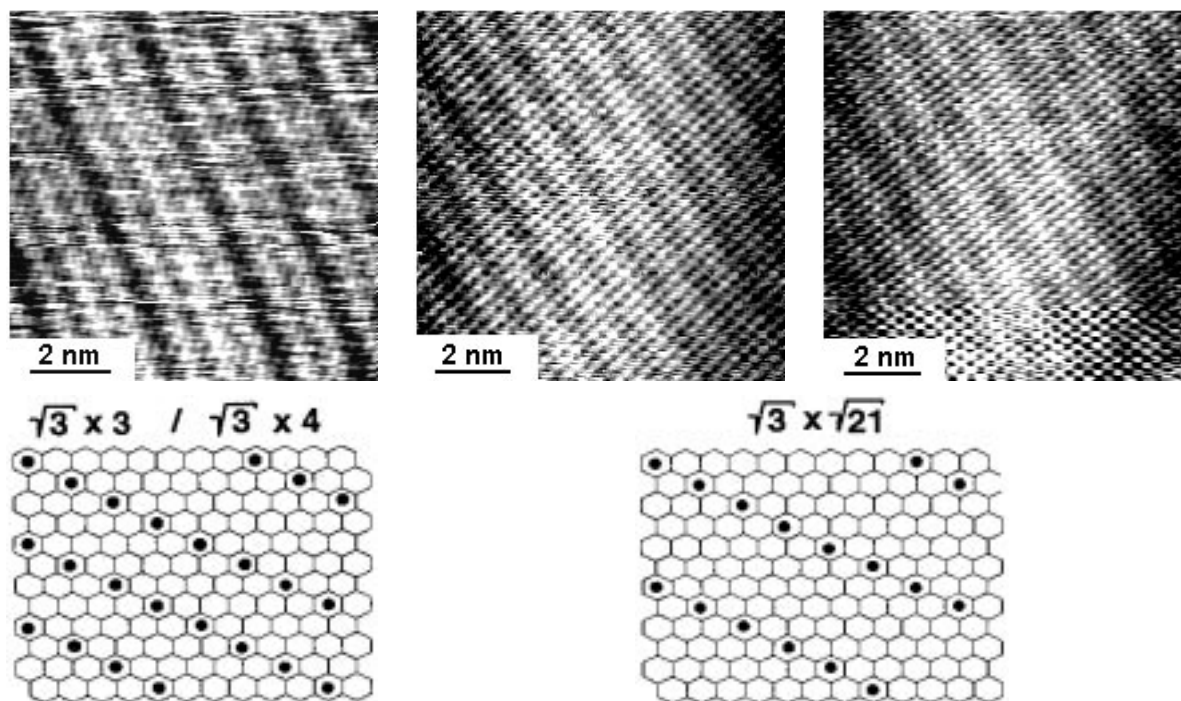


Figure 4.21: *LEFT:* Atomic resolution STM images showing different linear superstructures in a Cs-GIC: $\sqrt{3} \times 3 / \sqrt{3} \times 4$. A schematic is given below. *MIDDLE:* Regularly spaced linear superstructure (Cs-GIC): $\sqrt{3} \times \sqrt{21}$ (to be compared to the model shown below). *RIGHT:* $\sqrt{3} \times \sqrt{21} / \sqrt{3} \times \sqrt{28}$. This image was recorded a few minutes later than the one shown in the middle. This is an important clue for the depletion of the galleries during STM imaging (interaction with tip).

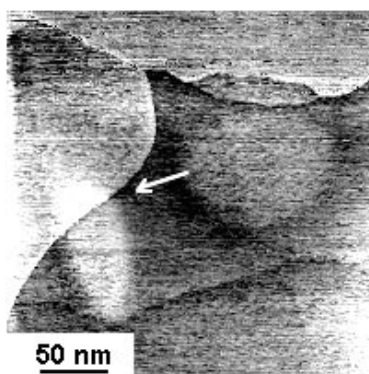


Figure 4.22: Constant current STM survey image of a stage-1 KCs-GIC sample showing an ellipsoidally-shaped island of apparently increased topographic height ($I_t = 1$ nA, $U_s = -100$ mV). The island is marked by an arrow.

On the atomic scale a variety of superlattice structures is observed at the surface of stage-1 KCs-GIC's. Figures 4.23 and 4.24 show two different types of 2×2 superlattices. In fig. 4.24 the graphite host lattice can be simultaneously observed with the superstructure whereas in fig. 4.23 only the intercalant is imaged. Note that no distinction between the different alkali metals is possible. During STM imaging the regular 2×2 superlattices are found to transform to a linear $\sqrt{3} \times 4$ superstructure (see fig. 4.25).

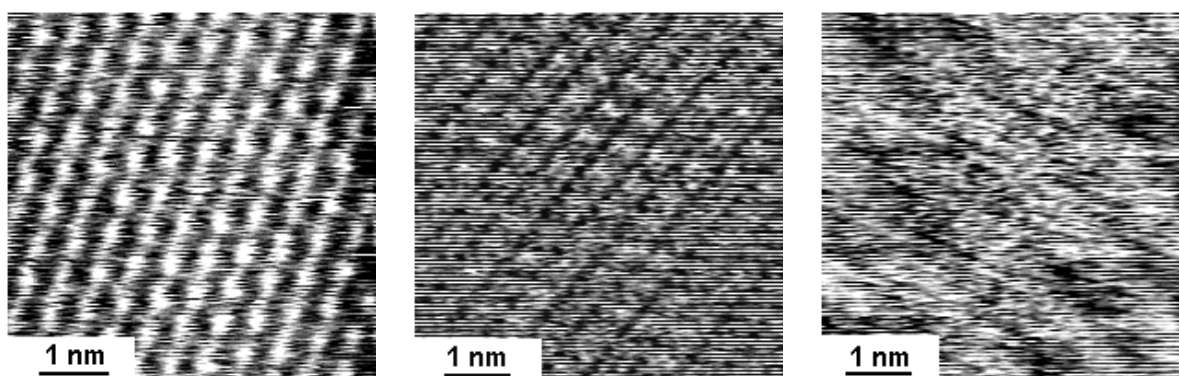


Figure 4.23: *LEFT:* Atomic resolution STM image showing a 2×2 superlattice of the K and Cs intercalant atoms. Note that the two atomic species cannot be distinguished.

Figure 4.24: *MIDDLE:* This image shows both the 2×2 superstructure and the graphitic host lattice.

Figure 4.25: *RIGHT:* Within 15 min. of STM imaging the regular 2×2 superlattice has transformed into a $\sqrt{3} \times 4$ superlattice implying the gradual emptying of the galleries.

Finally, a nonhexagonal rectangular superlattice with a (1.9 ± 0.1) nm period has been observed at the surface of stage-1 KCs-GIC's (see fig. 4.26). This rectangular superlattice is similar to the one observed at the surface of stage-1 K-GIC's (fig. 4.17). Interestingly, the STM image of fig. 4.26a shows in fact two different super-imposed superlattices in addition to the underlying graphitic host lattice, namely the novel rectangular superlattice already mentioned and the 2×2 superlattice. This can best be extracted from a STM image analysis based on the two-dimensional Fourier transform shown in fig. 4.26b. Clearly, three groups of spots can be distinguished in Fourier space, two groups with hexagonal symmetry corresponding to the graphitic host lattice (back-transformed to real space by selecting the spots located in the outmost ring in the Fourier spectrum, see fig. 4.26c) and the 2×2 superlattice (fig. 4.26d based on the middle ring spots in fig. 4.26b), and one group with rectangular symmetry (fig. 4.26e) corresponding to the novel superlattice that dominates the STM image presented in fig. 4.26a. The simultaneous observation of two superimposed superlattices of different symmetry at the surface of stage-1 KCs-GIC's has important implications for the interpretation of the superlattice structures, as will be argued in the discussion section.

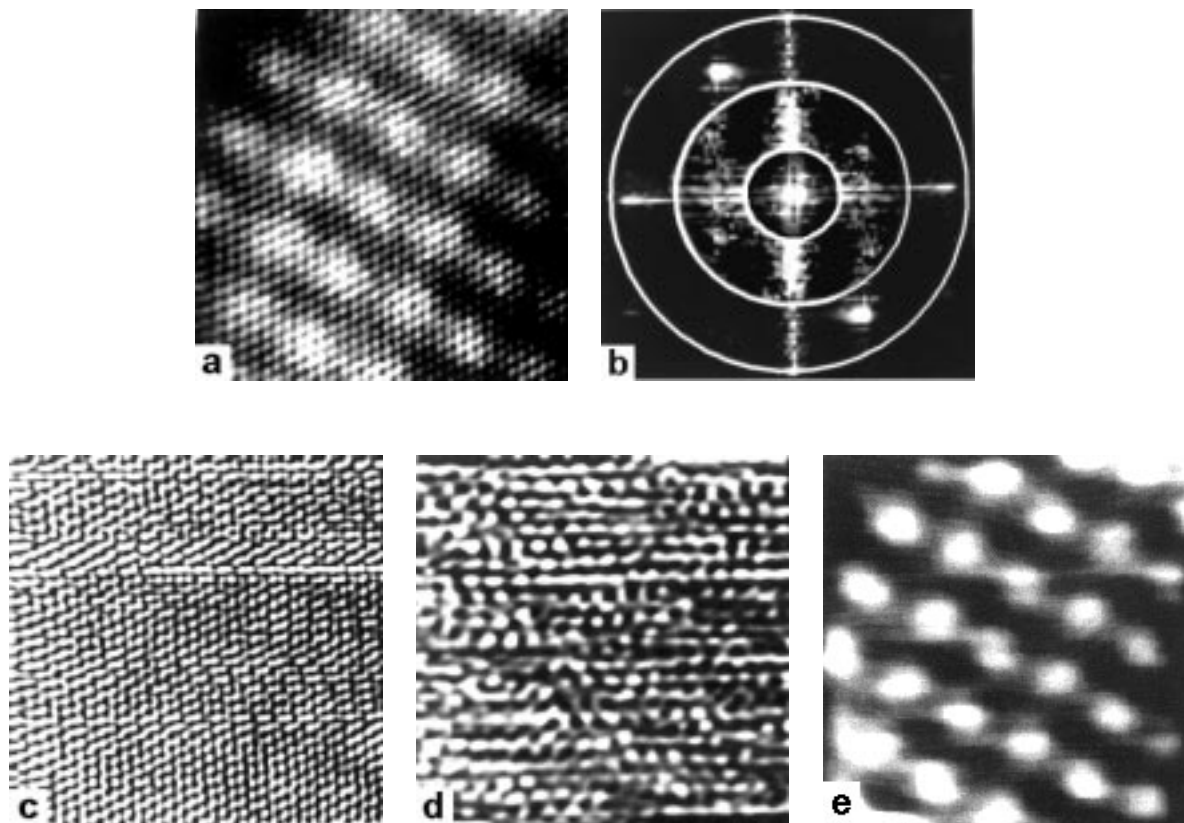


Figure 4.26: (a) Atomically resolved STM image showing a novel rectangular superlattice with a periodicity of about 1.9 nm on a stage-1 KCs-GIC ($I_t = 1$ nA, $U_s = -65$ mV). A Fourier-space-based analysis of the image yields several superstructures. (b) Two-dimensional Fourier transform of the topography image: three groups of spots are observed. Circles are indicated to separate the groups of spots. (c) Back-transform to real space of the outermost group of Fourier spots reveals the presence of the graphitic host lattice in the raw data image. (d) Back-transform to real space of the group of Fourier spots located in the middle ring in the Fourier spectrum yields the 2×2 superlattice. (e) Back-transform to real space of the innermost group of Fourier spots gives the novel rectangular superlattice.

4.2.4.2 CsRb-GIC's of stage-1

RbCs-GIC's show analogous structures to those observed in KCs-GIC's: A grain boundary is marked by an arrow in the large scale image of a RbCs-GIC (see fig. 4.27, top left). The topographic height difference between the two grains is 0.55 nm (slightly smaller than the interlamellar spacing).

Figure 4.27, top right, displays a 2×2 superlattice. Fig. 4.27, bottom left, additionally shows the underlying graphite host lattice. Figure 4.27, bottom right, shows the linear $\sqrt{3} \times 4$ superlattice which is only found at a later stage of the STM experiment (similar to K-, Cs-, Rb- and KCs-GIC's).

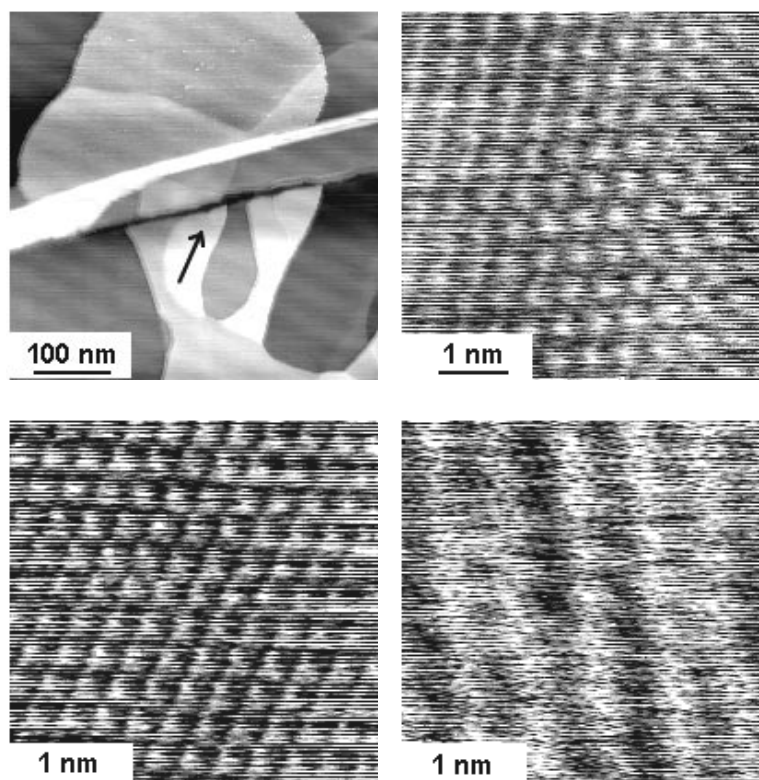


Figure 4.27: *TOP LEFT:* Large scale STM image of a CsRb-GIC (step heights: 0.6 and 1.1 nm). A grain boundary is marked by an arrow. *TOP RIGHT:* STM image of a 2×2 superlattice. No difference is observed between Cs and Rb intercalant atoms. *BOTTOM LEFT:* 2×2 intercalant superlattice and graphitic host lattice imaged simultaneously by STM. *BOTTOM RIGHT:* STM image of a $\sqrt{3} \times 4$ superlattice found after scanning the surface for 20 minutes.

4.2.5 Discussion

The variety of superlattice structures found at the surface of binary and ternary AM-GIC's is certainly surprising. The simultaneous observation of two different superlattices in addition to the underlying graphitic host lattice as in the case of stage-1 KCs-GIC's indicates that different superlattices might have different origins. In the following, possible origins of the observed superlattices will be discussed. A very limited number of theoretical calculations [4.30] – [4.32] has been devoted to STM studies of GIC's so far. These calculations are partly based on drastic assumptions concerning the treatment of

the superlattices, which are not justified by the experimental observations. Therefore, the interpretation of the superlattices is at least partly at a speculative stage.

To start the discussion of the experimental STM results on AM-GIC's, the experimental conditions have to be clarified first. As described in section 4.2.2, the samples are freshly cleaved prior to each series of STM measurements. For a stage-1 compound, cleavage of the sample is expected to lead initially to two parts, with the freshly cleaved surfaces equally covered with the intercalant, which is consequently diluted compared with the intercalated layers in the bulk. The alkali metal at the surface is, however, likely to evaporate off in the inert-gas environment. Therefore, the top surface layer for most of the studied stage-1 AM-GIC's is supposed to be a graphitic layer followed by the first intercalated layer. This explains the easiness of the simultaneous observation of the graphitic host lattice in addition to the superlattices that are induced by the presence of the intercalated layers. In the case of stage-1 Li-GIC's, however, there are indications that the top surface layer might consist of lithium [4.11, 4.12]. This assumption would explain three different experimental observations: First, in contrast to the STM results obtained for the heavier alkali-metal GIC's, simultaneously imaging of the graphitic host lattice in addition to the observed hexagonal superlattices at the surface of stage-1 Li-GIC's was never successful. Second, the experimentally measured corrugation amplitudes at low bias voltages (< 200 mV) were found to be considerably higher [4.11, 4.12] than theoretically predicted [4.30]. This discrepancy could be explained by the fact that in the calculations [4.30] a graphitic top layer was assumed. Third, the easiness of transformation between the three experimentally observed hexagonal superlattices at the surface of stage-1 Li-GIC's [4.11, 4.12] and figs. 4.12ff. could best be explained by a lithium layer being at the top of the surface. Under the assumption of a lithium top layer at the surface of stage-1 Li-GIC's, the STM images are likely to directly reflect the local distribution of lithium at the surface. Atomic and electronic structure effects might of course both contribute to the measured corrugation amplitudes. For the heavier alkali-metal GIC's, where the top surface layer is assumed to be a graphitic layer, the interpretation of the experimental STM results might be much more sophisticated. Three different types of superlattices have mainly been observed: the 2×2 superlattice and the nonhexagonal one-dimensional, as well as rectangular, superlattices. The presence of a 2×2 superlattice of the intercalated layers is well known from bulk diffraction experiments on these compounds. Therefore, it is likely that the STM observation of this superlattice at the surface of these compounds directly reflects the ordered arrangement of the alkali metal in the first gallery of the graphitic host lattice. The STM image contrast can, however, have different origins: First, the STM probes the electronic states near the Fermi level at the distance of a few angstroms from the surface, which are influenced by the presence of the intercalated layers. Second, the STM is also sensitive to elastic distortion fields, which cause the top graphitic layer to buckle due to the presence of the underlying intercalant layer [4.33, 4.34]. At present, it is difficult to estimate the relative contributions of these two different image contrast mechanisms to the observed experimental STM results. A comparative STM and atomic-force microscopy (AFM) [4.35] study would certainly help to disentangle the contributions of the different contrast mechanisms, since the AFM

predominantly probes the local elastic distortion field [4.33]. Another issue is the observed similarity of the STM images of the 2×2 superlattice at the surfaces of binary and ternary AM-GIC's. No indications exist of a two-component intercalant layer in the STM images of the 2×2 superlattice at the surface of ternary AM-GIC's. For a two-component intercalant layer, one would expect, for instance, a locally varying corrugation amplitude over the 2×2 superlattice, which is not experimentally observed. X-ray studies of the structure of stage-1 $K_{1-x}Rb_x$ -GIC's [4.36] have shown that the mixed alkali-metal layers form a commensurate 2×2 superlattice with complete site disorder among the two different types of alkali-metal ions. Further experimental investigations are necessary to explain the uniformity of the 2×2 superlattice observed at the surface of ternary AM-GIC's. Besides the hexagonal 2×2 superlattice, it is also possible to observe nonhexagonal one-dimensional superlattice structures superimposed on the graphitic host lattice at the surfaces of binary and ternary AM-GIC's. The one-dimensional chain-like structures are observed with different periodicities [4.15, 4.16] and in some cases they are not regularly spaced at all. Typically, no corrugation is measured along the chains after subtracting the corrugation resulting from the underlying graphitic host lattice. Two possible explanations can be given for the observed one-dimensional superlattice structures: First, a quasi-one-dimensional chain-like ordering of the alkali-metal intercalant, leading to nonhexagonal superlattices such as $\sqrt{3} \times 4$ or $\sqrt{3} \times \sqrt{13}$ [4.15, 4.16] or irregularly spaced quasi-one-dimensional chains, can explain the STM observations. The existence of a one-dimensional chain-like ordering of the alkali metal in the bulk of high-stage Cs-GIC's has already been confirmed earlier by scanning transmission electron microscopy [4.37]. Under the assumption of a chain-like ordering of the alkali-metal intercalant, the STM image contrast can again be explained either by an electronic contribution of the intercalant layer or by the elastic distortion field associated with the one-dimensional ordering of the intercalant. To explain the absence of a corrugation along the chains, a close packing of the alkali-metal ions in this direction has to be assumed. For a commensurate structure this would be fulfilled by a $\sqrt{3} \times a_0$ spacing of the alkali-metal ions along the chains, where a_0 is the lattice constant of the graphite host. One may speculate whether such alkali-metal chains in GIC's would be metallic. If the STM image contrast is mainly due to the electronic contribution of the intercalant layer, the absence of a measured corrugation along the chains would certainly indicate such a metallic behavior. A second possible explanation for the observed one-dimensional superlattice structures would be the existence of charge-density waves (CDW's) at the surface of AM-GIC's. An indication for the existence of a surface-driven CDW in stage-1 Cs-GIC's has already been found by means of angle-resolved photoemission spectroscopy [4.38]. It is well known that STM is highly sensitive to CDW modulations [4.39, 4.40]. On the other hand, the AFM response to CDW's is considerably less, and is often not visible at all [4.41, 4.42]. Therefore, a comparative STM and AFM study of GIC's would again help to clarify the origin of the observed superlattices. If the observed one-dimensional superlattice structures would indeed be due to a surface CDW, the observed defects [4.16] as well as the irregular spacing found at the surface of stage-1 KCs-GIC's would be remarkable.

Finally, the observation of the rectangular superlattices at the surfaces of stage-1 K-

GIC's (fig. 4.17) and stage-1 KCs-GIC's (fig. 4.26) will be discussed. In the case of the stage-1 KCs-GIC's this rectangular superlattice was simultaneously observed together with the 2×2 superlattice and the underlying graphitic host lattice. The observation of the 2×2 superlattice undoubtedly suggests a hexagonal 2×2 superlattice ordering of the intercalant layer. Therefore, the simultaneously observed nonhexagonal rectangular superlattice cannot be explained by electronic contributions or elastic distortion fields due to intercalant layer. It is therefore most likely that the observed rectangular superlattice has its origin in a surface CDW. This would then be direct evidence for the presence of a CDW state in GIC's. Since the same type or rectangular superlattice is also observed at the surface of stage-1 K-GIC's, we also expect the presence of a CDW at the surface of this compound. The larger period of 1.42 nm observed for stage-1 KCs-GIC's compared with the 0.95-nm period for stage-1 K-GIC's would then indicate a lower degree of charge transfer from the KCs intercalant to the graphitic planes, leading to a decreased Fermi surface size, which, in fact, would increase the wavelength of the CDW. More experimental work is, of course, needed to clarify this point, e.g., by an observation of the superlattice period as a function of the relative concentrations in $M_x M'_{1-x}$ -GIC's where M and M' are two different alkali metals, and by the direct STM measurement of a CDW energy gap in stage-1 AM-GIC's.

4.2.6 Summary

The various superlattice structures observed in binary and ternary alkali-metal GIC's of stage-1 and the steady evolution with time from denser $\sqrt{3} \times \sqrt{3}$ and 2×2 packing, over more dilute one-dimensional linear structures such as $\sqrt{3} \times 3$ to no superstructures at all are strong indications of the intercalant depletion in the first gallery of the GIC's. Although the STM experiments [4.43, 4.44, 4.45] are performed in an argon-filled glove box with very low impurity levels, some intercalant may evaporate off the GIC sample. This continuous emptying of the first gallery causes the observed structural transformations with time. The high vapour pressures of the alkali metals renders impossible the investigation of these GIC's in ultrahigh vacuum.

Li-GIC's of stage-1 are believed to exhibit a Li metal top surface layer [4.11, 4.43] for the following reasons: first, the graphite host lattice could never be simultaneously imaged with the superlattice; and second, the measured corrugation amplitudes are much smaller than those of other alkali-metal GIC's and compare better to those of a metal.

The heavier alkali-metal GIC's most likely have a graphitic top surface layer since cleavage of these compounds leaves surfaces only partially covered by alkali-metal which is likely to evaporate off in the inert gas environment. Two processes could be responsible for the image contrast in the STM images. First, the intercalant layers directly influence the electronic density of states near the Fermi level and the electronic structure of the GIC's is imaged by STM; or second, the underlying intercalant layer causes a buckling of the top graphite layer and the topographic structure is imaged. Both effects may contribute to the actual STM image, but at present, they cannot be easily separated.

4.3 Diamond

4.3.1 Introduction

The second traditional allotrope of carbon is diamond. In cubic diamond, space group $Fm\bar{3}O$, each carbon atom is tetrahedrally coordinated to four others through bonds by sp^3 hybridized orbitals. Diamond is due to its extreme hardness, high uv-vis-ir transmission, its inertness, high temperature stability and large heat capacity a very special material. However, natural and artificially grown diamond crystals are expensive and difficult to combine with industrial device production – like in semiconductor device-engineering – to take advantage of the favourable properties of diamond.

This problem has been overcome by the growth of diamond films by Chemical Vapour Deposition (CVD) based on experiments by *Spitsyn et al.* [4.46] and *Matsumoto et al.* [4.47]. Possible applications are the use as an electronic material for devices [4.48] and as a semiconductor in high-temperature, high power electronics [4.49].

The films are usually grown in a hot filament reactor using a gas mixture of 1-5 % methane in hydrogen. Although most of the films are polycrystalline current efforts are concentrated on studying the relationship between morphology and texture of the films [4.50] – [4.55] and the investigation of the growth process [4.56] – [4.66].

The use of STM⁹ and AFM has already contributed to a better understanding of the growth process of diamond films [4.67] – [4.70], [4.73]. On studying diamond(100) faces a 2×1 reconstruction has been observed [4.67] – [4.73] explained by dimer row formation similar to the Si(100) 2×1 reconstruction [4.71, 4.72].

4.3.2 Experimental conditions

The Low Pressure CVD (LPCVD) process for diamond utilises temperature and pressure conditions favouring graphitic stability but kinetic factors allow diamond to be produced by reactant gases at less than atmospheric pressure containing > 95% hydrogen. Hydrogen is activated by passing it through a plasma before deposition on a substrate, held typically at 800-1000°C [4.74] – [4.79]. Conducting and non-conducting homoepitaxial films of 1.5–3.0 μm and 0.8–1.0 μm in thickness were grown on (100) and (110) type 1A polished substrates respectively. The homoepitaxy of diamond on diamond puts this work¹⁰ in contrast to other groups [4.74] – [4.79] using polished silicon wafers as a substrate. These films were grown by the conventional microwave discharge process [4.80] at temperatures of about 945°C with a 99.7% H_2 /0.3% CH_4 ratio. Additionally, the conducting p-type films were doped with B_2H_6 – with B/C ratio: 0.001. Both film types were grown under identical conditions and the addition of boron doping for the p-type

⁹Pure diamond films are supposed to be insulators. The use of a tungsten filament in the reactor during the film growth process possibly introduces impurities in the film. This may explain why some groups have reported on STM investigations of undoped diamond films.

¹⁰Here I would like to thank H.G. Maguire (Dept. Electrical and Electronic Engineering, Nottingham Polytechnic, Nottingham NG1 4BU, England, UK) and M. Kamo (National Research in Inorganic Materials, Namiki 1-1, Tsukuba, Ibaraki 305, Japan) for the successful collaboration.

films does not affect their structural morphology as derived from low energy electron diffraction.¹¹ For the STM investigations the boron doped films have been used.

4.3.3 STM on homoepitaxial diamond films on diamond(110)

STM investigations of homoepitaxial diamond LPCVD films on diamond(110) reveal a quite smooth surface (the height variation is below 3 nm over an area of $2 \times 2 \mu\text{m}^2$, see fig. 4.28). Some tip-shaped troughs (marked by 'T') are present.

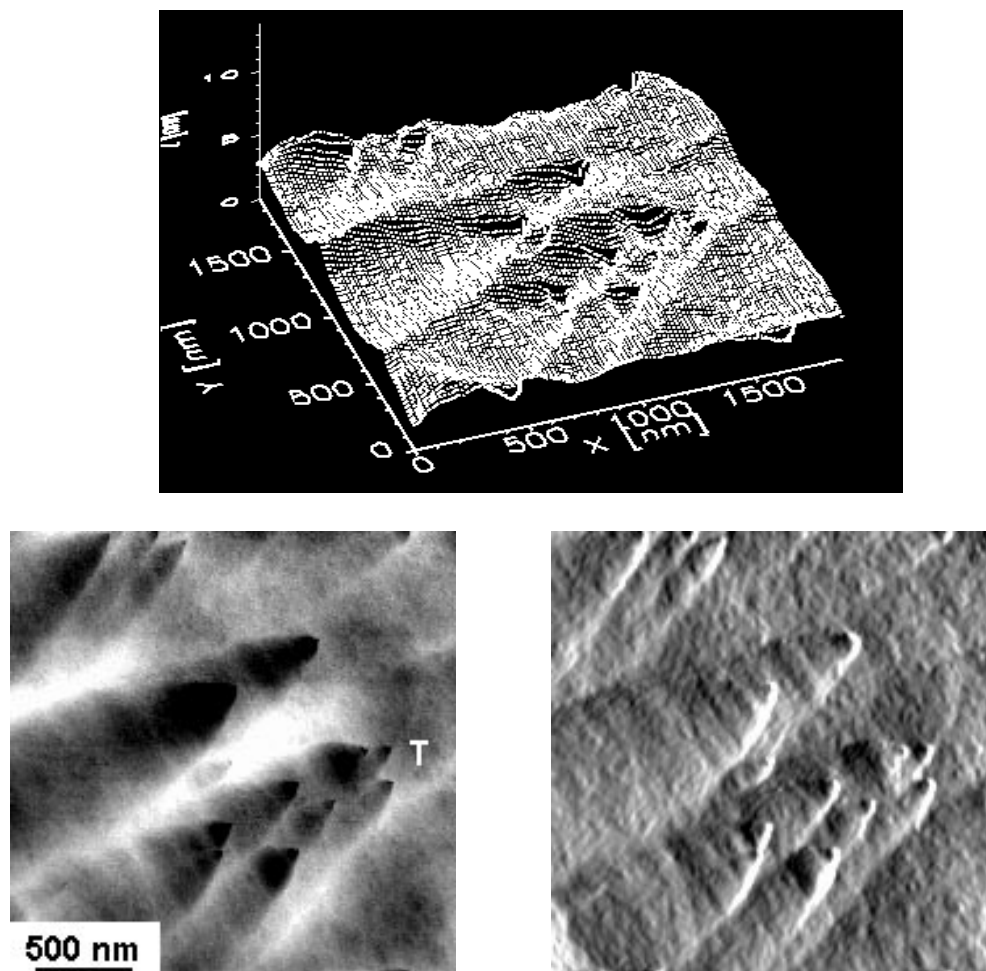


Figure 4.28: *TOP:* Three-dimensional rendition of a large scale STM image of a diamond films homoepitaxially grown on polished diamond. *BOTTOM LEFT:* Topview image of the STM 3D rendition shown above. One of the tip-shaped troughs is marked by the label 'T'. *BOTTOM RIGHT:* Rendition as an illuminated image of the image shown left mediating a better impression of the morphology of the film surface.

¹¹H.G. Maguire, private communication.

4.3.4 Herringbone-type atomic structure

On an atomic scale different structures have been observed. In some regions of the sample a striated herringbone structure has been found, not previously observed for any type of diamond film (see fig. 4.29). From these observations it is not possible to determine whether epitaxial growth occurs multidirectionally, simultaneously and/or sequentially. This structure consists of well defined striated ridges with height differences between successive striations of about 0.09 nm. The herringbone angle of about 60° between neighbouring striated areas is numerically equivalent to the intersecting angle between (110) planes of the diamond lattice (see fig. 4.30). Along this direction growth occurs most rapidly [4.79]. Also seen in fig. 4.29 are features which appear to have a ring-like structure in the process of merging to produce growth lines (striations). Central to these considerations for the creation of nucleation centres, are hydrocarbon cage compounds which serve as diamond precursors since these structures have the symmetry found in vapour grown diamond. An isolated ring structure - shown labelled by 'R' in fig. 4.29 - is frozen in along a striation. It has been suggested that ring compounds are a likely kinetic channel for film growth since these molecules have easy sites for the atom addition to a nucleation site [4.58].

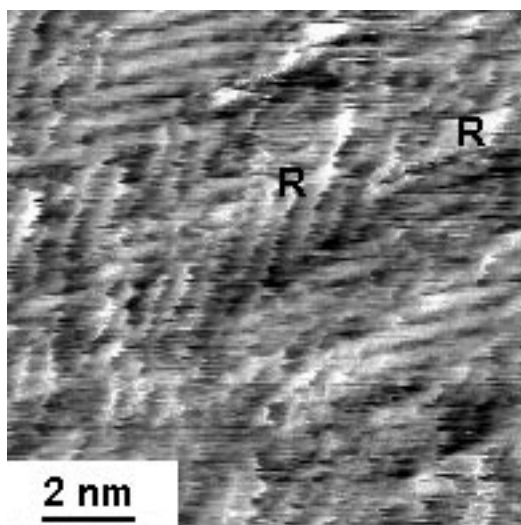


Figure 4.29: Striated herringbone structure with a herringbone angle of about 60° possibly due to intersection of (110) planes. Note the atomic ring features ('R').

4.3.5 Diamond(100)2x1 reconstruction

Detailed experimental studies of the atomic and electronic structure of various diamond surfaces have been performed by *Lurie et al.* [4.81] and *Pate et al.* [4.82]. Experiments with adatoms on carbon surfaces are found in refs. [4.83] – [4.86]. A 2×1 reconstructed surface structure as observed by others [4.67] – [4.70], [4.87] has also been imaged by

STM on a homoepitaxial diamond film.

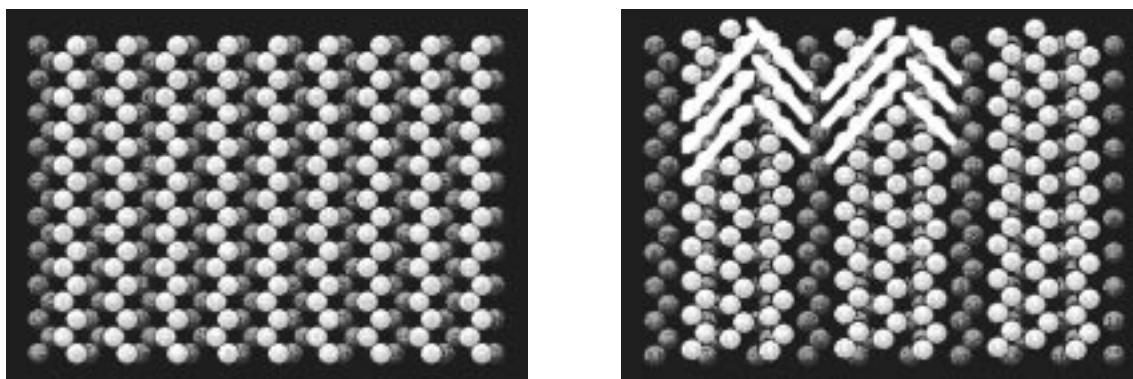


Figure 4.30: *LEFT:* Model of the unreconstructed diamond(110) surface. The top-most layer is shown in light-grey. The zig-zag rows of carbon atoms exhibit an angle of about 60° . *RIGHT:* A suggestion for a reconstructed diamond(110) surface compatible with the herringbone structure. Every third zig-zag row is fixed, whereas the remaining two are shifted towards the fixed one.

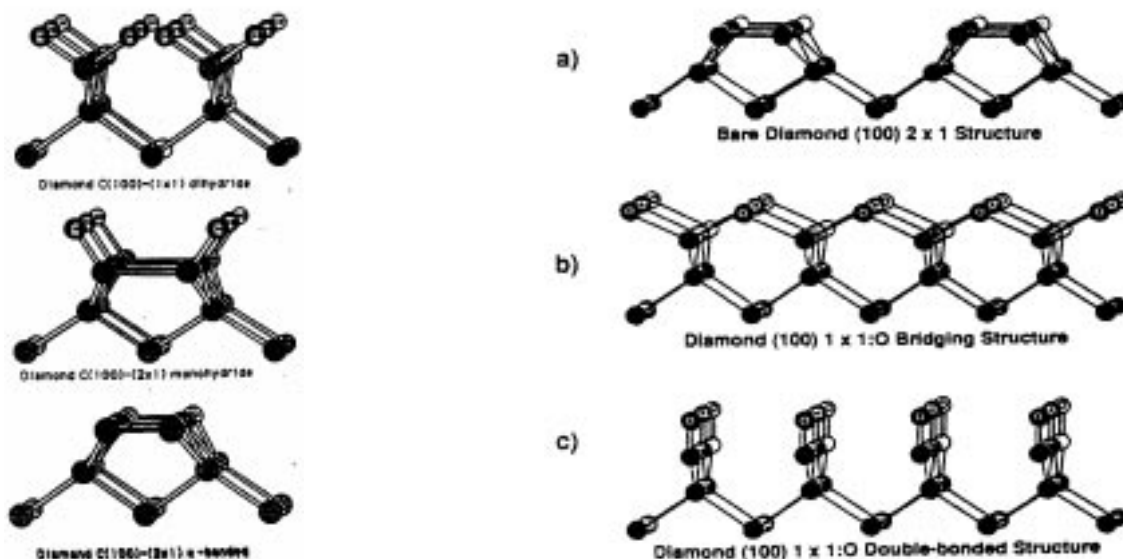


Figure 4.31: *LEFT COLUMN (TOP):* Different diamond (100) terminations as interpreted from LEED results. Figure reproduced from: *A. V. Hamza et al.*, *Surf. Sci.* 237 (1990) 35.

Figure 4.32: *RIGHT COLUMN (TOP):* Diamond(100) surfaces as derived from LEED experiments. Figure reproduced from *R.E. Thomas et al.*, *J. Vac. Sci. Technol. A* 10 (1992) 2451.

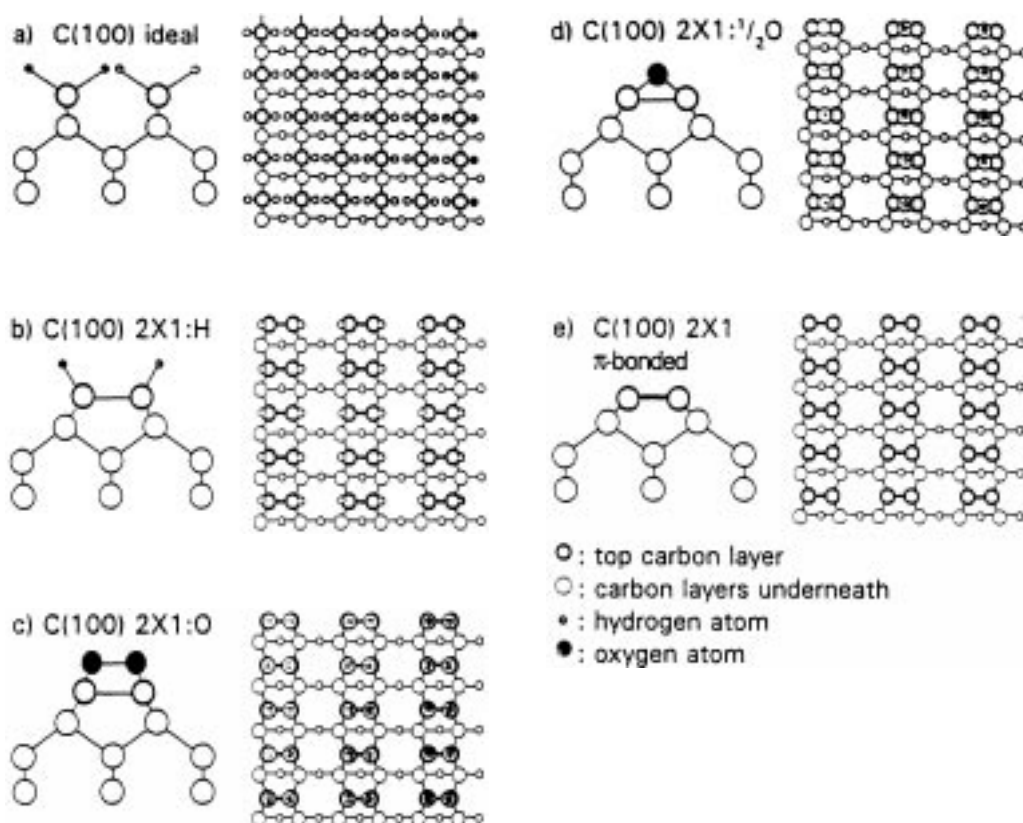


Figure 4.33: Schematic drawings of possible molecular structures of the diamond (100) surface. The left panel shows cross-sections normal to the surface and the right panel shows top views: (a) Unrelaxed structure, the two dangling bonds at each surface atom are saturated by atomic hydrogen.

Figure 4.34: (b) $2 \times 1:H$ reconstruction: one dangling bond of each surface atom has formed a bond with an adjacent surface atom and the remaining dangling bonds are saturated by hydrogen.

Figure 4.35: (c) $2 \times 1:O$ reconstruction: one oxygen atom per surface atom is bonded to the surface and the two oxygen atoms at each dimer form one additional O-O bond.

Figure 4.36: (d) $2 \times 1:\frac{1}{2}O$ reconstruction, here one oxygen atom is bonded to the two remaining dangling bonds at each dimer.

Figure 4.37: (e) $2 \times 1:\pi$ -bonded reconstruction: here all dangling bonds of the ideal surface contribute to the dimer formation such that no heteroatoms are chemically bonded to the surface. All 2×1 structures shown (b-e) are consistent with the STM images shown in literature. Caption text and figure reproduced from *H.G. Busmann et al*, *Diamond Relat. Mater.* 1 (1992) 979.

Models for growth of diamond on diamond(100) and surface sensitive investigation techniques predict a 2×1 reconstructed diamond surface with different possibilities for a termination. Different models are compiled in figs. 4.31 [4.86], 4.32 [4.88] and 4.33–4.37 [4.70].

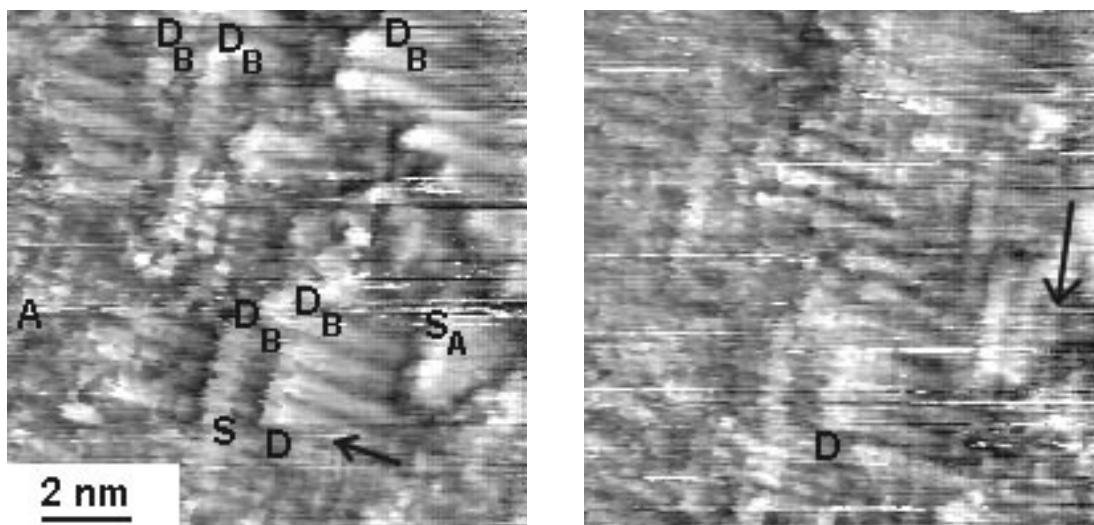


Figure 4.38: Two successive STM images of a 2×1 reconstructed diamond(100) surface. *LEFT:* Note the simultaneous presence of different surface structures: 'D' denotes double dimer rows, 'S' indicates single dimer rows and 'A' marks atomically resolved single atomic rows. The arrow on terrace 'D' indicates the direction of the dimer rows. S_A and D_B denote special types of steps discussed below.

Figure 4.39: *RIGHT:* Same area on the surface a few seconds later. Now the terrace lying above the one labelled by 'D' in the figure on the left is resolved into dimer rows. The running direction of the dimer rows (arrow) is perpendicular to the one on terrace 'D' implying the presence of a monostep.

Figure 4.38 and 4.39 show subsequently recorded STM images of the $(100)2\times 1$ reconstruction of diamond. The atomic rows are clearly resolved. A detail is shown in fig. 4.41: the 2×1 unit mesh is indicated by black lines. Please note some special structural features in fig. 4.38: at the location marked by 'D' dimer rows are observed. The dimer rows are resolved into individual (single) atomic rows at a lower lying terrace labelled with 'S'. The step height difference between the two terraces is 0.28 nm. This is a double step since the dimer rows are running parallel on both terraces. The arrow indicates the direction of the dimer rows. However, the terrace lying above the one labelled with 'D' is separated by a monostep. This can be inferred from fig. 4.39 showing the same area on the sample. The arrow in fig. 4.39 indicates the direction of the dimer rows on the terrace lying above terrace 'D' in fig. 4.38. Since the dimer rows on both terraces are aligned at an angle of 90° to each other it is to be expected that the step is monatomic. Measuring the step height actually yields 0.14 nm being compatible with a monostep.

Using *Chadi's* notation [4.71] introduced for the characterization of the Si(100) 2×1 reconstruction monosteps and double steps can be differentiated: single steps (monosteps) always exhibit dimer rows running on both terraces being perpendicular to each other. A step is called a S_A step when the running direction on the upper terrace is parallel to the step edge, it is termed a S_B step if the direction of the dimers is perpendicular to the step edge. Double steps always show dimer rows running parallel on both terraces. In case of a D_A step the dimer row direction is parallel to the step edge, in case of a D_B step it is perpendicular to the step edge. Figure 4.40 illustrates the four cases.

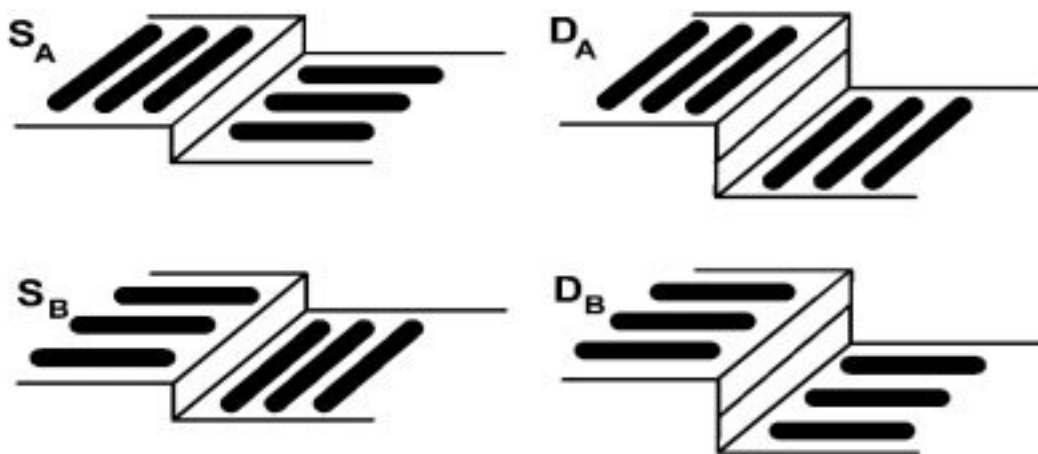


Figure 4.40: Chadi's notation for single and double steps on 2×1 reconstructed Si(100). The same applies for diamond(100) 2×1 .

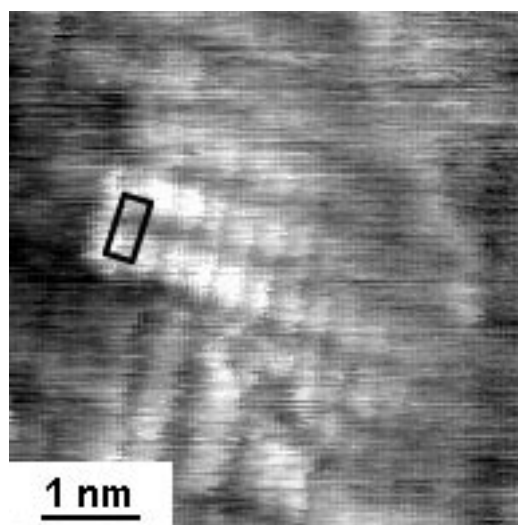


Figure 4.41: Detailed view of a 2×1 reconstructed diamond(100) terrace. The unit mesh of the reconstruction is indicated by black lines.

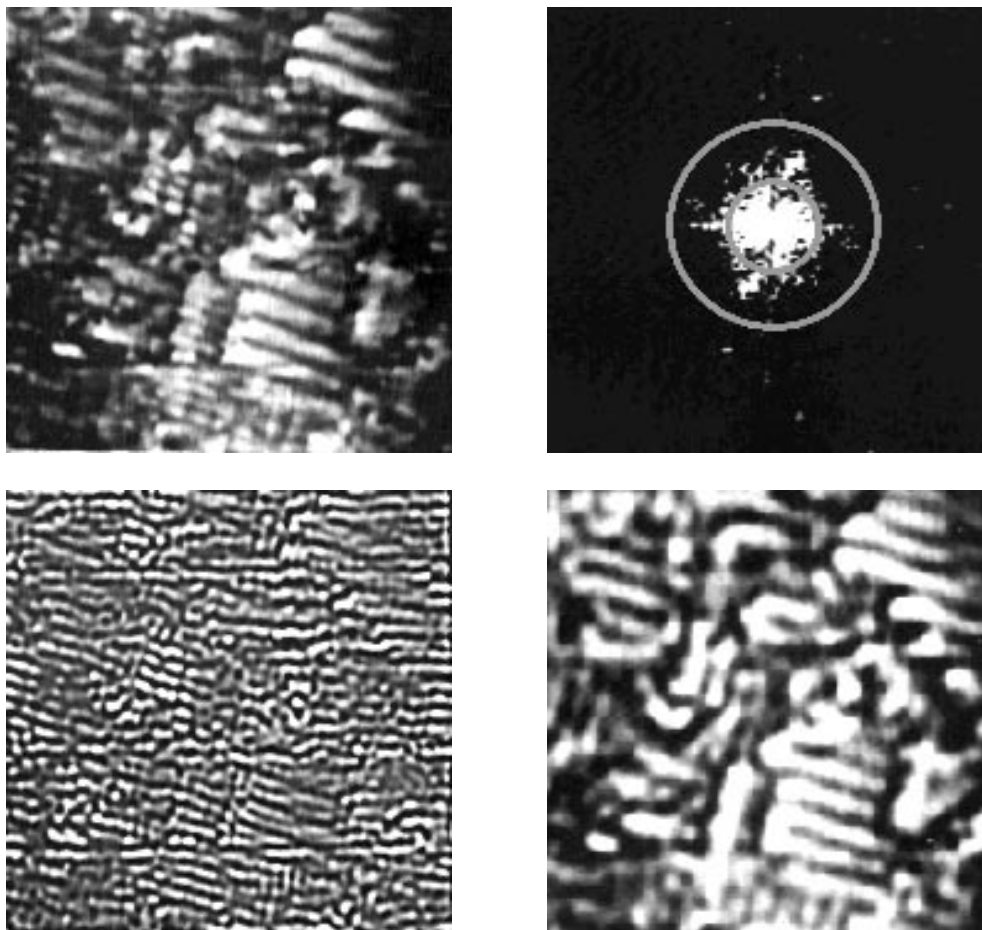


Figure 4.42: Fourier space based analysis of the STM image shown above for a discussion of the distribution of S_A , S_B , D_A and D_B steps in the diamond(100) 2×1 reconstruction. *TOP LEFT:* Original image. *TOP RIGHT:* 2D-Fourier transform. An inner circular and an outer annular region are marked. *BOTTOM LEFT:* Back-transform of the annular region to real space. *BOTTOM RIGHT:* Back-transform of the inner region. The presence of a preferential direction implies the dominance of D_B steps.

Chadi has calculated that the step formation energy for S_A steps is lower than for D_B , S_B and D_A steps favouring S_A and D_B steps. For larger miscut angles more D_B steps are expected to be found than D_A steps (see fig. 4.38). The reason for this is that the silicon atoms at step S_B have an extraneous dangling bond at the surface whereas the Si atoms at S_A do not have a dangling bond [4.71]. The UHV preparation of Si(100) diminishes the number of adatoms on the surface drastically. For that reason the situation with diamond(100) 2×1 will be somewhat different due to the CVD preparation method at a moderate vacuum. It is expected that available adatoms will lead to a more uniform distribution of all types of steps. Anyway, there are energy differences for the formation of S_A and D_B steps in diamond as well favouring the formation of D_B steps. This has already been discussed in detail by *Busmann et al.* [4.70]. To tackle this question a Fourier space based analysis of fig. 4.38 was executed. The images in fig. 4.42 show the original image, its two-dimensional Fourier transform (with a inner circular area and an outer annular region), and the back-transforms to direct space using the frequency information confined in the annular and the circular area of the Fourier transform. The back-transformed images reveal a preferential direction implying the dominance of D_B steps due to the large miscut angle off the (100) face of approximately 5° (calculated from a terrace width of 3 nm between D_B steps).

In some regions of fig. 4.38 also atomically resolved (single) dimer rows are observed (see label 'A' in fig. 4.38) demonstrating the complexity of the diamond(100) 2×1 surface. Concluding the results it may be stated that many of the proposed models for the diamond(100) 2×1 reconstruction (see figs. 4.31 – 4.37) are compatible with the STM results.

4.4 Conclusion

Scanning tunneling microscopy has demonstrated its capability to study complex surfaces with atomic resolution on traditional carbon allotropes as well. The atomic lattice imaged on graphite recalls that the information obtained by STM is based on the electronic structure of a surface having a symmetry different from the atomic lattice¹². Graphite intercalation compounds exhibit a vast variety of superstructures which reflect the electronic nature of the GIC surface as well, especially in the case where a superlattice is imaged simultaneously with the graphitic host lattice.¹³

In boron-doped diamond, imaged by STM under ambient conditions, a surface with adatoms is encountered. The STM images may be interpreted as partly or fully oxygenated or hydrogenated diamond surfaces. In some cases different structures (or resolution levels) are observed within a single STM image.

¹²The atomic lattice of graphite is of honeycomb shape with six-membered rings of carbon atoms with a interatomic spacing of 0.142 nm. In contrast to that STM images a hexagonal lattice with a spacing of 0.25 nm being identical to the second nearest neighbour lattice of graphite.

¹³The graphitic host lattice and the intercalant species are at a different distance from the surface. STM images a superposition of both electronic structures of graphite and of the intercalant.

References

- [4.1] I.P. Batra, N. Garcia, H. Rohrer, H. Salemink and S. Ciraci, *Surf. Sci.* 181 (1987) 126.
- [4.2] D. Tománek, S.G. Louie, H.J. Mamin, D.W. Abraham, R.E. Thomson, E. Ganz and J. Clarke, *Phys. Rev. B* 35 (1987) 7790.
- [4.3] D. Tománek and S.G. Louie, *Phys. Rev. B* 37 (1988) 8327.
- [4.4] G. Binnig, H. Fuchs, Ch. Gerber, H. Rohrer, E. Stoll and E. Tosatti, *Europhys. Lett.* 1 (1986) 31.
- [4.5] *Graphite Intercalation Compounds*, edited by H. Zabel and S. A. Solin. Springer Series in Materials Science Vol. 14 (Springer Verlag New York, 1990).
- [4.6] Levi-Setti, G. Crow, Y . L. Wang, N. W . Parker, R. Mittleman, and D. M. Hwang, *Phys. Rev. Lett.* 54 (1985) 2615.
- [4.7] D. M. Hwang, R. Levi-Setti, G. Crow, Y. L. Wang, N. W. Parker, R. Mittleman, X. W. Qian, and S. A. Solin, *Synth. Met.* 12 (1985) 73.
- [4.8] S. Gauthier, S. Rousset, J. Klein, W. Sacks, and M. Belin, *J. Vac. Sci. Technol. A* 6 (1988) 360.
- [4.9] M. Tanaka, W. Mizutani, T. Nakashizu, N. Morita, S. Yamazaki, H. Bando, M. Ono, and K. Kajimura, *J. Microsc.* 152 (1988) 183.
- [4.10] D. Anselmetti, R. Wiesendanger, V. Geiser, H. R. Hidber, and H.-J. Güntherodt, *J. Microsc.* 152 (1988) 509.
- [4.11] D. Anselmetti, R. Wiesendanger, and H.-J. Güntherodt, *Phys. Rev. B* 39 (1989) 11135.
- [4.12] R. Wiesendanger, D. Anselmetti, V. Geiser, H. R. Hidber, and H.-J. Güntherodt, *Synth. Met.* 34 (1989) 175.
- [4.13] S. P. Kelty and C. M. Lieber, *J. Phys. Chem.* 93 (1989) 5983.
- [4.14] S. P. Kelty and C. M. Lieber, *Phys. Rev. B* 40 (1989) 5856.
- [4.15] D. Anselmetti, V. Geiser, G. Overney, R. Wiesendanger, and H.-J. Güntherodt, *Phys. Rev. B* 42 (1990) 1848.
- [4.16] D. Anselmetti, V. Geiser, D. Brodbeck, G. Overney, R. Wiesendanger, and H.-J. Güntherodt, *Synth. Met.* 38 (1990) 157.

- [4.17] C. H. Olk, J. Heremans, M. S. Dresselhaus, J. S. Speck, and J. T. Nicholls, *Phys. Rev. B* 42 (1990) 7524.
- [4.18] C. H. Olk, J. Heremans, M. S. Dresselhaus, J. S. Speck, and J. T. Nicholls, *J. Vac. Sci. Technol. B* 9 (1991) 1055.
- [4.19] S. P. Kelty and C. M. Lieber, *J. Vac. Sci. Technol. B* 9 (1991) 1068.
- [4.20] S. P. Kelty, Z. Lu, and C. M. Lieber, *Phys. Rev. B* (to be published).
- [4.21] Peter Pfluger, *Synthetische Metalle in der Form von Graphiteinlagerungsverbindungen*, Inauguraldissertation, Basel (1980).
- [4.22] Urs Michael Gubler, *Photoemissions-Untersuchungen an Alkali-Graphiteinlagerungsverbindungen*, Inauguraldissertation, Basel (1981).
- [4.23] A. Hérold, *Bull. Soc. Chim. Fr.* (1955) 999.
- [4.24] D.E. Nixon and G.S. Parry, *J. Phys. D* 1 (1968) 291.
- [4.25] K. Fredenhagen and G. Kadenbach, *Z. allg. anorg. Chem. B* 18 (1932) 1.
- [4.26] J. M. Soler, A. M. Baro, N. Garcia, and H. Rohrer, *Phys. Rev. Lett.* 57 (1986) 444.
- [4.27] D. M. Hwang, X. W. Qian, and S. A. Solin, *Phys. Rev. Lett.* 53 (1984) 1473.
- [4.28] G. Overney, W. Zhong, and D. Tománek (unpublished).
- [4.29] C. Fretigny, D. Marchand, and M. Lagues, *Phys. Rev. B* 32 (1985) 8462.
- [4.30] A. Selloni, C. D. Chen, and E. Tosatti, *Phys. Scr.* 38 (1988) 297.
- [4.31] X. Qin and G. Kirczenow, *Phys. Rev. B* 39 (1989) 6245.
- [4.32] X. Qin and G. Kirczenow, *Phys. Rev. B* 41 (1990) 4976.
- [4.33] D. Tománek, G. Overney, H. Miyazaki, S. D. Mahanti, and H.-J. Güntherodt, *Phys. Rev. Lett.* 63, (1989) 876.
- [4.34] Y. Cai, J. S. Chung, M. F. Thorpe, and S. D. Mahanti, *Phys. Rev. B* 42 (1990) 8827.
- [4.35] G. Binnig, C. F. Quate, and Ch. Gerber, *Phys. Rev. Lett.* 56 (1986) 930.
- [4.36] P. C. Chow and H. Zabel, *Phys. Rev. B* 38 (1988) 12837.
- [4.37] D. M. Hwang, N. W. Parker, M. Utlaut, and A. V. Crewe, *Phys. Rev. B* 27 (1983) 1458.
- [4.38] M. Lagues, J. E. Fischer, D. Marchand, and C. Fretigny, *Solid State Commun.* 67 (1988) 1011.

- [4.39] R. V. Coleman, B. Drake, P. K. Hansma, and G. Slough, *Phys. Rev. Lett.* 55 (1985) 394.
- [4.40] R. V. Coleman, B. Giambattista, P. K. Hansma, A. Johnson, W. W. McNairy, and C. G. Slough, *Adv. Phys.* 37 (1988) 559.
- [4.41] E. Meyer, D. Anselmetti, R. Wiesendanger, H.-J. Güntherodt, F. Levy, and H. Berger, *Europhys. Lett.* 9 (1989) 695.
- [4.42] E. Meyer, R. Wiesendanger, D. Anselmetti, H. R. Hidber, H.-J. Güntherodt, F. Levy, and H. Berger, *J. Vac. Sci. Technol. A* 8 (1990) 495.
- [4.43] H.P. Lang, R. Wiesendanger, V. Thommen-Geiser and H.-J. Güntherodt, *Phys. Rev. B* 45 (1992) 1829.
- [4.44] H.P. Lang, V. Thommen-Geiser and R. Wiesendanger, *Ultramicroscopy* 42-44 (1992) 624.
- [4.45] H.P. Lang, V. Thommen-Geiser and H.-J. Güntherodt, accepted for publication in *J. liq. and mol. crystals* (1994).
- [4.46] B. V. Spitsyn, L. L. Bouilov and B. V. Derjaguin, *J. Cryst. Growth.* 52 (1981) 219.
- [4.47] S. Matsumoto, Y. Sato, M. Kamo and N. Setaka, *Jpn. J. Appl. Phys.*, 21 (1982) L183.
- [4.48] M. Geiss, *Proc. First Int. Symp. on Diamond and Diamond-Like Films, Electrochem. Soc. Proc.* 89-12 (1989) 404.
- [4.49] K. Shenai and B.J. Baliga, *Proc. First Int. Symp. on Diamond and Diamond-Like Films, Electrochem. Soc. Proc.* 89-12 (1989) 405.
- [4.50] C. Wild, N. Herres, J. Wagner, P. Koidl and T. R. Anthony, *Electrochem. Soc. Proc.* 89-12 (1989) 283. Ch. Wild, N. Herres and P Koidl, *J. Appl. Phys.* 58 (1990).
- [4.51] K. Kobashi, K. Nishimura, K. Miyata, K. Kumagai and A. Nakaue. *J. Mater. Res.*, 3 (1990) 2469.
- [4.52] R. E. Clausing, L. Heatherly, E. D. Specht and K. L. More. *Proc. 2nd Int. Conv. on New Diamond Science and Technology, Materials Research Society, Pittsburgh. PA.* 1991, p. 575.
- [4.53] C. Wild, P. Koidl, N. Herres, W Müller-Sebert and T. Eckermann. *Electrochem, Soc. Proc.*, 91-8 1991) 224.
- [4.54] Z. L. Wang, J. Bentley, R. E. Clausing, L. Heatherly and L. L. Horton. in Y. Tzeng, M. Yoshikawa, M. Murakawa and A. Feldman (eds.), *Applications of Diamond Films and Related Materials*, Elsevier, Amsterdam. 1991, p. 489.
- [4.55] R. E. Clausing, L. Heatherly, L. L. Horton, E. D. Specht, G. M. Begun and Z. L. Wang, *Proc. 2nd European Conf. on Diamond. Diamond-like und Related Coatings, Nice, 1991, in Diamond Relat. Mater.*, 1 (1992) 411.

- [4.56] M. Frenklach and K. E. Spear, *J. Mater. Res.*, **3** (1988) 133.
- [4.57] M. Frenklach, *J. Appl. Phys.*, **65** (1989) 5142.
- [4.58] J. C. Angus, F. A. Buck, M. Sunkara, T. F. Groth, C. C. Hayman and R. Gat, *MRS Bull.*, (October 1989) 38.
- [4.59] S. J. Harris and A. M. Weiner, *Appl. Phys. Lett.*, **55** (1989) 2179.
- [4.60] T. R. Anthony, *Mater. Res. Soc. Symp. Proc.*, **162** (1990) 61.
- [4.61] S. J. Harris and A. M. Weiner, *J. Appl. Phys.*, **67** (1990) 6520.
- [4.62] S. J. Harris, *Appl. Phys. Lett.*, **56** (1990) 2298.
- [4.63] Y. Matsui, H. Yabe and Y. Hirose, *Jpn. J. Appl. Phys.*, **69** (1990) 1552.
- [4.64] S. P. Mehandru and A. B. Anderson, *Surf. Sci.*, **248** (1991) 369.
- [4.65] P. Deák, J. Giber and H. Oechsner, *Surf. Sci.*, **250** (1991) 287.
- [4.66] P. K. Bachmann, D. Leers and H. Lydtin, *Diamond Relat. Mater.*, **1** (1991) 1.
- [4.67] T. Tsuno, T. Imai, Y. Nishivayashi, K. Hamada and F. Fujimori, *Jpn. J. Appl. Phys.*, **30** (1991) 1063.
- [4.68] W. Zimmermann-Edling, H.-G. Busmann, H. Sprang and I. V. Hertel, *Ultramicroscopy* **42-44** (1992) 1366.
- [4.69] H. G. Maguire, M. Kamo, H. P. Lang, E. Meyer, R. Wiesendanger and H.-J. Güntherodt, *Diamond Relat. Mater.*, **1** (1992) 634.
- [4.70] H.-G. Busmann, W. Zimmermann-Edling, H. Sprang, H.-J. Güntherodt and I.V. Hertel, *Diamond Relat. Mater.* **1** (1992) 979.
- [4.71] D.J. Chadi, *Phys. Rev. Lett.* **43** (1979) 43.
- [4.72] R. Wiesendanger, D. Bürgler, G. Tarrach and H.-J. Güntherodt, *Surf. Sci.* **232** (1990) 1.
- [4.73] M. G. Lagally, Y.-W. Mo, R. Kariotis, B. S. Schwartzentruber and M. B. Webb, in M. G. Lagally (ed.), *Kinetics of Ordering and Growth at Surfaces*, Plenum, New York, 1990.
- [4.74] K.E. Spear, *J. Am. Ceram. Soc.* **72** (1989) 171.
- [4.75] J.C. Angus and C.C. Hayman, *Science* **241** (1988) 913.
- [4.76] R.C. De Vries, *Annu. Rev. Mater. Sci.* **17** (1987) 161.
- [4.77] D.V. Fedosev, V.P. Varnin and B.V. Deryagin, *Russ. Chem. Rev.* **53** (1984) 435.

- [4.78] A.R. Badzian and R.C. De Vries, *Mater. Res. Bull.* 23 (1988) 385.
- [4.79] K.E. Spear and M. Frenklach, *Proc. First Int. Symp. on Diamond and Diamond-Like Films, Electrochem. Soc. Proc.* 89-12 (1989) 122.
- [4.80] M. Kamo, H. Yurimoto and Y. Sato, *Appl. Surf. Sci.* 33/34 (1988) 553.
- [4.81] P. G. Lurie and J. M. Wilson, *Surf. Sci.*, 65 (1977) 543.
- [4.82] B. B. Pate, *Surf. Sci.*, 165 (1986) 83.
- [4.83] T. E. Derry, C. C. P. Madiba and J. P. F. Sellschop, *Nucl. Instrum. Methods, Phys. Res.* 218 (1983) 559.
- [4.84] T. E. Derry, L. Smit and J. F. van der Veen, *Surf. Sci.*, 167 (1986) 502.
- [4.85] A. V. Hamza, G. D. Kubiak and R. H. Stulen, *Surf. Sci.*, 206 (1988) L833.
- [4.86] A. V. Hamza, G. D. Kubiak and R. H. Stulen, *Surf. Sci.*, 237 (1990) 35.
- [4.87] H.-G. Busmann, H. Sprang, I.V. Hertel, W. Zimmermann-Edling and H.-J. Güntherodt, *Appl. Phys. Lett.* 59 (1991) 295.
- [4.88] R.E. Thomas, R.A. Rudder and R.J. Markunas, *J. Vac. Sci. Technol. A* 10 (1992) 2451.

Appendix A

List of Publications

HTSC single crystals

- 01 H.P. Lang, J.P. Ramseyer, D. Brodbeck, T. Frey, J. Karpinski, E. Kaldis, Th. Wolf: *Atomic Resolution of Single Crystalline $Y_2Ba_4Cu_{6+N}O_{14+N}$ ($N=0,1,2$) and laser-ablated thin film $YBa_2Cu_3O_7$ HT_cSC by STM*, Proceedings of STM'91 International Conference, Interlaken, Ultramicroscopy 42-44 (1992) 715-720.
- 02 H.P. Lang and H.-J. Güntherodt: *Surface structure of cleaved $Bi_2Sr_{2.2}M_{0.8}Cu_2O_{8+\delta}$ single crystals ($M = Ca, La$) imaged by STM*, Helv. Phys. Acta 66 (1993) 65-66.
- 03 J. Karpinski, H. Schwer, K. Conder, E. Jilek, E. Kaldis, C. Rossel, H.P. Lang, T. Baumann: *High oxygen pressure ($P_{O_2} < 3000$ bar) synthesis and properties of $YBaCuO$ Phases*, Proceedings of World Congress on Superconductivity, Munich, Applied Superconductivity, 1 (1993) 333-349.
- 04 H.P. Lang, J. Karpinski, E. Kaldis, J.-P. Ramseyer and H.-J. Güntherodt: *Atomic force microscopy study of the fractal shape of residual barium cuprate / copper oxide flux on the surface of $Y_2Ba_4Cu_7O_{15}$ and $YBa_2Cu_4O_8$ single crystals*, J. Vac. Sci. and Technology, Proc. STM'93 International Conference, Beijing, will be published (1994).

YBCO thin films

- 05 H.P. Lang, T. Frey and H.-J. Güntherodt: *Atomic Resolution and Nanostructure of $YBa_2Cu_3O_7$ Laser-Ablated Thin Films Studied by Scanning Tunneling Microscopy (STM)*, Europhys. Lett. 15 (1991) 667-670.
- 06 H.P. Lang, T. Frey, R. Sum and H.-J. Güntherodt: *Atomic Resolution and Nanostructure of $YBa_2Cu_3O_{7-\delta}$ Laser-Ablated Epitaxial Thin Films on Various Substrates Studied by Scanning Tunneling Microscopy*, in *EMRS/ICAM '91 Proceedings, High T_c Superconductor Thin Films*, L. Correra (Editor), Elsevier Science Publishers B.V. (1992) 789-794.
- 07 H.P. Lang, T. Frey, R. Sum and H.-J. Güntherodt: *Atomic Resolution and Nanostructure of $REBa_2Cu_3O_{7-\delta}$ ($RE=Er, Eu, Ho$ and Y) Laser-Ablated High T_c Superconductor Films Studied by Scanning Tunneling Microscopy*, L'actualité chimique, Mars-Avril 1992, 165-167, (Proc. Nanoscope Users Meeting, Mulhouse 1991, p. 8.).
- 08 H.P. Lang, H. Haefke, G. Leemann and H.-J. Güntherodt: *A Study of Growth and Structure of $YBa_2Cu_3O_{7-\delta}$ Thin Films*, Conference Proceedings of 3rd International Sympo-

- sium On Trends and New Applications in Thin Films (TATF 1991), Strasbourg, Le Vide, les Couches Minces - Supplément au n° 259 (1991) 38-40.
- 09 D.G. Schlom, D. Anselmetti, J.G. Bednorz, R. Broom, A. Catana, T. Frey, Ch. Gerber, H.-J. Güntherodt, H.P. Lang, J. Mannhart: *Screw Dislocation Mediated Growth of Sputtered and Laser-Ablated $YBa_2Cu_3O_{7-\delta}$ Films*, Z. Phys. B 68 (1992) 163-175.
 - 10 F. Baudenbacher, K. Hirata, P. Berberich, H. Kinder, W. Assmann, and H. P. Lang: *Extremely smooth YBCO-Films on MgO with high critical current densities*, Physica C 185-189 (1991) 2177-2178.
 - 11 H. Haefke, H.P. Lang, G. Leemann, and H.-J. Güntherodt: *Preparation of $Y_1Ba_2Cu_3O_{7-\delta}$ thin films with thickness gradients for studying different growth stages by scanning tunneling microscopy*, Appl. Phys. Lett. 60 (1992) 3054.
 - 12 H.P. Lang, H. Haefke, G. Leemann, and H.-J. Güntherodt: *Scanning Tunneling Microscopy Study of different growth stages of $YBa_2Cu_3O_{7-\delta}$ thin films*, Physica C 194 (1992) 81-91.
 - 13 H.P. Lang, H. Haefke, G. Leemann and H.-J. Güntherodt: *Surface structure of thick $YBa_2Cu_3O_{7-\delta}$ films*, Helv. Phys. Acta 65 (1992) 864-865.
 - 14 H. Haefke, H.P. Lang, R. Sum and H.-J. Güntherodt, L. Berthold and D. Hesse: *Mg_2TiO_4 as a novel substrate for high-temperature superconducting thin films*, Appl. Phys. Lett. 61 (1992) 2359-2361.
 - 15 H.P. Lang, R. Sum, J.-P. Ramseyer, H. Haefke and H.-J. Güntherodt: *STM study of $YBa_2Cu_3O_{7-\delta}$ thin film growth on $MgO(001)$* , Proc. ICMAS-92, Paris (21-22 Oct. 92) p. 209-213.
 - 16 D. Hesse, L. Berthold, H. Haefke, H.P. Lang, R. Sum, and H.-J. Güntherodt: *Structure and growth of $YBa_2Cu_3O_{7-\delta}$ thin films on $Mg_2TiO_4(001)$, I. Growth conditions and film structure: transmission electron microscopy*, Physica C 202 (1992) 277-288.
 - 17 H.P. Lang, H. Haefke, R. Sum, H.-J. Güntherodt, L. Berthold, and D. Hesse: *Structure and growth of $YBa_2Cu_3O_{7-\delta}$ thin films on $Mg_2TiO_4(001)$, II. Surface morphology: scanning probe methods*, Physica C 202 (1992) 289-297.
 - 18 H. Haefke, H.P. Lang, R. Sum, H.-J. Güntherodt, L. Berthold, and D. Hesse: *Growth and structure of $YBa_2Cu_3O_{7-\delta}$ thin films studied by scanning tunneling and electron microscopy*, Thin solid films 228 (1993) 173-177.
 - 19 L. Berthold, D. Hesse, R. Sum, H.P. Lang, H. Haefke, and H.-J. Güntherodt: *Structure and growth of $YBa_2Cu_3O_{7-\delta}$ thin films on $Mg_2TiO_4(001)$ - Part I: Growth conditions and film structure*, Helv. Phys. Acta 66 (1993) 61-62.
 - 20 R. Sum, H.P. Lang, H. Haefke, H.-J. Güntherodt, L. Berthold and D. Hesse: *Structure and growth of $YBa_2Cu_3O_{7-\delta}$ thin films on $Mg_2TiO_4(001)$ - Part II: Orientation and growth morphology*, Helv. Phys. Acta 66 (1993) 63-64.
 - 21 H.P. Lang, R. Sum, H. Haefke, and H.-J. Güntherodt: *Surface Morphology of $YBa_2Cu_3O_{7-\delta}$ Thin Films on $SrTiO_3(100)$ Studied by Scanning Tunneling Microscopy*, Journal of Alloys and Compounds, 195 (1993) 97-100.

- 22 D. Hesse, L. Berthold, R. Sum, H.P. Lang, H. Haefke and H.-J. Güntherodt: *Bulk and surface structure of epitaxial $YBa_2Cu_3O_{7-\delta}$ thin films grown on $Mg_2TiO_4(001)$ substrate layers: Part I. Bulk structure investigated by TEM*, Journal of Alloys and Compounds, 195 (1993) 109-112.
- 23 R. Sum, H.P. Lang, H. Haefke, L. Berthold, D. Hesse, and H.-J. Güntherodt: *Bulk and surface structure of epitaxial $YBa_2Cu_3O_{7-\delta}$ thin films grown on $Mg_2TiO_4(001)$ substrate layers: Part II. Orientation and surface structure*, Journal of Alloys and Compounds, 195 (1993) 113-116.
- 24 K. Hirata, F. Baudenbacher, H.P. Lang, H.-J. Güntherodt and H. Kinder: *Scanning Tunneling Microscopy Study on $YBa_2Cu_3O_{7-\delta}$ Films with Growth Stop by observing Reflection High-Energy Electron Diffraction Oscillations*, Journal of Alloys and Compounds, 195 (1993) 105-108.
- 25 H. Kinder, F. Baudenbacher, P. Berberich, S. Corsepius, O. Eibl, H.J. Güntherodt, K. Hirata, H.P. Lang, W. Prusseit, and M. Zwerger, *Epitaxial YBCO Films on MgO, SrTiO₃, Si and GaAs by thermal co-evaporation*, in: *Electronic properties of High- T_c superconductors*, ed. H. Kuzmany, M. Mehring, J. Fink, Springer Series in Solid State Sciences, Vol. 113 (1993) 45-49.
- 26 R. Sum, R. Lüthi, H.P. Lang, and H.-J. Güntherodt: *Single crystal substrates for thin film growth of HT_cSC studied by scanning force microscopy*, Helv. Phys. Acta 66 (1994) 883-884.
- 27 H.J. Scheel, C. Klemenz, F.-K. Reinhart, H.P. Lang and H.-J. Güntherodt: *Monosteps on extremely flat LPE-grown surfaces of $YBa_2Cu_3O_{7-x}$* , Appl. Phys. Lett. (1994), submitted.
- 28 R. Sum, R. Lüthi, H.P. Lang and H.-J. Güntherodt: *Scanning force microscopy on polished single crystalline $SrTiO_3(100)$ substrates used for high T_c superconductor thin film deposition*, Proceedings M²S-HTSC IV, Grenoble 1994 (submitted).
- 29 H.P. Lang, R. Sum, N.D. Zakharov, D. Hesse, J.-P. Ramseyer and H.-J. Güntherodt: *$ErBa_2Cu_4O_8(001)$ Thin Films Studied by Scanning Tunneling Microscopy and High Resolution Transmission Electron Microscopy*, Proceedings M²S-HTSC IV, Grenoble 1994 (submitted).
- 30 R. Sum, H.P. Lang and H.-J. Güntherodt: *Pulsed laser deposition and nanometer scale characterization of $YBa_2Cu_3O_{7-\delta}$ thin films by scanning probe methods*, Proceedings E-MRS Spring 1994 (submitted).

Graphite Intercalation Compounds

- 31 H.P. Lang, V. Thommen-Geiser, and R. Wiesendanger: *Scanning Tunneling Microscopy Study of Ternary Alkali-Metal Graphite Intercalation Compounds*, Proceedings of STM'91 International Conference, Interlaken, Ultramicroscopy 42-44 (1992) 624-629.
- 32 H.P. Lang, R. Wiesendanger, V. Thommen-Geiser, and H.-J. Güntherodt: *Atomic Resolution Surface Studies of Binary and Ternary Alkali-Metal-Graphite Intercalation Compounds by Scanning Tunneling Microscopy*, Phys. Rev. B 45 (1992) 1829-1837.

- 33 H.P. Lang, V. Thommen-Geiser and H.-J. Güntherodt: *Atomic resolution surface imaging of binary and ternary stage 1 alkali metal graphite intercalation compounds by scanning tunneling microscopy*, ISIC 7 Proceedings, accepted for publication in: Journal of liquid and molecular crystals (1994).

Diamond

- 34 H.G. Maguire, M. Kamo, H.P. Lang, H.-J. Güntherodt: *Localised Structure in Non-Conducting and Conducting Homoepitaxial Diamond Films*, Ultramicroscopy 42-44 (1992) 689-695.
- 35 H.G. Maguire, H.P. Lang, M. Kamo: *Tunneling and Force Microscopy of Various Diamond Surfaces*, Proc. 42nd Diamond Conference, Oxford 1991, 3.1.
- 36 H.G. Maguire, M. Kamo, H.P. Lang, E. Meyer, R. Wiesendanger, H.-J. Güntherodt: *The structure of conducting and non-conducting homoepitaxial diamond films*, Proc. 2nd Conf. on Diamond and Related Materials. Diamond and Related Materials 1 (1992) 634-638.
- 37 H.G. Maguire, M. Kamo, H.P. Lang, and H.-J. Güntherodt: *Surface Morphology Determination of LPCVD Homoepitaxial Diamond Using Scanning Tunneling and Atomic Force Microscopy*, 1st Intl. Symp. on Atomically Controlled Surfaces and Interfaces (1991) Tokyo, Japan, Applied Surface Science 60/61 (1992) 301-307.
- 38 H.G. Maguire, M. Kamo, H.P. Lang, and H.-J. Güntherodt: *Surface morphology of Epitaxial Diamond in tribology*, Nordtrib '92, Tribologia volume 11, 2 (1992) 243.
- 39 H.G. Maguire, H.P. Lang, and H.-J. Güntherodt: *Scanning Probe Microscopy Determination of Homoepitaxial Diamond Surface Morphology*, Proc. 43rd Diamond Conference, Cambridge 1992, to be published.
- 40 H.G. Maguire, M. Kamo, H.P. Lang and H.-J. Güntherodt, *Multiphase surface morphologies of doped homoepitaxial diamond films*, Applied Surface Science 75 (1994) 144-150.

Fullerenes

- 41 M. Kraus, S. Gärtner, M. Baenitz, M. Kanowski, H.M. Vieth, C.T. Simmons, W. Krätschmer, V. Thommen, H.P. Lang, H.J. Güntherodt, and K. Lüders: *Investigations on superconducting $RbTl_{1.5}$ - doped fullerene*, Europhys. Lett. 17 (1992) 419-422.
- 42 H.P. Lang, V. Thommen-Geiser, J. Frommer, A. Zahab, P. Bernier, and H.-J. Güntherodt: *Scanning tunneling microscopy study of C_{60} on polycrystalline platinum*, Europhys. Lett. 18 (1992) 29-32.
- 43 H.P. Lang, K. Lüders, R. Wiesendanger, M. Kraus, S. Gärtner, W. Krätschmer, and H.-J. Güntherodt: *Scanning Tunneling Microscopy Study of granular C_{60} and $(MTl_{1.5})_3C_{60}$ ($M=K,Rb$)*, Physica B 182 (1992) 223-226.
- 44 H.P. Lang, V. Thommen-Geiser, C. Bolm, M. Felder, J. Frommer, R. Wiesendanger, R. Schlögl, A. Zahab, P. Bernier, G. Gerth, D. Anselmetti, and H.-J. Güntherodt: *Determination of C_{60} / C_{70} Ratios in Fullerene Mixtures and Film Characterization by Scanning Tunneling Microscopy*, Appl. Phys. A 56 (1993) 197-205.

- 45 S. Behler, H.P. Lang, S. Pan, V. Thommen-Geiser, and H.-J. Güntherodt: *Imaging C₆₀ fullerite at 4.5 K by scanning tunneling microscopy*, Z. Phys. B (Rapid Note) 91 (1993) 1-2.
- 46 H.P. Lang, V. Thommen-Geiser, R. Hofer and H.-J. Güntherodt: *Surface imaging by scanning tunneling microscopy of C_{60/70} thin films on Au(111) with different C₆₀ / C₇₀ ratios*, in *Electronic Properties of Fullerenes*, Springer Series in Solid-State Sciences 117 (ed. H. Kuzmany, J. Fink, M. Mehring, S. Roth), pp. 228-231 (1994).
- 47 S. Behler, H.P. Lang, S.H. Pan, V. Thommen-Geiser, R. Hofer, M. Bernasconi and H.-J. Güntherodt: *Low temperature scanning tunneling microscopy study of C₆₀ fullerite*, in *Electronic Properties of Fullerenes*, Springer Series in Solid-State Sciences 117 (ed. H. Kuzmany, J. Fink, M. Mehring, S. Roth), pp. 232-235 (1994).
- 48 H.P. Lang, V. Thommen-Geiser and H.-J. Güntherodt: *Scanning tunneling microscopy study of fullerene thin films on Au(111)*. ISIC 7 Proceedings, accepted for publication in: Journal of liquid and molecular crystals (1994).
- 49 H.P. Lang, V. Thommen-Geiser, K. Lüders, M. Kraus, M. Baenitz and H.-J. Güntherodt: *Scanning tunneling microscopy study of granular intercalated fullerenes*, ISIC 7 Proceedings, accepted for publication in Journal of liquid and molecular crystals (1994).
- 50 H.P. Lang, K.M. Heeger, V. Thommen-Geiser, and H.-J. Güntherodt: *Determination of the C₇₀/C₆₀ Ratio on fullerene thin films in dependence on the sublimation distance and the substrate temperature using scanning tunneling microscopy*, will be published in: Phil. Mag. B (1994).
- 51 H.P. Lang, R. Wiesendanger, V. Thommen, R. Hofer and H.-J. Güntherodt: *Local Transformation of C₆₀ fullerite into a new amorphous phase of carbon using a STM*, J. Vac. Sci. and Technology, Proc. STM'93 International Conference, Beijing, will be published (1994).
- 52 R. Lüthi, H. Haefke, E. Meyer, L. Howald, H.P. Lang, G. Gerth and H.-J. Güntherodt: *Frictional and atomic-scale study of C₆₀ thin films by scanning force microscopy*, will be published in: Z. Phys. B (1994).
- 53 St. Kluthe, J. Roos, M. Mali, D. Brinkmann, H.P. Lang, V. Thommen-Geiser, H.-J. Güntherodt: *¹³C NMR in Rb₃C₆₀ samples - temperature and pressure dependence of the relaxation*, will be published in the proceedings of Kirchberg Intl. Winter School on Fullerenes (1994).
- 54 M. Warden, R. Schauwecker, P. Erhart, V.A. Ivanshin, H. Keller, H.-J. Güntherodt, H.P. Lang and V. Thommen-Geiser: *Magnetic and superconductivity properties of Rb₃C₆₀*, Proceedings M²S-HTSC IV, Grenoble 1994 (submitted).
- 55 G. Els, P. Lemmens, G. Güntherodt, H.P. Lang, V. Thommen-Geiser and H.-J. Güntherodt: *Determination of the Superconducting Energy Gap of Rb₃C₆₀ by Raman Scattering*, Proceedings M²S-HTSC IV, Grenoble 1994 (submitted).

Miscellaneous

- 56 J. Eitle, P. Gantenbein, H.P. Lang and P. Oelhafen, E. Zuberbühler, D. Mathys and R. Guggenheim: *Properties of Spectral Selective Nb-Films*, Proc. International Symposium on Optical Materials Technology for Energy Efficiency and Solar Energy Conversion XI, May 18-22, 1992, Toulouse-Labege (France).
- 57 D. Anselmetti, M. Dreier, J. Frommer, J. Fünfschilling, G. Gerth, H.-J. Güntherodt, H. Haefke, H.-R. Hidber, L. Howald, H.J. Hug, T.H. Jung, H.P. Lang, R. Lüthi, E. Meyer, A. Moser, I. Parashikov, P. Reimann, T. Richmond, M. Rüetschi, H. Rudin, U.D. Schwarz, U. Stauffer, R. Sum (editor: U. Dammer), *Scanning Probe Microscopy for Industrial Applications: Selected examples*, Scanning 15 (1993) 257.
- 58 H.P. Lang, A. Rossberg, M. Piechotka and E. Kaldis: *Layer-by-layer etching of mercuric iodide crystals in the atomic force microscope*, J. Cryst. Growth (submitted).

Appendix B

Oral presentations

HTSC single crystals

- T01 16.8.91: *Atomic resolution of single crystalline YBCO $246+N$ ($N=0,1,2$) and laser-ablated YBCO 123 films by STM*, STM '91 International Conference, Interlaken.
- T02 12.9.91: *STM Untersuchungen an YBCO $246+N$ ($N=0,1,2$) Einkristallen*, Seminarvortrag ETH Zürich Höggerberg.
- T03 1.10.92: *Surface Structure of Cleaved $Bi_2Sr_{2.2}M_{0.8}Cu_2O_{8+\delta}$ Single Crystals ($M=Ca, La$) imaged by Scanning Tunneling Microscopy*, SPG Basel (Reunion d'Automne, 1992).
- T04 12.8.93: *AFM study of the fractal shape of residual $BaCuO_2$ flux on the surface of $Y_2Ba_4Cu_7O_{15}$ and $YBa_2Cu_4O_8$ single crystals*, 7th International Conference on Scanning Tunneling Microscopy, Beijing (China).

YBCO thin films

- T05 26.4.91: *Atomare Auflösung und Nanostruktur von laser-ablatierten YBCO Hochtemperatursupraleiterfilmen mit STM*, Karlsruher HT_cSL Treffen, Karlsruhe (Deutschland).
- T06 29.5.91: *Atomic resolution and nanostructure of laser-ablated thin YBCO films studied by STM*, EMRS/ICAM 91 Spring Meeting, Strasbourg (France).
- T07 10.7.91: *Atomic resolution and nanostructure of laser-ablated thin REBCO films studied by STM*, Nanoscope User Meeting 91, Mulhouse (France).
- T08 29.11.91: *STM an YBCO Oberflächen*, Seminarvortrag an der Technischen Universität München (Gruppe Prof. H. Kinder).
- T09 23.1.92: *Beziehungen zwischen Mikrostruktur und supraleitenden Eigenschaften der Hochtemperatursupraleiter*, Supra 2+ Workshop, Gwatt.
- T10 17.3.92: *Abbildung atomarer Stufen- und Gitterstrukturen auf laserablatierten $YBa_2Cu_3O_{7-\delta}$ Filmen mit dem Rastertunnelmikroskop*, Frühjahrstagung der DPG 1992 in Regensburg.
- T11 8.4.92: *Different growth stages of thin $YBa_2Cu_3O_{7-\delta}$ films observed by STM*, SPG Neuchâtel (Reunion de printemps, 1992).

- T12 9.4.92: *STM Untersuchung verschiedener Wachstumsstadien dünner $YBa_2Cu_3O_{7-\delta}$ Schichten*, HTcSL Treffen Karlsruhe (Deutschland).
- T13 21.10.92 *STM study of $YBa_2Cu_3O_{7-\delta}$ thin film growth on $MgO(001)$* , ICMAS 92, Paris.
- T14 3.11.92 *Surface Morphology of $YBa_2Cu_3O_{7-\delta}$ thin films on $SrTiO_3(100)$ studied by STM/SFM*. E-MRS Fall Meeting, Strasbourg.
- T15 7.6.93: *Rastertunnelmikroskopie an Hochtemperatursupraleiter-Schichten und -Einkristallen*, Seminarvortrag, Institut für angewandte Physik, Univ. Hamburg, Deutschland.
- T16 29.10.93: *Beiträge der Rasterelektronenmikroskopie zur Untersuchung der HTSL*, Zürcher Hochschul-Industrie Seminar, ETH Zürich.
- T17 18.2.94: *Zusammenhänge zwischen Mikrostruktur und makroskopischen Eigenschaften der HTSL – RHEED Oszillationen und MXPS*, NFP 30 Workshop, ABB Baden Dättwil.
- T18 22.3.94: *Abbildung der atomaren Struktur der $YBCO(001)$ Oberfläche mit Rastertunnelmikroskopie und Interpretation mit monochromatischer Röntgenphotoemission*, DPG Frühjahrstagung 1994, Münster, Deutschland.

Graphite Intercalation Compounds

- T19 16.8.91: *STM study of binary and ternary alkali-metal GICS*, STM '91 International Conference, Interlaken.
- T20 17.3.92: *Abbildung der Oberflächenstruktur von undotierten und alkalimetalldotierten C_{60} Filmen mit dem Rastertunnelmikroskop und Vergleich mit Stufe 1 Alkalimetall Graphiteinlagerungsverbindungen (AM-GEV)*, Frühjahrstagung der DPG 1992 in Regensburg.

Fullerenes

- T21 30.1.93: *Preparation of thin fullerene films on $Au(111)$ and characterization by STM*, Edgar-Lüscher Seminar, Serneus (CH).
- T22 24.3.93: *Real space surface structure of fullerene thin films on $Au(111)$ imaged by scanning tunneling microscopy*, SPG Herbsttagung, Neuchâtel.
- T23 2.4.93: *Surface structure of thin fullerene films on $Au(111)$ imaged by scanning tunneling microscopy: Determination of the C_{60} / C_{70} ratio*. 13th General conference of the Condensed Matter Division, European Physical Society, Regensburg, 1993.
- T24 9.6.93: *STM an Fullerenen*, Seminarvortrag, Max-Planck-Institut für Mikrostrukturphysik, Halle, Deutschland.
- T25 14.6.93: *Neue STM Resultate an HTc's und Fullerenen*, Seminarvortrag, Fachbereich Experimentalphysik, Freie Universität Berlin, Berlin, Deutschland.
- T26 13.8.93: *Local transformation of C_{60} fullerite into a new amorphous form of carbon using a STM*, 7th International Conference on Scanning Tunneling Microscopy, Beijing (China).
- T27 24.3.94: *Bestimmung des $C(70)/C(60)$ Verhältnisses in dünnen Fullerschichten mit Rastertunnelmikroskopie in Abhängigkeit von Substrattemperatur und Sublimationsdistanz*, Frühjahrstagung der DPG 1994 in Münster, Deutschland.

Appendix C

Poster presentations

HTSC single crystals

- P01 J. Karpinski, S. Rusiecki, E. Kaldis, S. Jilek, H.P. Lang: *High oxygen pressure investigations in the $Y_2Ba_4Cu_{6+N}O_{14+N}$ family*, Poster presented at EMRS/ICAM '91, Strasbourg, 29.5.91
- P02 J. Karpinski, E. Kaldis, H.P. Lang, C. Rossel, *Single crystals of the Double Chain Compounds $Y_2Ba_4Cu_7O_{14+x}$; Growth and Characterization*. Poster presented at EMRS 92 Fall Meeting, Strasbourg (France), 5.11.92.
- P03 H.P. Lang, J. Karpinski, E. Kaldis, T. Wolf, H.-J. Güntherodt: *Atomic resolution imaging of $Y_2Ba_4Cu_{6+N}O_{14+N}$ ($N=0,1,2$) High T_c superconductors by STM*, Poster presented at HT_cSL Treffen, Karlsruhe, 24.10.91.

YBCO thin films

- P04 H.P. Lang, T. Frey, R. Sum, G. Leemann, E. Kaldis, J. Karpinski, T. Wolf, H. Haefke, J.P. Ramseyer, S. Siegmann, and H.J. Güntherodt: *Structural Investigation of High T_c superconductors by Scanning Tunneling Microscopy*, Poster presented at the 15th Gwatt Workshop on the Phenomenology of superconductivity, Gwatt, 18.11.91.
- P05 H.P. Lang, R. Sum, J.P. Ramseyer and H.J. Güntherodt: *Beziehungen zwischen Mikrostruktur und supraleitenden Eigenschaften der Hochtemperatursupraleiter*, Supra 2+ Workshop, Gwatt, 23.1.92.
- P06 K. Hirata, F. Baudenbacher, H.P. Lang, H.-J. Güntherodt, H. Kinder, *STM study on $YBa_2Cu_3O_{7-x}$ films with growth stop by observing Reflection High-Energy Electron Diffraction Oscillations*. Poster presented at EMRS 92 Fall Meeting, Strasbourg (France), 4.11.92.
- P07 L. Berthold, D. Hesse, R. Sum, H. Haefke, H.P. Lang, H.-J. Güntherodt, *Structure and Growth of $YBa_2Cu_3O_{7-\delta}$ thin films on $Mg_2TiO_4(001)$: Growth conditions and film structure; Transmission electron microscopy*. Poster presented at EMRS 92 Fall Meeting, Strasbourg (France), 6.11.92.
- P08 R. Sum, H.P. Lang, H. Haefke, H.-J. Güntherodt, L. Berthold, D. Hesse, *Structure and Growth of $YBa_2Cu_3O_{7-\delta}$ thin films on $Mg_2TiO_4(001)$: Surface morphology; Scanning probe methods*. Poster presented at EMRS 92 Fall Meeting, Strasbourg (France), 6.11.92.

- P09 H.P. Lang, R. Sum, J.P. Ramseyer and H.J. Güntherodt: *Strukturelle Untersuchungen an dünnen laserablatierten $YBa_2Cu_3O_{7-\delta}$ Schichten*, Poster, NFP 30 Workshop ABB Baden, 5.2.93.
- P10 R. Sum, H.P. Lang, H. Haefke, H.-J. Güntherodt, L. Berthold and D. Hesse, *Surface morphology of $YBa_2Cu_3O_{7-\delta}$ thin films on $\{001\}$ faces of $SrTiO_3$, MgO and Mg_2TiO_4 studied by Scanning Tunneling Microscopy*, 13th General conference of the Condensed Matter Division, European Physical Society, Regensburg, 1.4.93.
- P11 R. Sum, R. Lüthi, H.P. Lang und H.-J. Güntherodt: *Untersuchung der Nanostruktur dünner YBCO Schichten und deren Substrate mittels Rasterelektronenmikroskopie*. Doktorandentreffen Nanotechnologie, Hasliberg, Schweiz, 14.4.94.

Graphite Intercalation Compounds

- P12 H.P. Lang, V. Thommen-Geiser and H.-J. Güntherodt: *Atomic resolution surface imaging of binary and ternary stage 1 alkali metal graphite intercalation compounds by scanning tunneling microscopy*. ISIC 7 (7th International Symposium on Intercalation Compounds), Louvain-la-Neuve, Belgique, 10.5.93.

Diamond

- P13 H.G. Maguire, H.P. Lang, M. Kamo and H.-J. Güntherodt: *Localized structure of homoepitaxial diamond*, Poster presented at STM' 91, Interlaken, 13.8.91

Fullerenes

- P14 S. Behler, H.P. Lang, S.H. Pan, M. Bernasconi, V. Thommen-Geiser and H.-J. Güntherodt: *Imaging C_{60} Fullerenes at 4.5 K by Scanning Tunneling Microscopy*, International Winterschool on Electronic Properties of Novel Materials, Fullerenes and related compounds, Hotel Sonnalp, Kirchberg (Tyrol), Austria, 9.3.93.
- P15 H.P. Lang, V. Thommen-Geiser and H.-J. Güntherodt: *Surface imaging by scanning tunneling microscopy of thin fullerene films on $Au(111)$ with different C_{60} / C_{70} ratios*. International Winterschool on Electronic Properties of Novel Materials, Fullerenes and related compounds, Hotel Sonnalp, Kirchberg (Tyrol), Austria, 9.3.93.
- P16 H.P. Lang, V. Thommen-Geiser and H.-J. Güntherodt: *Scanning tunneling microscopy study of fullerene thin films on $Au(111)$* . ISIC 7 (7th International Symposium on Intercalation Compounds), Louvain-la-Neuve, Belgique, 13.5.93.
- P17 H.P. Lang, V. Thommen-Geiser und H.-J. Güntherodt: *Abbildung und Modifikation dünner $C(60/70)$ Schichten auf Nanometerskala mit dem STM*. Doktorandentreffen Nanotechnologie, Hasliberg, Schweiz, 15.4.94.

Appendix D

Acknowledgements

This work has been realized by contributions and efforts of many, not only of mine. First of all I would like to thank *Prof. H.-J. Güntherodt*, my tutor for the PhD thesis, for his continuous interest in my work and for generously providing me technical equipment and support whenever this was needed. His encouragement to do front-end-research and the possibility to attend many scientific conferences I highly appreciated.

I would like to thank *Prof. H. Rudin* for co-refereeing this thesis.

Funding has been received from the *Swiss National Science Foundation*, the *Kommission zur Förderung der Wissenschaftlichen Forschung (KWF)* and from *Basel-Stadt*.

I would like to thank my current and former colleagues from the Basel superconductivity group for collaboration, stimulating discussions and assistance. Especially, I thank *Robert Sum* for the instantaneous and continuous preparation of HTSC thin films by pulsed laser deposition. His efforts in proof reading this thesis text and his skills to solve any \LaTeX problem I could think of, were essential. I am grateful to *Jean-Pierre Ramseyer* who prepared various types of bulk superconductors and constructed many practical tools, also for preparing many ink-drawings and critically reading the thesis text. *Nils Detlefsen* and *Dirk Noy* contributed during their pre-graduate works interesting new results. The fundamentals of the present work have been established by the former members of this group: *Harald Jenny*, *Tony Frey*, *Gerhard Leemann*, *Stefan Gutzwiller*, *Stephan Schiegg*, *Stefan Siegmann* and *Stephan Clerc*. I especially emphasize the continuous efforts by *Tony Frey* in the preparation of HTSC thin films, even at night using *Prof. J.P. Maier's* laser at the Basel Physics Chemistry Institute.

Without the continuous effort of *Vreni Thommen-Geiser* the fullerene and GIC's research would not have been possible. Her skills in preparing alkali-metal doped fullerenes and graphites are a valuable advantage.

From the former and current members of the Basel STM/AFM group I have learnt many hints and enjoyed many fruitful discussion:

D. Anselmetti, *A. Baratoff*, *St. Behler*, *M. Bernasconi*, *Th. Bonner*, *M. Bopp*, *D. Brodbeck*, *D. Bürgler*, *R. Buser*, *U. Dammer*, *M. Dreier*, *L. Eng*, *O. Fritz*, *J. Frommer*, *W. Gutmannsbauer*, *P. Grütter*, *H. Haefke*, *H. Heinzelmann*, *S. Hild*, *R. Hofer*, *L. Howald*, *H. Hug*, *P. Jess*, *Th. Jung*, *Th. Lacoste*, *R. Lüthi*, *A. Meixner*, *E. Meyer*, *A. Moser*, *G. Overney*, *R. Overney*, *S. Pan*, *I. Parashikov*, *P. Reimann*, *T. Richmond*, *M. Rüetschi*, *L. Scandella*, *Th. Schaub*, *U. Schwarz*, *U. Staufer*, *B. Stiefel*, *P. Streckeisen*, *R. Sum*, *G. Tarrach*, *K. Terashima*, *A. Wadas*, *R. Wiesendanger*, *A. Wolf*, *W. Zimmermann-Edling*.

Thanks to former or current members of other groups in this institute, especially to: *I. Amstutz*, *Th. Enderle*, *R. Lapka*, *B. Walz*, *D. Wirz*, *Th. Zingg*, *B. Zurfluh*.

A special thank is due to the creators of the magnificent SXM image processing software: *D. Brodbeck, D. Bürgler, R. Hofer* and *G. Tarrach*. Especially the efforts by *Remo Hofer* was been appreciated. He incorporated within very short time any additional subroutines in the SXM program which were needed to process my data.

Many manuscripts have been improved by the knowledge of *H. Haefke, J. Frommer* and *T. Richmond*.

I express my thank to the electronic workshop, directed by *H.R. Hidber*, who patiently answered my questions related to VAX-VMS, and the former and current co-workers: *R. Maffolini, M. Monfreda, D. Müller, S. Rüegg, R. Schnyder, A. Tonin*. The mechanical workshops, that of *P. Cattin* and co-workers, especially *W. Roth*, and that of *H. Breitenstein* and his co-worker *S. Messmer*, who realized many essential constructions. *P. Reimann* prepared some BSCCO samples by melt-spinning and splat-cooling. Not to forget is the work by *P. Schmid* and *H. Dingnis*.

I very much appreciated the collaboration of *J. Vetter* in administrative concerns.

I acknowledge following former and current collaborations:

- Aachen, RWTH, II. Phys. Institut: *G. Els* and *G. Güntherodt*, Raman scattering and DC-SQUID experiments on Rb_3C_{60} .
- Basel, Institute of Physics: *S. Behler, S. Pan, P. Jess*, low temperature STM on Rb_3C_{60} .
- Basel, Institute of Physics: *H.-G. Boyen, P. Gantenbein, P. Oelhafen*. MXPS on YBCO.
- Basel, Institute of Physics: *R. Lüthi*, friction force microscopy.
- Basel, Institute of Physics: *R. Seydoux, P. Streckeisen, A. Mazitoff*, NMR on C_{60} and Rb_3C_{60} .
- Basel, Institute of Organic Chemistry: *M. Felder, C. Bolm*, HPLC on $\text{C}_{60/70}$.
- Basel, Institute of Physical Chemistry: *S. Schlag*, fine-grained YBCO.
- Berlin, FU: *M. Kraus, M. Baenitz, M. Kanowski, K. Lüders*, AC-susceptibility, DC-SQUID and NMR on doped fullerenes.
- Frankfurt, Institute of Inorganic Chemistry: *R. Schlögl, H. Werner*, granular C_{60} .
- Frankfurt, HOECHST AG: *P. Häussler, B. Schulte*, MOCVD YBCO films.
- Halle, MPI Mikrostrukturphysik: *L. Berthold, D. Hesse, S. Sens*, TEM, Mg_2TiO_4 .
- Halle, MPI Mikrostrukturphysik: *G. Gerth*, Au films on mica.
- Hamburg, Institute of Applied Physics: *R. Wiesendanger*.
- Lausanne, EPFL Cristallogenese, *C. Klemenz, H.J. Scheel*, LPE YBCO.
- München, TU Garching, *F. BAudenbacher, K. Hirata, H. Kinder*, MBE YBCO.
- Nottingham, Trent University, *H.G. Maguire*, diamond.
- Zürich, ETHZ, *J. Karpinski, E. Kaldis*, YBCO 124 and 247 single crystals.
- Zürich, ETHZ, *A. Rossberg, M. Piechocka, E. Kaldis* HgI_2 .
- Zürich, Physikinstitut, *R. Schauwecker, D. Zech, Ph. Zimmermann, St. Lee, M. Warden, St. Kluthe, P. Erhart, H. Keller*, DC-SQUID, μSR , ESR, NMR on Rb_3C_{60} .

Many interesting discussions are related to *D. Tománek* (Michigan State University), *J.B. Suck* and *J. Halbritter* (KfK Karlsruhe).

I am grateful to *R. Guggenheim, D. Mattis, E. Zuberbühler* and *M. Düggelin* from the Basel Laboratory for Scanning Electron Microscopy for some SEM images and the donation of the Cambridge SEM, which is now operated in the Physics Institute.

Finally, I thank my relatives for supporting me during my studies: my mother and my father – who died in 1983 and 1991 – my sister *Elisabeth, Gerold Scherrer* and my girl-friend *Ruth Nüesch* who have contributed to this work in their special way.

Index

- (SrBiO)₂(CuO₂Ca)_{n-1}CuO₄, 22
BM_rB(CuO₂Ca)_{n-1}CuO₂, 22
BaCuO₂ / CuO flux, 30, 36, 37, 40
Bi₂Sr₂Ca₂Cu₃O₁₀, 20
Bi₂Sr₂LaCu₂O₈, 56
CuO₂ planes, 24
Hg₁Ba₂Ca₂Cu₃O₉, 20
La_{1.85}Ba_{0.15}CuO₄, 20
T_c vs. year, 21
Tl₂Ba₂Ca₂Cu₃O₁₀, 20
YBa₂Cu₃O_{7-δ}, 20
YBa₂Cu₄O₈, thick crystals, 18
Y₂Ba₄Cu_{6+N}O_{14+N}, 22
*sp*² hybridization, 25
*sp*³ hybridization, 25
(Sr_{0.7}Ca_{0.3})_{0.9}Cu₂, 20
(Cs,Rb)₃C₆₀, 224
(K,Tl)₃C₆₀, 224
(Rb,Tl)₃C₆₀, 224
A-B signal, 16
C-D signal, 16
- Activity, 75
Ad-atom, 66
AFM, 15
Allotropes, 25
Amorphous carbon, 25
Amorphous carbon, bonding-type distribution, 222
Angle resolved photoemission, 115
Angular distribution function, 219
Applications of HTSC, 232
Archimedian spiral, 73
Argon glove box, 55, 143
Atomic force microscopy, 15
Au(111) film preparation, 183
Azimute angle, 80
Backscattered electrons, 12
Backward scan, 16, 42
BCF theory, 73
Bi2212, 48
Binary GIC's, 141, 144
Box counting method, 38
Bragg-Brentano geometry, 80
BSCCO 2212, 48
BSCCO 2212 atomic resolution, 56
BSCCO 2212 characterization, 48
BSCCO 2212 SFM, 54
BSCCO 2212 STM, 55
BSCCO 2212 structure, 50
BSCCO 2212 superstructure, 50, 55
BSCCO 2212 TEM, 50
BSCCO structures, 22
BSLCO 2212, 56
C60, (111) face, 177
C60, bandgap, 175
C60, conductivity of monolayers on metal substrate, 178
C60, electronic structure, 175
C60, epitaxial growth, 183
C60, film casting, 178
C60, high pressure transformations, 211
C60, HOMO/LUMO shift, 178
C60, HPLC, 186, 189
C60, interstitials, 205
C60, intramolecular contrast, 209
C60, materials, 227
C60, NMR, 186
C60, pair correlation function, 218
C60, properties, 172
C60, pure film, 195

- C60, purification, 183
- C60, solid, 177
- C60, stacking boundary, 207
- C60, step structure, 191
- C60, structure, 174, 182
- C60, sublimation, 184, 187
- C60, submolecular resolution, 180
- C60, substrate, 179
- C60, TGA/DTA, 185, 187
- C60, twin boundary, 208
- C60, UV-VIS spectroscopy, 185
- C60, vacancy, 205
- C60, variation of coverage, 203
- C60/C70 mixtures, 192
- C70, pure film, 195
- C70/C60 ratio, 186
- C70/C60, dynamic processes, 201
- C70/C60, variation of sublimation distance, 197
- C70/C60, variation of substrate temperature, 200
- Cantilever, 15
- Carbon allotropes, nearest-neighbour distances, 219
- Carbon vaporization experiment, 172
- Ceramic HTSC, 22
- Chadi's notation, 164
- Charge density wave, 141
- Charge reservoir blocks, 24
- Chemical vapour deposition, 60
- Collapsed fullerite, 211
- Collapsed fullerite, angular distribution function, 220
- Collapsed fullerite, bonding-type distribution, 221
- Collapsed fullerite, pair correlation function, 218
- Columnar defect, 127
- Conductivity contrast, 12
- Control interaction, 15
- Critical nucleus, 73
- Crystal defects, 66
- Crystal growth, 46
- Crystallinity, 81
- CuO double chains, 30
- Deflection, 15
- Diamond, 25, 158
- Diamond, (100)2x1, 160
- Diamond, herringbone structure, 160
- Diamond, LPCVD, 158
- Dimer rows, 163
- Distinguish different materials, 42
- Distorted HOPG structure, 179
- Doped fullerenes, 224
- Doped fullerenes, (111)/(311) face, 228
- Doped fullerenes, grain size effects, 227
- Doped fullerenes, penetration depth, 228
- Doped fullerenes, Tl based compounds, 229
- EDAX, 12, 38, 48
- Edge contrast, 12
- Edge dislocation, 66
- EDS, 48
- Epitaxy, 80
- Feedback loop, 15
- FFM, 16, 42
- Flux migration, 41
- Forces in STM, 212
- Forward scan, 16, 42
- Four-quadrant-detector, 16
- Fractal boundary line, 38
- Fractal dimension, 39
- Frank-van-der-Merwe growth, 65
- Friction contrast, 44
- Friction force microscopy, 16, 42
- Friction loop, 42
- Friction properties, 16, 42
- Fullerene, name, 173
- Fullerenes, 25
- Gallery, 140
- Gas phase reaction, 141
- GIC's, staging, 141
- GIC's, X-ray diffraction, 143
- Graphene layer, 140

- Graphite, 25, 137
 Graphite Intercalation Compounds, 140
 Half shadow technique, 64
 Hausdorff dimension, 38
 High pressure experiments, 212
 High resolution electron microscopy, 96
 High-temperature superconductors, 20
 Higher T_c as 132 K, 20
 Hollow core, 127
 HOPG, 137
 HOPG, angular distribution function, 220
 HPLC, 183
 HREM, 96
 HTSC single crystals, 30
 Improved preparation of HTSC, 22
 Indentation, 34
 Infinite layer compound, 20, 22
 Intercalant layer, 140
 Intercalated fullerenes, 224
 K_3C_{60} , 224
 Kink, 66
 Lateral force, 43
 Lattice image, YBCO(001)/(100), 96
 Ledge, 66
 Lenses, 14
 Liquid phase epitaxy, 126
 Liquid phase reaction, 142
 Local probe methods, 14
 LPE, 126
 Materials, 20
 Metalorganic CVD, 100
 Methods, 10
 Microscopical standard techniques, 10
 Modification experiment (YBCO crystals), 34
 Molecular beam epitaxy, 103
 Mosaic spread, 80
 Optical microscopy, 10
 Pair correlation function, 217
 Pair of like sign, 76
 Pair of opposite sign, 75
 Physical vapour deposition, 60
 Piezo positioning system, 14
 Plane tilt contrast, 12
 PLD, 62
 Polarized light, 30
 Positioning system, 14
 Pulsed laser deposition, 62
 Radioastronomy, 172
 Rb_3C_{60} , 224
 Reflection electron microscopy, 10
 RHEED oscillations, 110
 Roughness, 81
 Scanning electron microscopy, 12
 Scanning force microscopy, 15
 Scanning tunneling microscopy, 14
 Screw dislocation, 61, 66, 67
 Seah-Dench plot, 117
 Secondary electrons, 12
 Self-flux technique, 48
 SEM information depth, 12
 SFM, 15
 Shading contrast, 12
 Sign of a screwdislocation, 73
 Spring constant, 43
 Stage-1 GIC's, 143
 Staging, 140
 STM, 14
 Stranski-Krastanov growth, 65
 Sublimation, 182
 Substrate tilt, 108
 Superlattice, 141
 Superstructure, 140, 144
 Superstructure modulation, 50, 55
 Surface wetting, 41
 SXM resolution, 16
 TEM, 50, 93
 TEM, BSCCO(2212), 50
 Ternary GIC's, 150
 Thermal co-evaporation, 103

- Thickness-gradient film, 64, 69, 88
Thin film growth, 65
Thin films, 60
Tip excursion, 213
Torsion, 16
Transmission electron microscopy, 50, 93
Tunneling, 14
Tunneling current, 15
Turbostratic graphite, 25
Twinning, 30
- Vacancy, 66
Vollmer-Weber growth, 65
- X-ray diffraction, 80
XPS, information depth, 117
XRD, ϕ -scan, 80
XRD, Θ -scan, 80
XRD, $\Theta - 2\Theta$ scan, 81
- Yardstick, 39
YBCO, $[2 \ 4 \ (6+N)]$, 22
YBCO, atomic lattices, 34
YBCO, atomic resolution, 112
YBCO, carbonate and hydroxide formation, 119
YBCO, crystal growth, 38
YBCO, degradation, 119, 125
YBCO, film growth, 80
YBCO, film preparation, 63
YBCO, first growth stages, 69
YBCO, growth hills, 71
YBCO, growth pits, 72
YBCO, high pressure synthesis, 31
YBCO, HREM, 96
YBCO, late growth stage, 72
YBCO, lattice parameters, 31
YBCO, MBE, 103
YBCO, phase diagram (p-T), 32
YBCO, photoelectron spectroscopy, 115
YBCO, pinning centres, 61
YBCO, single crystals, 30
YBCO, structural defects, 61
YBCO, structures, 22
YBCO, surface modification, 76
YBCO, TEM, 93
YBCO, thick crystals, 36
YBCO, thin crystals, 32
YBCO, thin films, 60
YBCO, thin films, STM, 69
YBCO, thin films, supercond. props., 69
YBCO, toplayer, 122
YBCO, XPS, 115